ISBN 978-82-326-5256-3 (printed ver.)
ISBN 978-82-326-5974-6 (electronic ver.)
ISSN 1503-8181 (printed ver.)
ISSN 2703-8084 (electronic ver.)

NTNU
Norwegian University of
Science and Technology

Doctoral thesis

Dirren Govender

Doctoral theses at NTNU, 2023:56

NTNU
Norwegian University of
Science and Technology
Thesis for the degree of
Philosophiae Doctor
Faculty of Engineering
Department of Energy and Process Engineering

NTNU

Doctoral theses at NTNU, 2023:56

Dirren Govender

Three-Dimensional Measurement of Azimuthally Forced Flames in an Annular Combustor

NTNU
Norwegian University of
Science and Technology

Dirren Govender

Three-Dimensional Measurement of Azimuthally Forced Flames in an Annular Combustor

Thesis for the degree of Philosophiae Doctor

Trondheim, February 2023

Norwegian University of Science and Technology
Faculty of Engineering
Department of Energy and Process Engineering

NTNU
Norwegian University of
Science and Technology

NTNU
Norwegian University of Science and Technology

Thesis for the degree of Philosophiae Doctor

Faculty of Engineering
Department of Energy and Process Engineering

© Dirren Govender

ISBN 978-82-326-5256-3 (printed ver.)
ISBN 978-82-326-5974-6 (electronic ver.)
ISSN 1503-8181 (printed ver.)
ISSN 2703-8084 (electronic ver.)

Doctoral theses at NTNU, 2023:56

PRINTED IN
NORWAY
NO - 1598

NORDIC SWAN ECOLABEL
Printed matter
2041 0731

Printed by Skipnes Kommunikasjon AS

Preface

This thesis is submitted to the Norwegian University of Science and Technology (NTNU) for partial fulfillment of the requirements for the degree of philosophiae doctor. The doctoral work has been performed at the Department of Energy and Process Engineering (EPT) from November 2018 to November 2022. The work has been supervised by Professor Nicholas A. Worth.

The Ph.D. has been part of the project Breaking the paradigm: A new approach to understanding and controlling combustion instabilities, funded by the European Research Council (ERC) under grant agreement 677931 TAIAC

The thesis consists of 5 chapters and 3 scientific papers. The chapters provide an introduction in thermoacoustics in annular combustors, the experimental setups and methods and data processing techniques used in this thesis. Chapter 4 provides a summary of the research articles which are included in full length at the end of this thesis. Finally, Chapter 5 provides the conclusions and recommendations.

Article I

Tomographic reconstruction of an azimuthally forced flame in an annular chamber
Dirren Govender, Hecong Liu, Fan Peng, Weiwei Cai and Nicholas, A. Worth
Proceedings of the Combustion Institute,

Author's contributions: Dirren Govender and Nicholas A. Worth conceived the idea for this work. Dirren Govender performed the tomographic experiment and performed the preliminary data processing. Hecong Li, Fan Peng and Weiwei Cai used the data to develop the calibration model and applied the reconstruction algorithms. Dirren Govender and Nicholas, A.

Worth analysed the data and wrote the manuscript. All authors read and contributed to the manuscript.

Article II

Large volume scanning laser induced fluorescence measurement of a bluff-body stabilised flame in an annular combustor
Dirren Govender, Samuel Wiseman, James R. Dawson, and Nicholas A. Worth
Experiments in Fluids, 63:62, 23 February 2022

Author's contributions: Dirren Govender, Samuel Wiseman and Nicholas A. Worth conceived the idea for this work. Dirren Govender and Samuel Wiseman performed the Scanning PLIF experiment. Dirren Govender developed the codes for calibration, processing and reconstruction of the three-dimensional FSD fields. Dirren Govender developed the codes for the synthetic PLIF study. Dirren Govender and Nicholas A. Worth analysed the data and wrote the manuscript. All authors read and contributed to the manuscript.

Article III

Scanning PLIF measurement of azimuthally forced swirling flames in an annular combustor
Dirren Govender and Nicholas, A. Worth
Under consideration for Combustion and Flame.

Author's contributions: Dirren Govender and Nicholas A. Worth conceived the idea for this work. Dirren Govender performed the experiment and performed the data processing. Dirren Govender and Nicholas, A. Worth analysed the data and wrote the manuscript. All authors read and contributed to the manuscript.

Trondheim, 10th February 2023
Dirren Govender

Abstract

This thesis aims to better understand thermoacoustic instabilities in annular combustors. Thermoacoustic instabilities are a topic of interest since it is a challenge to operate gas turbines in a lean regime that reduces harmful emissions. Extensive research has gone into understanding thermoacoustics in single-flame burners. However, many gas turbines comprise of closely confined flames in an annular arrangement. Unlike single-flame burners, this configuration can give rise to azimuthal rather than axial modes, which subject flames to both azimuthal and axial pressure and velocity fluctuations. Previous studies have shown that the global Heat Release Rate (HRR) response varies depending on the nature or direction of these azimuthal modes, and the local flame response is often asymmetric, motivating the application of full three-dimensional methods. This thesis applies two different three-dimensional diagnostics to better understand the response of flames in an annular combustor subjected to azimuthal modes.

The first method, Computed Tomography of Chemiluminescence (CTC), is applied to a single swirling flame in an annular combustor subjected to azimuthal spinning modes in the anticlockwise (ACW) and clockwise (CW) directions. When investigating the global HRR response, it was found that the flame response is the same irrespective of mode direction in the absence of flame-flame or flame-wall interaction. Three-dimensional analysis of the single flame, however, showed that the timing of the axial and azimuthal velocity fluctuations played a significant role in the flame response, thus providing insight into the mechanism behind the asymmetry.

Limitations of implementing the CTC method were highlighted, and a second three-dimensional technique, a new variant of Scanning Planar Laser Induced Fluorescence (PLIF), was developed and applied to overcome these drawbacks. This technique was used to study a single flame in a multi-flame annular combustor. The development of this technique is carefully outlined, with a complementary synthetic experiment that helped identify errors in the method. A bias error due to laser sheet orientation with respect to the flame was identified and was overcome by introducing a second orthogonal scan direction. The resulting technique was used to highlight asymmetries in the flame shape due to the annular confinement of an unforced flame without swirl.

Scanning PLIF was then applied in the investigation of the three-dimensional HRR response of flames with and without swirl subjected to spinning and standing modes respectively. In each case, the structure of the flames and the timing between the local phase and oscillation amplitude are identified. In terms of the flame response to standing modes, three cases are presented. A symmetric response is observed at the pressure antinode, whereas an asymmetric response is observed at the pressure node and an intermediate case between the pressure node and antinode. The Scanning PLIF technique is then applied to closely interacting flames subjected to ACW and CW spinning modes. The HRR response is seen to be dependent on the mode direction, as shown in previous studies, with a larger global HRR response to ACW as opposed to CW modes. Given access to the three-dimensional HRR response field, it could be demonstrated that this was due to the timing between the axial velocity and azimuthal velocity fluctuations for the different cases, resulting in a phase shift in the local response in some regions of the flame.

The findings in this thesis help to better understand the flame response when subjected to azimuthal modes and this greater understanding will eventually enable better design of such combustors. This study also provides the necessary background into implementing three-dimensional techniques in annular combustion systems.

Acknowledgements

This journey defined me in many ways, and I would like to thank the people that made it possible. I would first like to thank Nicholas Worth. Nick shaped me into the researcher that I am today. Through his patience and leadership, he taught me what science meant: patience, dedication and, most of all, quality. Our conversations were not limited to research but also shaped how I view life. Thank you, Nick. None of this would be possible without you. I would like to thank my opponents for taking the time to read my thesis. It is an absolute honour to have the leaders in my field as my opponents.

In the field of science, one needs to gauge the bigger picture, defeat the ego and patiently await for the unknown to unravel. It was Samuel Wiseman, (like samwise gamshee), who carried me through my experimental ventures into the depths of Scanning PLIF (MOrdor). I appreciate your teachings and patience, and I owe a lot of what we accomplished to you, Thank you Sam.

Thank you to Jose for your teachings in thermo-acoustics, I was always happy to entertain your curiosity in thermo-acoustics and life, I appreciate your guidance. I would also like to thank Håkon, who provided support in understanding the tempest that is the annular combustor. Your insights were extremely valuable, you were always willing to share your knowledge and your efforts in the lab are invaluable. It was also a pleasure to have someone that knows the struggle. It has been a privilege to stand on the shoulders of giants.

To my lab colleagues Loïc Duffo and Yi Hao. Thank you for the countless help you provided in and outside the lab.

I always found it interesting how nature produces harmonic sinusoidal responses. Life too has its ups and downs and in the cusps is when you find the meaning of friendship. There are many people that made this journey special, in no specific order. My roommates, Loïc and Alisa, who were always

eager to hear my complaints, pushed me up when I was down, and made me realise that every day has a highlight. Yannick (Chan) and Clara, for our many adventures together, your support, your friendship, your laughter and the intensity of boardgames. Yi Hao, thank you for always being there for me, especially your amazing cheese cake, and unbound friendship. Jose thank you for adding a bit of craziness to this adventure. My first office mate Philip, our love for metal was a great start to an amazing friendship, I look forward to many adventures to come. Frida, for always pushing the boundaries of physical activity and inspiring us all, I look forward to seeing you in the Olympics one day. Thanks to Harish for the many theromacoustic and life conversations. To the real machine, Girish, Thanks for making us feel like we were one of the team. To my favourite Canadian, Leon, who always made me want to be the better man. To Olav my fishing buddy, I am always around if you need some good luck. To Vipin for his countless support. To the original pulkers, Marek and Andy, for all the crazy nights out. To Tong, it was a pleasure to have you as a friend. To, Tarik, le boss, thank you for teaching me about France. To Pim for being an amazing ski instructor, looking forward to skiing those bumps with you soon. To Shu for your positivity. To Melissa for the interesting conversations. To Anna for the countless support. To the amazing climbers, Jonas, Thomas, Ben, and Eirik, thank you guys for pushing me up the wall. Elena who motivated me to swim in this ocean of chaos. To Aina for your persistent support. Thank you to my good friends Rafael, Belma, Sondre, Yngve, Marcel, Farid, Hallvard, and Vitor that opened the world up me in many ways. To Srikar, for keeping the party going and always being there for me, thanks bro. To my loving neighbors, Au, Helena, Magnus and Marlin, you guys changed my life, thank you. A special thanks to my close friend, Edda, for always being there for me, and always willing to listen to my Phd drama, I appreciate you. When I look back I see how I have made real bonds and connections to all of you, you were my family away from home, thank you.

To Keegan and Virosha for always showing their support and belief, and to my friends back home (legion of 9). Last and most importantly, I would like to thank my family. To my brothers, Cyan and Sherwin, who were always willing to give me their strength and support. To my parents, it was the countless calls, complaints, encouragement and the belief that you have in me that got me here. This is a dedication to you, mum and dad, you either never had the opportunity or scarified your own so I could have mine. Thank you.

10th February 2023

Dirren Govender

Contents

List of Tables

List of Figures

Nomenclature

The nomenclature describes abbreviations, physical parameters and notation used throughout this thesis. The nomenclature might differ slightly in the individual publications, which are appended at the end of the thesis.

Abbreviations

ACW	Anti-clockwise
AN	Antinode
ART	Algebraic Reconstruction Technique
CTC	Computed Tomography of Chemiluminescence
CT	Computed Tomography
CW	Clockwise
FDF	Flame Describing Function
FFT	Fast Fourier Transform
ff	far field
FOV	Field Of View
HRR	Heat Release Rate
IL	Intermediate location between antinode and node
IRO	Intensified Relay Optics
LOS	Line Of Sight
MART	Multiplicative Algebraic Reconstruction Technique
nf	near field

N	Node
PLIF	Planar Laser Induced Fluorescence
SLPM	Standard litre per minute
SNR	Signal to Noise Ratio
TI	Thermoacoustic Instability
UV	Ultraviolet
VLIF	Volumetric Laser Induced Fluorescence
VOI	Volume of Interest

Latin Symbols

$\mathbf{G}$	Intrinsic Matrix
$\mathbf{R}$	Extrinsic Matrix
FDF	Flame Describing Function
FSD	Flame Surface Density
FTF	Flame Transfer Function
$A_{\pm}$	complex-valued pressure amplitudes of two counter-propagating waves travelling in the axial direction
A_f	Flame surface area
$B_{\pm}$	complex-valued pressure amplitudes of two counter-propagating waves travelling in the azimuthal direction
c	Speed of sound [m/s]
E_{OH}	Flame Object
f	Frequency [Hz]
f_f	Forcing frequency [Hz]
f_{ob}	Object matrix
$k_{\pm}$	Wavenumber of two counter-propagating waves

L	Occupancy rate
Ma	Mach Number
n	Order of azimuthal mode
p	pressure [Pa]
P_r	Projection at each pixel
q	Heat release rate [W]
r	Radial distance from center of bluff body [m]
S_{swirl}	Swirl number
SR	Spin Ratio
T	Time for single oscillation period [s]
t	Time [s]
u	velocity [m/s]
U_b	Bulk velocity [m/s]
W	Weighted matrix

Greek Symbols

ϕ_{sig}	signal generator offset [rad]
χ	Nature angle [rad]
δ	Laser sheet thickness [mm]
$\Delta\delta$	Laser sheet overlap
λ	Wavelength [nm]
λ_c	Convective wavelength [nm]
ω	Angular frequency [Hz]
ϕ	Equivalence ratio
ρ	density [kg/m^3]
Θ	Azimuthal angle around combustor [rad]

θ	Azimuthal angle around bluff body [rad]
Θ_p	spatial offset of speaker pairs [rad]
φ	Position of pressure antinode [rad]

Modifiers

$(\cdot)'$	Fluctuation in $(\cdot)$
$\angle(\cdot)$	Fourier phase of $(\cdot)$
$\hat{(\cdot)}$	Fluctuation in frequency domain of $(\cdot)$
$\langle(\cdot)\rangle$	Spatial average of $(\cdot)$
$\overline{(\cdot)}$	Time average of $(\cdot)$

Somewhere, something incredible is waiting to be known
— *Carl Sagan*

1

Introduction

The advances in emerging economies and the increase in population have resulted in an exponential growth in the global energy demand (Olabi and Abdelkareem 2022). This growth, tied with the prolonged use of fossil fuels in energy production, has led to the presence of dangerously high volumes of greenhouse gases (GHG) in the atmosphere. As a result, the effect of climate change on our world has reached devastating records, with the last decade producing the hottest period over the past 125000 years (Xu et al. 2020). Therefore, immediate goals need to be set to provide effective change. The United Nations Environmental Programme (UNEP) has put forth such goals, with one primary goal being the reduction of 30 gigatonnes of greenhouse gases by the year 2030 (United Nations Environment Programme 2021). UNEP has also identified different sectors where this goal can be achieved, with energy being the most significant sector for improvement, providing the potential of 8.2 gigatonne reduction in GHG emissions. Thus the need for decarbonisation in energy production is of great importance.

Extensive research has gone into cleaner technologies to meet the ever-growing energy demand. However, while there are successful implementations and promise in cleaner technologies such as wind turbines, solar panels and renewables, the energy demand in the near future will rely on existing technologies (Owusu and Asumadu-Sarkodie 2016). Common power-providing technologies such as land-based gas turbines are still likely to provide a significant portion of the global energy demand (Stefan et al. 2022). Gas turbines have been popular in the energy sector due to their compact size, higher power output and fuel type flexibility (Breeze 2016). Gas turbines will therefore be fundamental in the transition to cleaner technologies by helping meet the demand for intermittent renewable energy sources. Thus highlighting the importance of running gas turbines cleaner and in a more environmental manner.

Nitrogen Oxides (NO_x), produced during the combustion of fossil fuels, are a significant source of atmospheric contamination and act as a greenhouse gas. The reaction of NO_x with the atmosphere results in acid rain, photochemical smog, acidification of aquatic ecosystems, and promotes the depletion of the ozone layer (Han et al. 2019). During combustion, the formation of NO_x occurs in three gas-phase chemical reaction pathways: (i) during the oxidation of nitrogen in combustion air, (ii) through the oxidation of fuel nitrogen found in the fuel itself, known as prompt NO_x and, (iii) the nitrogen fixation of hydrocarbon fragments (Srivastava et al. 2005). Pathway (iii) produces the lowest concentration of NO_x while reaction pathway (i) produces the largest, and is also referred to as thermal NO_x. The formation of thermal NO_x is produced at high flame temperatures, usually greater than 1800 K (Sarofim and Flagan 1976). Therefore, an adopted strategy to lower the formation of NO_x is by operating combustion systems within the lean premixed regime (Candel 2002). In this regime, excess air is introduced to keep the flame temperature low (Brewster et al. 1999) and the fuel and air mixture are well mixed or premixed before ignition, providing more homogeneous combustion by limiting high-temperature hot spots in the combustor chamber (Docquier and Candel 2002).

This is an effective strategy as it lowers the formation of NO_x but also maintains the thermal efficiency of the combustor. However, this strategy does not lower the formation of CO_2. Therefore, switching out hydrocarbon fuels with alternatives that produce less carbon dioxide is a potential means to reduce carbon emissions. A viable option is using hydrogen, which allows for a completely carbon-free combustion substitute when produced from renewable sources such as wind or solar (Stefan et al. 2022). While the energy density per unit volume of hydrogen may be lower than conventional fuels, the emission benefit of the fuel makes hydrogen an attractive alternative in the transition to a carbon-free future (Chiesa et al. 2005).

However, running existing equipment with fuels such as hydrogen or operating in new envelopes like the lean regime introduces new challenges to the gas turbine industry. One of these challenges is the susceptibility to thermoacoustic instabilities (TI) (Lieuwen, Timothy C and Yang 2005, Poinsot 2017) during combustion. The occurrence of TI hinders the transition to cleaner gas turbine operations. Therefore, it is important to understand TI better to effectively limit them at the design stage.

1.0.1 An introduction Thermoacoustic Instabilities (TI)

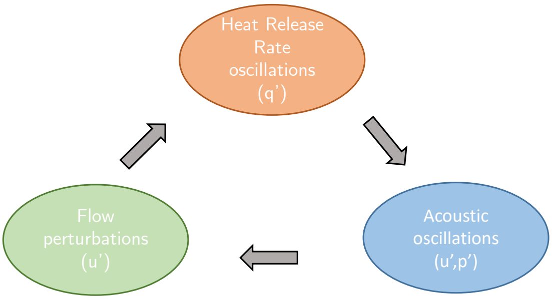

Figure 1.1: Thermoacoustic feedback loop adapted from Sun and Wang (2020). Flow perturbations result in Heat Release Rate oscillations, which in turn creates acoustics oscillations.

Thermoacoustic Instabilities occur due to the coupling of flow and combustion processes to the acoustic resonant modes of the combustor (Candel 2002). To demonstrate the coupling mechanism behind TI, consider a confined, unsteady turbulent flame like the one shown in Fig. 1.2(a). The flame produces an unsteady Heat Release Rate (HRR), q', that generates sound in the form of pressure oscillations, p', that propagate upstream and downstream of the flame. The pressure oscillations propagate through the combustor and reflect at the boundaries. Propagation of the pressure waves back to the flame result in oscillations of the velocity flow field, u', exciting vortical structures in the flow field. Constructive interference results when the system's pressure oscillations and the flame's Heat Release Rate response are in phase, inducing higher oscillations in the flow field, resulting in larger oscillations in the HRR, thus closing a feedback loop. Thermoacoustic instabilities occur when this feedback loop, represented in Fig. 1.1, can self-sustain the oscillation amplitude over time. An example of pressure and HRR oscillations during a self-excited TI for a single confined flame is shown in Fig. 1.2(a). The system is stable at $t = 0$, and the amplitude of oscillations in both pressure and HRR couple at $t > 0$, eventually the oscillations grow in size until a limit cycle is reached at $t > 0.2s$ and large oscillations in both pressure and HRR are sustained.

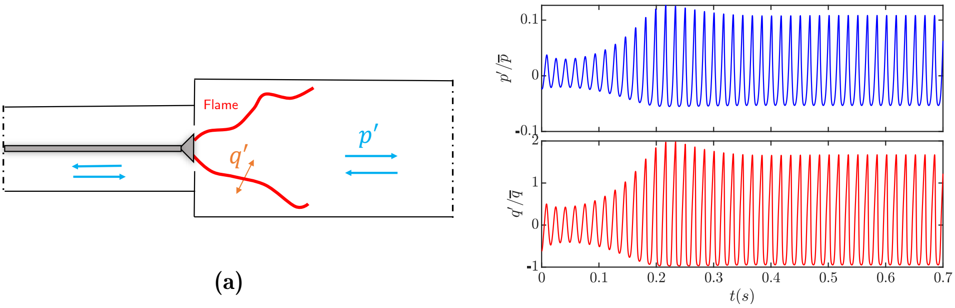

(a)

(b)

Figure 1.2: (a) Representation of a single turbulent flame in a confined geometry. q' represents the unsteady Heat Release Rate fluctuations of the flame, and the blue arrows represent the direction of propagating pressure oscillations, p', in the combustor (b) (Top) pressure oscillations simulated in a single flame confinement shown in (a). (Bottom) Subsequent HRR oscillation of the flame in (a) during a self-excited thermoacoustic instability. Here $\overline{p}$ and $\overline{q}$ represent mean quantities. Adapted from Gopalakrishnan et al. (2022).

The phase required to sustain a self-excited oscillation is given by the Rayleigh criterion (Rayleigh 1878). Rayleigh (1878) postulated that pressure and HRR oscillations need to be in phase ($\pm 90°$) to maintain a self-excited oscillation. Lord Rayleigh used a swinging pendulum to demonstrate that force needs to act on, and not against, an oscillation to provide energy and enhance an oscillation (Rayleigh 1878). A modified version of the Rayleigh criterion is shown below (Lieuwen and Yang 2006):

$$\int_T \int_V p'(x,t) q'(x,t) dt dV \geq \int_T \int_V \sum_i L_i(x,t) dt dV \tag{1.1}$$

where V, T, p', q' and L_i are the volume, time period for a single oscillation, acoustic pressure fluctuation, Heat Release Rate fluctuation, and sources of acoustic energy losses, respectively. The right-hand side of the inequality defines the system damping in the form of viscous or radiative dissipation of acoustic energy at the boundaries (Lieuwen and Yang 2006). The left-hand side of the inequality 1.1, known as the Rayleigh index, defines the local driving force of the acoustic oscillations in the form of heat addition by the unsteady combustion process (Lieuwen and Yang 2006). This inequality states that acoustic oscillations will excite when the rate of energy input to the acoustic field from the combustion process is larger or equal to the rate of acoustic energy dissipated in the combustor or transmitted at the

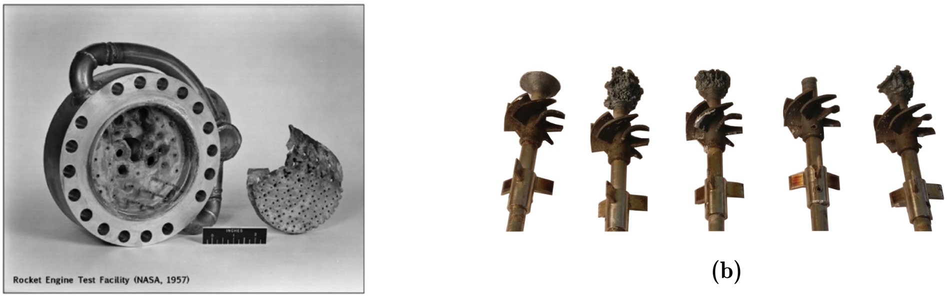

(a)

(b)

Figure 1.3: (a) An example of an engine after a TI during the tests performed by NASA's Saturn V launcher. Adapted from Poinsot et al. (1987). (b) Bluff bodies removed from a pressurised annular combustor after a TI adapted from Indlekofer (2021).

boundaries (Lieuwen and Yang 2006).

The occurrence of TI can be catastrophic. A famous example of the drastic effects of TI occurred in the 1950s during the design of NASA's F-1 rocket engine. NASA set out in a competitive race to quickly design a large-scale rocket engine on their journey to the moon (Oefelein and Vigor 1993). However, testing of the engine resulted in TI that destroyed the rocket engine in a matter of milliseconds, costing the development programme billions of dollars (Oefelein and Vigor 1993). An image showing one of the damaged rocket engines during NASA's testing period is shown in Fig. 1.3(a). It was later discovered that introducing baffles to the rocket engine prevented the occurrence of thermoacoustic instabilities (Oefelein and Vigor 1993). However, the fundamental mechanism of why the baffles prevented the instability was not well known at the time.

In present day, TI is a common challenge in running cleaner gas turbines. Another example of combustor structural damage due to TI is shown in Fig. 1.3(b), which shows a set of bluff bodies that were installed in a lab-scale pressurised annular combustor at the Norwegian University of Science and Technology (NTNU) (Indlekofer 2021). During ethylene combustion, large pressure oscillations caused large flow oscillations in the injector exits that eventually resulted in flame flashback in some injectors of the annular combustor. The bluff body shown on the left of Fig. 1.3(b) was undamaged, but those on the right-hand side of Fig. 1.3(b) have partially melted due to the flame anchoring upstream following flashback. It is, therefore, essential to improve our understanding of such instabilities to eliminate them at the

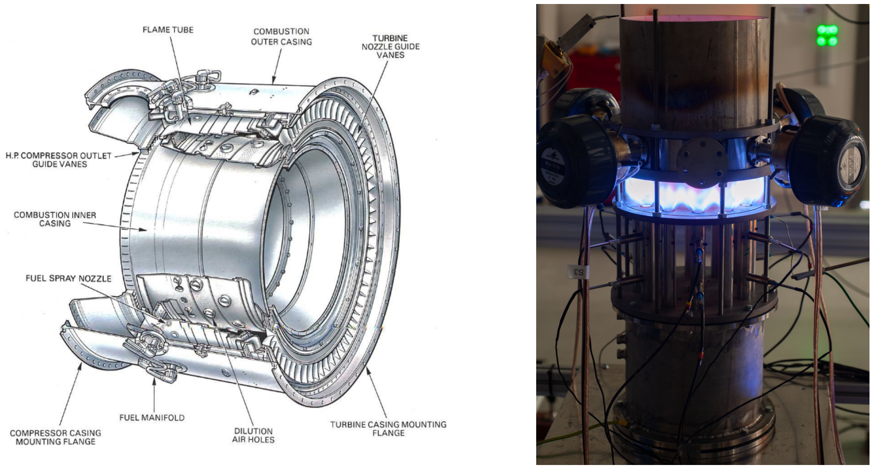

(a)

(b)

Figure 1.4: (a) Common design of an annular combustor outlining different sections of the engine, adapted from Breeze (2016). (b) NTNU lab-scale annular combustor consisting of 12 injector burners, optical access into the combustor shows interaction of flames inside the combustor.

design stage. TI are not only specific to rocket engines but is a common problem in the operation of many practical thermal systems such as boilers/heat exchangers, stationary gas turbines, and aero-engines (Lieuwen, Timothy C and Yang 2005, Poinsot 2017, Mark and Selwyn 2016, Oefelein and Vigor 1993, Huang and Yang 2009).

The Rijke tube displays the simplest form of a TI and consists of a heat source, a vertical tube with open ends and a preheated metal gauze (Rijke 1859, Raun et al. 1993). The heated gauze is placed in the tube to produce sound due to the coupling between the gauze's unsteady heat release rate and the tube's acoustics. This simple setup provides the underlying principle of TI, in which a feedback loop exists between the flame source and acoustics that can be applied to any combustion system. Similarly, a gas turbine is an example of a combustion system that exhibits thermoacoustic instabilities: the flames create a heat source, the fuel-air mixture creates a flow field, and the combustion chamber forms an enclosure. The most commonly used combustor design in land-based gas turbines and aero-engines are the can-annular and annular configurations (Poinsot 2017). The annular design consists of multiple injectors arranged around a continuous annular chamber, as opposed to a can-annular combustor, where each flame is confined in a tube that is arranged in a circle. Two examples showing the design of annular combustors are shown in Fig. 1.4. The annular design helps to achieve uniform combustion with a smaller wall surface area relative to the volume of the combustor (Mark and Selwyn 2016). The design of these combustors promotes a more uniform turbine exit temperature with a lower pressure drop than single burner designs (Mark and Selwyn 2016). These configurations are complex, with multiple highly swirled burners closely arranged circumferentially. TI of premixed flames in a lab-scale annular combustor will be the focus of this thesis, and the following sections are aimed at providing a relevant background in TI as well as motivating the need for advanced measurement methods applied in the current thesis.

1.0.2 Single flame subject to axial excitation

Before introducing TI in annular combustors, it is first worth outlining some features of thermoacoustics in simpler systems consisting of a single flame. The Rayleigh criterion outlines the importance of the relationship between oscillations in pressure and HRR and how the phase or timing between them plays a role in the stability of the system. Early studies by Merk (1957) provided a simplified and common approach to relate oscillations in HRR to oscillations of system parameters such as temperature, pressure, density and the velocity upstream of the flame. The formulation consists of a linear approximation making use of transfer functions, and a modified version from Lieuwen (2009) is shown below:

$$\frac{\hat{q}}{\overline{q}} = F_u \frac{\hat{u}}{\overline{u}} + F_p \frac{\hat{p}}{\overline{p}} + F_\phi \frac{\hat{\phi}}{\overline{\phi}} \tag{1.2}$$

where ϕ represents equivalence ratio, $(\hat{\cdot})$ quantities are Fourier amplitudes, and $(\bar{\cdot})$ refers to temporal mean quantities. The transfer functions, F_u, F_p and F_ϕ, are with respect to oscillations in velocity, pressure and equivalence ratio, respectively. The pressure term in Eq. 1.2 is usually negligible for low Mach number flows since the oscillations in pressure are significantly smaller than those of the velocity oscillations (Polifke 2020). The transfer function F_ϕ is neglected for premixed combustion that minimises variations in ϕ and applies to the flows studied in this thesis. Neglecting these effects, Eq. 1.2 simplifies to the Flame Transfer Function (FTF) for premixed flames:

$$\mathrm{FTF}(\omega) = \frac{\hat{q}(\omega)/\overline{q}}{\hat{u}/\overline{u}} \tag{1.3}$$

where ω representing angular frequency and is related to the excitation frequency (f) by $\omega = 2\pi f$ (Noiray et al. 2008). The $\hat{q}$ and $\hat{u}$ quantities are measured at the injector outlet and the left-hand side of Eq. 1.3 can also be expressed in terms of a gain, $G = |\mathrm{FTF}|$, and phase, $\varphi = arg(\mathrm{FTF})$ (Noiray et al. 2008). The FTF has been extensively used to characterise flame responses to TI due to its simplicity in purely relating the HRR response to the system's acoustic flow disturbances (Schuller et al. 2020). Furthermore, the combination of the FTF with lower-order modelling allows a systems stability to be predicted and this approach has been extensively tested (Boyer and Quinard 1990, Chao and Law 1993, Clavin and Sun 1991, Darabiha and Candel 1992, Fleifil et al. 1996, Law 1989, Schadow et al. 1992). The ability to predict system stability by use of low order modelling and the FTF reduces the need for parametric studies using high fidelity Large Eddy Simulations (LES) (Wolf et al. 2012, Hernández et al. 2013, Chen et al. 2019) or Direct Numerical Simulation (DNS) (Courtine et al. 2015, Kashinath et al. 2013, Hemchandra 2012, Wiseman et al. 2021), saving on hours of computational cost (Polifke 2020). However, the FTF must be determined to completely describe the combustion system. This is mainly done through experiments (Ducruix et al. 2000, Kunze et al. 2004, Külsheimer and Büchner 2002, Schuller et al. 2003, Schuermans et al. 2003, Lawn and Schefer 2006, Palies et al. 2010, Lawn and Polifke 2004, Hirsch et al. 2005, Alemela et al. 2010, Kim et al. 2010, Cuquel et al. 2013, Æsøy et al. 2020, Nygård and Worth 2021), or by use of Computational Fluid Dynamics (CFD) or simulation of reacting flows (Courtine et al. 2015, Ducruix et al. 2000, Armitage et al. 2006). Experimentally, the FTF is determined by applying external acoustic fluctuations to a stable flame, usually by installing a set of speaker pairs downstream of a burner (Kunze et al. 2004, Hirsch et al. 2005, Æsøy et al. 2020). The speakers are operated across a range of frequencies and amplitudes that introduce fluctuations in the duct of the flame and, therefore, oscillation in the velocity. The velocity and HRR response is measured for each forcing level, and an FTF is constructed.

The FTF has proven useful in predicting the linear stability of fluctuations in simple burner setups. However, the FTF does not provide information on a system's oscillation amplitude or growth rates; therefore, the FTF can not predict the limit cycle of the system (Stow and Dowling 2004). The Flame Describing Function (FDF) extends the dependence of the FTF to the non-linear regime and is defined by (Dowling 1997):

$$\mathrm{FDF}(\omega, \hat{u}/\overline{u}) = \frac{\hat{q}(\omega, \hat{u}/\overline{u})/\overline{q}}{\hat{u}(\omega)/\overline{u}} \tag{1.4}$$

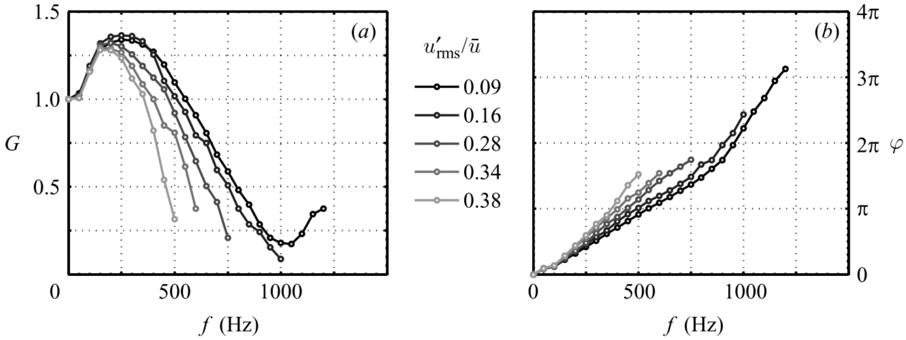

Figure 1.5: Experimental Flame Transfer Functions at different forcing levels representing the (a) Gain and (b) Phase. Adapted from Noiray et al. (2008).

The FDF explicitly includes the velocity dependence on the HRR fluctuations and accounts for the non-linear regime (Rani and Rani 2018). Nonlinearity was seen by saturation of the FTF at large amplitude oscillations (Noiray et al. 2008, Balachandran et al. 2005). Using the FDF in combination with an acoustic solver, one can predict the limit cycle amplitude when the HRR saturates (Noiray et al. 2008, Stow and Dowling 2001). Figure 1.5 provides an example of a range of FTFs for different forcing levels showing the (a) Gain, and (b) Phase, adapted from Noiray et al. (2008). Several features of FTFs are presented here. Firstly, the FTF produces a unity gain in the absence of forcing. This feature is always true for perfectly premixed flames due to the flame's slow response to the fuel flow rate and, therefore, results in a slow response in the HRR response. The equivalence ratio is constant for premixed flames and changes in the mass flow will result in an equivalent change in HRR (Polifke and Lawn 2007). This feature would change for non-premixed flames and falls out of the scope of this thesis. Secondly, the phase evolves linearly, representing the time lag between the flame response and the velocity oscillation at the location of the measurement. The time lag is usually constant for a forcing level and is sensitive to the flow velocity and flame length (Noiray et al. 2008). The third notable feature is the low-pass filter behaviour of the flame response at high frequencies. Large frequencies produce small wavelength disturbances resulting in smaller fluctuations or flame wrinkling, and hence a lower gain is achieved (Ducruix et al. 2000).

The study by Balachandran et al. (2005) investigated the origin of the saturation phenomenon of the HRR for premixed flames at large forcing levels. This study was performed on a single flame setup, and speakers were installed on the combustor to introduce large amplitude longitudinal modes in the combustor. Usually, the predominant acoustic mode is the longitudinal mode in typical single burner configurations which acts in the axial direction. The effect on the subsequent flow field is symmetric and oscillations fluctuate in the direction of the mean flow resulting in symmetric disturbances (O'Connor et al. 2015). A single flame experiencing a longitudinal mode in an axisymmetric confinement couples with the flow field and has the ability to change the flame behaviour by directly effecting the flame surface area, equivalence ratio, consumption speed, and mixture composition (O'Connor et al. 2015).

The mechanisms driving combustion instabilities include flame surface oscillations, equivalence ratio fluctuations, and hydrodynamic instabilities (Huang and Yang 2009). Flame dynamics by acoustic disturbances can be related to convective transport by fluctuations in vorticity, flame shape, and equivalence ratio Polifke (2020). Lawn and Polifke (2004) outline the mechanism behind fluctuations in the HRR by acoustic velocity fluctuations for single flame setups. The oscillations due to the velocity fluctuations at the inlet of the injector or duct result in large-scale changes in the flame surface area that changes the overall reaction rate. Additionally, acoustic waves can affect the burning velocity through three fundamental mechanisms in which the acoustic velocity fluctuations (Lawn and Polifke 2004): (1) along the flame front result in kinematic oscillations resulting in area changes and effectively changes in the HRR response (2) in the shear layer promoting oscillations in the length scale and turbulent intensity resulting in the development of large-scale vortex structures that contribute to oscillations in the turbulent burning velocity and fuel consumption. (3) at the fuel or air injection, resulting in oscillations in the equivalence ratio, producing oscillations in the burning velocity and enthalpy of reaction per unit volume of pre-mixture, directly affecting the flame area and rate of the heat release rate per unit area. It is important to point out that these mechanisms, require an effective experimental technique or well resolved simulations to evaluate the local or spatial HRR response to better understand the flame dynamics.

An example of a single confined bluff body stabilised flame subjected to a longitudinal mode taken from the study of Balachandran et al. (2005) is presented in Fig. 1.6. The series of images show the phase-averaged Flame Surface Density (FSD) over a cycle of forcing. FSD is used as a marker for the HRR (Paul and Najm 1998), and the images provide insight into the flame front oscillations that directly affect the HRR (Candel 2002). As

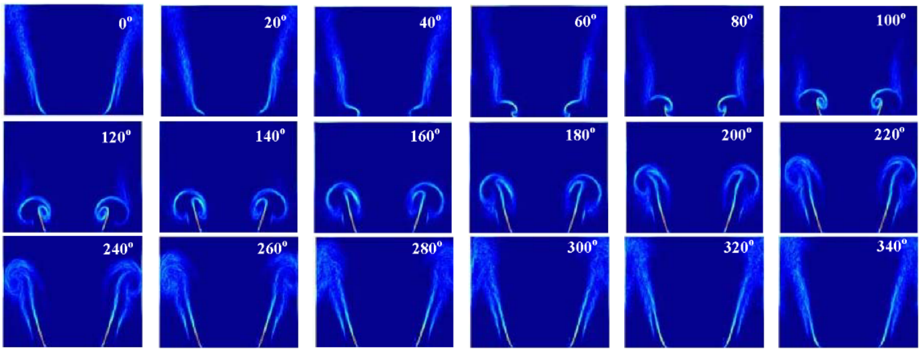

Figure 1.6: Phase-averaged Flame Surface Density (FSD) of a lean ethylene ($\phi = 0.55$) flame over a cycle of strong longitudinal forcing (Balachandran et al. 2005).

described by Balachandran et al. (2005), the flame is anchored by the shear layer due to the presence of a bluff body at the injector exit. The flame was subjected to large amplitude forcing in axial velocity fluctuations at the base of the flame resulting in a roll-up of the inner and outer shear layers producing a pair of counter-rotating vortices. The resulting roll-up of the flame surface grow in size as it is convected downstream, eventually impinging on the combustion wall close to the tip of the flame before a new vortex is formed at the base of the flame. Periodic velocity fluctuations cyclically impose this flame behaviour. By integrating the FSD at different regions of the flame, Balachandran et al. (2005) showed that the rate of HRR oscillations decreases in regions above the vortex roll-up close to the injector exit due to flame surface destruction or annihilation events that modulate the global HRR response. The study concludes with the use of time-resolved measurements to show that the vortex roll-up plays a fundamental role in the non-linearity in the HRR response for large forcing amplitudes. This study showcases how optical measurements are used to evaluate flame dynamics by measuring local HRR of flames in response to TI. Experimental techniques of this type form the basis of the investigation of this thesis and will be introduced in § 1.2.

Some features of the Flame Transfer Function and flame dynamics associated with TI in single flame combustors are covered in this section, and a more comprehensive review of longitudinal thermoacoustic instabilities can be found in Lieuwen, Timothy C and Yang (2005), Huang and Yang (2009) and Candel et al. (2014). The publications cited in this section is not exhaustive. However, the large number of citations are a showcase of the

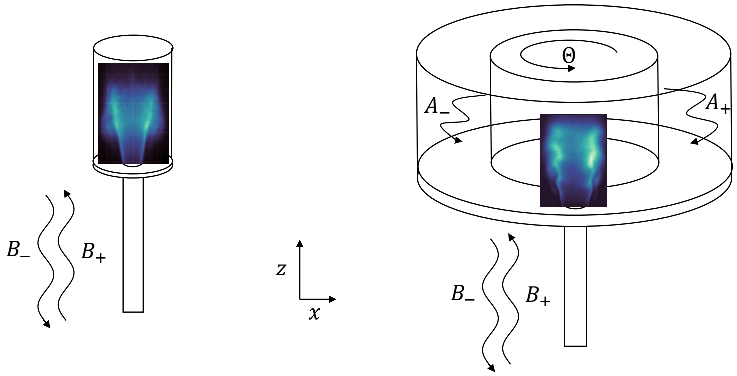

Figure 1.7: (left) A single flame combustor shows a snapshot of an OH* image of a methane flame under a self-excited thermoacoustic instability (Duffo 2023). Oscillations in the velocity at the inlet of the injector result in an axisymmetric flame response. Graphical pressure waves are shown alongside the burner to show the direction of oscillations in this setup. (right) OH* chemiluminescence of a flame in an annular combustor experiencing an azimuthal mode in which fluctuations of velocity and pressure are simultaneously acting on the flame from both the axial and transverse directions resulting in a non-axisymmetric flame response.

literature devoted to single flame TI studies. In contrast, similar studies on annular systems are limited.

1.0.3 Characterisation of azimuthal modes

The previous section introduced longitudinal modes, where axial fluctuations are aligned to the axis of propagation coinciding with the burner axis (Saurabh and Paschereit 2017). This configuration is shown on the left-hand side of Fig. 1.7 in which the flame is shown to produce an axisymmetric response. In Fig. 1.7, $B\pm$ and are complex-valued pressure amplitudes of two counter-propagating waves travelling in the axial direction. The pressure oscillations in the injector are related to these amplitudes by (Æsøy et al. 2020):

$$p'_{inj}(z,t) = [B_+ \exp(-ik_+ z) + B_- \exp(ik_- z)] \exp(i\omega t) \tag{1.5}$$

where w, k and t represents the angular frequency, wave number, and time, respectively. The equations represented in this section will be derived in Chapter 2 and are presented here to aid in the characterising of azimuthal modes.

Due to the axisymmetric response of longitudinal modes, it is safe to assume that 1D models are sufficient in describing the acoustic field in two or three dimensions (Saurabh and Paschereit 2017). However, this assumption falls short when describing TI in annular combustors. Azimuthal modes produce fluctuations in velocity and pressure transverse to the burner axis, as shown by the counter-propagating pressure waves around the annular chamber ($A_{\pm}$) on the right side of Fig. 1.7. In addition, transverse oscillations induce axial fluctuations of the flow entering the annular chamber, as indicated by $B_{\pm}$ pressure oscillations on the right-had side of Fig. 1.7. Therefore, in contrast to longitudinal modes, the flow entering the annular chamber is subject to fluctuations in two directions simultaneously. The pressure fluctuations in the annulus are defined by two counter-propagating acoustic plane waves with amplitudes A_+ and A_- rotating in the anti-clockwise and clockwise direction, respectively (Nygård et al. 2019):

$$p'_{annular}(\Theta, t) = [A_+ \exp(-in\Theta) + A_- \exp(in\Theta)] \exp(i\omega t) \tag{1.6}$$

The chamber is a continuous structure, meaning acoustic waves can propagate without obstruction around the annulus. Therefore azimuthal modes are degenerate in nature (Nygård and Worth 2021). The degenerate nature of the modes provides a rich space for potential modal states. The nature of the azimuthal mode can either be standing, spinning in the clockwise (CW), spinning anti-clockwise (ACW) directions, or a combination of both spinning and standing, with the potential to vary between modal states (Worth and Dawson 2013). In annular combustors, the circumference is much larger than the length of the combustor resulting in the first azimuthal mode (first order) being the most unstable (Schuermans et al. 2003, Krebs et al. 2002). Azimuthal modes were first defined by decomposing the mode into two counter-propagating spinning waves in the annulus (Worth and Dawson 2013, Bourgouin et al. 2013, Wolf et al. 2012, Vignat et al. 2020). With an emphasis on modelling, studies by Ghirardo and Bothien (2018) also defined the azimuthal modes in terms of two standing waves. However, the spinning wave formulation is more widely used in experimental applications. To this end, the definition of the Spin Ratio (SR) has aided in characterising the nature of azimuthal modes (Bourgouin et al. 2013), and is defined as:

$$SR = \frac{|A_+| - |A_-|}{|A_+| + |A_-|} \tag{1.7}$$

where, A_+ and A_- are the amplitudes defined in Eq. 1.6. A study by Ghirardo and Bothien (2018) redefined the characterisation of the azimuthal

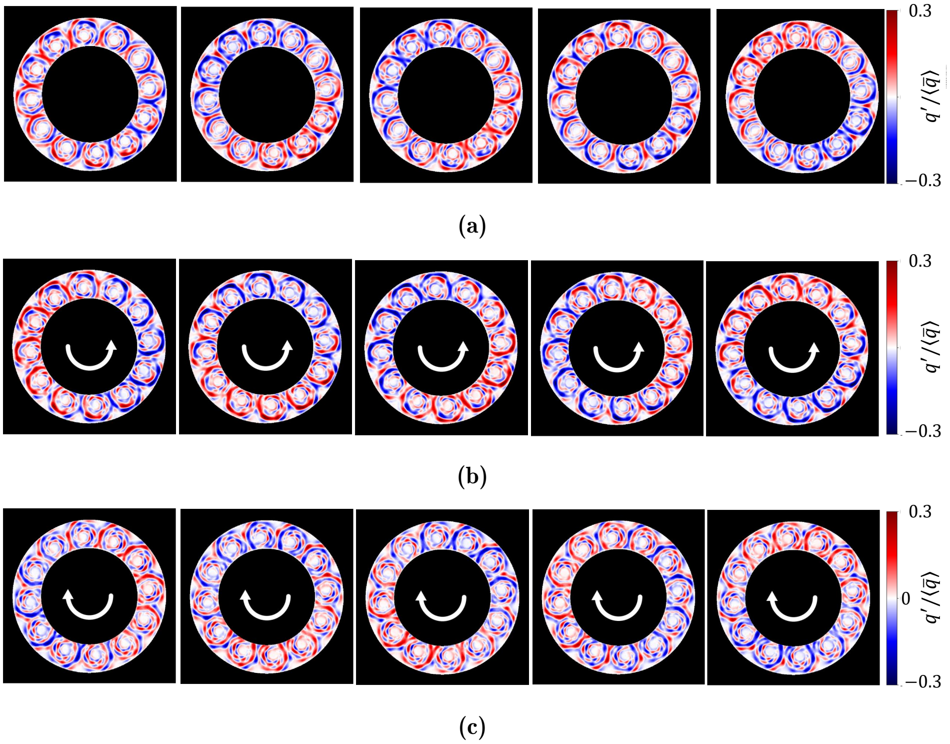

Figure 1.8: 5 snap shots of phase averaged HRR oscillations for forced a) standing , b) ACW spinning c) CW spinning modes (Nygård et al. 2021).

modal states in hypercomplex quaternion formalisation, which made modelling the system easier. The formulation describes the modes with four state space variables: (i) Mode amplitude A, (ii) Orientation angle θ_0, (iii) Nature angle χ and (iv) Temporal phase φ. In this definition, the azimuthal pressure fluctuations of order, n, can be defined by the quaternion formulation (Ghirardo and Bothien 2018):

$$p'(\theta,t) = A\cos n(\theta-\theta_0) cos(\chi) cos(\omega t+\varphi) + A\cos n(\theta-\theta_0)\sin(\chi)\sin(\omega t+\varphi) \tag{1.8}$$

In this formulation, the nature angle can be related back to the Spin Ratio by $SR = tan(\chi)$. Either formulation can be adopted to characterise the azimuthal modal behaviour.

An example of HRR response to a standing, a CW spinning, and a ACW spinning mode is shown in Fig. 1.8, in a 12 burner annular combustor. A standing wave mode results when $A_+ = A_-$ ($SR = 0$). The transverse velocity fluctuations in the annulus during a standing mode are 90° out of phase from the pressure fluctuations (O'Connor et al. 2015), producing a position in the combustor where the transverse pressure oscillations are at the maximum, and the transverse velocity oscillation is at a minimum, also known as a pressure antinode. Conversely, for an azimuthal order of one, two positions in the combustor will experience a maximum transverse velocity oscillation with a minimum pressure oscillation. This location is known as a pressure node. A line through these locations is known as a nodal line. Consequently, the pressure node and antinode are at positions in the standing wave that produces the minimum and maximum axial velocity oscillations, respectively. Every azimuthal location between the pressure node and antinode will produce a combination of azimuthal pressure and velocity fluctuations for a standing wave mode. In contrast, spinning modes do not have a fixed nodal line, and waves propagate circumferentially around the annulus in the CW direction when $A_+ \approx 0$ and ACW direction when $A_- \approx 0$ with the nodal line travelling around the annulus at the speed of sound in the direction of the mode. Figure 1.8(b) and 1.8(c) show how the HRR oscillations rotate in the respective directions around the annulus. Figure 1.8 is a showcase of the HRR oscillation response to azimuthal modes, and all cases produce an asymmetric response. The understanding of this asymmetric response is an important part of this thesis and will be discussed further in § 1.1. Knowing whether the mode is spinning or standing has two important practical industrial applications (O'Connor et al. 2015): (i) Placement of sensors needs to account for potential standing mode locations to avoid the pressure nodal position (ii) Similarly, the effectiveness of installing resonators depends on the position of standing waves in combustors. However, further complexity arises when taking into account the time dependence on these modes.

1.0.4 Transverse Oscillations

To simplify the geometry of annular combustors and isolate the effects of transverse and axial oscillations, researchers such as (Saurabh and Paschereit 2017, O'Connor et al. 2013, Lespinasse et al. 2013, Hauser et al. 2010) constructed individual single burner test rigs that isolate a sector of an annular combustor. The rig design eliminates curvature and wall effects by unwrapping a portion of the annulus to produce a high aspect ratio rectangular combustion chamber. Further simplifications are often made by only investigating a single flame removing the complexity of flame-flame inter-

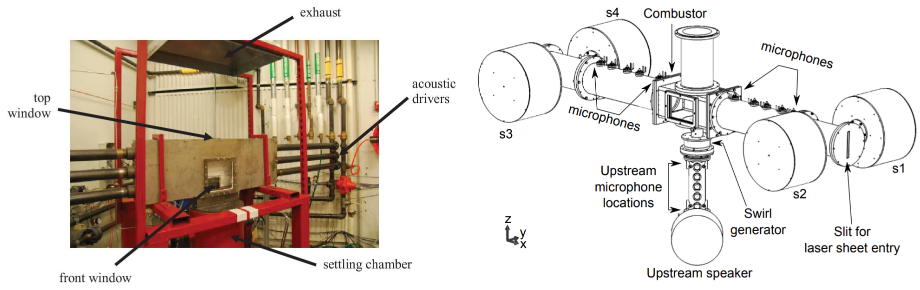

(a) **(b)**

Figure 1.9: Examples of transverse experimental setups, adapted from (a) O'Connor and Lieuwen (2012) and (b) Saurabh and Paschereit (2013).

actions. A comprehensive review of transverse combustion instabilities in atmospheric combustors can be found in O'Connor et al. (2015). A few fundamental studies significant to the aim of this study will be outlined here.

Transverse modes in the rectangular combustion setup are emulated via the installation of speakers. One of the first implementations is a study by O'Connor and Lieuwen (2011), who used three adjustable speaker pairs connected transversely on both sides of a single flame of interest. The speakers were used to produce standing waves inside the combustion chamber, and the phase between the speaker drivers was altered to change the position of the wave with respect to the flame. An image of the experimental setup is shown in Fig. 1.9(a).

Transverse pressure oscillations induce axial pressure and velocity oscillations, which drive the flame response and can be graphically described by Fig. 1.10. The figure highlights the potential pathways that influence the response of transversely excited flames. As outlined by O'Connor et al. (2015), the pathway F_T represents the effect of direct transverse acoustic velocity fluctuations on the flame response. The coupling of the transverse acoustic field and nozzle acoustics, also known as injector coupling (Davis and Chehroudi 2004), is represented by pathway F_{TL}. Both these pathways have the potential to couple with flow instabilities inducing vortical velocity fluctuations on the flame response, F_ω. The F_ϕ pathway is the fuel/air ratio coupling due to longitudinal disturbances, and the additional pathway $F_{\omega\phi}$ is disturbances in fuel/air ratio based on the flow instabilities. This definition of flame response pathways by O'Connor et al. (2015) is based on transverse forcing, however, based on the similarities between

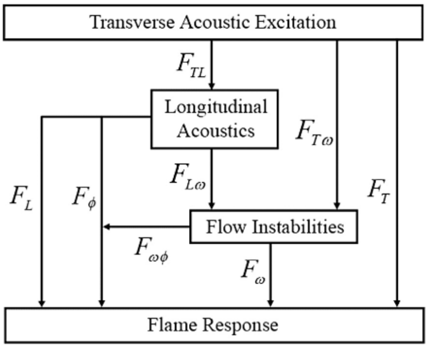

Figure 1.10: Potential flame response pathways subjected to transverse acoustic excitation adopted from O'Connor et al. (2015).

transverse forced systems and annular systems, similar pathways may exist when subjected to azimuthal acoustic excitation.

The studies by O'Connor and Lieuwen (2012) and Malanoski et al. (2014) investigated the effects of transverse forcing on a swirled flame. These studies showed that the flame shape and the local and global HRR fluctuations were significantly affected by flame position within the standing wave.

It was also shown that the flame HRR fluctuations produced at the pressure node were negligible, and the pressure antinode produced a maximum. At the pressure node, transverse velocity oscillations are dominant, and the flame produces an anti-axisymmetric flapping motion that results in HRR fluctuation cancellation (O'Connor and Lieuwen 2011). This result was confirmed with simulations by Acharya et al. (2012) and Steinbacher and Polifke (2022) for a transversely excited laminar axisymmetric premixed flame. In contrast, the flame at the pressure antinode responded similarly to that of flames subjected to longitudinal excitation resulting in symmetric vortex roll-up of the outer shear layers in the absence of transverse velocity oscillations (O'Connor and Lieuwen 2011). The presence of vortex structures created by flow oscillations drives the flame response. The delayed combustion and ignition of entrained reactants in these structures in the flow field has the ability to sustain the mechanism of feeding energy into an oscillation (Candel 2002). As explained by Candel (2002), the transport of reactants into combustion regions is controlled by the vortex roll-up. Thus this process controls the unsteady conversion of reactants. There are few studies that focus on intermediate positions in a standing mode, which is something this thesis aims to address by investigating the HRR response

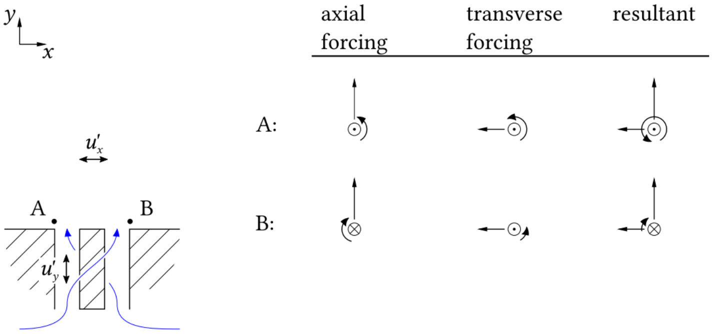

Figure 1.11: Illustration of outer shear layer interaction with axial(u'_y) and transverse(u'_x) acoustic velocity oscillations. Blue lines represent mean flame swirl flow, and arrows show the magnitude of velocity oscillations on the right. The length of the curved arrows represents vorticity. Resultant vorticity direction and magnitude are shown for cases A and B. Adapted from Saurabh and Paschereit (2017).

of a flame at three positions along a standing wave. This analysis will be presented in Chapter 3.

A study by Lespinasse et al. (2013) showed that transverse oscillations induce axial longitudinal fluctuations in the nozzle that dominate the overall flame response. Studies by Saurabh and Paschereit (2017) andSaurabh and Paschereit (2019) improved the conventional transverse set-up by controlling the timing/phase of transverse and axial oscillations, creating travelling waves to closely mimic the response in an annular combustor. An example of the experimental rig used by Saurabh and Paschereit (2017) is shown in Fig. 1.9(b). A major finding from this study was the difference in HRR oscillations based on generating similar amplitude travelling waves in two different directions, which should produce the same response due to symmetry. The differences in the HRR response were attributed to slight asymmetries in the burner itself changing the HRR response. A similar result was observed in studies by Acharya et al. (2012) and Acharya and Lieuwen (2019). The effect of asymmetry on the HRR response is significant when considering the annular configuration in which many sources of asymmetries can arise. Further discussion on potential asymmetries will be discussed in § 1.1.

Studies by O'Connor et al. (2010), O'Connor and Lieuwen (2011) and Hauser et al. (2010) show that the change in the flame shape directly affects the HRR response due to local oscillations combined with the acoustic response of the swirler. A potential mechanism to explain the interaction between axial and transverse oscillations on a swirled flame was illustrated by Saurabh and Paschereit (2017) and is shown in Fig. 1.11. In this schematic, the interaction between axial and transverse velocity oscillations controls the timing of vortex roll-up at the injector exit. In Fig. 1.11, locations A and B on either side of the burner are considered. The blue lines represent the mean swirl flow at a hypothetical frozen state of the flow field. The arrows on the right-hand side of the figure show the relative magnitude of the transverse and axial velocity oscillations. The axial velocity fluctuations at point A and B are equal in the positive y direction, and the transverse oscillations at both points act in the negative x-direction. However, the transverse oscillations produce vorticity at different magnitudes, as indicated by the length of the circular arrows. The resultant fluctuation is shown, in which the difference in vorticity results in different responses on each side of the flame—showing that transverse oscillations can either enhance or reduce the disturbance of axial oscillation, and the response depends on the timing or phase between the axial and transverse forcing and the location of the generated vorticies (Saurabh and Paschereit 2017).

The effectiveness of emulating the annular combustor thermoacoustic responses using a transverse forced setup was evaluated by O'Connor et al. (2013), in which the authors compare the flame responses of an azimuthally self-excited flame in an annular combustor to transversely forced flame for two positions in a standing wave. The comparison showed that asymmetric and symmetric responses of the flame at the node and pressure antinode, respectively, were well captured by the single transversely forced flame. The study also explains that four major characteristics are required to accurately represent the flow and flame dynamics of the annular combustion (O'Connor et al. 2015): (i) the flow field must have the ability to capture vortex structures, (ii) the flame shape needs to be representative in terms of stabilisation, (iii) the acoustic resonance and compactness needs to be representative, (iv) the flame spacing needs to representative as annular combustors often contain flames in close proximity with the ability to interact. However, this list is not exhaustive and additional characteristics will be discussed in § 1.1.

The mentioned studies are useful in isolating the flame response to both transverse and axial forced systems. However, these studies neglect flame interaction or wall curvature, which has recently been shown to be important in annular combustors Nygård et al. (2021), and will be discussed in § 1.1. Therefore, while transversely forced setups are useful to isolate some features that arise in response to transverse oscillations, they do not capture all

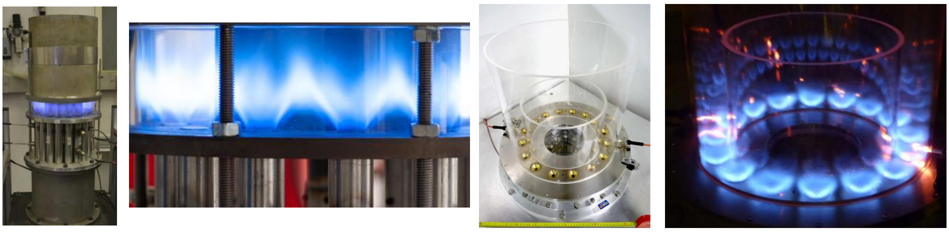

(a) (b)

Figure 1.12: Examples of lab-scale annular combustors. a) Cambridge annular combustor(left) with zoomed-in image showing closely confined interacting flames adapted from Worth and Dawson (2013) and b) MICCA combustor (left) and an image showing equally spaced flames in combustor(right) adapted from Bourgouin et al. (2013).

relevant effects, and azimuthal oscillations in annular geometry should also be investigated. The following section will highlight some studies on annular combustors.

1.1 Azimuthal Oscillations

Investigations of thermoacoustic instabilities on commercial scale gas turbines like the studies performed by Orthmann et al. (1998) and Krebs et al. (2002) provide a more realistic view of industrial annular combustors. These studies were the first to obtain experimental data on thermoacoustic instabilities on an industrial gas turbine. However, isolating or quantifying specific attributes that contribute to thermoacoustics is difficult due to the lack of optical access and the large expense in running these combustors. In light of this, researchers (Worth and Dawson 2013, Bourgouin et al. 2013) have designed and built simpler lab-scale annular combustors. Examples of these are shown in Fig. 1.14. Two widely reported lab-scale annular combustor configurations are the Cambridge annular combustor (Worth and Dawson 2013) featuring either 12, 15, or 18 burners and the 16 burner MICCA combustor (Bourgouin et al. 2013). Both configurations permit optical access to flames and have been able to produce self-excited instabilities. A more detailed description of these annular combustors can be found in the review by Vignat et al. (2020), and the relevant findings regarding thermoacoustic instabilities in these combustors will be discussed herein.

1.1.1 Pressure response to to annular combustor thermoacoustic instabilities

Azimuthal mode preference and dynamics

The time-varying nature or modal dynamics of azimuthal modes were first experimentally shown by Krebs et al. (2002) and Orthmann et al. (1998) on a full-scale industrial gas turbine and was later confirmed by the use of Large Eddy Simulations (LES) by Wolf et al. (2012), who showed that self-excited azimuthal modes had a tendency to switch between spinning or standing wave modes. This result was also experimentally confirmed on two lab-scale annular combustors by Worth and Dawson (2013) and Bourgouin et al. (2013). Noiray and Schuermans (2013) experimentally measured simultaneous pressure oscillations circumferentially around an annular combustor during a self-excited TI. Statistical analysis showed that the modes continuously switched between standing, clockwise, and anti-clockwise travelling waves and the modal preference was sensitive to the noise level in the combustor. Numerical studies by Ghirardo and Bothien (2018) and Ghirardo et al. (2021) showed that spinning wave solutions were positive stable periodic attractors in the absence of combustion noise. Therefore, the system had a preference to spinning wave solutions. However, combustion noise, typical of industrial gas turbines, drives the solution to standing mode solutions. Detailed theoretical studies by Bothien et al. (2015), Schuermans et al. (2003) and Schuermans et al. (2006) show that a potential source of this modal shift behaviour is a result of asymmetries in the flow field or HRR spatial distribution.

Several studies of self-excited azimuthal modes have observed a dependence of the mode state on operating conditions (Worth and Dawson 2017, Prieur et al. 2017, Indlekofer et al. 2021). A study by Prieur et al. (2017) investigated the effects of injector velocity and equivalence ratio on azimuthal modes in the MICCA combustor. The study showed that standing and spinning modes were observed for the same operating condition. In this context, mode selection were based on the path taken to reach the operating condition, that is increasing the equivalence ratio from lean conditions resulted in spinning modes. In contrast, standing modes were observed when the equivalence ratio was decreased from rich conditions. Worth and Dawson (2017) showed that the equivalence ratio not only changed the modal preference between standing or spinning modes in the Cambridge annular combustor but also produced unique pathways between the changing of these modes. A recent numerical study by Faure-Beaulieu et al. (2021) showed that tur-

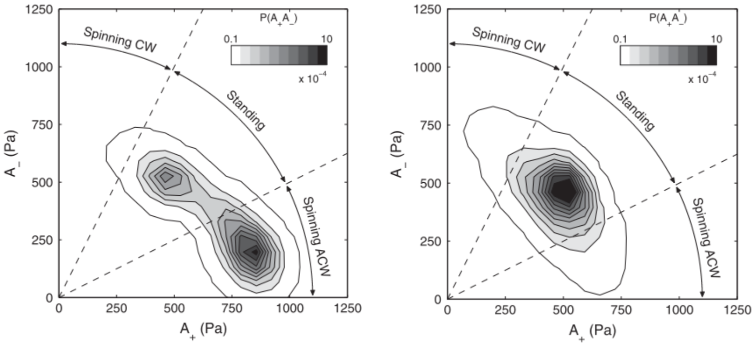

(a) ACW swirl case **(b)** Alternating swirl case

Figure 1.13: Joint probability density function of A_- and A_+ for self-excited azimuthal modes in an annular combustor with an (a) anti-clockwise swirler and (b) alternating swirler orientation. Adapted from Worth and Dawson (2013).

bulent combustion noise prevalent in gas turbines combustors played a significant role in the switching behaviour of azimuthal thermoacoustic modes.

A graphical representation of the modal switching behaviour seen in the study by Worth and Dawson (2013) is represented in Fig. 1.13. The study by Worth and Dawson (2013) used probability density functions to highlight the amplitudes of azimuthal modes and showed that modal preference for either spinning or standing modes was statistically based on the distance between neighbouring flames and the orientation of the injector swirlers. A mean azimuthal flow pattern in the combustion chamber was induced when the swirlers were in the same direction. However, when the swirlers were alternately orientated in the opposite direction, the presence of the bulk flow was eliminated, and the modal preferences statistically tended towards standing modes.

Swirled flames are of importance to the gas turbine community since they play a crucial role in flame stabilisation, promoting an anchoring of flame by introducing a rotational component in the axial flow-field (Vignat et al. 2020). The swirler also induces central and outer recirculation zones that circulate hot combustion products that ignite fresh reactants (Vignat et al. 2020). Many studies devoted to understanding the effects of the swirler and the potential pathways of direct and indirect excitation have been given much attention. A comprehensive review is provided by Candel et al. (2014).

However, it is also interesting to examine the azimuthal modal behaviour in the absence of swirl. Mazur et al. (2019) performed a study in the absence of a bulk swirl motion. Results showed that azimuthal modal response tended towards ACW and CW spinning modes. A study by Bourgouin et al. (2015) modified the original MICCA design to eliminate the mean azimuthal flow (bulk azimuthal flow) by installing widely spaced matrix burners. This new configuration showed that the dominant mode was spinning modes when self-excited. Further studies on the modified MICCA setup were performed by Prieur et al. (2017) to show that the modal preference between standing, spinning and slanted modes were dependent on flow properties, and studies by Aguilar et al. (2021) showed how asymmetries change the modal dynamics of the MICCA combustor when an individual or multiple injectors are blocked. The study by Aguilar et al. (2021) found that the limit cycle achieved can be changed when large asymmetries (blocking multiple injectors) are introduced into the system, whereas small asymmetries (blocking of a single injector) usually maintain the modal preference, further highlighting its sensitivity to geometric asymmetries.

Dawson and Worth (2015) investigated the effects of installing baffles on the modal behaviour of the Cambridge annular combustor. The baffle installation creates a boundary in the azimuthal direction preventing any switching or drift behaviour in the azimuthal modes of the combustor. It was found that the presence of the baffles resulted in standing wave modes. In a similar approach, Mazur et al. (2018) installed Helmholtz resonators in an annular combustor. The addition of resonators, as expected, increased the damping of the pressure oscillations in the system but did not eliminate the instability.

Understanding the selection and dynamics of azimuthal mode states continues to be a focus of research efforts. This thesis aims to better understand the flame response to different modal states thus improving the prediction of which states are excited. Due to the degenerate nature of azimuthal modes, the flame response in an annular combustor is subjected to a rich space of azimuthal modes. The flame response depends on the type, frequency and amplitude of the modes and is sensitive to operating conditions, combustor noise, asymmetries and geometry. Furthermore, the confinement of the flame and the flame-flame interaction potentially plays a role in the HRR response when subjected to self-excited TI. The following section will discuss some of these effects.

Forced azimuthal modes

The degenerate nature of azimuthal modes makes isolating a given self-excited modes in an annular combustor difficult. Similar to those in the

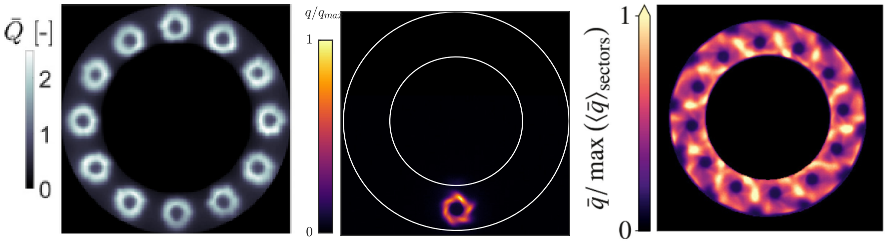

(a) **(b)** **(c)**

Figure 1.14: Overhead OH* chemiluminescence mean image for a) 12 unswirled ethylene flames adapted from Mazur et al. (2019), b) of a single swirled ethylene flame determined experimentally in this thesis, and, c) 12 swirled ethylene flames (Nygård et al. 2021) in an annular combustor.

transversely forced experimental setups, forcing allows for the investigation of individual modes, especially in isolating non-frequent self-excited modes. However, forcing on an annular combustor can be more complex than single flame setups. A significant advancement in annular combustor forcing was a study by Moeck et al. (2010), which produced standing, spinning and mixed modes by installing speakers downstream of the injectors in an annular Rikje tube. The technique was later improved by Humbert et al. (2021), who produced azimuthal modes in a more controlled manner. Following a similar approach, studies by Worth and Dawson (2017) used a combination of two downstream out-of-phase speakers to study standing modes. The recent advances made by Nygård et al. (2019) and Nygård et al. (2021) on an improved forcing setup have shown that the careful control of azimuthal modes has been fundamental in understanding the behaviour of the azimuthal responses. This thesis will make use of forcing to isolate azimuthal modes in an annular combustor to better understand their HRR response.

1.1.2 Confinement

The flames under confinement tend to change flame shape depending on the extent of the confinement (Cuquel et al. 2013, Æsøy et al. 2020, Fu et al. 2005). Studies by Cuquel et al. (2013) show that confinement creates an over-pressure of the surrounding burnt gas, which induces an acceleration of fresh reactants. This effect increases the flame height when increasing the confinement ratio (radius of burner over a unit radius of confinement). A study by Nygård and Worth (2021) was aimed at evaluating the Flame Transfer Function (FTF) and flame dynamics of a single highly swirled confined flame within a square enclosure across a wide operating envelope.

The setup promoted close flame-wall interaction, and the varied flow conditions induced a range of wall interactions by changing the flame height. These types of wall-flame interactions are also prevalent in annular combustors. Experimental data was captured in this thesis for a configuration of a single-swirled flame in an annular combustion chamber. An overhead OH* chemiluminescence image of the mean flow is shown in fig 1.14(b), accompanying the 12 unswirled flames from the study of Mazur et al. (2019) and an image of 12 swirled flames from the study by Nygård et al. (2021). The equivalence ratios and flow speeds of all three cases are the same, however, the flame shape drastically changes in each configuration. The unswirled cases produced symmetric circular flames with little interaction. The single flame takes on a distinct asymmetric shape based on the effect of the swirler, and when the neighbouring flames are ignited in fig 1.14(c), this shape is then changed again, creating a more asymmetric flame structure. The extent of the confinement changes the acoustic response of flames or, specifically, the Flame Transfer Function by changing the time delay between acoustic mode and HRR (Nygård and Worth 2021).

The three configurations shown in Fig. 1.14 also differ in terms of wall material, with the first and last configuration enclosing the combustor by steel walls whereas the configuration in Fig. 1.14(b) having an outer quartz enclosure and inner steel wall. Different wall materials changes the heat transfer loses due to conductivity and directly effects quenching and flame burning rates (Daou and Matalon 2002). Both properties which could potentially alter the flame shape and the response to azimuthal modes. Studies by McIntosh and Clarke (1984), Mcintosh (1987), Schreel et al. (2002) and Kedia et al. (2011) have shown that the flame-wall interaction has the potential to alter burning velocity fluctuations and flame anchoring. The effects of wall conductivity and confinement will be investigated in Article II of this thesis.

1.1.3 Interacting flames

The flame response to thermoacoustics alters the flames surface area (Dowling 1997). Flame surface area changes can occur due to anchoring of the flame, flow perturbations downstream and the complex geometry of its shear layers (Driscoll 2008). The flame surface area is also altered in the presence of flame-flame interaction. Annular combustors can feature closely spaced flames making flame interaction an important point of interest in studying thermoacoustic instabilities. When individual flames are brought together, large-scale flow structures and the distribution of the HRR start to change, which has been described as *macro-level* flame-flame interactions (Tyagi

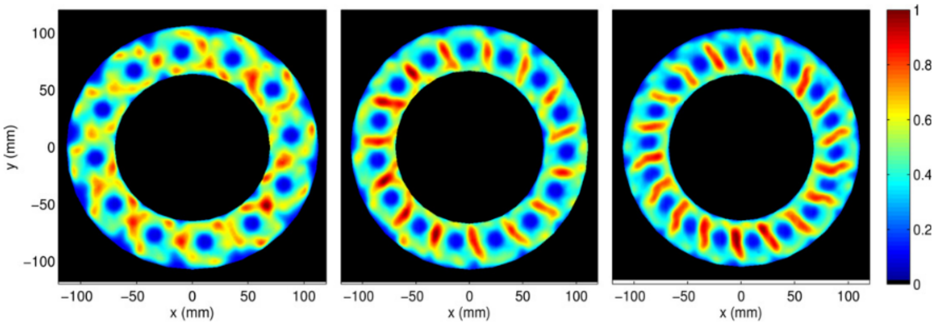

Figure 1.15: Overhead OH* chemiluminescence for a 12, 15 and 18 swirled ethylene/air annular combustor configuration, adapted from Worth and Dawson (2013).

et al. 2019). A comparison between a single burner and an annular burner was extensively covered by Kunze et al. (2004), Fanaca et al. (2008) and Fanaca et al. (2010). These studies demonstrated that fluctuations in the flame shape resulted in differences in the Flame Transfer Function (FTF). Worth and Dawson (2012) isolated effects of flame-flame interaction using planar Laser Induced Fluorescence (LIF) by investigating two interacting bluff-body stabilised flames in a square enclosure while subjected to longitudinal forcing. The study showed that flame-flame interactions played a significant role in flame dynamics. Worth and Dawson (2012) showed that large-scale flame front merging occurred when flames were brought close to each other, resulting in a three-dimensional asymmetric flame structure. The study outlined the importance of 3D methods in resolving the three-dimensional unsteady flame structure. A later study by Worth and Dawson (2013) investigated the effects of the distance between neighbouring flames on azimuthal modal dynamics by varying the number of burners inside the combustion chamber. Overhead OH* imaging was used to characterise the HRR response of the different configurations when self-excited, and pressure measurements were used to characterise the azimuthal modal states. Figure 1.15 is a top view comparison of the averaged HRR distribution of the three configurations investigated in Worth and Dawson (2013). The first image represents a 12 annular flame configuration. In this configuration, the flames take an approximately axisymmetric structure with six points of high intensity that the authors account for as the effect of the upstream six-vaned swirler. The next two images represent the flames being brought together in a 15 burner configuration and a 18 burner configuration, resulting in large-scale merging flame structures between adjacent flames with regions of high HRR. The interaction zones are also angled in the direction of the

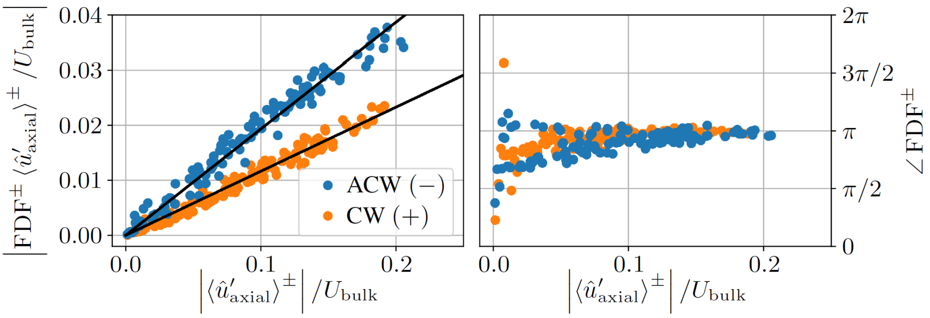

Figure 1.16: Experimentally determined azimuthal Flame Describing Function of ACW and CW modes of swirled flames in an annular combustor. The gain of the FDF representing the magnitude of the HRR oscillation is represented on the left. The respective phase is represented on the right. Adapted from Nygård (2021).

swirler. The formation of an interaction region between adjacent flames has also been shown to significantly alter the spatial HRR distribution for both annular (Worth and Dawson 2013, Dawson and Worth 2014), multi-injector can configurations (Samarasinghe et al. 2013, 2017), and Mesoscale burner arrays (Rajasegar et al. 2019), again altering their thermoacoustic response.

1.1.4 HRR response to annular combustor thermoacoustic instabilities

A few studies have quantified the HRR response of annular combustor flames subjected to azimuthal modes. A study by Mazur et al. (2019), as earlier mentioned, investigated self-excited unswirled flames in annular combustor. An overhead OH* chemiluminescence image from this study is shown in fig 1.14(a) representing 12 unswirled mean unforced flames. The measurement technique was useful in picking up high bands of intensity that showed that more HRR response was present on the side of the flame that was incident to the modal direction. A significant result was that the spatial HRR distribution were highly axisymmetric in both the spinning directions but the HRR response of both spinning directions were identical. Using azimuthal forcing, studies by Nygård et al. (2019) and Nygård et al. (2021) investigated the HRR response of ACW and CW spinning modes of swirled in an annular combustor in a similar arrangement to Mazur et al. (2019). In contrast to Mazur et al. (2019), results showed that the HRR response differed between the spinning directions (Nygård and Worth 2021). This was shown by defining an azimuthal FDF describing the flame response to azimuthal axial velocity fluctuations in the modal direction, as shown in

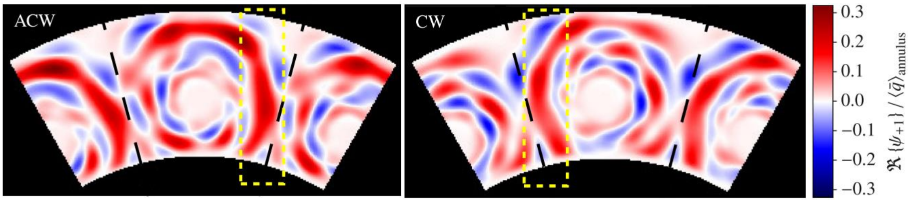

Figure 1.17: Rotational average from bloch kernel representing the spatially integrated HRR response of the ACW and CW modes highlight a single flame in an annular combustor. Adapted from Nygård et al. (2021).

Fig. 1.16. This allowed for the isolation of the HRR fluctuations to the ACW and CW component of the azimuthal axial velocity fluctuations. It is clear from Fig. 1.16 that the HRR response differs between the modal direction and the HRR response is larger for the ACW mode. However, the phase for both directions is fairly constant. To investigate the difference in the HRR response, Nygård et al. (2021) used integrated line of sight imaging to isolate a flame in the annular combustor for both ACW and CW modes. The authors used a technique known as Bloch theory (Bloch 1929) to aid in isolating the HRR response from these images. More details on this method can be found in Nygård et al. (2021), and the result is shown in Fig. 1.17 and can be interpreted as the response of the flames to a pure ACW and CW mode. Large bands of high intensity are seen in both responses and are highlighted by the yellow dashed lines. The ACW case produces brighter bands of intensity representing large HRR oscillations close to the outer combustor wall and at the interaction of an adjacent flame. In both responses, a spiral-like pattern is observed that is not mirrored around the centered axis, and the spatial HRR distribution is different for each modal direction implying that the response is three-dimensional in nature. The authors relate the findings to the swirl orientation of the flames and the effects of the curved enclosure.

The use of integrated line of sight overhead imaging and phase averaging in this study helped identify large-scale structural differences in the response, however, the cause of the asymmetry is not well understood. This result provides the motivation for this thesis, which aims to better understand why this difference occurs. Planar or 2D integrated line of sight techniques offer advantages in the spatial distribution or global HRR oscillation measurements, respectively. However, this is restricted to two dimensions limiting our understanding of flames that are non-axisymmetric or produce complex three-dimensional large-scale flame dynamics (Worth and Dawson 2013).

This thesis focuses on developing and implementing three-dimensional techniques to isolate flame dynamics which result in differences in the flame response during ACW and CW modes. The studies on annular combustors show that the flame response can be highly asymmetric, making the use of three-dimensional techniques necessary. The use of three-dimensional measurement on flames is extensive, however, there are no experimental applications of such techniques directly on annular combustors with respect to thermoacoustics and subsequent flame dynamics. This particular configuration has features which makes the application of certain methods challenging. Experimental techniques for investigating HRR oscillations will be discussed in the next section.

1.2 Experimental Measurement Techniques to determine HRR

Studies in thermoacoustics have benefited from the use of Flame Transfer Functions and the analysis of flame dynamics through imaging techniques that isolate the HRR response of flames. These analyses rely on quantifying the HRR response of combustion processes under the influence of TI. Thus providing the motivation for experimental techniques that can non-intrusively measure the HRR and its response to thermoacoustics instabilities. The direct measurement of HRR can be challenging and involves precise measurement of simultaneous species concentrations and temperature to determine the local HRR from Law (2006):

$$\hat{q} = \sum_{\alpha=1}^{N} \dot{\omega}_\alpha h^\circ_{f,\alpha}, \tag{1.9}$$

where N, $h^\circ_{f,\alpha}$,α and $\dot{\omega}_\alpha$ represents the number of species α, heat of formation, and reaction rate respectively. Typically fuels comprise of thousands of species and reactions making the direct measurement of HRR by this formulation an extremely difficult task (Lu and Law 2009). An easier and more practical approach would be to measure a scalar quantity that can be correlated back to HRR (Najm et al. 1998).

However, authors have reported that the choice of scalar quantity for HRR is not universal and is sensitive to chemical and physical attributes of the combustion process (Ferrarotti et al. 2020). Najm et al. (1998) and Nikolaou and Swaminathan (2014) suggest that this sensitivity is related to the the system operating conditions and properties of the fuel mixture. For example, studies by Najm et al. (1998) and Paul and Najm (1998) showed that the formyl radical, HCO, is a good marker for HRR in rich and stoichiometric conditions. Other studies such as Vagelopoulos and Frank (2005) showed that the HRR of undiluted reactant mixtures are better captured by tracking CH concentrations. The proposal of HCO as marker in the former case by Najm et al. (1998) and Paul and Najm (1998) was based on the radical's ability to represent the largest fractional distribution of HRR, the molecule is also an intermediate in the oxidation of methane and the concentration is dependent on the production rate of CO_2. The use of HCO is promising however, Mulla et al. (2016) and Minamoto and Swaminathan (2014) practically showed that the tracking of HCO concentration produces a low signal to noise ratio. Thus more reliable markers such as OH or CH_2O were adopted in combustion diagnostics due to the ease of measuring the species signal and its direct impact on HCO formation via the equilibrium reaction, $OH + CH_2O = HCO + H_2O$ (Ferrarotti et al. 2020). An effective use of these markers to investigate forced flames has been demonstrated by Balachandran et al. (2005), in which the authors use a combination of OH and CH_2O LIF to investigate flame dynamics when a single flame is perturbed by longitudinal forcing. Other flame investigations involving the use of the OH/CH_2O for use of HRR tracking include Böckle et al. (2000), Vagelopoulos and Frank (2005), Ayoola et al. (2006), Gordon et al. (2009), Dworkin et al. (2009), Ayoola et al. (2009a), Ayoola et al. (2009b), Röder et al. (2013) and Gabet et al. (2012). In combination these radicals are good markers in tracking HRR, however, tracking multiple species can be expensive, laser based techniques would require multiple lasers to obtain simultaneous data or multiple cameras equipped with respective filters would be required. Conventionally chemiluminescence of naturally excited species such as OH^* or CH^* and the use of laser excitation (Balachandran et al. 2005, Paul and Najm 1998, Najm et al. 1998) have been applied to successfully investigate the reaction zone and topology of flame dynamics (Ferrarotti et al. 2020, Doan and Swaminathan 2019) outlining the two common means in assessing HRR. In the latter case of laser excitation the method requires the tracking of the flame front to determine the Flame Surface Density (FSD) that is then related back to HRR. It is therefore important to understand how each technique provides advantages in determining HRR and its relevance to more advanced 3D methods for better interpretation of thermoacoustic instabilities.

1.2.1 Chemiluminescence

Unlike other chemical processes, the combustion process results in the emission of light by the presence of a visible flame. The quality of light emis-

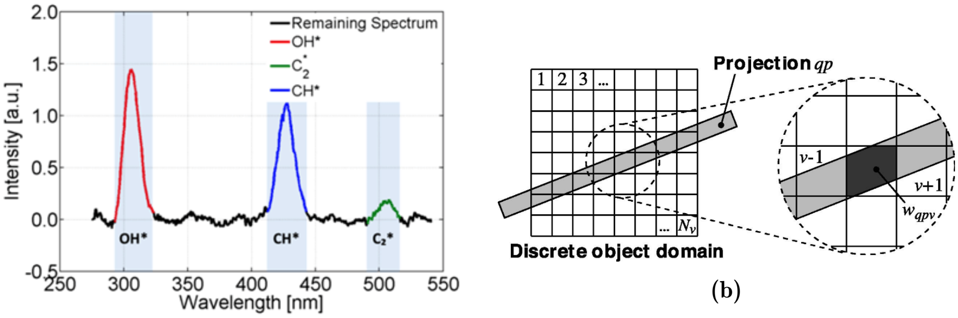

(a)

(b)

Figure 1.18: (a) Flame spectrum highlighting chemical species at different excited states for a hydrocarbon flame. Broadband spectrum and thermal radiation has been subtracted to highlight the peaks in the signal. Adapted from Najafabadi et al. (2017). (b) Graphical representation showing a pixel contribution in a single Line-Of-Sight through a discretised volume during tomographic reconstruction. Adapted from Floyd and Kempf (2011).

sion, known as light spectrum, has been fundamental in studying combustion processes (Gaydon 1974). Each flame produces a distinct spectrum: hydrogen flames produce faint visible light, but strong bands of ultra-violet light, fuel-rich hydrocarbon flames produce light with strong green bands, whereas lean hydrocarbon flames produce violet bands. Taking advantage of these unique responses, the measurement of flame spectra have been used to distinguish between different flame types and operating conditions (Gaydon 1974). A common combustion diagnostic tool that relies on flame spectra is flame chemiluminescence imaging (Schulz et al. 2007). Chemiluminescence is a process in which molecules emit light while returning to a fundamental state, as it follows different pathways, the molecules emit a spectrum of characteristic bandwidths representing respective radicals (Alviso et al. 2017). Figure 1.18(a) represents the flame spectrum of chemiluminescence emitted radiation of a hydrocarbon flame with peaks representing the light emission of radical species at different wavelengths, adapted from Najafabadi et al. (2017). During combustion, hydrocarbon radicals form a unique primary combustion zone where visible bandwidths such as CH* (431 nm) and C_2^* (516 nm) are present. However, modern lean premixed gas turbine combustors operate in the regime where flame chemiluminescence from species such as CH* and C_2^* are significantly lower than OH* (Haber and Vandsburger 2003). The largest peak in Fig. 1.18(a) represents the OH* (306.4 nm) radical that corresponds to the ultraviolet bandwidth, and the emission of the radical is found in the outer zone of the flame, representing a secondary combustion process (Alviso et al. 2017). An experimental means to study flame behaviour is by analysis of the time and space resolved emission of these excited species (Liu et al. 2020). These radicals form within the high temperature reaction zone and have been used to determine macroscopic flame properties such as the identification of the reaction zone (Kojima et al. 2005, Shim et al. 2018, He et al. 2019), equivalence ratio (Hardalupas et al. 2004, Quintino et al. 2018), and Heat Release Rate (Hardalupas and Orain 2004, Panoutsos et al. 2009, Hardalupas et al. 2010, Hossain and Nakamura 2014, Lv et al. 2017, Liu et al. 2019, Hu et al. 2019, Lauer and Sattelmayer 2010). The latter application of flame chemiluminescence is of interest to this thesis, and OH^* chemiluminescence has been adopted to qualitatively measure HRR responses.

The process of chemiluminescence is sensitive to equivalence ratio (Hardalupas and Orain 2004, Tripathi et al. 2012), temperature (Gaydon 1974, Nori and Scitzman 2009) and pressure (Ikeda et al. 2002, Lee and Santavicca 2003, Kojima et al. 2000). Numerical studies by Najm et al. (1998) found that 2D chemiluminescence measurements do not predict local HRR in regions where the local flame structure experiences large curvature and strain effects. Due to this sensitivity and potential limitations, consensus on chemiluminescence measurement being representative of HRR is still debatable in literature (Hardalupas et al. 2010). Nonetheless, The popularity of using 2D chemiluminescence is that the technique (Hardalupas et al. 2010): (i) is an optical diagnostic making it non-intrusive and attractive for harsh environments, (ii) does not require external excitation due to the natural occurrence of chemiluminescence during combustion, and (iii) is a cheap and robust technique that does not require complicated alignment.

A significant limitation of 2D chemiluminescence measurements is the ambiguities created in spatial resolution since the acquired two-dimensional image is formed from integrated Lines-Of-Sight (LOS) (Ma et al. 2016). Furthermore, The flame front structure of turbulent flames is inherently three-dimensional and transient (Xu et al. 2015). Therefore, the technique performs well in terms of global HRR measurement (Lee and Santavicca 2003), but identification of flame dynamics becomes difficult when flames produce non-axisymmetric responses. This limitation of the technique can be minimised by extending the technique to three dimensions to produce spatially resolved data (Ma et al. 2017).

Computed Tomography of Chemiluminescence

Computed Tomography (CT) was introduced in the early 1970s as a medical diagnostic tool capable of reconstructing a density distribution based on x-ray measurements. Since then, the CT method has been adopted to produce a non-intrusive three-dimensional technique in numerous applications of engineering and science (Upton et al. 2011). Such applications include Computed Tomography of Chemiluminescence (CTC) that has been used to resolve the complete three-dimensional spatial HRR field (Worth and Dawson 2013, Floyd and Kempf 2011, Cai et al. 2013, Dreizler et al. 2018, Ishino and Ohiwa 2005). CTC uses image reconstruction by producing a volume distribution of a scalar function from projected line integrals (P_i) along a finite number of lines with known locations (Herman and Lent 1976).

The problem of reconstruction from projections was first solved by Radon in 1917 Herman and Lent (1976). Radon proposed an analytical expression known as the inverse Radon transformation that maps infinite continuous line integrals to determine a distribution of a property along a projection. In this formulation, all lines are known, however, in reality, recording a finite number is possible, and when coupled with unavoidable measurement uncertainty, the inverse Radon transformation becomes ill-posed (Madych 2004). Therefore, reconstruction methods for finite projections have adopted a discretised approach to solving the reconstruction problem. An algebraic formulation is usually used to reconstruct a volume in which projections are modelled as a linear system of basis functions with unknown weights (Upton et al. 2011). Each basis function represents the distribution of each local voxel on a defined regular grid. An illustration of the contribution and weighting of a single voxel along a projection line is shown in Fig. 1.18(b), and is mathematically represented in Eq. 1.10. As per the illustration, the projections are presented by the sum of weighted basis function coefficients (Upton et al. 2011). In this formulation, the reconstruction is defined as:

$$W f_{ob} = P_r \tag{1.10}$$

where P_r are projections, f_{ob} represents the object matrix, and W represents a weighting matrix that relates the projection to every discretised point in the object volume. Equation 1.10 results in a set of simple linear equations. However, the size of the problem requires large computational expense. A large set of image algorithms are available in solving Eq. 1.10 and can be categorised into iterative, simultaneous or block-iterative. Iterative methods provide better convergence than simultaneous schemes, and although block-iterative schemes have shown to be beneficial, they are more unstable than pure iterative schemes (Byrne 1998). Other reconstruction algorithms also include genetic algorithms (Goldberg and Holland 1988). These algorithms are used in the biological field with emphasis on the mechanics of genetic principles and have been recently getting attention (Foo et al. 2022, Unterberger and Mohri 2022) due to the algorithms ability to reconstruct a field based on limited projections (Kihm and Lyons 1996). However, the most widely used iterative reconstruction algorithm is the Algebraic Reconstruction Technique (ART) or Multiplicative Algebraic Reconstruction Technique (MART) in CTC implementations (Worth and Dawson 2013, Floyd and Kempf 2011, Cai et al. 2013, Wang et al. 2015). These algorithms are commonly used since (Floyd and Kempf 2011): (i) reconstructions do not require a large number of views, (ii) implementation is robust in the presence of noise, (iii) it is easy to incorporate a-prior information, and (iv) the algorithm is not restrictive by object shape or geometry. A comprehensive review of the choice of basis functions and reconstruction algorithms can be found in Verhoeven (1993). Due to the simplicity and mentioned advantages in implementation, the ART algorithm was chosen for a CTC reconstruction in this thesis.

The reconstruction process from CTC requires multiple LOS measured over a range of independent viewing angles (Floyd and Kempf 2011). However, a large viewing angle requires that the flame of interest has sufficient optical access, which can sometimes prohibit the technique's applicability to confined combustion processes. This may affect reconstruction accuracy, which is sensitive to the number and angles used in the reconstruction process (Wiseman et al. 2017). A typical approach is to use an array of many cameras simultaneous capturing the flame field (Unterberger et al. 2018, Meyer et al. 2016, Gilabert et al. 2007, Ishino et al. 2008), a large collection of optical fibres in combination with a single camera (Liu et al. 2019, Yu et al. 2020, Moinul Hossain et al. 2012, Mohamad et al. 2006) or a single camera reposition across multiple views (Floyd and Kempf 2011, Worth and Dawson 2012, Wiseman et al. 2017). However, the latter application removes the possibility of time-resolved data, meaning only, phase-averaged or time averaged data can be resolved.

Other practical considerations should also be taken into account when experimentally implementing CTC. These include choosing a mapping function to transform the camera coordinates from pixels into real-world coordinates. In addition, the accuracy of the reconstruction process depends on the precision of the camera calibration model (Elsinga et al. 2006) and is sensitive to the experimental optical setup (Wieneke and Taylor 2006). Further experimental considerations will be outlined in Chapter 2 and a comprehensive review of volumetric emission tomography measurements can be found in Grauer et al. (2023)

A study in this thesis outlines some limitations when applying the CTC method (Article I), one major drawback was that all flames within the combustor could not be ignited during acquisition. This removes some complexity in flame interaction. However, this changed the original set-up from that of Nygård et al. (2021). Therefore, one of this thesis's aims was to develop a separate three-dimensional technique to overcome this limitation. This technique is known as Scanning Planar Laser Induced Fluorescence (PLIF) and is discussed in the next section.

1.2.2 Laser Induced Fluorescence and Flame Surface Density

Laser Induced Fluorescence (LIF) is the spontaneous emission of an atom or a molecule when excited by laser radiation. The radiative stimulation of the atom receives energy by absorption, resulting in an unstable excited state that slowly decays by emitting energy (Daily 1997). The emission of energy produces fluorescence and can be captured by a detector. The recording of the fluorescence signal provides the concentration of the excited states, and when a single molecule is excited, one can measure the concentration of that species. LIF has been instrumental in combustion diagnostics and has been used to investigate flame topology (Filatyev et al. 2005, Hult et al. 2007), characterisation of reaction zones Ryan et al. (2009), Tanahashi et al. (2005), measurement of species concentration (Zhao et al. 2011, Yan et al. 2010, Koochesfahani and Dimotakis 1985, Zhao et al. 1994, Medford et al. 2011), velocity measurement (McDaniel et al. 1983) and temperature measurement (Seitzman et al. 1985, Eckbreth 1996).

A typical experimental setup, as shown in Fig. 1.19, consists of a laser source, optics to collimate a thin laser sheet, and a detector, in this case, a camera fitted with a filter to measure a specific excited species in the flame. Usually, the laser sheet required is made to be as thin as possible to minimise out-of-plane effects (Crimaldi 2008). To isolate the fluorescence of a single molecule, the laser source is tuned to a specific absorption transition. An example of an OH-PLIF image is also shown in Fig. 1.19, in which a large intensity gradient is observed in the burnt gas that corresponds to the concentration of the OH radical. In contrast, a low signal is observed in the unburnt gas regions. The difference in gradients between these regions makes OH-PLIF attractive in identifying the instantaneous flame front. The identification of the flame front is useful in Flame Surface Density calcula-

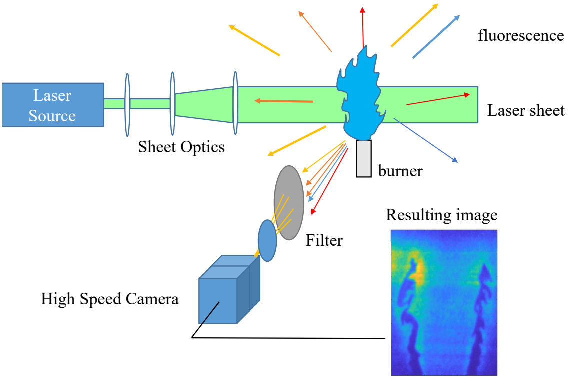

Figure 1.19: An example of a typical Planar Laser Induced Fluorescence experimental setup consisting of a laser source, a series of optics to collimate the laser output into a sheet, and a camera system fitted with a filter to capture a specific wavelength. The image shown in the figure is an example of an OH PLIF image of an ethylene/air flame.

tions.

FSD has been used to infer flame HRR (Dawson and Worth 2014, Paul and Najm 1998, Knikker et al. 2002, Halter et al. 2009). FSD is defined as the flamelet surface area per unit volume, averaged over time, under the assumption of a flamelet framework for premixed turbulent flames. In this frame work it is assumed that the effect of turbulence is limited to the flame surface (Zhang et al. 2015). Halter et al. (2009) relates FSD to the flame burning rate by assuming that all chemical reactions are located in a thin region separating burnt and unburnt gases, then the mean local reaction rate is defined as:

$$\omega_k = \rho_0 \langle S_k \rangle \mathrm{FSD} \tag{1.11}$$

where ρ_0, and $\langle S_k \rangle$ are the density of fresh gas and mean reaction rate of species k per unit flame area. FSD is directly proportional to HRR from equation 1.9 and 1.11. FSD of turbulent combustion systems provides the means to accurately model reaction rates in tools such as RANS (Reynolds Averaged Navier-Stokes equations) and LES and is determined by solving balance equations Candel and Poinsot (1990) or calculated algebraically (Bray 1990), spectrally (Wirth and Peters 1992), through fractal modelling (Gouldin et al. 1989) or experimentally using two-dimensional Planar

Laser Induced Fluorescence.

In the latter case, the realization of a three-dimensional instantaneous flame front visualization is rare since three-dimensional techniques are not trivial to implement. When implementing 2D measurements, it is usually assumed that the out-of-plane flame wrinkling is negligible.As discussed earlier, this assumption falls short for turbulent flames.

LIF has been fundamental in the experimental determination of FSD and the formulation by Pope (1988) has been crucial in its calculation:

$$\text{FSD} = \lim_{\Delta x \to o} \frac{\overline{A}_f}{\Delta x^3} \tag{1.12}$$

where $\overline{A}_f$ is the flame surface area over an interrogation volume Δx^3. As per Eq. 1.12, the calculation of FSD is inherently three-dimensional. However, many calculations of FSD are done from two-dimensional images where the interrogation box is based on a square window, and the flame surface is represented as a two-dimensional arc length. In two dimensions, Veynante et al. (1994) showed that the formulation could be experimentally determined by isolating overlapping square windows over the domain of tomographic images. The size of the window chosen was a compromise between limiting noise effects which occur in small boxes and limiting artificial diffusion that occurs in large boxes (Veynante et al. 1994). After binarising the images and identifying the flame front, the arc length in each interrogation window is determined. The binarising process is done by isolating burnt and unburnt gases by tracking a process variable that takes a value of 1 in the burnt gas and 0 in the unburnt gas. FSD is then calculated based on the average flame length within the interrogation box divided by the window area, and the resulting value of FSD is allocated to the center of the interrogation box. This calculation neglects any 3D effects in the highlighted plane. The dependence on the interrogation box was later evaluated by Donbar et al. (2000), who suggested that the size limitation of the interrogation box needs to be smaller than the flames brush. A thorough review of FSD calculation can be found in Driscoll (2008) for both experimental and theoretical applications. The experimental FSD procedure as defined by Veynante et al. (1994) has been extensively used in the investigation of flame dynamics of bunsen burners (Lee et al. 2000, Deschamps et al. 1996, Chen and Bilger 2002, Bell et al. 2007), V-flames (Veynante et al. 1996, Shepherd 1996), low swirling flames (Shepherd et al. 2002), wide-angled diffuser (Lawn and Schefer 2006) and flat flames (Shepherd and Cheng 2001). The mentioned applications are for axisymmetric flows, making 2D measurements ideal for studying such flames.

Many studies extend 2D measurement to infer 3D FSD. For example, a study by Balachandran et al. (2005) calculated 2D Flame Surface Area (FSA), which represented the flame length per unit area, from a single measurement plane and inferred a 3D distribution of FSD by rotation under the assumption of axisymmetry. The resulting global FSD was then related to integrated OH* measurements of Heat Release Rate fluctuations, showing good agreement. However, the authors highlight that FSD calculated from 2D images neglects fine-scale wrinkling typically present along the surface of turbulent flames. A study conducted by Halter et al. (2009) showed that the errors associated with these planar measurements in using FSD to determine the total reaction rate are around 25-30 percent for atmospheric flames and estimated to be great than 50 percent for pressurized flames. However, Halter et al. (2009) also showed that the total reaction rate estimation could be approximately around 3 to 10 percent for atmospheric flames when estimating the total flame surface in cases where the flow is statistically axisymmetrical with regards to its mean flow.

Much effort has been put into converting 2D flame surface density to estimate the 3D flame response. However, limitations to these methods will persist for flames that produce non-axisymmetric flame shapes. Therefore the use of three-dimensional techniques in determining FSD is important.

Scanning Planar Laser Induced Fluorescence

A means to produce a three-dimensional analysis using LIF is by combining PLIF with scanning optics known as Scanning PLIF. In Scanning PLIF, a laser sheet is rapidly scanned across a volumetric domain, and planar images are acquired through the scan that are then stacked together to form a three-dimensional measurement (Kychakoff et al. 1987, Cho et al. 2014, Miller et al. 2014, Wellander et al. 2014, Yip et al. 1986, 1994, Li et al. 2017, Weinkauff et al. 2015). In Scanning PLIF, temporal resolution is based on the speed of a complete scan defined by the time taken for the laser sheet to sweep the entire volume. Obtaining temporally resolved three-dimensional data would require the scanning speed to be an order of magnitude faster than the flow to effectively *freeze* the flow (Ma et al. 2017). Even with recent advances in camera acquisition and laser repetition rates, this restriction requires that scan frequencies be in the order of 0.1 to 3 MHz to temporally resolve turbulent reacting flows (Cho et al. 2014). Mechanical devices that can scan at these speeds are currently not possible, and most implementations of time-resolved Scanning LIF come at a trade-off between scan speed and scan depth (Römer and Bechtold 2014). A potential device with the ability to produce high scan speeds is an Acousto-Optic Deflectors with scan frequencies in the order of 100 KHz, and such devices have been used in the scanning application of a turbulent lifted jet flame (Li et al. 2017). However, the speed of the scan was restricted by camera acquisition and laser repetition rates. Furthermore, the scanning speed also restricted the implementations to a small volume (13.7 mm).

A study by Weinkauff et al. (2015) applied Scanning PLIF to investigate the time-resolved 3D flame structure of a lifted jet flame. The study showed that the scan rate is sensitive to in-depth spatial resolution. As the authors increased the scan rate, fewer sheets were able to resolve the flow field. The study used Scanning PLIF to identify time-resolved and spatially resolved flame events, while highlighting how the 3D interpretation resolves some ambiguities in 2D measurements. Weinkauff et al. (2015) estimated the size of vortical structure in the flow field to define the scan speed to sufficient resolve these structures, showing that a scan speed of 5 kHz was sufficient. However, as suggested by Weinkauff et al. (2015) improving spatial resolution would require laser repetition rates in the order of 1 MHz. In Scanning PLIF, the in-plane resolution is set by the camera resolution, and the number of laser sheets sets the in-depth resolution. The number of laser sheets is defined by the number of positions in the scan at which images are acquired. A study by Cho et al. (2014) performed time-resolved scanning 3D OH PLIF to investigate jetting events on the combustion of a droplet and solid propellant combustion. The experiment consisted of a 5 kHz OH PLIF system. Although 3D reconstructions were possible at a scan speed of 5 kHz, at this scan rate, only 6 images were acquired for every scan, limiting the spatial resolution of the scan depth. Nonetheless, the dynamics events of the multiphase combustion system were identified in 3D. However, the technique could resolve events in the order of 100 Hz.

This thesis evaluates flames with a bulk flow velocity of 17-18 m/s and a required scan depth of 40 mm. Based on these parameters, a minimum scan rate greater than 40 kHz will be required to freeze the flow. This estimation was based on calculating the time a single particle takes to move 1 pixel distance in the flow field. Therefore, a complete scan must be faster than the time taken for the flame front (particle) to move 1 pixel distance. The pixel resolution was taken from Article II in this calculation to convert a pixel to mm. An acquisition system for Scanning PLIF at this rate is not possible, and, therefore, this thesis investigated azimuthal modes on a phased-averaged basis removing the need for temporal resolution and allowing for a large scan depth with a large number of laser positions.

1.2.3 Other three-dimensional techniques

It is also useful to understand other 3D combustion techniques, one of which includes Volumetric Laser Induced Fluorescence (VLIF) (Ma et al. 2017, Meyer et al. 2016, Xu et al. 2017, Jiang et al. 2016, Wu et al. 2015, Halls et al. 2016). The technique is a combination of LIF and tomography in which a thick laser sheet covers the domain of interest while multiple cameras creating many viewing angles are used to tomographically reconstruct the three-dimensional distribution of the measured scalar quantity. Meyer et al. (2016) used VLIF to track soot formation in turbulent jet diffusion flames. The reconstruction was based on 14 simultaneous views with 8 cameras, however, the authors show that 4 cameras were sufficient to resolve a 20 mm field of depth. Despite the success in reconstruction, the authors also point out the lack of spatial resolution due to poor laser intensity distribution. A study by Wu et al. (2015) show how VLIF can be used for larger volumes and were able to reconstruct a 50 mm field of view of a non-reactive turbulent jet of nitrogen seeded with iodine vapour. However, the authors note that the spatial resolution of PLIF offers superior resolution, and again, numerous views are required for reconstruction. Regarding combustion diagnostics, Ma et al. (2017) performed VLIF on a turbulent bunsen flame with a depth of volume of 5 mm and 5 independent views. The authors use the tracking of the CH radical to overcome limitations in laser non-uniformity that makes reconstruction difficult. Again the authors compare the 3D VLIF reconstruction with PLIF showing that even though the spatial resolution of PLIF is better, more flame elements can be tracked in 3D with the VLIF technique. The VLIF technique's ability to accurately reconstruct three-dimensional scalar fields, its drawbacks and advantages are outlined in Xu et al. (2017). One of the limitations outlined in the study is the technique's ability to reconstruct large volumes. This limitation is a consequence of laser power, and therefore, the technique is usually applied to small volumes of interest. The technique was not adopted in this thesis due to these limitations. A few diagnostic tools have been outlined here. However, these are not exhaustive, and a comprehensive review can be found in Schulz et al. (2007).

1.2.4 Comparison of Chemiluminescence and PLIF

In this thesis LIF and Chemiluminescence are both used in implementing three-dimensional techniques. Both the techniques are promising in the investigation of flame dynamics. However, as presented, these techniques have drawbacks. Ratner et al. (2000) performed a comparison of OH PLIF, NO PLIF and chemiluminescence on a single acoustically forced flame. The study showed that while chemiluminescence is an easier method to implement experimentally, the PLIF method provides better insights into spatial localisation and flame structure (Ratner et al. 2000). Chemiluminescence, however, does not require any excitation of the flow field, as outlined by Mulla et al. (2016). LIF-based measurements are often not used in actual combustion engines due to spatial restrictions; therefore, the preferred strategy is usually chemiluminescence. Nonetheless, in terms of its applications to laboratory burners, LIF-based techniques have been extensively used since the accuracy outweighs the complexity of the technique. Another study by Ma et al. (2016) compared 2D CH* PLIF with 3D tomographic chemiluminescence on a turbulent flame. Both techniques imaged the flame simultaneously, and a center slice of the 3D measurement was directly compared to PLIF at the same location. The comparison by Ma et al. (2016) showed that although the PLIF measurement was superior in temporal and spatial resolution in a plane, the 3D measurement captured more flame elements, allowing for 3D curvature unobtainable in the 2D measurement. Each technique has advantages and disadvantages, and the successful implementations should be defined based on the application. In this thesis, both CTC and Scanning PLIF were applied to the annular combustor to study TI. In both these implementations, drawbacks and success are discussed.

1.3 Research Objectives

This thesis aims to provide a better understanding of the HRR response to azimuthal modes in an annular combustor.Section 1.1.4 presented the differences in the HRR response of annular combustor flames when azimuthally forced in ACW, and CW directions observed by Nygård et al. (2021). The fundamental mechanism for the difference in this response is unknown, and this thesis aims to provide insight into this. This aim will be realised by focusing on the flame dynamics of an individual flame in the annular combustor during azimuthal excitation. This will be accomplished by implementing two three-dimensional techniques to measure the HRR within the combustor. The 3D HHR spatial field will help explain the global response to different modal conditions. To achieve these aims, the following objectives of this thesis are defined:

1. **Investigate the dynamics of a single flame subjected to ACW and CW azimuthal modes inside an annular combustor**

Section 1.1.4 highlighted the motivation in understanding the flame dynamics of ACW and CW modes to isolate regions in the flame that produces a difference in their response. To address this, Computed Tomography of Chemiluminescence will be implemented on an annular combustor to spatially resolve the HRR response of azimuthally forced flames in three dimensions. The investigation will isolate a single forced flame within the confinement of the annular combustor. The absence of neighbouring flames makes the CTC method ideal for understanding the flame response.

2. **Develop a three-dimensional technique that overcomes limitations of the CTC method for the evaluation of flame dynamics in an annular combustor**
   This objective will be executed by evaluating Scanning PLIF as an alternative three-dimensional technique to resolve the HRR response in a multi-flame annular combustor. Flame Surface density will be used as a marker for the HRR response. A phase-averaged approach will be implemented allowing for a large volume to be reconstructed. Limitations of the Scanning PLIF method will also be evaluated and where possible solutions will be proposed.

3. **Apply the Scanning PLIF technique to investigate the three-dimensional HRR response of unswirled flames in a standing wave**
   With the use of Scanning PLIF, the HRR response for different positions along a standing wave will be investigated for unswirled flames in an annular combustor. Section 1.1 and Section 1.0.4 outlined studies that investigated positioning a flame at the node and antinode of a standing wave for both transverse and annular setups. In this thesis, the complexity of the swirler was omitted to remove flame-flame and flame-wall interactions, and also remove the spatial redistribution of the HRR oscillations due to to swirl, simplifying the response.

4. **Apply the Scanning PLIF technique to investigate the three-dimensional HRR response to spinning modes**
   A three-dimensional analysis will be applied to understand the HRR response to CW and ACW modes of swirled flames in a 18 injector annular combustor configuration. This configuration promotes flame-flame interaction and the FOV will isolate two half flames while resolving the complete flame-flame interaction zone. The analysis will be aimed at identifying flame structures and the timing of the response and how these impact the HRR for each modal direction. Thus provid-

ing insight into why different HRR responses occurs between spinning azimuthal modes.

1.4 Thesis Outline

This thesis is organised into 5 Chapters. Chapter 1 provides background and motivation, outlining some studies in thermoacoustics in single, transverse and, most importantly, annular combustors. Experimental methods are also outlined in Chapter 1, and the Chapter concludes with the research aims. Chapter 2 presents experimental methods, setups and data processing methods. Some results were not yet published and will be briefly outlined in Chapter 3. In Chapter 4, three publications will be summarised, and the full-length articles are presented at the end of this thesis. Finally, Chapter 5 provides conclusions and describes how the main aims have been achieved.

We are certainly not to relinquish the evidence of experiments for the sake of dreams and vain fictions of our own devising; nor are we to recede from the analogy of Nature, which is wont to be simple and always consonant to itself

— *Isaac Newton*

2

Experimental setup and diagnostics

The primary aim of this thesis is to provide an understanding of the response of flames within an annular combustor to azimuthal excitation. This was accomplished by undertaking four different investigations using a modified version of the Cambridge annular combustor built by Worth and Dawson (2013). This combustor was built at the Norwegian Institute of Science and Technology (NTNU), and the design and dimensions are outlined in § 2.1. A forcing array was attached to the combustor to create azimuthal modes, which is discussed in § 2.2.3, together with the equations that define the acoustic response in the annular combustor. The investigations were conducted by using two different three-dimensional experimental measurement techniques, Scanning PLIF and Computed Tomography of Chemiluminescence (CTC). Both techniques reconstruct the three-dimensional Heat Release Rate field from which flame dynamics were assessed. The description of these techniques are outlined in § 2.3 and § 2.6, respectively. A synthetic study, that involved creating Scanning PLIF images from artificial flame objects, helped improve the implementation of the technique and identify its shortcomings. This Synthetic PLIF study's methodology is presented in § 2.5.

2.1 Experimental set-up

This section outlines the experimental facility used in this thesis, detailing the combustor dimensions and the limitations of the geometry. This section also outlines the characterisation of annular modes by pressure measurements and the procedure of implementing acoustic forcing using a speaker array to create azimuthal modes in the combustor.

2.1.1 Annular combustor

A cross-section of the annular combustor used in this thesis is outlined in Fig. 2.1 and an image of the combustor is also shown in Fig. 2.2. A premixed mixture of air and fuel enters the base of the combustor and each flowrate was controlled using an Alicat MC mass flow controller with a range of 0-1000 SLPM and 0-500 SLPM, respectively, and flow variability of 0.4%. The fuel type and flow velocities, along with minor differences in the combustor setup are outlined in Table 2.1. The separate lines containing fuel and air are connected to the combustor by a single inlet via a T-junction connection attached 1 m upstream of the combustor to provide sufficient premixing of the air-fuel mixture. The mixture flows through an expansion at the base of the combustor through a perforated plate with a porosity of 64 % and into a plenum of diameter, $D_p = 211$ mm and length $D_{pl} = 200$ mm. The expansion and impinging jet at the entry of the combustor also promotes further mixing of the incoming air-fuel mixture. A hemispherical flow divider with a diameter of $D_h = 140$ mm was attached close to the exit of the plenum to ensure that flow is uniformly distributed at the outlet of the plenum. At the exit of the plenum, the flow passes through a second perforated plate with a porosity of 57 % to provide additional flow conditioning before entering individual injector tubes. The combustor was designed to account for two interchangeable injector and retention plates to allow for either 12 (Article I, II & Chapter 3) or 18 (Article III) equally spaced flames around a circle of diameter 170 mm.

An injector base plate encloses the plenum with machined holes that secure individual injectors. Rubber gaskets were placed between the injector tubes and the machined base plate holes to prevent leakage. Figure 2.3(a) provides a detailed view of the injectors used in this thesis. The injector tubes had a height of $l_i = 145$ mm and a diameter of $D = 19$ mm, and each injector was fitted with a rod of diameter $D_{rod} = 5$ mm spanning the entire length of the injector. The rod terminated with a bluff body of diameter $D_{bb} = 13$ mm and a half angle of 45°. The rod was centered in each injector at two points, at the base of the injector in which a webbed insert held the base

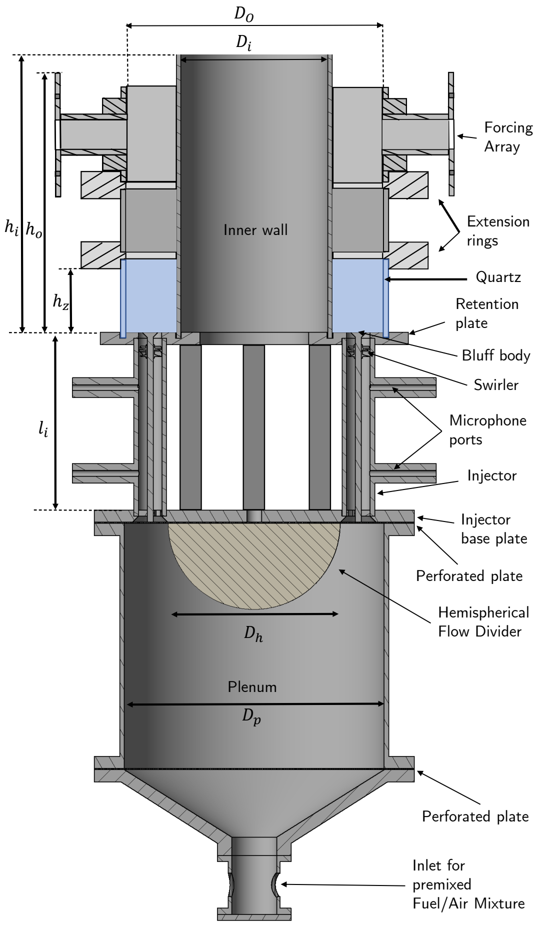

Figure 2.1: Cross section of annular combustion rig with forcing array and quartz optical access

of the rod, and 65 mm upstream of the combustion chamber with three M4 grub screws arranged equidistantly around the injector tube. In the investigation of swirled flames, a 6 vaned swirler was installed onto the rod $h_s = 10$ mm downstream from the bluff body edge to the trailing edge of the swirler. A 3D visualisation of the swirler is shown in Fig. 2.3(a) and Table 2.1 outlines which studies were applicable to a swirler installation. The arrangement of the swirler produces ACW swirl when viewed from a downstream point of view, as shown in Fig. 2.3(b). Swirlers were oriented such that the line formed by two vanes' trailing edges were aligned along the annular radial direction to ensure the rotational symmetry of the combustor was not broken. The swirler trailing edge angle was 60° with respect to the axial direction and produced a swirl number of 0.65 measured 10 mm downstream of the dump plane (Nygård and Worth 2021).

A retention plate was fitted at the top end of the injector tubes and was clamped down via threaded rods onto the injector plate securing the injectors in place. The retention plate formed the dump plane of the combustor creating a sudden flow expansion into the combustion chamber. The bluff bodies in each injector were installed flush to the dump plane, creating a blockage factor of 50 %. Two different designs of the injector tubes were used, one as outlined in Fig. 2.3(a), and the other was identical to the first except the inclusion of the microphone ports. The former design was used to measure pressure at two points within the injectors, and hence, two pressure transducers were installed flush in each port at heights $h_{m1} = 45$ mm and $h_{m2} = 105$ mm from the dump plane. Three pairs of pressure transducers were placed 120° apart around the annulus and were used to characterise the mode within the combustor; further details on the characterisation of annular modes are outlined in § 2.2. The pressure transducers used were Kulite XCS-093-0.35D differential pressure transducers. Each was fitted with O-rings when installed in the pressure mounts, shown in Fig. 2.3(a), to prevent any vibrations, provide electrical insulation, and to seal the sensors within the mount. Two Fylde FE-579-TA bridge amplifiers amplified the signals from the transducers, and NI-9234 24-bit DAQ modules acquired the resulting signals at a sampling rate of 51.2 kHz. DAQ modules with twenty four channels were used to acquire relevant signals during the experiment.

The combustion chamber of the annular setup confined flames between an inner steel wall and an outer wall consisting of quartz, steel and the forcing ring as outlined in Fig. 2.1. The inner wall had a height, $h_i = 194$ mm and diameter, $D_i = 127$ mm. The total height of the outer wall was $h_o = 175$ mm with an outer diameter of $D_o = 212$ mm. The quartz tube was placed at

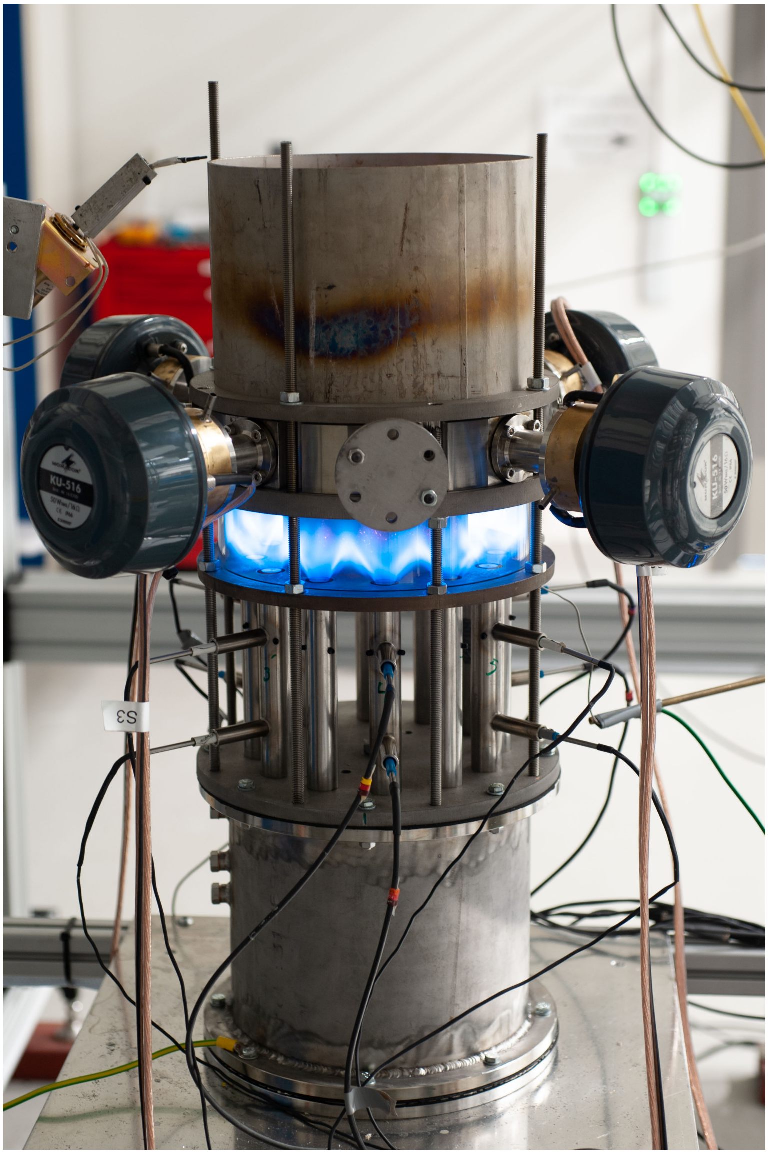

Figure 2.2: Annular combustor experimental forced setup. Note that the setup used in this thesis was not exactly the same as the configuration shown.

Annular Combustor Operating Conditions				
Properties	Article I	Article II	Article III	Chapter 3
Fuel type	C_2H_4	C_2H_4	C_2H_4	C_2H_4
Equivalence ratio	0.8-1.1	0.8	0.8	0.7
Swirler	Yes	No	Yes	No
Number of burners	1	12	18	12
Bulk flow velocity	18 m/s	17 m/s	18 m/s	17 m/s
Forced	Yes	No	Yes	Yes
Diagnostic Type	CTC	Dual Scanning PLIF	Single Scanning PLIF	Dual Scanning PLIF

Table 2.1: Operating conditions for various experiments in this thesis. The reported bulk flow velocities are measured at the combustor injector exit.

the base of the outer wall with a height of $h_q = 50$ mm permitting optical access for the CTC and Scanning PLIF techniques. An outer extension wall was placed above the quartz to ensure that the forcing array was sufficiently high to prevent any interaction with the flames, which may result in damage to the speakers. It was important to run under stable conditions allow reasonable control of the forced azimuthal modes. The chosen equivalence ratio (fuel to air ratio) ensured thermoacoustic stability. The pressure measurements were used to assess the stability of operating conditions in the injectors (method outlined in § 2.2.3). A temperature probe was installed on the inner wall at the flame of interest during all the experiments to monitor thermal conditions.

The forcing array terminated the outer wall of the combustor. Four Monacor KU-516 horn drivers were installed equidistantly around the forcing ring. Two images outlining the forcing ring are presented in Fig. 2.7. The design of the forcing ring allowed for the installation of eight speakers, however, it was found that four speakers provided a simpler means of control, and the four speaker arrangement was used throughout the study when forcing was applicable. Two QTX PRO1000 amplifiers powered the speaker pairs and a 4-channel Aim-TTi TGA1244 signal generator controlled the frequency and amplitudes of the signal sent to the speakers.

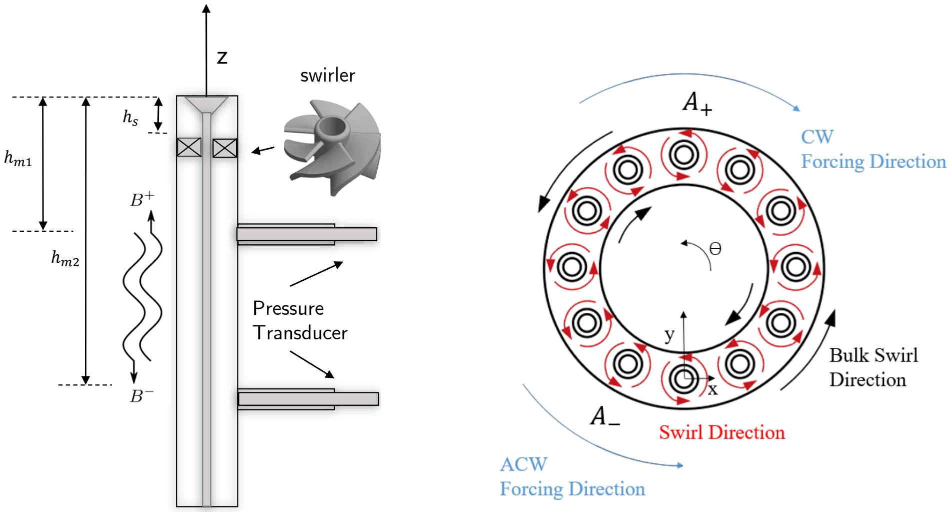

(b)

(a)

Figure 2.3: (a) Injector geometry outlining bluff body, swirler and position of pressure transducers. (b) Schematic of annular rig and directional orientation of ACW, CW swirler and bulk flow. Adapted from Dawson and Worth (2014).

2.2 Modal characterisation of annular combustor

Most of the studies outlined in this thesis provide an understanding of the forced response of flames within the annular combustor subjected to azimuthal excitation. Pressure measurements in three separate injectors equally spaced around the combustor were used to characterise these azimuthal modes within the combustor. This section outlines the procedure for determining the response of the forced states in terms of pressure and velocity oscillations.

Pressure Sensor Calibration

The pressure measurements around the annulus are used to characterise the mode in the annular combustor. It was important that these measurements were consistent. Therefore, the Kuilte pressure sensors used in this study were calibrated before installation into the respective injector tubes of the combustor. A relative calibration was performed in which the sensors were calibrated against each other to ensure that the response from each sensor was similar. To do this, the pressure sensors were placed in a pipe which is terminated at one end with a loudspeaker. The speaker operated across

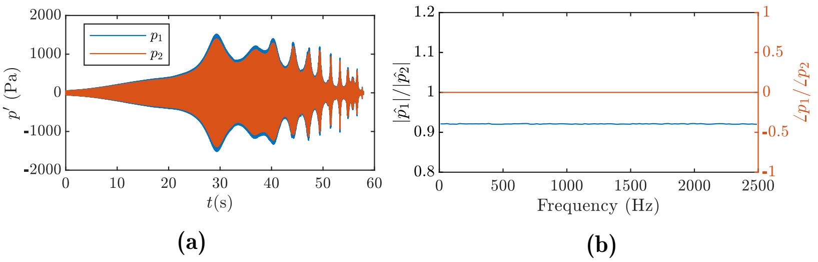

Figure 2.4: (a) Time series showing the response during a calibration between pressure sensors p_1 and p_2 over a frequency sweep (b) Transfer function showing the gain (left y axis) and phase (right y axis) between pressure sensors p_1 and p_2.

a frequency range while the signal from the sensors were acquired. A time series of two pressure sensors are shown in Fig. 2.4(a) for two microphones p_1 and p_2. The gain and phase were assessed for each microphone and an example of the transfer function between the two microphone responses is shown in Fig. 2.4(b). In this example, the gain of p_1 was around 8% less than p_2, and a correction was applied to ensure the response was the same for both pressure sensors. The phase between the microphones is also assessed, the result was that no significant phase differences were encountered.

2.2.1 Determining the mode in the injector tubes

The pressure inside the combustor could not be directly measured due to the proximity of the flames. Therefore, the pressure fluctuations inside the annulus was approximated from the pressure fluctuations inside the injector tubes. First, the convective wave equation was used to describe a pressure disturbance ($p'(z,t)$) with a mean flow (U) in an arbitrary geometry as (Dowling and Stow 2003):

$$\left[\frac{1}{c^2}\frac{D^2}{Dt^2} - \nabla^2\right]p' = 0 \tag{2.1}$$

$$\frac{D}{Dt} = \frac{\partial}{\partial t} + (U \cdot \nabla) \tag{2.2}$$

where c represents the speed of sound. The coordinate system represented in this section is shown in Fig. 2.3(a). Redefining Eq. 2.1 and Eq. 2.2 with respect to the pressure disturbance inside an injector tube (p'_{inj}), required the following assumptions: (i) the properties in the injector are one dimensional, and variations in the radial and azimuthal components are ignored since the length of the injector tube is much larger than its diameter, (ii) viscous effects in the duct are neglected and therefore it is assumed that the flow is governed by the Euler equations, and (iii) the properties of the flow can be decomposed into a mean and a fluctuation. Therefore, Eq. 2.1 and Eq. 2.2 reduce to:

$$\frac{\partial^2 p'_{inj}}{\partial z^2} = \frac{1}{c^2}\left(\frac{\partial}{\partial t} + U\frac{\partial}{\partial z}\right)^2 p'_{inj} \tag{2.3}$$

Assuming that the disturbances in the duct can be described as two counter-propagating plane waves, the solution to Eq. 2.3 is given as:

$$p'_{inj}(z,t) = [B_+ \exp(-ik_+ z) + B_- \exp(ik_- z)]\exp(i\omega t) \tag{2.4}$$

where B_+ and B_- represent the complex-valued pressure amplitudes of two counter-propagating waves and ω represents the angular frequency. Since the modes in this study were forced, ω in this formulation is specific to the forcing frequency (ω_f). The definition of forcing frequency is outlined in § 2.2.3. In Eq. 2.4 $k_\pm$ represents the wave numbers as follows:

$$k_\pm = (\omega_f/c)/(1 \pm Ma) \tag{2.5}$$

where Ma represents the Mach number with $Ma = U_b/c$, and U_b represents the bulk flow velocity in the duct. In a similar formulation, the axial velocity disturbance, u'_{inj} was calculated using the one-dimensional linearised momentum equation Dowling and Stow (2003):

$$\frac{\partial u'_{inj}}{\partial t} + U\frac{\partial u'_{inj}}{\partial z} + \frac{1}{\rho}\frac{\partial p'_{inj}}{\partial z} = 0 \tag{2.6}$$

where ρ represents the density of the fluid in the duct. From Eq. 2.6 the solution for axial velocity oscillation was estimated as :

$$u'_{inj}(z,t) = (1/\rho c)[B_+ \exp(-ik_+ z) - B_- \exp(ik_- z)]\exp(i\omega t) \tag{2.7}$$

The parameters of ρ, ω_f, c and U_b are known and were calculated at standard temperature and pressure (STP). The acoustic velocity and pressure oscillations were calculated from Eq. 2.4 and Eq. 2.7, respectively. Both equations contain two unknowns, $B\pm$, and were calculated from pressure measurements by use of the Multi-Microphone Method (MMM) (Seybert and Ross 1977). The pressure measurements taken at the locations outlined in Fig. 2.3(a) were used to determine the $B_{\pm}$ in Eq. 2.4 using:

$$\begin{bmatrix} \hat{p}_{inj}(z_1) \\ \hat{p}_{inj}(z_2) \end{bmatrix} = \begin{bmatrix} \exp(-ik_+z_1) & \exp(ik_-z_1) \\ \exp(-ik_+z_2) & \exp(ik_-z_2) \end{bmatrix} \begin{bmatrix} B_+ \\ B_- \end{bmatrix} \tag{2.8}$$

here $\hat{p}_{inj}(z)$ represents the complex pressure that contains Fourier amplitude and phase of the pressure oscillations. The complex pressure is related to the injector pressure measurement by $p'(z,t) = \hat{p}_{inj}(z)\exp(i\omega t)$. The Fourier amplitude was determined by performing a Fast Fourier Transform (FFT) of the pressure time series. Sufficient zero padding ensured the frequency bin was located at an integer multiple of the forcing frequency, and Hann windowing (Oppenheim and Schafer 2009) reduced the dependence on the limited sample size. The shortest duration of experimental data acquisition, in this thesis, was 1 second corresponding to the study in Article I. The values of $B_{\pm}$ were then determined by a least square fitting of Eq. 2.8 and Fig. 2.5(a) shows an example of the fitted pressure oscillation amplitude ($|\hat{p}_{inj}|$) and phase ($\angle\hat{p}_{inj}$) inside the injector with data points representing the measurement. Fig. 2.5(a) shows a good fit between the experimental and fitted data. In this formulation, it is assumed that the amplitudes $B_{\pm}$ are constant throughout the acquisition of experimental data, therefore, a single value for $B_{\pm}$ is sufficient to describe the response over the acquisition period. The pressure and velocity measurements presented are with respect to the oscillations in the injector tube of the combustor. However, understanding the modes in the combustor requires characterisation of the pressure oscillations in the annular combustion chamber. Therefore, pressure and velocity oscillations were propagated using the MMM to obtain the complex pressure at the exit of the injector/dump plane. However, the acoustic effects of the swirler, when present, and the flow contraction due to the bluff body at the injector exit needed to be accounted for.

Under the assumption of low Mach numbers, $Ma << 1$, the pressure and mass flow oscillations are conserved for small area changes (Dowling and Stow 2003). The area change is assumed to be smooth and was estimated in discrete steps. A large number of steps would make this approximation continuous, however, ten steps were sufficient. The amplitudes $B_{\pm}$ were solved using the MMM method at these ten discrete steps across the bluff body while maintaining the mass and pressure flux at these locations. The change in area and geometry of the swirler results in partial reflections

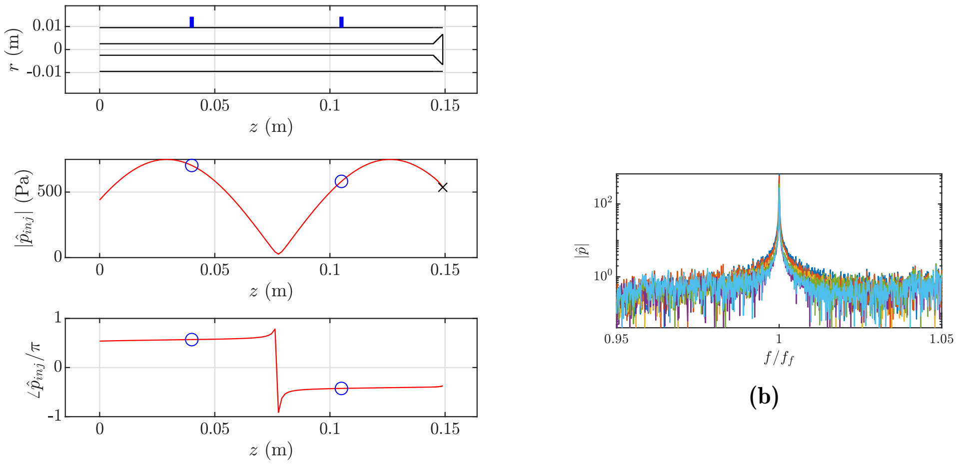

(a)

(b)

Figure 2.5: (a) (Top) Plot of injector geometry including bluff body, (middle) pressure fluctuation fit (red) line and measured data (blue markers) inside the injector tube, (bottom) phase of pressure fluctuation inside the injector the tube. (b) Spectrogram of all six microphones when flame is forced at 1790 Hz. Note the peak shown in the figure corresponds to the forcing frequency for all six microphones.

of acoustic waves by the swirler which needs to be accounted for. The swirler position inside the injector has been shown in Fig. 2.3(a), and the details of its installation were discussed in § 2.1. Taking a black box-approach, a transfer matrix was used to model the acoustic effects of the swirler. The transfer matrix was experimentally determined by Indlekofer et al. (2021) and used in this study to calculate the $B_{\pm}$ before and after the swirler. The transfer matrix was measured by taking pressure measurements at multiple locations along an injector tube that contained a swirler with similar dimensions and orientation to that used in this thesis. Indlekofer et al. (2021) determined the acoustic response for a range of frequencies, and the transfer matrix used in this thesis was taken at the forcing frequency.

2.2.2 Determining the mode in the annulus

Three pairs of pressure sensors were used to project pressure and velocity oscillations to the dump plane at three discrete locations around the annulus. These points were then used to define the azimuthal mode in the combustor. This was done in two ways, (i) the Multiple Microphone Method (MMM) - defining the acoustic response as a superposition of two counter-propagating plane waves and (ii) the hypercomplex formulation proposed by Ghirardo and Bothien (2018). The first method was used in Article I, and the second applies to Article III. Both methods will be outlined in this section. The former method uses a similar approach as outlined in § 2.2.1.

Multiple Microphone Method

In this formulation, the azimuthal pressure mode is given as (coordinate system in annular coordinates is shown in Fig. 2.3(b)):

$$p'(\Theta, t) = [A_+ \exp(-i(\Theta - \Theta_{nl})) + A_- \exp(i(\Theta + \Theta_{nl}))] \exp(i\omega t) \tag{2.9}$$

where A_+ and A_- represents the complex-valued pressure amplitudes of counter-propagating waves in the anticlockwise (ACW) and clockwise (CW) direction, respectively. Θ_{nl} is the nodal line location. Eq. 2.9 can be recast in the frequency domain as:

$$\hat{p}(\Theta, \omega) = A_+ \exp(i(\Theta - \Theta_{nl})) + A_- \exp(i(-\Theta + \Theta_{nl})) \tag{2.10}$$

In a similar approach to Eq. 2.10 the azimuthal velocity oscillation is defined as:

$$v'(\Theta, t) = (1/\rho c)[A_+ \exp(-i(\Theta - \Theta_{nl})) - A_- \exp(i(\Theta - \Theta_{nl}))] \exp(i\omega t) \tag{2.11}$$

Similarly to calculating $B_\pm$ in § 2.2.1, the values of the $A_\pm$ and Θ_{nl} are calculated from Eq. 2.10 using the complex pressure oscillations at three azimuthal locations ($\Theta = 0°, 120°, 240°$) around the annulus using a least square approach. Note that the physical parameters of the system in Eq. 2.11 are calculated based on the adiabatic flame temperature of the fuel of interest. The values of $A_\pm$ were used to define the azimuthal pressure and velocity oscillations in the annulus and the characterisation of the modes inside the annulus via the Spin Ratio (SR) Bourgouin et al. (2013):

$$SR = \frac{|A_+| - |A_-|}{|A_+| + |A_-|} \tag{2.12}$$

The Spin Ratio defines the mode such that a value of $SR = 0$ denotes a standing mode, $SR = 1$ represents a ACW spinning mode, and $SR = -1$ represents a CW spinning mode and SR values in between spinning and standing modes produce mixed modes. This formulation has been discussed

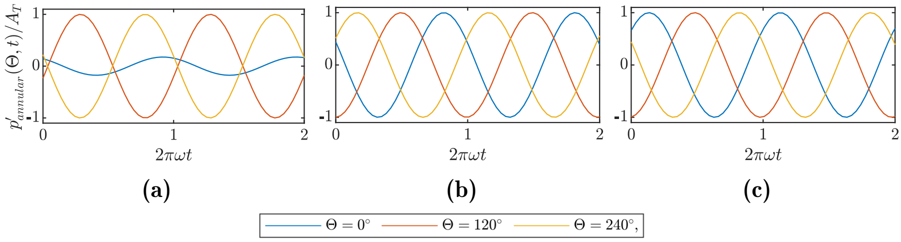

(a) **(b)** **(c)**

Figure 2.6: Experimental propagated pressure fluctuations of (a) Standing wave with $SR \approx 0$ ($A_+ \approx A_-$). Note the pressure node is at microphone location $\Theta = 0°$ (b) CW spinning mode with $SR \approx -1$ ($A_+ \approx 0$) (c) ACW spinning mode with $SR \approx 1$ ($A_- \approx 0$).

in Chapter 1 and is revisited here. The total pressure oscillation amplitude of the azimuthal mode is given by,

$$A_T = \sqrt{A_+^2 + A_-^2} \tag{2.13}$$

An example of a time series of propagated pressure is shown for a standing mode in Fig. 2.6(a), CW spinning mode in Fig. 2.6(b) and ACW spinning mode in Fig. 2.6(c). The response to the pressure fluctuations for the standing wave differs from the response of the spinning waves. The pressure oscillation at the location, $\Theta = 0°$ is at a pressure node. As shown, this location experiences the lowest pressure fluctuation. The other two locations presented show symmetric responses. In contrast, the spinning waves produce similar pressure responses with a time delay equal to the azimuthal angle separating each measurement by $\Theta = 120°$. The direction of each spinning wave is schematically shown with respect to the annulus in Fig. 2.3(b).

Quaternion formulation

Ghirardo and Bothien (2018) proposed an alternative method to define the azimuthal pressure fluctuation in terms of the hypercomplex quanternion formulation. It should be noted that either Eq. 2.9 or the Quaternion formulation proposed here will produce the same result. However, the definition in Eq. 2.9 is based on derived quantities of the acoustic field and the Quaternion formulation defines the system based on state space variables that directly define the nature of the mode. This derivation has made modelling applications easier. Ghirardo and Bothien (2018) defines the azimuthal pressure mode by:

$$\begin{aligned} p'(\Theta,t) = {} & A\cos\left(\Theta-\Theta_0\right)\cos\left(\chi\right)\cos\left(\omega t+\varphi\right) \\ & +A\cos\left(\Theta-\Theta_0\right)\sin\left(\chi\right)\sin\left(\omega t+\varphi\right) \end{aligned} \tag{2.14}$$

where A, Θ_0, χ and φ are the amplitude of the azimuthal pressure mode, the position of the pressure antinode, the nature angle and the temporal phase, respectively. As outlined in Chapter 1, χ describes the nature of the mode and takes values within the interval $-\pi/4 \leq \chi \leq \pi/4$. The complete derivation of equation (2.14) can be found in Ghirardo and Bothien (2018). The propagated injector exit pressure fluctuations at three azimuthal annular locations are used to determine A, Θ_0 and φ. The state space parameters in Eq. 2.14 are determined by pressure measurements using the method outlined in Ghirardo and Bothien (2018) and is briefly outlined here. First a quaternion analytical signal (ξ_a) is defined as:

$$\xi_a = \xi_1(t) + i\xi_2(t) + j\mathcal{H}[\xi_1(t)] + k\mathcal{H}[\xi_2(t)] \tag{2.15}$$

where ξ_1 and ξ_2 are projected signals. Symbols, i,j and k are three imaginary units of quaternions and $\mathcal{H}$ represents the Hilbert transform. The pressure signal is related to the analytic signal by two orthogonal eigenmodes:

$$p'(\Theta,t) = \xi_1(t)\cos(n\Theta) + \xi_2(t)\sin(n\Theta) \tag{2.16}$$

The projected signals ξ_1 and ξ_2 are determined using the pressure signals around the annulus:

$$\begin{bmatrix} p'(\Theta_1,t) \\ p'(\Theta_2,t) \\ \vdots \\ p'(\Theta_N,t) \end{bmatrix} = \begin{bmatrix} \cos(n\Theta_1) & \sin(n\Theta_1) \\ \cos(n\Theta_2) & \sin(n\Theta_2) \\ \vdots & \vdots \\ \cos(n\Theta_N) & \sin(n\Theta_N) \end{bmatrix} \begin{bmatrix} \xi_1(t) \\ \xi_2(t) \end{bmatrix} \tag{2.17}$$

where N is the number of pressure measurements around the annulus. A least square approach was used to solve for ξ_1 and ξ_2 in Eq. 2.17 for each time step, resulting in the full time series of ξ_a in Eq. 2.15. The state space variables in Eq. 2.14 are determined from ξ_a as outlined in the appendix of Gharib et al. (1998). A band-pass filter was applied to the pressure signals before solving Eq. 2.17. A 5^{th} order Butterworth filter was used and the frequency chosen corresponded to the forcing frequency. Similarly, the state

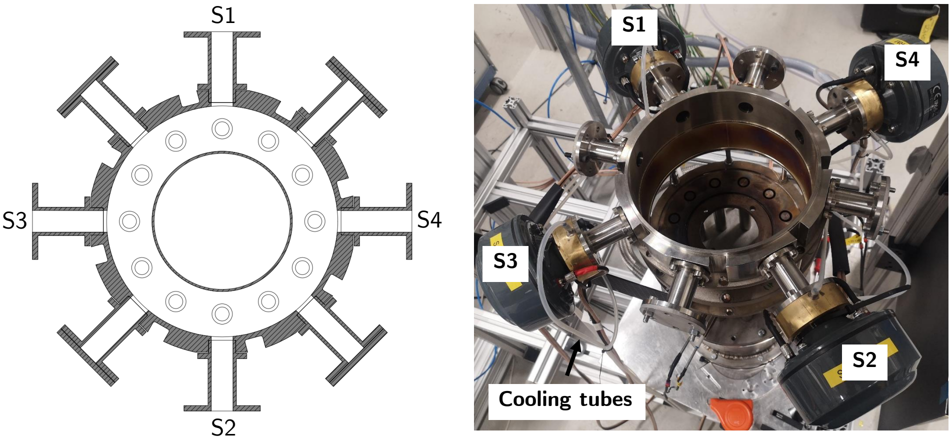

Figure 2.7: Cross sectional drawing of forcing array (left). Forcing array on experimental setup outlining the speaker positions (right).

space variables in Eq. 2.14 were used to determine the azimuthal acoustic velocity fluctuations as follows:

$$\begin{aligned} v'(\Theta,t) = (1/\rho c)[&A\cos(\Theta-\Theta_0)\cos(\chi)\cos(\omega t+\varphi) \\ &-A\cos(\Theta-\Theta_0)\sin(\chi)\sin(\omega t+\varphi)] \end{aligned} \tag{2.18}$$

In Article III, the nature angle, χ, is used for modal characterisation and can be related back to Spin Ratio by $SR = \tan(\chi)$. Nature angles of $\chi = +\pi/4$ and $\chi = -\pi/4$ define spinning modes in the ACW and CW directions, respectively. The amplitude A is related to A_T in Eq. 2.13 as follows Ghirardo and Bothien (2018):

$$\frac{A}{\sqrt{2}} = A_T \tag{2.19}$$

2.2.3 Forcing setup

A study by Mazur et al. (2018) produced a stability map outlining operating conditions at which self-excited azimuthal instabilities occur for non-swirled ethylene flames on a similar annular setup as described in this thesis. These self-excited modes are of interest in understanding the azimuthal response of the annular rig. However, these modes are degenerate in nature making the isolation of specific mode difficult. Therefore, the studies in this thesis relied on acoustic forcing to prescribe the modal behaviour in the annular combustor. The forcing setup used in this study was developed by Nygård (2021) and will be summarised herein.

Figure. 2.7 presents a schematic and an image of the forcing array installed on the annular combustion rig. The forcing array consisted of four equally spaced speakers which were connected in pairs as labelled in Fig. 2.7. A single signal from a 4-channel Aim-TTi TGA1244 signal generator was sent to each pair. The speakers in each pair are driven with a phase offset of π, which was set by connecting one speaker in each pair with reverse polarity. This configuration creates an azimuthal standing wave in the combustor, and spinning modes are generated by offsetting the phase between the speaker pairs. Note that a standing wave can be created with a single speaker pair, but it has been shown by Nygård (2021) that the two pairs produce a more symmetric response. Nygård (2021) outlines the mathematical definition of azimuthal modes created by the two speaker pair setup. In this formulation, the response in the annulus is defined as two 1D counter-propagating waves, and it is shown that the nature angle of azimuthal modes is a function of the signal generator offset, ϕ_{sig}, as follows:

$$\tan(\chi) = \frac{|\cos(1/2(\Theta_p - \phi_{sig}))| - |\cos(1/2(\Theta_p + \phi_{sig}))|}{|\cos(1/2(\Theta_p - \phi_{sig}))| + |\cos(1/2(\Theta_p + \phi_{sig}))|} \tag{2.20}$$

Here Θ_p represents the spatial offset of the speakers around the annulus. In the setup described here, $\Theta_p = \pi/2$ and Eq. 2.20 reduces to :

$$2\chi = \begin{cases} \phi_{sig} - \pi, & \pi \leqslant -\phi_{sig} < -\pi/2 \\ \phi_{sig}, & -\pi/2 \leqslant \phi_{sig} \leqslant \pi/2 \\ \pi - \phi_{sig}, & \pi/2 \leqslant \phi_{sig} \leqslant \pi \end{cases} \tag{2.21}$$

Eq. 2.21 covers the complete range of nature angles, $-\pi/4 \leqslant \chi \leqslant \pi/4$ and setting ϕ_{sig} equal to 0, $-\pi/2$ or $\pi/2$ will produce a standing mode ($\chi = 0$), CW spinning mode ($\chi = -\pi/4$) or ACW spinning mode ($\chi = \pi/4$), respectively.

A frequency sweep was performed before setting up the modes in the combustor. The aim was to find the highest amplitude response of the combustor, this frequency defined earlier as the forcing frequency (ω_f) is sensitive to combustor geometry and operating conditions. The procedure involved setting up a standing mode in the combustor, observing the response and repeating the procedure for a range of frequencies. Each frequency was evaluated by igniting the rig and running for 30 seconds while recording the response. The rig was then extinguished and cooled to a reference temperature before a new frequency was evaluated. The forced data was acquired

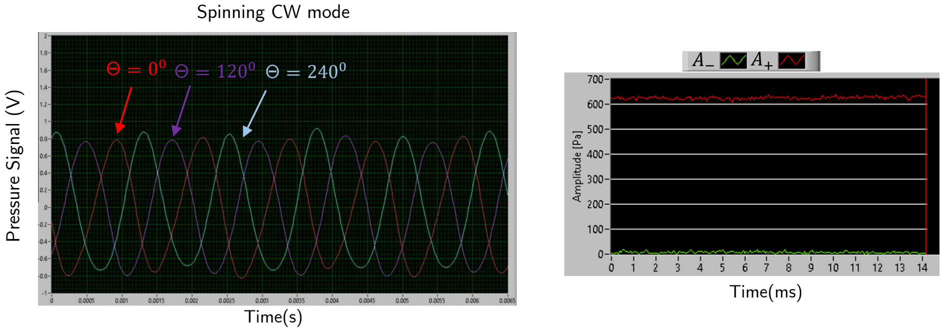

Figure 2.8: Lab view Graphical User Interface (GUI) used in forcing setup (left) to track pressure waves inside the annular rig at respective microphone positions and (right) tracking of the azimuthal amplitude in the annular chamber with $B = A_+$ and $A = A_-$. The example shown is with respect to a CW spinning mode.

after 20 seconds to ensure a relative thermal equilibrium. However, reaching a complete thermal equilibrium was impossible in the annular rig since the speaker setup was not designed to withstand the thermal equilibrium temperature range. Therefore, data was acquired before total thermal equilibrium.

High temperatures are still reached in the combustor, therefore, cooling tubes were installed to supply each speaker with flushing air ensuring hot gas does not contact the speaker. The cooling tubes can be seen in Fig. 2.7. During acquisition, a LabView program tracked the Spin Ratio, the raw pressure signals and the $A_\pm$ amplitudes of the azimuthal modes in the combustion chamber in real time. An example of the LabView user interface displaying the pressure signals at three injector exit locations and the $A_\pm$ values for a CW spinning mode is shown in Fig. 2.8. Access to the LabView program helped maintain amplitudes between runs and during acquisition.

Procedure in setting up standing and spinning modes

As shown earlier, spinning/standing modes are created by setting an offset in phase between the speaker pairs. This formulation, however, is for an ideal case in which the rig is completely symmetric, and each speaker pair provides the same output. In reality, this was not the case, and fine-tuning was required to maintain azimuthal modes in the combustion chamber. In the case of standing waves, an offset of zero, as described by Eq. 2.21 was set between the speaker pairs to produce a repeatable and controllable standing mode. In some cases, adjustments around ±5° in the phase offset were required to ensure a nature angle or spin ratio of zero. However, setting up pure spinning modes ($SR \approx \pm 1, \chi \approx \pm \pi/4$) is more challenging. The procedure requires that either A_- or A_+ of each standing wave set by each speaker pair perfectly cancels out the other by destructive interference. In the case of a CW spinning mode, this implies that the A_- of each speaker pair must perfectly match the other to ensure destructive inference resulting in a single wave inside the chamber propagating with $A_+ >> A_-$. Since each pair creates a standing wave, a single speaker pair was switched on after 20 seconds of ignition with a frequency determined from the frequency sweep. The A_- value was monitored over 20 seconds. The combustor is extinguished, cooled and ignited again. The second speaker pair was turned on, and while monitoring the A_- magnitude, careful tuning of the amplitude was applied till the A_- value matches the first pair. The rig was extinguished and cooled again. This step was repeated to ensure that the response of A_- perfectly matched the other speaker pair. The rig was also run for a fixed amount of time, and the estimation of the amplitude response was usually the value taken after 20 seconds; this was the time frame for images acquisition during the experiment. Therefore, if adjustments could not be made within this time frame, the step was repeated due to the temperature dependence on the modes. When the amplitude was matched, an offset was applied between the speaker pairs, in this case $\pi/2$ for the CW case. The combustor was then ignited from cold with both speakers on; fine adjustments are made to ensure an SR close to -1 (CW). If the desired value is not achieved, an iterative process of fine adjustments were made on the phase difference and the amplitude of each pair. When the desired SR is achieved, the combustor was ignited from cold for two to three more times with the desired settings to ensure a repeatable mode. When no more adjustments were required, the combustor was again ignited from cold, and data acquisition was performed. In terms of ACW modes, the procedure was identical but A_+ was monitored, the speaker offset was estimated to be $-\pi/2$ and a SR of 1 was desired. The studies outlined in Article I and III are specific to spinning modes; in both articles spinning modes were achieved with minor variations. The careful control outlined here aided in accomplishing the repeatability of these data sets.

The dynamics of a flame located at three different positions within a standing wave will be presented in Chapter 3. The position of the flame with respect to the standing wave was changed by rotating the forcing ring. The three positions in the standing wave were a pressure antinode, a pressure node and a position between the pressure antinode and node. Figure 2.9 is an example of the variability of the mode while acquiring Scanning PLIF

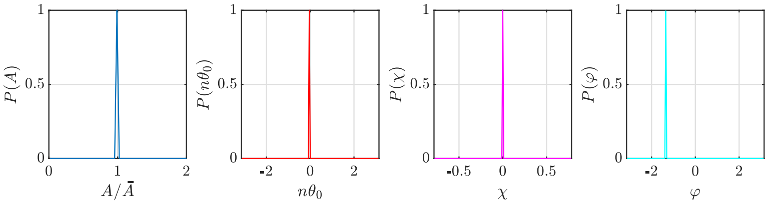

Figure 2.9: PDF of amplitude A with respect to the mean amplitude ($\overline{A}$), nodal position ($n\theta_0$), nature angle (χ) and position of pressure antinode (φ) and as per quaternion formulation Eq. 2.14 for a standing wave over an entire scan of the Scanning PLIF technique (7 seconds).

data for a pressure node that is presented in Chapter 3. The plot illustrates the variation in azimuthal quarternion parameters over an acquisition time of 7 seconds corresponding to the acquisition time of Scanning PLIF. Each quarternion variable produces a sharp distribution with little to no variation, showcasing the careful control of the modes during acquisition.

2.3 Scanning PLIF design and setup

The Scanning PLIF method is capable of reconstructing the three-dimensional Heat Release Rate (HRR) field, which was inferred from the three-dimensional FSD field. Most scanning techniques aim to resolve the field in time. However, this application used a time-averaged approach in order to reconstruct large volumes. The use of LIF was advantageous since it could highlight a single flame in an annular multi-flame setup, which would not be possible with conventional CTC methods (this limitation is discussed in § 2.6).

The Scanning PLIF method involves scanning a laser sheet across a flame of interest in the annular combustor. First, the laser sheet moves through a Volume Of Interest (VOI) in which PLIF images are captured at each laser sheet location. Next, the flame front from each image is detected and averaged to produce an occupancy rate at each imaged pixel location. Finally, occupancy rates are transformed from image space to real space, and a three-dimensional FSD calculation reconstructs the 3D FSD field from which the HRR distribution is inferred. The details outlined in this section is the focus of Article II. In addition to what is outlined in Article II, this section will introduce more details on the calibration methods, edge detection procedure and the reconstruction process.

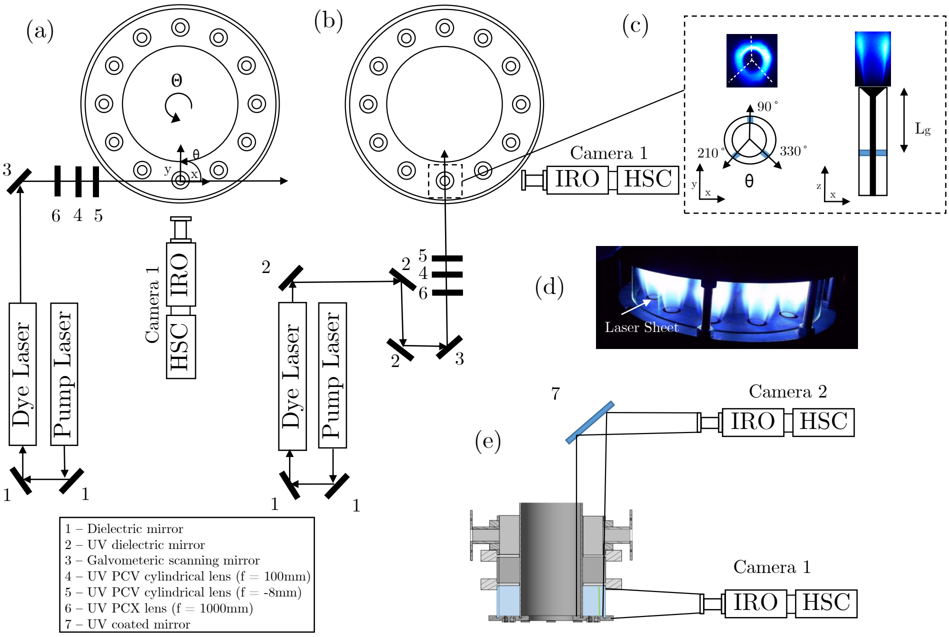

Figure 2.10: Schematic of experimental setup for Scanning PLIF from (a) scan direction 1 and (b) scan direction 2, (c) injector configuration of flame of interest highlighting grub screws in blue and OH* chemiluminescence from overhead and side imaging, (d) image of combustor during experiment, (e) experimental setup of cameras with respect to the combustor.

2.3.1 Laser and scanning mirror setup

The use of OH-PLIF in determining FSD was outlined in § 1.2.2 of Chapter 1. In the Scanning PLIF setup, the excitation of the OH radical in the flame was performed using a Sirah Credo dye laser, pumped with a Nd:YAG Edgewave IS 400-2-L laser that provided a pulse energy of 10 mJ at a frequency of 10 kHz. The laser wavelength was tuned to 283.5 nm aimed at exciting a transition $Q_1(7)$ with $A^2\sum^+ \leftarrow X^2\Pi$ which produces the maximum fluorescence for the OH radical (Rojas Chavez et al. 2021). However, fine tuning of the wavelength around 283.5 nm was performed to ensure that the laser wavelength was at the highest transition line within the band.

The laser produced an elliptical beam that was converted to a thin collimated sheet using a series of optics as shown in Fig. 2.10. The laser sheet thickness produced in the Scanning PLIF studies was $\delta \approx 0.4$ mm and was measured during the calibration procedure as outlined in § 2.3.2. The laser sheet was traversed through the VOI by a Galvanometric scanning dynAXIS

XS UV coated mirror across a total depth of 40 mm. The mirror was controlled using a voltage signal with a range of 0.5 V, and the timing of the sheet location was set to match the desired number of images required at each position. The mirror was estimated to have a precision of 4 $\times 10^{-5}$ V which translates to a sheet positional precision of 0.003 mm at the location of interest. A total of 200 laser sheets were used to scan the volume of interest, producing a laser sheet overlap of 50 % based on the sheet thickness. The effects of laser sheet overlap on reconstructing the FSD volume was investigated in Article II, and the value of 50 % produced a reasonable reconstruction accuracy. A dual scan method was adopted since it was found that a single scan direction produced a bias in determining the FSD at the edges of the flame. Therefore, a second orthogonal scan direction was introduced. The schematic in Fig. 2.10 illustrates the optical setup for both scan directions. Each data set was independently processed, and the final flame three-dimensional FSD volume was determined by combining the FSD from the individual scan directions. The method of calibration, edge detection and projection into real space in the following sections is described from a single scan direction but is applicable to both scan directions.

2.3.2 Camera and laser spatial calibration

Two Phantom v2012 cameras were used in the Scanning PLIF experimental setup, as shown in Fig. 2.10. Camera 1 was used for acquiring PLIF images, and the overhead camera, Camera 2, was used to calibrate the laser sheet positions in the scan. Both cameras required spatial calibration to convert images coordinates into real-world coordinates when reconstructing the three-dimensional field. Camera 1 was equipped with a Lavision Intensified Relay Optics (IRO), a 100 mm focal length Cerco 2178 UV lenses, and a 310 nm UV filter with a full width half maximum of 10 nm. Camera 2 was equipped with a 200 mm Nikon lens and the aperture on both cameras were set to f/8. The aperture was set by evaluating the depth of field when placing a calibration target at the extremes of the field of view ($\pm 20\ mm$) and images were taken for different aperture settings. The image rate for both cameras was set to 10 kHz with an image resolution of 1280 by 890 pixels.

2.3.3 Camera calibration

The camera calibration aims to convert the images taken during the experimental procedure into real space coordinates and to tie both imaging systems to a single global coordinate system as defined in Fig. 2.10. The calibration procedure involves gathering calibration data of known dimensions.

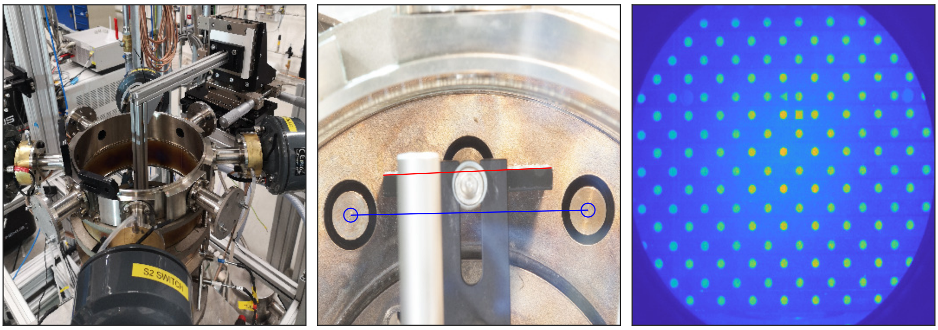

(a) **(b)** **(c)**

Figure 2.11: (a) Traverse setup for the calibration of Camera 1, mechanical arm is placed into the combustor that is carefully controls the movement of the calibration plate over the volume of interest (b) Overhead Calibration image. (c) Resulting image of calibration target on Camera 1.

This was done by use of a calibration target as shown in Fig. 2.11(c). The image space locations of the dots were identified and since the dimensions of the plate are known, a model was fitted to convert any pixel into a line of sight in real space. The calibration target was traversed through a depth of 42 mm, and calibration images were taken at 3 mm increments resulting in 15 separate planes of calibration data. The traverse setup is shown in Fig. 2.11(a) and consisted of a three-stage 50 mm TravelMax traverse connected to a mechanical arm that allowed for the precise movement of the calibration plate through the VOI. The vernier of the traverse provides graduations every 10 μm, with coarse adjustments of 0.5 mm per a revolution and fine adjustments of 50 μm per a revolution. The calibration plate was assumed to be parallel with the x-axis as it was traversed through the VOI and overhead images of the calibration plate from Camera 2 were taken at each location to correct any misalignment of the plate. An example of this image is shown in Fig. 2.11(b). The VOI of the camera was set to capture the two adjacent bluff bodies. During the alignment correction, the centers of these bluff bodies were identified along with the edge of the calibration plate. A binarisation was used to find the pixels along the upper edge of the calibration plate, and a centroid approach was used to find the center of the adjacent bluff bodies. A line was then fitted along the edge of the plate, and another line was fitted through the center of each adjacent bluff body, indicated by a red and blue line, respectively, in Fig. 2.11(b). The gradient between these lines was then used to assess any misalignment in the plate with respect to the global coordinate system. In cases when these lines were not parallel, the misalignment was then included in the orientation of the plate in the calibration procedure. After gathering calibration data for Camera 1, the traverse was additionally used to spatially calibrate the view from camera 2 for different heights. Two calibration plate positions were captured, one at the dump plane used for the calibration of the laser sheets and one at the height of the calibration plate to estimate the misalignment of the plate in real space. The overhead images also allowed for lines of sight of Camera 1 to be tied to the global coordinate system. The calibration images were then processed to develop a calibration model for each camera.

Calibration dot identification and model fitting

The calibration model fitting of Camera 1 and Camera 2 was performed using in-house MATLAB code. The most common calibration models are the pinhole camera model (Hartley and Zisserman 2004) and the polynomial model (Trindade et al. 2014). The pinhole camera model is based on physical laws of projection that volumetrically maps real and image space to an an ideal pinhole camera by assuming that light enters the camera through an infinitely small aperture (Paolillo and Astarita 2021). These models are advantageous since only a few parameters are required to describe the model. Furthermore, these parameters have physical meaning making it easier to ensure the model is representative of the physical space. However, the pinhole model fails in the presence of changes in refractive index since the model assumes that every LOS is a straight line (Paolillo and Astarita 2021). Therefore, additional corrections are often required to overcome this limitation. In contrast to the pinhole model, the polynomial model implicitly accounts for distortion or optical obstructions such as optical confinements (Willert 1997). The polynomial model is based on the mathematical fitting of a non-linear function to calibration data to estimate real-world coordinates. However, the polynomial model is only valid in 2D and therefore multiple planes are calibrated and used to construct LOS from each image space location to real space. The FOV in this thesis consists of changes of refractive index due to quartz and therefore, the polynomial model was used in the Scanning-PLIF methodology. The calibration plate used in the Scanning PLIF setup was a 058-5 Lavision 3D calibration plate with dot spacing of 5 mm, a dot diameter of 0.9 mm and the plate had markers on two parallel planes separated by a level spacing of 1mm. Image pre-processing consisted of applying a bandpass filter and background noise subtraction. An algorithm was then used to identify the dot locations based on a user provided starting dot location. Points found on the calibration

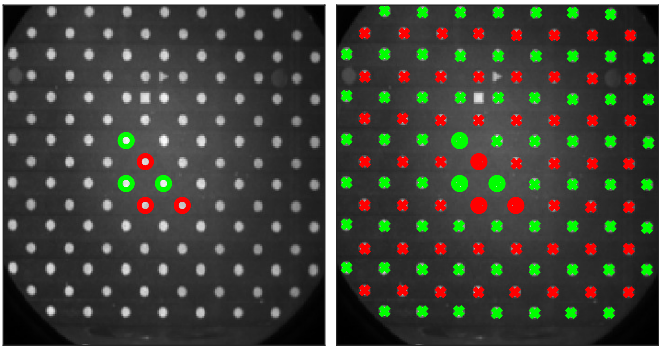
(a) (b)

Figure 2.12: (a) Calibration plate with user defined points on each level of the calibration plate from which all other points are identified, (b) Points found on calibration plate during calibration procedure marked with red and green crosses for inner and outer level of calibration plate respectively.

plate in the image space by this procedure are shown in Fig. 2.12(b). The calibration model or function was determined by estimating a series of coefficients in a third order Taylor series expansion for real space coordinates x and y for each z plane as per equation 2.22:

$$F_k(x_{image}, y_{image}) = \sum_{i=0}^{3} \sum_{j=0}^{2} f_{ij}^{k} (x_{image} - x_c)(y_{image} - y_c) \tag{2.22}$$

where F_k, x_c and y_c are the calibration function for the k^{th} line of sight and the coordinates of the center of the camera respectively. The coefficients, f_{ij}^{k}, were determined using a robust least square routine. To measure the accuracy of the model fit, the real space coordinates of the calibration dots were remapped onto image coordinates. An error estimate was then calculated using the mean difference of the original coordinates and the model.

2.3.4 Image synchronisation

Images taken at each laser sheet position in the scan were allocated a position in real space. To achieve this, the camera signal and signal sent to the scanning mirror needed to be synchronised. During acquisition, images were captured when a trigger signal was sent to the IRO attached to the camera. The camera trigger signal sent to the IRO was a 0-5 V signal that opens the gate of the IRO for each image. Therefore, the signal to the IRO starts the exposure time for each image. The DAQ system acquisition fre-

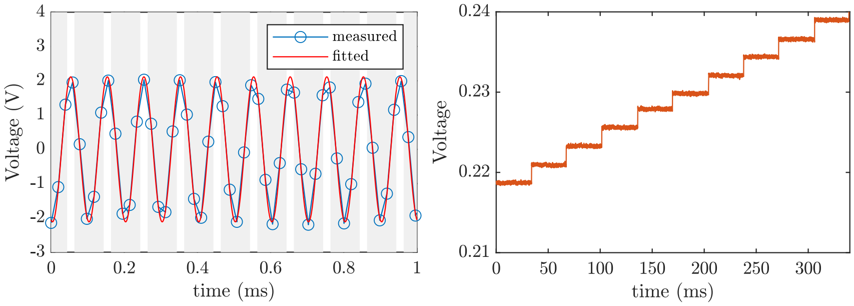

(a) **(b)**

Figure 2.13: (a) Camera signal over 1 millisecond (10 images). Grey bands show the exposure time for each IRO image. (b) Signal sent to galvanometer mirror showing the movement of the mirror across 10 positions. Note the duration at each location sets the amount of images taken for that location.

quency was 51.2 kHz, however, the raw camera signal acquisition rate was shorter than two consecutive sample points of the DAQ acquisition rate. Therefore, the IRO trigger signal was lengthened to identify the position in time of each image. During the acquisition, the IRO trigger signal was sent to a signal generator (Aim-TTi TGA1244 signal generator), to create a cosine waveform for every image. The amplitude of the cosine waveform was arbitrarily chosen, however, the frequency was set at a value greater than 12.5 kHz (assuming an imaging rate of 10 kHz). This frequency was large enough to have sufficient points in between each image to reconstruct the cosine wave and was greater than the exposure timing of the IRO between each image. A least square fitting regression was used to reconstruct the cosine waveform in post processing. Figure 2.13(a) shows good agreement between the fitted signal and raw data. Using the fitted signal, the location of each image was identified at the minima for each period of the cosine wave, and therefore, each image was aligned with the signals acquired by the DAQ system. The fit was used to reproduce an up-sampled version of the camera signal to more accurately determine the minima of each period. The mirror position is controlled by an output DAQ system. A custom Labview control program was used to generate a stepped voltage response to the galvanometric mirror. The LabView control program allowed for the duration between each step to be defined which controlled how long the laser sheet stayed in a single position. The output DAQ system was initiated by the IRO trigger signal and acquired by the DAQ acquisition system allowing for the alignment of the laser sheet position with the other signals. An example of the mirror signal is shown in Fig. 2.13(b). Note each step

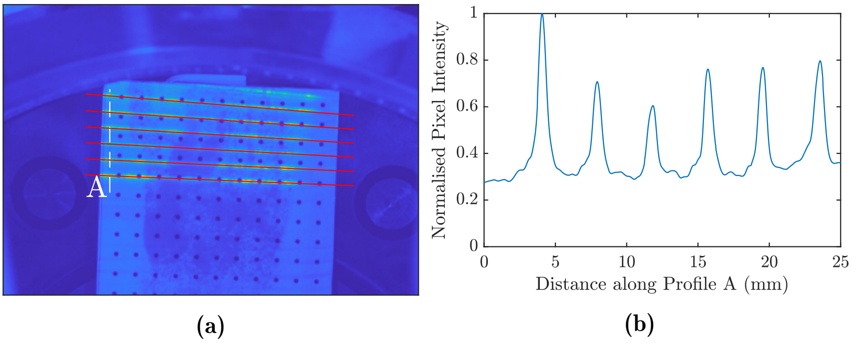

(a) (b)

Figure 2.14: (a) laser sheet positioned at 6 positions in the FOV on calibration target captured by overhead imaging. Red lines show line fit to each of the laser sheets as described in § 2.3.5 (b) Intensity profile along white line A on image presented in (a), peaks in the profile represents the center of the laser sheet location. The intensity profile of each laser sheet produces a Gaussian profile on the calibration target normal to the laser sheet.

in the voltage of this signal represents a position of the laser sheet in the scan, and the duration between each step sets the time for acquisition at that location.

2.3.5 Laser sheet positional calibration

The laser sheet calibration defined a model that places each image at the correct location in real space. In addition, the procedure also calculates the laser sheet thickness. The calibration involved placing a reflective target on the dump plane that covered the entire VOI. Images were then taken as the laser sheet scanned through the volume. These images were then averaged for each position in the scan and an example of 6 sheet positions in the scan is shown in Figure 2.14. Each laser sheet produces a Gaussian-like shape and the peak of these profiles were found which corresponds to the sub-pixel location for each laser sheet. The laser sheet thickness was determined from the width of the Gaussian profiles. Profiles are taken at multiple locations along the sheet, and the orientation of the laser sheet is identified. The locations of these sheets in image space is then converted to real space via the calibration of Camera 2.

Images of the laser sheet from Camera 1 were also recorded to assess any misalignment in the orientation of the laser sheet. An angled calibration target was placed in the field of view, and the laser sheet was swept across the target while images were captured. An averaged image of a single sheet position is shown in Fig. 2.15(a). Again, the camera and mirror signal

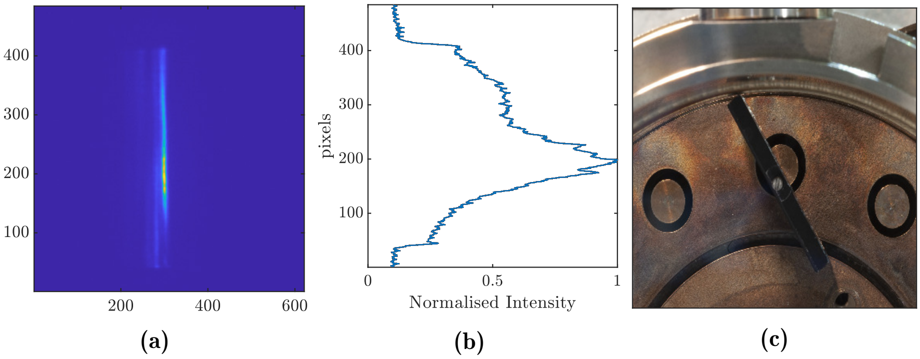

(a) (b) (c)

Figure 2.15: (a) Averaged image of laser profile along an angled target. (b) Normalised Intensity profile of laser in image (a). (c) overhead image of angled target.

synchronisation was used to isolate images for each laser position. The orientation of the target was imaged by Camera 2 (shown in Fig. 2.15(c)), from which the angle of the plate with respect to the global coordinate system was calculated. The image in Fig. 2.15(a) was used first to calculate the sheet thickness as compared to the thickness calculated from Camera 2. Secondly, the laser sheet image was used to calculate the vertical orientation of the laser sheet. It was found that the laser was slanted away from the vertical plane by 3.5°. Equations representing a plane were then fitted to each laser sheet position and using this model, each image position was placed in real coordinates. Images from this perspective also provides the laser profile which is quantified in Fig. 2.15(b). In some cases, this was used for an intensity correction of PLIF images prior to edge detection.

2.3.6 Edge detection

The identification of the flame front was required to determine the flame surface density. This section outlines the procedure used to find the flame fronts from PLIF images. An example of raw PLIF images are shown in Fig. 2.16. For demonstrative purposes, PLIF images from Article II will be shown in this section and the operating conditions for this case can be found in Table 2.1. In its simplest form, the edge of the flame front can be detected by isolating the burnt gas region, a region of high OH fluorescence, from the unburnt gas region, a region of zero OH fluorescence. A simple binarisation setting all pixels with a non-zero signal value to one, will completely isolate the burnt gas region. The edge between these regions is then identified as the flame front. In reality, this process is not as simple as discussed and many factors such as noise, flame recirculation zones, and intensity in-

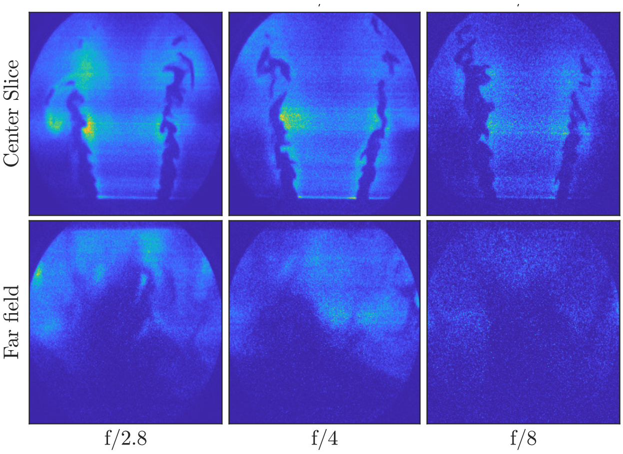

Figure 2.16: Example of PLIF images at center of the VOI and far field ($y = 20$ mm) for different aperture settings.

homogeneity make the definition of these regions difficult. Therefore, image pre-processing is required in identifying the flame front. As previously mentioned in § 2.3.2, an aperture setting of f/8 was chosen to ensure a sufficient depth of field. At this setting, the image signal to noise ratio (SNR) can be low, and further complexity arises in edge detection for images in the far and near fields. Figure 2.16 shows the comparison of PLIF imaging at different aperture settings, and one can see the noise associated with images with a smaller f-stop number. The figure also outlines the difference in PLIF images at the center and the far field of the volume of interest, and it is seen that images taken at the far and near field with a f/8 camera setting contain more noise resulting in a flame edge that is not visually well defined. Another notable feature of these images is the varying intensity of the signal at different heights of the flame due to the inhomogeneity of the laser sheet which complicates edge finding. However, it should be noted that these images were taken during the initial stage of testing camera aperture settings. The images shown in the far field are when the laser sheet does not pass directly through the flame front but correspond to sheet positions in a corner recirculation zone resulting in low intensity counts. These images were included as a means of assessing the aperture settings of the camera, and are not fully representative of experimental data collection, due to the location of the laser sheet, and unoptimised laser power and frequency. More representative images taken during experimental data collection are shown in Fig. 2.17. The images shown are binned to match the resolution in the scan direction (laser sheet spacing). The binning process increases the SNR

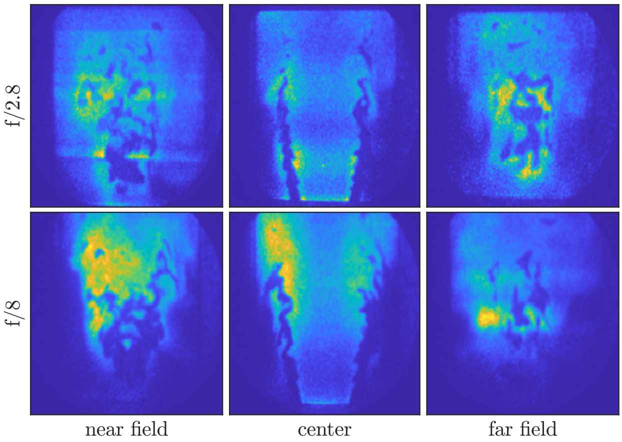

Figure 2.17: Example of PLIF images at center of the VOI and far field ($y = 20$ mm) for different aperture settings.

for these images. An assessment of SNR on edge detection is presented in § 2.3.7. The binning procedure involved a nearest neighbour interpolation over a 4 by 4 pixel window. The resizing of the image slightly reduced image noise. However, additional filtering was still necessary. Typically, the filtering of noise can be done by a Gaussian filter that applies a 2-D smoothing kernel with a specified standard deviation. An example of Gaussian filtering is shown in Fig. 2.18(b). The image signal is enhanced, and the use of the filter visually reduces the noise level, however, a common problem with Gaussian filtering, is the blurring of gradients which makes edge detection more difficult. Therefore, filtering needs to be carefully chosen since the filter needs to preserve the edges or large gradient between burnt and unburnt regions. Many filtering methods have been evaluated in this study, some of which included edge preserving median filters, bilateral filtering and non-local mean filtering. More details on these image filters can be found in Lim (1990). The filters were also tested in combination with each other and were visually assessed on the ability to find the flame front. The most effective filtering method, based on PLIF imaging taken in this study, was the use of an anisotropic diffusion filter. The use and development were first introduced by Perona and Malik (1990) and is a technique used in image noise removal while aiming at preserving edges or lines. The implementation of the filter involves applying an iterative algorithm that represents the diffusion process Palma et al. (2014):

$$I_s^{t+1} \approx I_s^t + \frac{\lambda_I}{|\eta_s|} \sum g(|\nabla I_{s,p}^t|, \gamma_I) \nabla I_{s,p}^t \tag{2.23}$$

where I_s^t represents the intensity of a pixel s in an image I at instant t. λ_I represents a scalar diffusion rate, and γ is a constant that defines the smoothing level. η_s are the adjacent pixels of s, the function g is an edge stopping function, and $\nabla I_{s,p}^t$ is the magnitude of the gradient across neighbouring pixels. Gerig et al. (1992) proposed a maximum value of $1/7$ for the ratio of $\lambda_I/|\eta_s|$ to ensure a monotonic variation of intensity. Eq. 2.23 provides a filter that preserves edges since, as outlined in Palma et al. (2014), edge pixels would produce opposite directional gradients, cancelling any smoothing done by function g. Secondly, the filter produces a cumulative effect around pixels with high gradients in the same direction, like clusters of noise pixels that usually produce distinct intensities in the surrounding pixels. Further details on the anisotropic diffusion formulation can be found in sources Perona and Malik (1990), Gerig et al. (1992) and Palma et al. (2014). An example of the filtered image using anisotropic diffusion is shown in Fig. 2.18 alongside a Gaussian filtered image. The edges are noticeably sharper in the diffusion filtered image, therefore this filter was applied to all PLIF images.

The next step in the edge detection procedure involved a normalisation step which corrects for intensity inhomogeneity. This was usually done with the aid of the laser beam profile shown in Fig. 2.15. Once the image had been corrected for inconsistencies in intensity and the region between the unburnt and burnt gases was enhanced by filtering, a canny edge detection algorithm (Canny 1986) was applied to each image. The canny edge detection algorithm finds edges by identifying the maximum local gradient in an image, the gradient is determined by using a Gaussian approximation, and the resulting gradients are assessed by a user-defined threshold of two values that define weak and strong gradients, respectively. An example of the edges found by the canny edge detection algorithm is shown in Fig. 2.18(d).

The bounds of the threshold values remove spurious edges during the procedure. The bounds of the gradient threshold required for the canny edge detection algorithm were assessed by quantification of the image gradients at different sheet positions. Although, images were normalised and filtered, the gradient between unburnt and burnt regions varied based on the position of the laser sheet. The gradient was sensitive to the position of the laser sheet with respect to the flame, as seen by the less sharp gradient distributions for slices away from the center slice in Fig. 2.19(a). The gradient

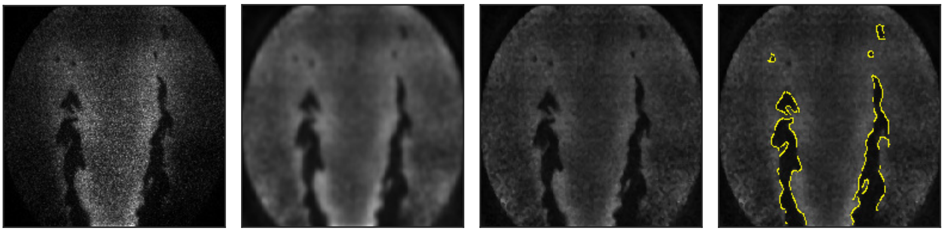

(a) Unfiltered (b) Gaussian Filter (c) Diffusion filter (d) With edges

Figure 2.18: Examples of pre-processing imaging methods on raw PLF image shown in Fig. 2.16 taken at the center of the VOI and aperture setting f/8.

distribution of PLIF images on every sheet was evaluated, and it was found that the gradient in between the flame front followed a Gaussian distribution centered around the center of the volume of interest. Therefore, the gradient threshold applied to the canny edge detection algorithm varied by the sheet position in the scan. The values are chosen for each position are shown in Fig. 2.19(b). Further discussion on gradient bias can be found in Article II.

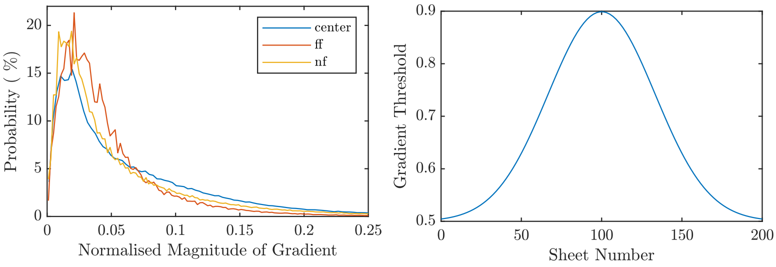

(a) (b)

Figure 2.19: (a) The gradient magnitude of raw PLIF images at the center, far field (ff) and near field (nf) of the FOV presented as a normal distribution.(b) Gradient threshold chosen for edge detection based on the position of the scan. Note that the 100th sheet is the center of the VOI in this example.

Phase Averaging

The process of phase averaging is introduced in Article I, Article III and Chapter 3 and was applied to the investigation of forced flames in this thesis. The process involves binning or averaging the edge detected images into specified bins conditioned on phase with reference to the forcing signal. In this thesis, the forcing signal was used as the reference signal and 16 equally spaced bins were allocated along this sinusoidal signal, as shown in

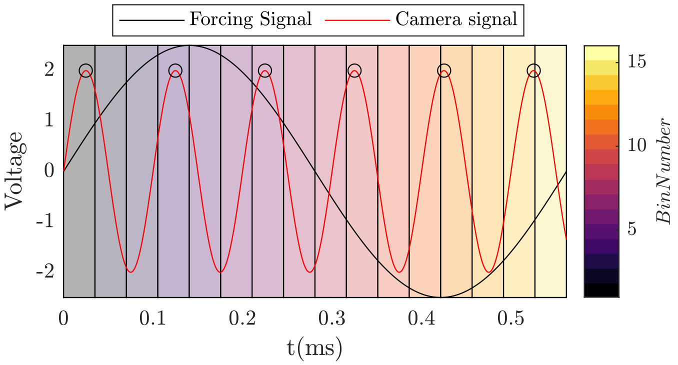

Figure 2.20: Visual representation of phase averaging process showing forcing signal, respective bins along the signal (color coded) and camera signal. Note that images are located at the peak of local maxima of the camera signal, therefore 7 images are captured over the period of the forcing signal shown.

Fig. 2.20. Based on the synchronisation discussed in § 2.3.4, images were then categorised into each of the 16 bins based on their respective position along the forcing signal, represented by the peaks of the reconstructed signal in Fig. 2.20. Each bin is evenly populated due to a frequency drift between the forcing frequency and camera acquisition frequency.

Positional averaging of flame front

Once the images were placed into respective bins, a second binning was performed to allocate images to their laser position in the scan, which was done based on the synchronisation of the mirror and camera signal. Binary images where flame fronts have a value of 1, and all other locations have a value of 0 were then averaged producing a single image with each pixel i and j representing the occupancy rate $(L(i,j))$ i.e. the probability of the flame occurring in a pixel in a time averaged sense. In terms of the unforced flame in Article II, averaging was performed based only on the position of the mirror.

2.3.7 Evaluation of flame front extraction

Description of PLIF images

It was essential to first quantify the raw PLIF signal intensity before applying any post-processing. The edge detection or flame contour identification is based on identifying regions with large gradients between reactants and products, and it is useful to understand the signal-to-noise ratio during this process. Figure 2.21 shows PDFs of pixel intensity and gradient magnitude,

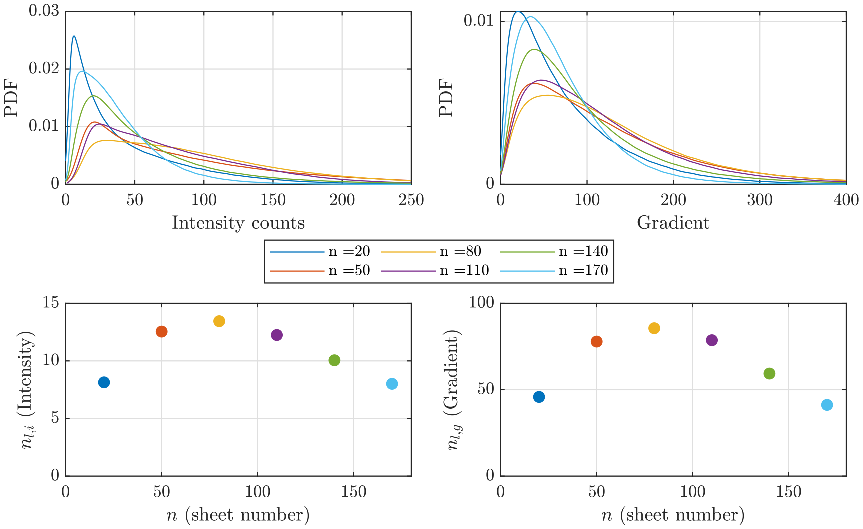

Figure 2.21: PDF's of intensity distribution and gradient distribution. Noise level based on intensity ($n_{l,i}$) and gradient magnitude ($n_{l,g}$) of slices through the volume of interest.

and noise level for each of these quantities from 300 PLIF images taken at 6 laser sheet positions through the VOI. The pixel gradient represented is the magnitude of the gradient determined by a central difference scheme. The example shown is with respect to the unforced case in the X-Z scan direction and was chosen since this data set was used in developing the scanning PLIF technique. The resulting intensity profiles of these images are shown in Fig.2.21. These profiles have distinct peaks at low intensities with a long tail showing that high intensity values occur less often. The low intensity peaks are larger for sheet locations towards the edges of the flame and the distribution is flatter for images close to the center of the VOI, with the largest mean intensity being at the center.

The peak of the PDF represents the noise level. To demonstrate this, a raw PLIF image at the center of VOI has been thresholded at an intensity value a few counts towards the right of the intensity signal's peak. The resulting image is shown in Fig. 2.22(b). The majority of pixels with non-zero intensity shown in this image are those within the unburnt gas regions or corner regions. Ideally, these regions should not contain any OH signal. Under this assumption, the finite intensity values of these pixels are a measure of image noise. Taking the variance of these pixel counts produces a noise level of 11.8. This value is consistent with the noise level ($n_{l,i}$) shown in

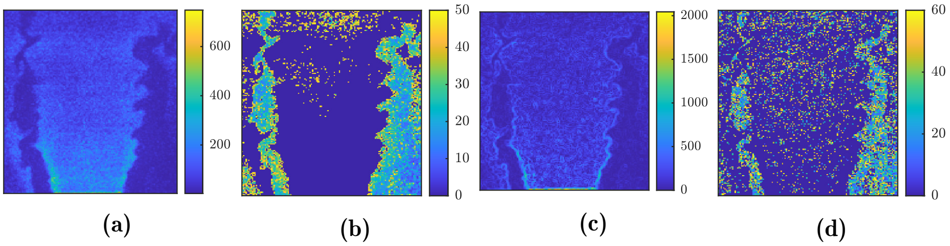

Figure 2.22: (a) Raw PLIF image, (b) Isolation of noise level based on intensity, (c) Pixel Gradient for slice at the center of VOI, and (d) Isolation of noise level based on gradient.

Fig.2.21, which was independently calculated using the method outlined in Immerkær (1996). Relatively high noise levels are present at each location. The noise level is highest at the centre of the VOI, scaling with mean pixel intensity. The upper right subfigure in Fig. 2.21 also includes the gradient distribution of the raw PLIF images as well as the noise level based on the gradient magnitude, $n_{l,g}$. The pixel gradient magnitude distribution and noise level has a similar shape to that of the intensity distribution and noise level based on intensity. An example of an image showing the gradient magnitudes is presented in Fig. 2.22(c). The variations of intensity are large, with distinct high gradient magnitudes outlining the flame contour. However, these gradient magnitudes are not high at all locations along the flame front. The distribution peak in the PDF represents the noise level in terms of gradient magnitude and represents the lower gradients in the unburnt gas. The noise level of the gradient magnitude are also shown in the bottom right corner of Fig. 2.21, which scales with the intensity noise shown in the bottom left corner Fig. 2.21. The relatively high noise level and broad range gradient magnitudes make finding an edge difficult and therefore, the image processing routine described previously in § 2.3.6 was implemented. The parameters of the diffusion filter were first assessed prior to implementation.

Parametric study of Diffusion filter

A sensitivity analysis was performed on the input parameters of the diffusion filter introduced in § 2.3.6. The main inputs for the filter are the number of iterations and the gradient threshold. These parameters have been varied to identify an optimal input value to reduce the noise of the binned experimental PLIF images. In this analysis, in addition to the image noise level, the mean gradient is used to assess the effectiveness of the filter. An estimate of the signal-to-noise ratio (SNR$_{mean}$) is calculated based on the noise

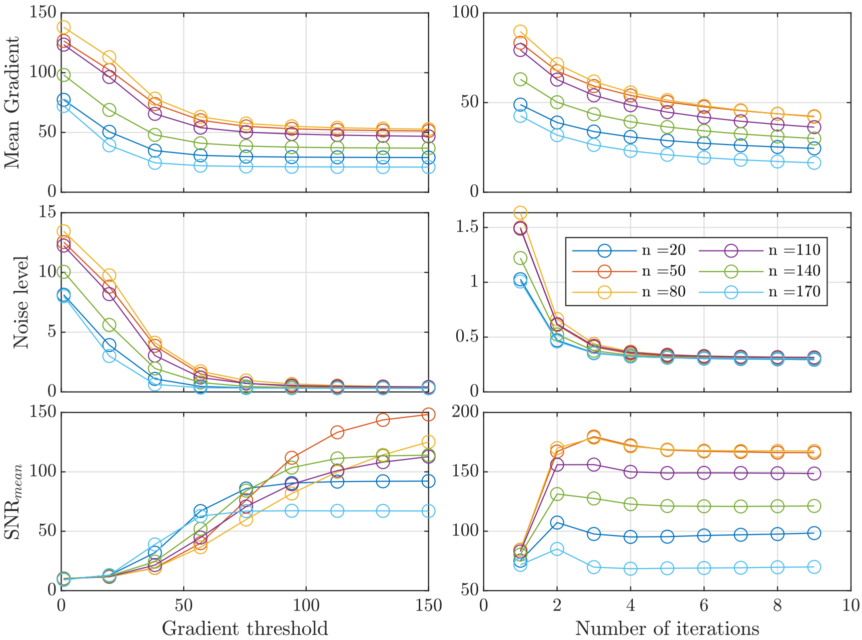

Figure 2.23: Sensitivity study results for diffusion filter parameters. Left and right-hand columns show the mean gradient, noise level, and SNR sensitivity to the filter gradient threshold and number of filter iterations, respectively.

level and mean gradient. The estimation of SNR will be discussed further in the next section. The sensitivity analysis was conducted for images at different locations in the VOI and the result is represented in Fig. 2.23. The filter threshold was first varied from values of 1-150 as shown in the left hand column. A threshold value close to 130 produces high SNR ratios for all sheet locations. This threshold was then kept constant and the number of iterations of the filter algorithm was varied. A default value of 5 is usually used. However, a value of 6 produced a higher SNR for all sheet locations and is therefore applied in the current study. It is interesting to note the filter effect is independent of the noise level and therefore, the parameters were kept constant for all images in the scan when applying post-processing.

Filter application and edge detection

An example of the diffusion filter on a PLIF image taken at the center of VOI is shown in Fig. 2.24(a). The noise in the image has been reduced to a value of 0.2. The gradient of the image is also shown in Fig. 2.24(b). The gradients close to the reaction zone are more distinct than in Fig. 2.22(c). The resulting distribution of the gradient magnitude for both the filtered

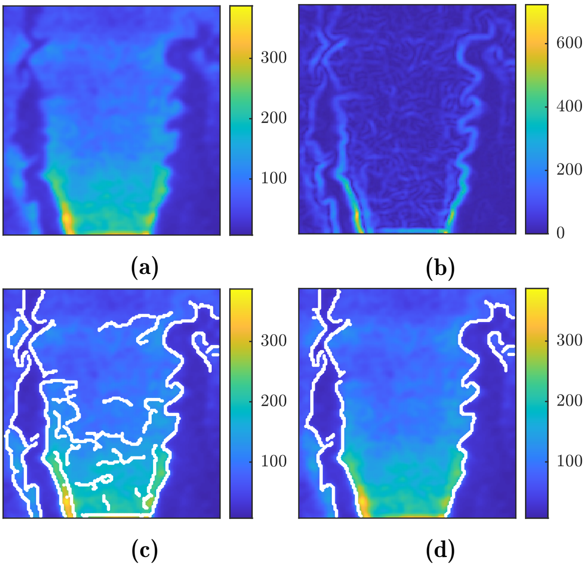

(a) (b) (c) (d)

Figure 2.24: (a) Filtered PLIF image, (b) Respective pixel gradient, (c) Edge detection using Canny edge detection and (d) Final edge detection after gradient threshold for slice at the center of the VOI.

and unfiltered image is shown in Fig. 2.26. The filtering reduces the size of the peak of the distribution, which reduces the quantity of lower gradients representative of noise. The gradient threshold applied is also shown on this distribution and is located just after the peak of the gradient signal removing low gradients of the distribution. Applying Canny edge detection on the filtered image identifies the edges shown in Fig. 2.24(c). Note that non-flame front edges are also detected. A final gradient threshold is applied that retains edges close to and above the threshold resulting in the edges found in Fig. 2.24(d). The gradient threshold is chosen based on the sheet location due to the changing signal and corresponding gradient magnitudes shown in Fig. 2.21.

An example of images for the respective image processing steps is shown in Fig. 2.25 at different locations in the scan. The bottom row of the figure shows the final result of the edge detection routine in which the edge is representative of the flame front location.

Estimation of signal to noise ratio

The SNR can be calculated for different positions in the scan. In the previous sections, SNR was calculated as the ratio of the mean to the median

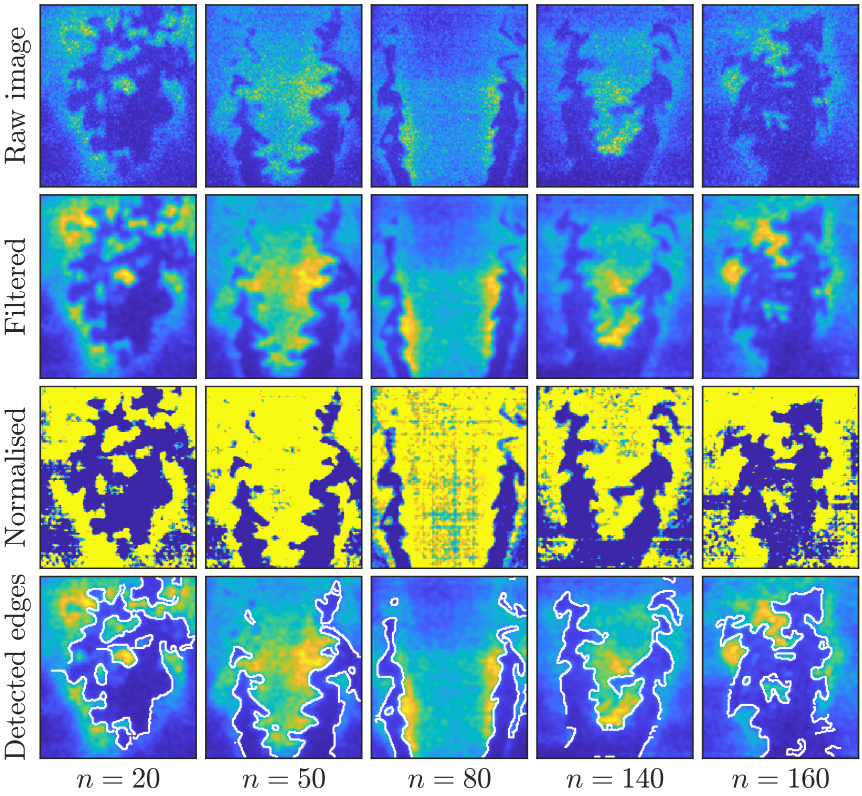

Figure 2.25: Example of images at steps during the edge detection routine for locations in the VOI for an unforced flame.

gradient magnitudes. This is a conservative estimate of the SNR as the regions of interest, close to the high gradient regions, typically include gradient magnitudes far higher than the mean gradient magnitude. The SNR based on the mean (SNR_{mean}) is shown in Fig. 2.27. The SNR drops close to the edges of the flame and is fairly constant towards the center of the VOI.

An alternative way to measure SNR is by isolating neighbouring pixels at locations where the flame contour is found. This metric then provides a more representative estimate of the SNR in only regions which are preserved during the final gradient magnitude threshold operation. A 5 by 5 pixel window around each detected edge pixel was isolated in each PLIF image. The gradient magnitude was then calculated at these pixel locations and compared with the noise level, which is referred to here as the edge gradient method, SNR_{edge}. This gradient distribution can be considered as the ‘signal’ in the SNR_{edge} since the flame contour identification depends

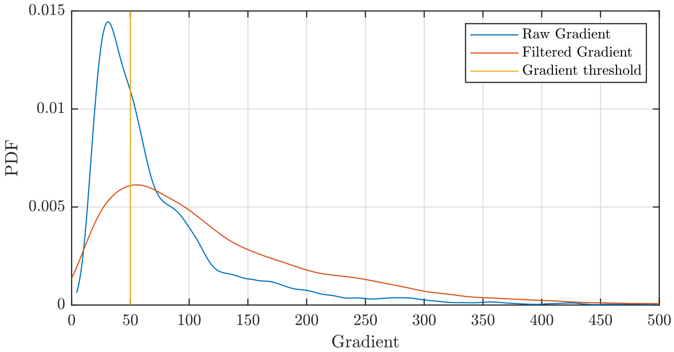

Figure 2.26: Gradient distribution of image shown in Fig. 2.24.

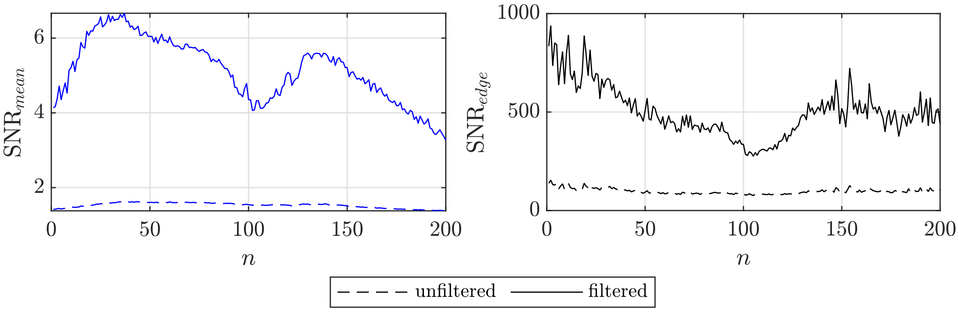

Figure 2.27: Calculation of averaged SNR for unforced case using 300 images PLIF images from the X-Z scan at each laser sheet location in VOI.

on the magnitude of these pixels. An SNR can be calculated based on the edge gradient method and is shown in Fig. 2.27. In addition, the SNR was calculated based on the mean gradient of all pixels in the PLIF images for sheet positions through the VOI. The SNR$_{mean}$ for unfiltered images are below 2. The filtering procedure increases this to an average value of 5. However, when using, the high gradient regions near detected edges to perform the SNR$_{edge}$ calculation, the values are increased by a factor of 100. It is important to note that these pixels are at the location of the parameter of interest i.e. the flame contour front, and arguably represent the important SNR in the images.

Comparing gradients for different modal cases

The SNR is dependent on each case studied in this thesis as the PLIF images vary with laser power, and laser power must be constantly optimised during experiments through tuning of the dye laser system. The mean gradient magnitude across the VOI of PLIF images of an unforced flame (Article II), a

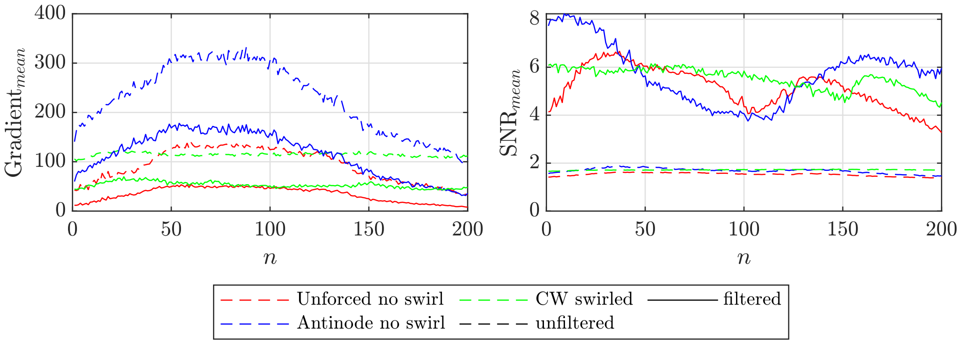

Figure 2.28: Comparison of (left) mean gradients and (right) SNR$_{mean}$ for an unforced flame scanned in the X-Z direction (Article II), a flame at the pressure antinode location (Chapter 3) and a swirled flame subjected to a CW spinning mode (Article III) for both filtered and unfiltered signals.

flame located at pressure antinode (Chapter 3) and images of a swirled flame subjected to a CW spinning mode (Article III), are shown in Fig. 2.28. The mean gradient magnitude is shown here as the SNR scales with it. Again, the use of the mean gradient metric provides a conservative estimate of the SNR. The signal-to-noise ratio for the unforced, antinode and CW swirled case were calculated by taking the mean gradient for every pixel on the PLIF images for 100 images at each laser sheet position. Note how the unswirled cases produce a distribution of mean gradient magnitudes that increases with laser sheet locations close to the centre of the VOI, and decreases towards the edges, following an approximately Gaussian distribution. It was mentioned in § 2.3.6 that the gradient chosen for the Canny edge detection was selected to be Gaussian based on the laser sheet location to account for this. The filtered signal in each case is also presented, which is seen to increase the signal and reduce the noise in each case. It is important to note that the swirled flame does not have the Gaussian distribution in terms of the gradient. This finding further motivated the omission of a second scanning direction in Article III. An image of the FSD for all three cases is shown in Fig. 2.29. It is also worth noting that the FSD image for the CW case is produced when sampling the volume in a direction orthogonal to the actual scanning direction and produces FSD values similar to those of the perpendicular slice. This was an issue when investigating the unswirled flames which motivated the need for a second scanning direction. This is likely due to the relative orientation of the mean gradient profile for the swirled case. The presence of the swirler results in larger radial velocities, and a higher exit angle for the reactants relative to the axial direction. The

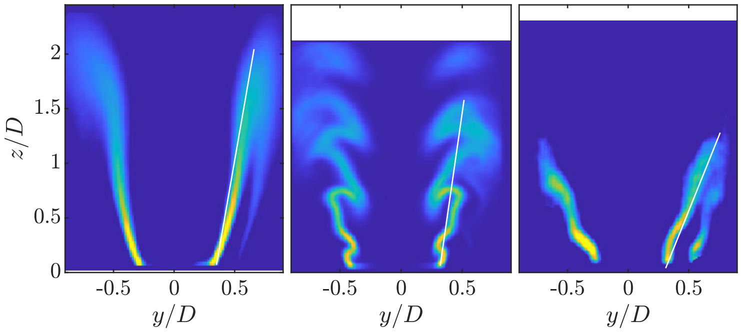

Figure 2.29: FSD of (left) unforced flame without swirl, (middle) flame without swirl forced at an antinode of a standing mode scanned in the Y-Z direction, and (right) swirled flame forced with a CW spinning mode scanned in the X-Z direction.

angle of the flame with respect to the dump plane was calculated for the three cases based on the white line plotted in each image. The respective angles of the flame with respect to the dump plane are 81, 83 and 60 degrees for an unforced flame with no swirl, a flame at the pressure antinode of a standing wave with no swirl and a swirled flame subject to a CW spinning mode. The higher flame angle for the swirled flame reduces instances of parallel alignment of the laser sheet and flame front, reducing the bias error described in Article II.

Alternative scanning approaches

A potential way to increase SNR would involve setting the aperture to f/2.8 and traversing the rig or the complete optical setup (laser and cameras) back and forth to traverse the plane of focus through the VOI, thereby ensuring that every plane is in focus and maximising the available signal. This approach was considered during the design of the experiment. However, this idea was not pursued since, firstly, it would have involved a complicated traverse system to move the combustor and support structure of considerable weight accurately over small increments (0.2 mm). Furthermore, up to 200 individual runs would need to be performed at each location to ensure the same scan resolution as the one achieved in this thesis. The acquisition of such a large number of cases increases the risk of experimental alignment errors. The combustor is not cooled, and thermal gradients exist during data acquisition. Therefore, operating for a long time duration is not feasible. Due to this issue with the thermal heating of the combustor, the tuning of the acoustic mode in the annular combustor is difficult, time-consuming, and subject to relatively large changes in spin ratio and amplitude. Therefore,

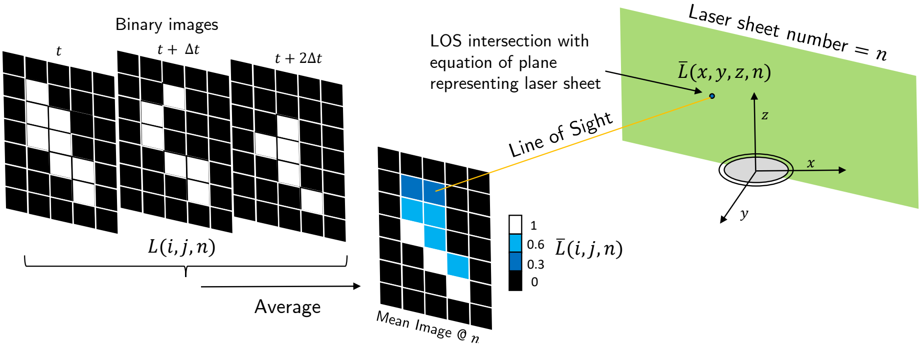

Figure 2.30: Process outlining the mapping of image occupancy rate to real three-dimensional space.

conducting many separate experiments may mean that the repeatability of the mode state between cases may be poor, introducing error.

Some compromise could be sought, with a reduced number of refocusing operations and short scans, but this would require many more separate runs to be conducted and any readjustment in the optics would introduce the possibility of misalignment errors through calibration. It was decided that it would be preferable to use a single set of calibrations and a single optical setup. While this comes at the expense of signal intensity, the SNR was assessed and deemed sufficient. Refocussing scanning may be considered again in future work.

2.3.8 3D Reconstruction

Flame Surface Density (FSD) calculation

Each pixel location (i, j) is projected as a line of sight through the VOI using the camera calibration. The intersection of the respective LOS with the respective laser sheet location results in the location of the image occupancy rate, $\overline{L}(i, j)$, in real space, $\overline{L}(x, y, z)$. The process of determining the mean occupancy rate in real space is shown in Fig. 2.30. The projection of $\overline{L}(i, j)$ in the scan into world coordinates creates occupancy rate data scattered in real space, and therefore a mapping step was included to create a regular array of $\overline{L}(x, y, z)$. The scattered data were mapped onto a regular discretised domain using a scattered linear interpolation scheme.

The choice of interpolation scheme was investigated in the development of the method. The schemes evaluated were the linear, nearest neighbour and natural neighbour interpolation methods. High order interpolation schemes were excluded to limit the required computational expense. A comprehensive description of these interpolation methods can be found in Amidror (2002). The speed of the scheme was also an important factor in choosing a interpolation scheme due to the large data sets. A scattered $\overline{L}$ volume contains millions of projected data points, and a large number of cases were recorded. A test case consisting of scattered data from a known object was used to evaluate the schemes and it was found that the linear scheme produced the best result in terms of speed and accuracy and was therefore chosen for the reconstruction procedure.

The resulting volumetric distribution from the interpolation of the scattered $\overline{L}(x, y, z)$ produced a time-averaged flame surface area $\overline{A}_f(x, y, z)$ volume. The interpolation takes into account the contribution of $\overline{L}(x, y, z)$ data within in a three dimensional volumetric space, and, therefore the resulting estimate is representative of an area and not a single point in space. From this volume, the FSD was determined using the following equation:

$$\mathrm{FSD} = \lim_{\Delta x \to \,\mathrm{o}} \frac{\langle \overline{A}_f \rangle}{\Delta x^3} \tag{2.24}$$

here $\langle \overline{A}_f \rangle$ represents the time-averaged surface area of the flamelets, which were spatially integrated over a voxel cubic interrogation volume, Δx^3. The interrogation volume chosen was a 5 × 5 × 5 voxel volume, and the size was based on the findings by Donbar et al. (2000), who proposed the interrogation window be smaller than the flame brush to prevent the smoothing out of large scale flame structures. Based on Eq. 2.24, the FSD of every voxel was determined by the sum of $\overline{A}_f$ in the interrogation volume, centered at that voxel, and normalised by the volume of the interrogation volume. FSD was used to assess the HRR of the flame since FSD is approximately proportional to the time-averaged distribution of HRR, under the assumption that the HRR per unit surface area is relatively constant for fuel-air mixtures with a Lewis number close to unity and is therefore in the wrinkled flamelet regime (Filatyev et al. 2005). In Chapter 3, Article II and Article III, FSD was used as a proxy for HRR such that $q(x, y, z) \approx \mathrm{FSD(x, y, z)}$ (Paul and Najm 1998).

The dual scan method reconstructs a three-dimensional FSD volume from two orthogonal scan directions. These are denoted as scan direction X-Z and scan direction Y-Z which refers to the scanning direction based on the coordinate system represented in Fig. 2.10. The method of combining

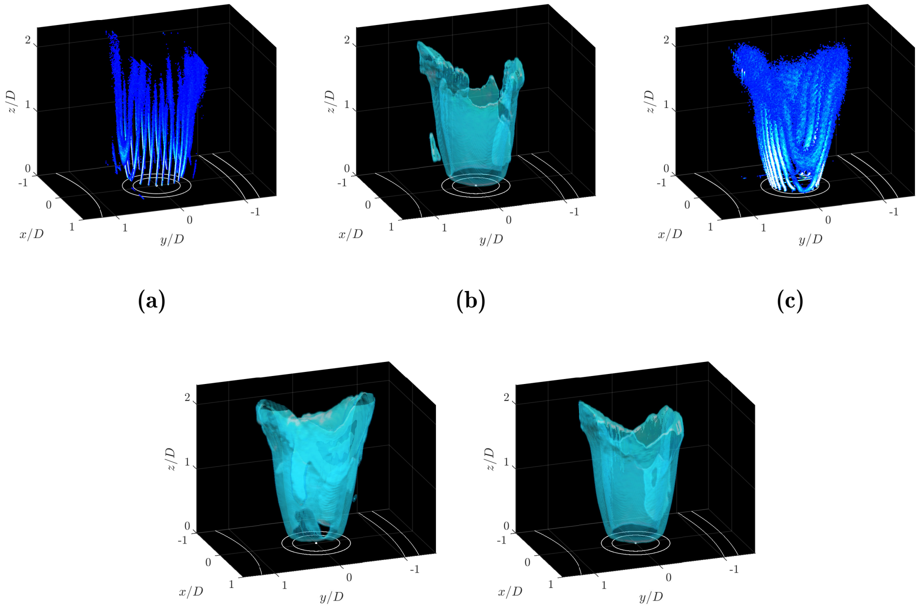

(a) **(b)** **(c)**

(d) **(e)**

Figure 2.31: Projected irregularly spaced $\overline{L}(x, y, z)$ data points for scan direction (a) X-Z, and (b) resulting isosurface representing FSD volume. Projected $\overline{L}(x, y, z)$ data points in scan direction (c) Y-Z and resulting (d) reconstructed three-dimensional FSD volume presented as an isosurface. (e) Isosurface of three-dimensional FSD volume from combined FSD volumes. White lines show schematic representation of annular chamber and burner inlet and the isosurface level is the spatial average of the FSD.

these volumes was investigated to ensure that the reconstruction produced a uniform intensity distribution around the flame. The combination methods considered in this work included: (i) performing the FSD calculation after projecting both volumes into real space and calculating a combined $\overline{A}_f(x, y, z)$, (ii) Performing an FSD calculation that only uses the maximum occupancy rate between the two independent $\overline{A}_f(x, y, z)$ volumes, (iii) Calculating the FSD of each volume and averaging both. It was found that the latter choice was optimal as it produced a uniform FSD volume in the θ direction, overcoming the bias error discussed in Article II. FSD volumes for both scan directions and a resulting combined scan volume is presented in Fig. 2.31(b), Fig. 2.31(d) and Fig. 2.31(e), respectively. Averaging the volumes had the drawback of under predicting flame elements in regions

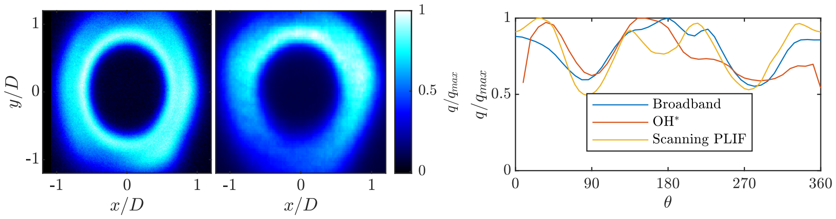

(a)

(b)

Figure 2.32: (a) A comparison of broadband (left) and OH* (right) chemiluminescence overhead mean unforced flame (b) A quantification Heat Release Rate (HRR) as function of θ comparing integrated 2D OH* and broadband chemiluminescence images with and FSD volume determined by Scanning PLIF.

only found by a single scan direction. The averaging procedure, in this case, would underestimate the FSD. However, this procedure was still adopted since it was shown in Article II that the resulting FSD distribution was similar for both scan directions, even though they differed in magnitude, minimising this error.

Many attempts at correcting the intensity of the individual volumes were made. One included correcting the intensity of the volume based on the shape of the flame. It was assumed that the flame was circular, and a weighting was assigned to each voxel based on the position of the laser sheet with respect to the flame. This correction assumes that the flame shape is known which is counter intuitive since the method was aimed at understanding the flame shape. The potential corrections tested during this work are not exhaustive and future work may improve the scanning PLIF method through use of appropriate corrections.

2.3.9 OH* chemiluminescence measurements

The Scanning PLIF method introduced in this thesis is relatively new. Therefore, it was essential to take additional measurements to compare or validate the technique. To this extent, OH* chemiluminescence imaging was also performed in conjunction with the scanning method. The measurement of OH* chemiluminescence has been used in many combustion studies to estimate HRR oscillations (q') (Hardalupas and Orain 2004). However, simultaneously taking these measurements was not possible due to the setup of Camera 2, which was configured for the laser sheet calibration. Therefore, an independent OH* chemiluminescence measurement was taken at the same operating conditions as the Scanning PLIF measurement. Overhead imaging was performed by installing a Lavision IRO, a 100mm focal length Cerco 2178 UV lens and a 310 nm UV filter similar to Camera 1. Simultaneous OH* chemiluminescence imaging was then taken from Camera 1 and Camera 2. Article II discusses some of the similarities of OH* chemiluminescence with the reconstruction of an unforced flame using Scanning PLIF, and it was shown that these measurements were in good agreement. The comparison is shown in Fig. 2.32.

In addition to the laser sheet calibration, Camera 2 was able to capture broadband chemiluminescence during the Scanning PLIF experiment. The possibility of using broadband chemiluminescence for comparisons of HRR was tested during the experimental design of the Scanning PLIF setup, and a brief comparison of the result is shown in Fig. 2.32. Figure 2.32(a) shows an overhead image of an unforced ethylene flame from Article II imaged using broadband chemiluminescence alongside the OH* chemiluminescence. The resulting flame shape between these images are similar in terms of the overall circular nature of the flame but differs in local intensity around the flame. To further assess the HRR response of these measurements, integrated azimuthal slices are plotted in Fig. 2.32(b). Both measurements produce a similar response with slight deviations close to the inner and outer walls of the combustor. The deviations of the HRR response at the inner and outer walls for the OH* chemiluminescence also differed from the Scanning PLIF technique, and it was possibly flame quenching at these regions of the combustor. The broadband chemiluminescence measurement follows the Scanning PLIF measurement. However, this was not realised during the experiment itself, but this result is shown here to provide possible improvements in the Scanning PLIF technique.

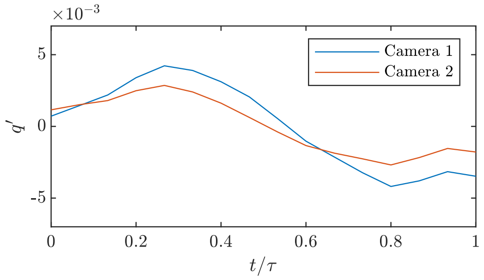

Figure 2.33: Comparison of HRR oscillations of forced flame determined from OH* chemiluminescence from overhead (Camera 1) and in plane positions (Camera 2).

OH* chemiluminescence imaging was simultaneously taken from both Camera 1 and Camera 2 and was used as a comparison for the Scanning PLIF result. It was important that both these measurements produce the same result. To analyse this a plot of the HRR response on a ACW forced flame is shown in Fig. 2.33. As shown, both these measurements are in good agreement, however slight deviations are present which is possibly due the differences in the the FOV.

2.3.10 Scanning PLIF acquisition experimental procedure

The previous sections outlined different aspects of the Scanning PLIF method. In this section, a step by step experimental procedure will be outlined.

Pre-experiment

- Install traverse to move plate vertically for calibration of Camera 2. Traverse plate across the volume of interest while imaging the calibration plate at dump plane and multiple heights.
- Install traverse horizontally for calibration of Camera 1. Image calibration plate from Camera 1 and Camera 2 at 15 calibration plate positions through the VOI.
- Angle plate and perform laser scan while imaging.
- Remove traverse and place calibration target on dump plane for laser sheet calibration. Perform laser scan while imaging from Camera 2.
- Remove calibration targets and install OH filter on Camera 1.

During experiment

- Ignite rig. In cases where forcing is used, the speakers are turned on after 10 seconds after ignition, and minor adjustments are made to the desired forced state if necessary.
- Capture images after 20 seconds from ignition, a temperature probe located at the inner wall close to the flame of interest is monitored to ensure that measurements are taken at the same temperature for each run.
- After a complete scan, the fuel to the combustor is cut, and the flames are extinguished .
- the rig is cooled to room temperature before the next run.
- The laser wavelength is tuned in between every 3-4 runs to find the wavelength that produces the maximum signal. The procedure consisted of a wavelength sweep while images were taken to assess the level of the signal.

Post experiment

- At the end of each day, a post camera and laser calibration is taken to check any errors in alignment.

2.4 3D weighted phase and amplitude analysis

Weighted phase plots were used in Article I, III, and Chapter 3 to characterise the asymmetric response of forced flames. The analysis provides a tool to assess the HRR oscillation amplitude and phase in three dimensions. This section outlines the weighted phase calculation procedure which has been adapted from Hauser et al. (2010). Figure 2.34 schematically outlines the process. In this illustration, a single voxel in an FSD volume for a single phase is outlined in Fig. 2.34(a) (note the voxel is enlarged for demonstrative purpose and an actual voxel is much smaller than the one displayed). The HRR oscillation, q', of this voxel over 10 cycles produces an approximately sinusoidal time series as shown in the upper plot of Fig. 2.34(b). The Fourier amplitude, $|\hat{q}|$, and phase, $\angle\hat{q}$, was calculated by taking the FFT of this time series. The resulting FFT amplitude is shown in the lower plot of Fig. 2.34(b). The Fourier phase and amplitude are calculated at the forcing frequency as represented by the red line in the plot. Sufficient zero padding was applied prior to the FFT to ensure that the frequency bin was located at an integer multiple of the forcing frequency. Hann windowing was also applied to reduce the dependence on the limited sample size. This process was done for every voxel containing a flame element shown in Fig. 2.34(a). This calculation produces two volumes, one that represents the Fourier amplitude as in Fig. 2.34(c) and one that represents the phase as in shown in Fig. 2.34(d). The resulting volumes were used in analysing the flame oscillations and evolution of the phase of the flame.

2.4.1 Convective wavelength analysis

The convective wavelength plays a vital role in flame acoustic response and perturbations (Steinbacher and Polifke 2022). The calculation of convective wavelength velocities formed part of the analysis in Article III, and the calculations and approach will be outlined in this section. The tracking of the Fourier phase was used to estimate the the velocity at which HRR disturbances are convected.

An example of the three-dimensional phase of the HRR oscillations are shown in Fig. 2.34(d). The phase evolves linearly with downstream distance and the orientation of lines of constant phase are close to parallel with the

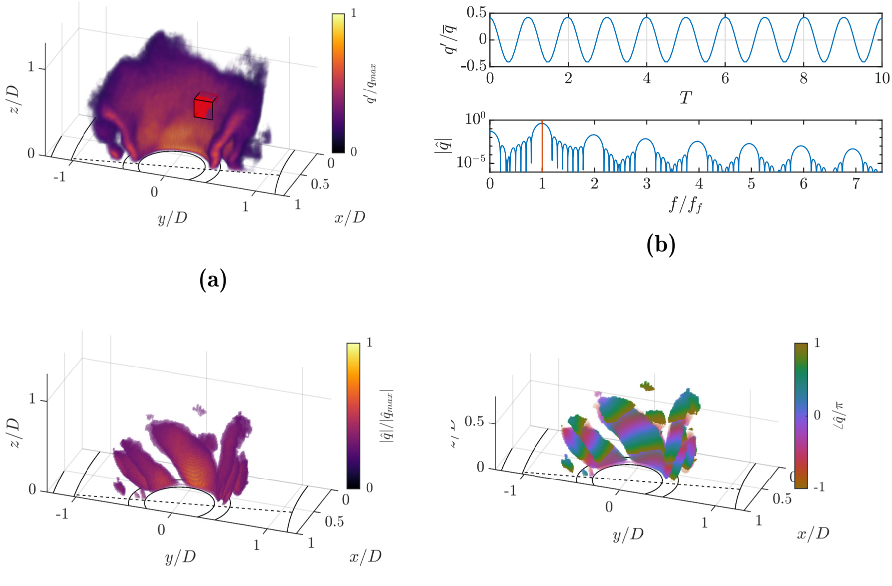

(a)

(b)

(c)

(d)

Figure 2.34: (a) Three dimensional FSD Reconstruction of an ethylene flame in an 18 burner configuration subject to an ACW spinning forced mode. The red box represents a single voxel in the FSD volume. Note the size has been enlarged for demonstrative purposes (b) (Top) time series of HRR in selected voxel over 10 cycles and respective (bottom) FFT of time series with red line showing the peak corresponding to the forcing frequency with amplitude $|\hat{q}|$ and phase $\angle|\hat{q}|$. (c) Volume with each voxel representing Fourier amplitude, $|\hat{q}|$, normalised by the maximum oscillation $|\hat{q}_{max}|$. (d) Volume with each voxel representing Fourier phase, $\angle\hat{q}$, normalised by π. A threshold was applied to (c) and (d) to show only the highest amplitude oscillations and respective phase.

dump plane. Using the three-dimensional phase volume, the convective wavelength can be defined as follows:

$$\lambda^{-1}(r,\theta,z) = \nabla(\angle\hat{q}) \tag{2.25}$$

where ∇ is the spatial gradient with respect to polar r, θ and z. Convective velocity fluctuations per voxel were calculated as:

$$\overline{u}_{\lambda}(r,\theta,z) = f\lambda(r,\theta,z) \tag{2.26}$$

Here f is the forcing frequency. The convective wavelength was first calcu-

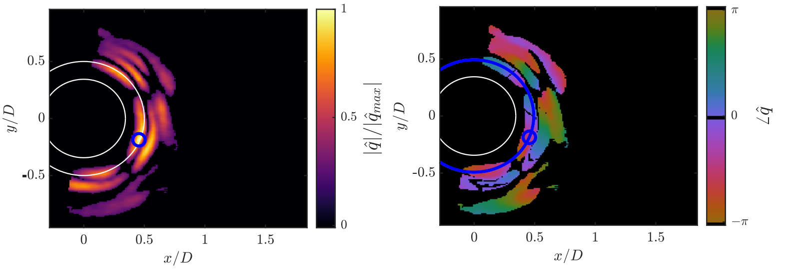

(a) **(b)**

Figure 2.35: Example shown is with respect to an ethylene flame in 18 burner configuration, half of as sector is shown outlining a single flame subjected to a forced ACW mode. (a) Slice of normalised Fourier amplitude volume at $z/D = 0.25$, blue dot represents location of highest HRR. (b) Corresponding phase volume with blue circle representing the query domain used for velocity calculations.

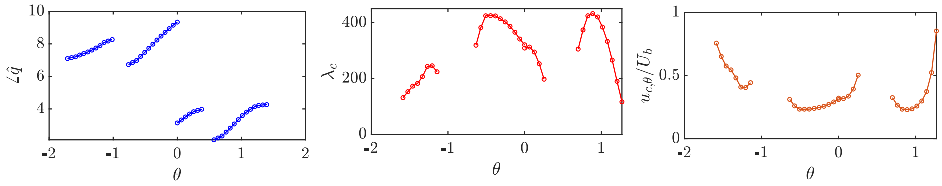

(a) **(b)** **(c)**

Figure 2.36: (a) Unwrapped phase along circle shown Fig. 2.35(b) (b) Respective λ_c of phase in Fig. 2.36(a) (c) velocity calculated from λ_c in Fig. 2.36(b).

lated by isolating regions of the flame with the highest oscillations. To do this, the largest amplitude oscillations were identified for each downstream flame slice. Figure. 2.35(a) shows an example of the location of the maximum amplitude oscillation on an arbitrary slice of the Fourier amplitude volume determined in § 2.4. The blue circle marker represents the location of the maximum HRR oscillation, and the convective wavelength with respect to the azimuthal component is determined along a radius passing through the marker. The calculation domain is defined in this way to ensure firstly that the velocity represents large oscillations in the HRR. Secondly, the calculation is performed at points where the phase is continuous, that is regions that have sufficient flame elements.

An example of the domain for the calculation for an arbitrary slice is shown in Fig. 2.35(b). The magnitude of the respective phase in the highlighted domain is shown in Fig. 2.36(a). The gradient of the phase was used to estimate the convective wavelength and an unwrapping step was first ap-

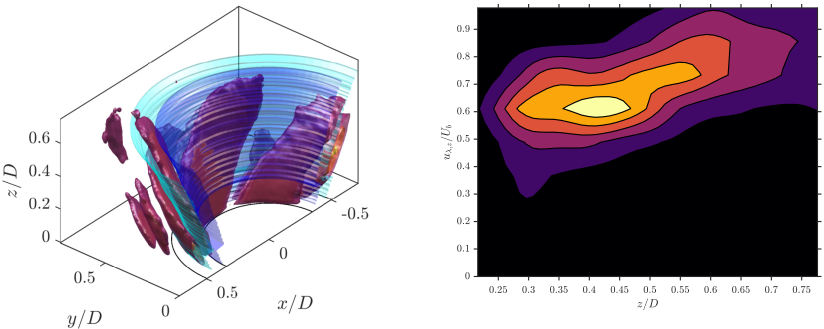

(a)

(b)

Figure 2.37: (a) Image shows the left hand side of the amplitude oscillations for the ACW case. For demonstrative purposes the flame is outlined with a surface in cyan and blue color showing outer and inner bounds of the data domain in velocity calculation (b) An example of the convective velocity oscillations calculated from (a) with respect to the axial component.

plied to account for any large jumps in phase. The gradient calculation was then performed using a least square approximation. The respective convective wavelength, λ_c, is shown in Fig. 2.36(b) from which the azimuthal convective wavelength velocity, $u_{c,\theta}$, was calculated using Eq. (2.26) and is shown in Fig. 2.36(c). This procedure was done for every downstream slice of the Fourier amplitude and phase volume, and the domain of the query points is shown in a three-dimensional plot in Fig. 2.37(a). An example of a PDF representing convective velocity with respect to the axial coordinate is shown in Fig. 2.37(b). This calculation provides the indirect measure of the convection velocity of dynamically important flow structures, and aided in the understanding the flame response as outlined in Article III. The access to the three-dimensional field allowed for assessment in the different directions.

In Article III, the convective mean swirl number was estimated from the convective wave length velocities in z and θ. The mean convective swirl number and was estimated as follows (Lilley 1977):

$$\overline{S}_{swirl} = \frac{\sum_{i=1}^{N} \overline{u}_{\lambda,z,i}\,\overline{u}_{\lambda,\theta,i}(r_i/R)^2}{\sum_{i=1}^{N} \overline{u}^2_{\lambda,z,i}(r_i/R)}$$

where $\overline{u}_{\lambda,z}$ and $\overline{u}_{\lambda,\theta}$ are the convective wavelength velocities in the downstream and azimuthal directions respectively.

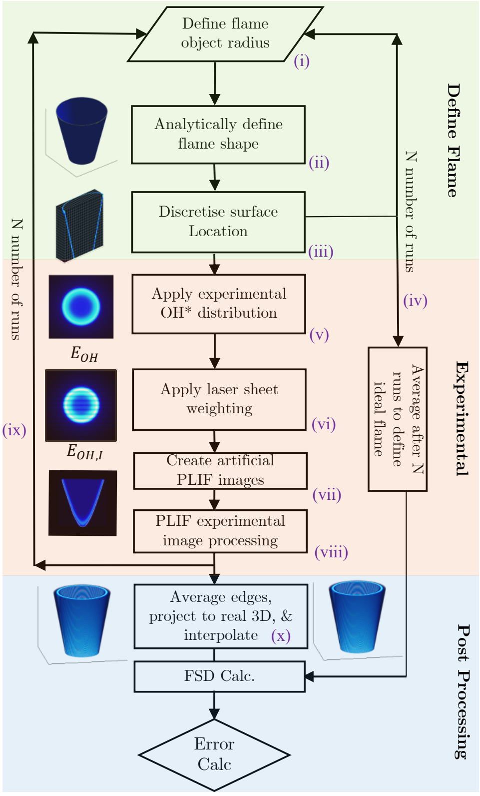

Figure 2.38: Synthetic PLIF procedure adapted from Article II.

2.5 Synthetic PLIF method

The study in Article II consisted of developing the Scanning PLIF method. To aid the development of the technique, synthetic PLIF images were generated for known flame structures. Images were then used to produce 3D volumes and an error estimation was made to assess the reconstruction procedure. Experimental parameters were also simulated to understand their effects. Although it should be noted that the synthetic images are not fully representative of the actual experimental images (it was not possible to simulate every part of the physical experiment), they were sufficient for optimising the processing procedure and provided insight into potential sources of error. In Article II, experimental parameters such as laser sheet thickness, laser sheet spacing, sheet orientation and image noise were assessed using the synthetic PLIF images. The method is briefly outlined here.

The procedure is graphically outlined in Article II, and is represented again in Fig. 2.38 to aid the description of the procedure. Additional annotations are included and will be referred to in the description that follows. Synthetic PLIF images are generated by first defining a flame object. For simplicity, a cone shape was chosen to represent the V-flame shape of typical bluff body stabilised flames. The cone's surface was defined by $r^2 = (5.7z + D_{bb}/2)^2$, where D_{bb} represents the diameter of the bluff body. A domain size of $40 \times 40 \times 40\ mm^3$ was chosen to be similar to the study in Article II. The equation used to produce the surface of the cone also ensured that the angle between the mean flame shape and the dump plane was similar to that of the experimental images of Article II. The Scanning PLIF method was designed to capture the time average flame structure, by averaging instantaneous realisations. Therefore, a similar approach was applied in the synthetic study. To achieve this, the radius of the ideal flame object was varied to replicate some features of the unsteady flame motion. Based on the experimentally measured flame brush, the distribution of the fluctuations showed that the flame's radii close to the bluff body formed a Gaussian distribution with a standard deviation of 1.3 mm. This distribution was applied as a probability density function changing the radii (presented as process (i)) of the ideal flame object over 160 instantaneous snapshots (N in Fig. 2.38) of the flame.

After defining the flame shape, the flame surface was determined from the equation of the cone in real space and discretised into a three-dimensional voxel volume using a linear scattered interpolation scheme (process (ii) and (iii)). The volume was discretised to 5 voxels/mm to maintain consistency with that of the experiment. The mean of all instantaneous flame objects represented the ideal flame object's surface ($\overline{A}_{f,ideal}$) and flame surface density ($\text{FSD}_{\text{ideal}}$) and was used for error calculations (pathway (iv)).

The OH intensity distribution of the synthetic PLIF images were determined experimentally over 10000 images taken at the center of the flame. A profile was taken on each image over a line perpendicular to the flame front. The grey region in Fig. 2.39(a) represents the standard deviation of this profile for 10000 raw PLIF images, and the black line represents the mean. The mean profile was used to introduce the OH distribution into the discretised volume and was aligned normal to the flame surface. The intensity along this line was then scaled based on the voxel intensity described by the discretised cone surface in combination with the OH distribution profile. This operation was applied directly to the discretised volume for simplicity (process (v)). The resulting flame object, E_{OH}, was then used to generate artificial PLIF

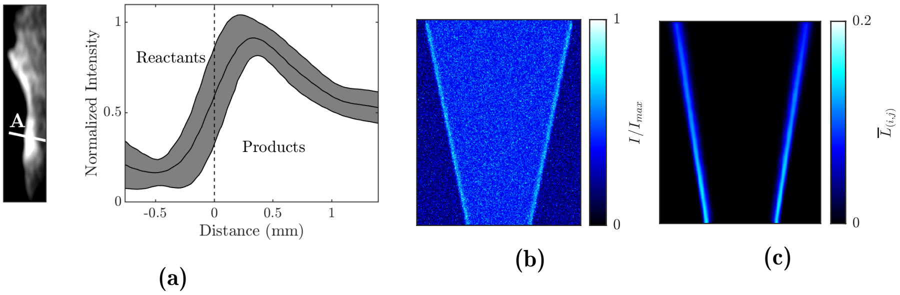

Figure 2.39: (a) PLIF image characteristics taken from experimental images of ethylene/air flame. OH distribution determined normal to flame surface, (left) raw PLIF image, with line A normal to flame surface.(b) Image of synthetic PLIF image with 30% noise level. (c) Image occupancy rate, $\overline{L}_{(i,j)}$ of synthetic PLIF images at the center of the VOI.

images.

The fluorescence due to the laser illumination in the experiment was simulated by assuming a Gaussian intensity profile. Then, the position of the laser sheet was modelled using an equation of a plane, and the illumination intensity, I, was a function of the normal distance from the plane as represented by Eq. 2.27 below (similar to Lawson and Dawson (2014)):

$$I(\mathbf{X}) = \exp(-8(d)^2/\delta^2) \tag{2.27}$$

where $\mathbf{X}$, defines the coordinates of a plane, d represents the normal distance from the plane, and δ, represents the sheet thickness. The sheet thickness was adjusted to examine the effect on reconstructing the 3D flame surface density field. The results are presented in Article II. The illumination distributes intensity into voxels based on the sheet position, resulting in a discretised illumination volume for each sheet location, E_I (process (vi)). The product of the laser illumination volume and the intensity volume scales the intensity for each laser sheet position, $E_{OH,I} = E_{OH} \cdot E_I$. This synthetic study neglected the effects of laser sheet inhomogeneity. This assumes that post-processing techniques were sufficient in removing such effects, and the sensitivity of these parameters on the reconstruction were negligible. A slice from volumes representing E_{OH} and $E_{OH,I}$ are shown in Fig. 2.38.

Synthetic PLIF images were produced by projecting non-zero voxels from the $E_{OH,I}$ volume. The projection was made using a simple camera pinhole model (as in Lawson and Dawson (2014)). Using an ideal camera model reduces any errors associated with camera calibration, although the model did allow for alignment variations of the calibration plate during parameter testing. The spatial resolution of 5 voxels/mm was chosen to match the experimental images taken in Article II. Synthetic images were produced for each laser sheet position, n. The number of sheets used to scan the volume and the laser sheet spacing was varied to understand its effects on the reconstruction process. Image noise was also a parameter that has been shown to directly affect the reconstruction accuracy since it was seen to reduce the precision of edge detection (in process (vii)). To understand the effect of image noise, spatially white, non-zero mean random noise was added to each synthetic image. This study evaluated noise levels up to 30 %, which was considered an extreme case since typical noise levels of experimental PLIF images were estimated to be 10 %. An example of an image after noise addition is shown in Fig. 2.39(b).

After noise addition, the synthetic PLIF images were processed by the edge detection procedure discussed in § 2.3.6 to determine the edge occupancy rate, $L_{sim}(i, j, n, N)$ for each snapshot N in image space. As shown in Fig. 2.38, the process loops again with an updated radius producing a new snapshot (pathway (ix)). The average of all N snapshots produces the average edge occupancy rate, $\overline{L}_{sim}(i, j, n)$ for laser each sheet position. An example of the occupancy rate for a single sheet location at the center of the VOI is shown in Fig. 2.39(c). The plane of $\overline{L}_{sim}(i, j, n)$ was then projected to real space and the process outlined in § 2.3.8 was used to reconstruct the three-dimensional representation of flame surface density, $\mathrm{FSD_{sim}(x, y, z)}$, volume (process (x)).

2.5.1 Error calculation of synthetic PLIF study

The accuracy of each reconstruction, $\mathrm{FSD_{sim}}$, was determined by a comparison to the ideal flame shape, $\mathrm{FSD_{ideal}}$. This was done by calculating the normalised correlation coefficient, R, between the volumes using the formulation proposed by (Elsinga et al. 2006).

$$R = \frac{\sum_{x,y,z} \mathrm{FSD_{ideal}(x, y, z)} \cdot \mathrm{FSD_{sim}(x, y, z)}}{\sqrt{\sum_{x,y,z} (\mathrm{FSD_{ideal}(x, y, z)})^2 \cdot \sum_{\mathrm{x,y,z}} (\mathrm{FSD_{sim}(x, y, z)})^2}} \tag{2.28}$$

A second definition of the normalised correlation coefficient was also used to assess the local reconstruction quality to evaluate any asymmetries in the reconstruction. This was achieved by defining the domain in cylindrical polar coordinates, giving rise to the evaluation of reconstruction quality in wedge-shaped regions as in Eq. 2.29.

$$R_\theta = \frac{\sum\limits_{r,z}\sum\limits_{\theta=\theta_1}^{\theta_2} \mathrm{FSD}_{\mathrm{ideal}}(\mathrm{r},\theta,\mathrm{z}) \cdot \mathrm{FSD}_{\mathrm{sim}}(\mathrm{r},\theta,\mathrm{z})}{\sqrt{\sum\limits_{r,z}\sum\limits_{\theta=\theta_1}^{\theta_2} \mathrm{FSD}_{\mathrm{ideal}}(\mathrm{r},\theta,\mathrm{z})^2 \cdot \sum\limits_{\mathrm{r,z}}\sum\limits_{\theta=\theta_1}^{\theta_2} \mathrm{FSD}_{\mathrm{sim}}(\mathrm{r},\theta,\mathrm{z})^2}} \tag{2.29}$$

It should be noted that the normalised correlation coefficient assesses accuracy through a comparison with the discretised surface location, E_{ideal}, rather than the analytical surface location. The current definition of this gives rise to the correlation coefficient behaviour shown in Fig. 2.40, which produces a minimal value of $R < 0.2$ for a surface distance of 10 voxels (2 mm) or greater. The results of this synthetic study are reported in Article II.

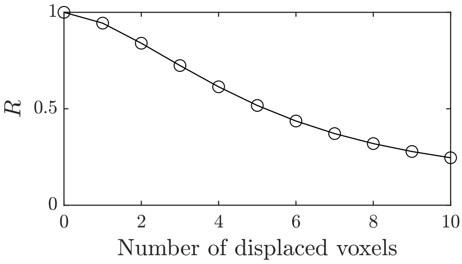

Figure 2.40: Reconstruction quality defined by spatially moving the ideal flame object relative to itself.

2.6 3D Computed Tomography of Chemiluminescence

2.6.1 Tomography Experimental Setup

The details within this section are with reference to Article I in which a single flame subjected to ACW/CW forcing in the annular combustor was investigated by a three-dimensional Computed Tomography of Chemiluminescence (CTC). The fundamentals of CTC are outlined in Chapter 1, and this section will focus on the implementation of the technique. The experimental setup used for the CTC method is shown in fig 2.41, and the experimental conditions are outlined in Table 2.1. Initially the 12 burner setup was used, however, this setup proved problematic in reconstructing the HRR field since it was difficult to isolate the intensity of the flame of interest. To illustrate this point, Fig. 2.42 shows a camera positioned at

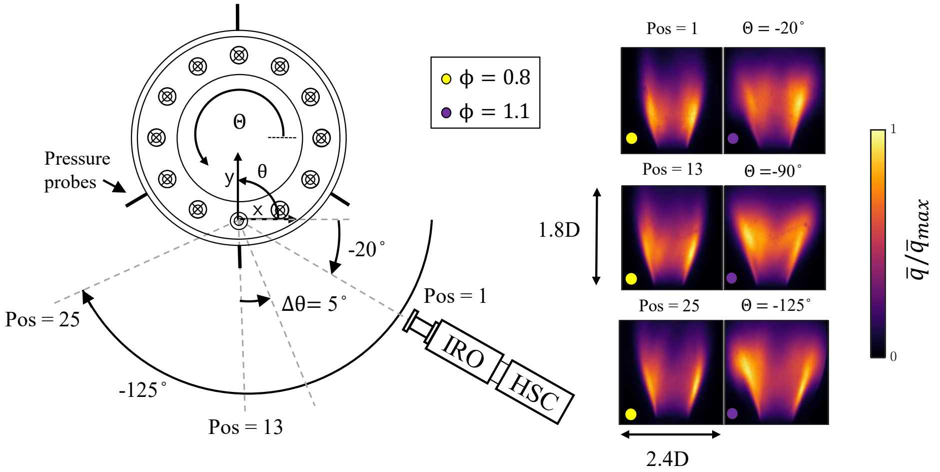

Figure 2.41: Tomographic experimental setup adapted from Article I. OH* chemiluminescence images accompany 3 views over the entire view range for ϕ=0.8 and ϕ=1.1.

a single viewing angle with 12 flames on. CTC is a line of sight method, and an example of a single line of sight is outlined in Fig. 2.42, showing that the total intensity captured along that line is based on the intensity of not just the flame of interest but also includes the intensity of the neighbouring flames. The additional intensity will not be placed correctly in the reconstruction, as only specific views will capture it, making reconstruction complicated. Therefore, unlike the conventional setup shown in fig 2.2, 11 of the burners have been blocked at the exit of the plenum using a gasket that only permitted the flow of the fuel/air mixture through a single injector of interest.

The CTC reconstruction was used to analyse the HRR response of forced flames and OH* chemiluminescence was used as a proxy for HRR. OH* chemiluminescence images were taken from 25 independent viewing angles via a single high-speed Phantom v2012 camera equipped with LaVision Intensified Relay Optics attached to a 100 mm focal length Cerco 2178 UV lens and a 310 nm bandpass filter. The camera aperture was set to f/8 to ensure a sufficient depth of field, and images at a resolution of 1280 by 800 pixels were acquired at an imaging rate of 10 kHz. The forcing signal was recorded during the image acquisition and was used to bin the images into 16 phases over 810 cycles. The phase averaging procedure was similar to that outlined in § 2.20.

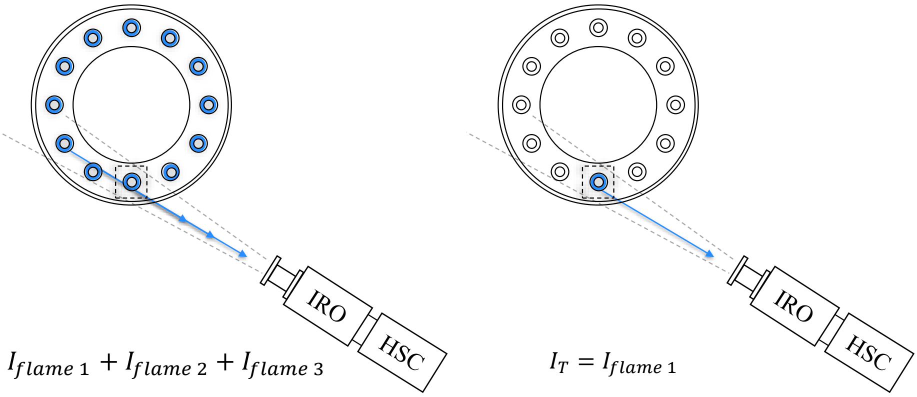

Figure 2.42: Example of the intensity along single LOS for a multi-flame setup (left) vs a single flame setup in the annular combustor (right).

The rotation of the camera was performed by a mechanical arm connecting the camera to the structure holding the combustion rig. The fulcrum of the arm was positioned directly below the burner of interest. A protractor was installed and aligned with the center of the fulcrum and the center of the burner and helped measure the camera angle with respect to the burner. One hand of the protractor was fixed to the rig structure while the other rotated with the arm attached to the camera, measuring an angle represented by θ in fig 2.41 which was set to 5° between each camera position. All 25 views covered a total angular separation of 125°.

2.6.2 Flame Describing Function (FDF) as a function of equivalence ratio

The implementation of the tomographic reconstruction was aimed at understanding the effects of ACW and CW forcing on a single flame within the annular combustor. It has been previously shown that the global HRR response varied between the directions of spinning azimuthal modes. In Article I, the FDF which measures the global HRR response was implemented to characterise the HRR response of a single flame in the annular confinement when subjected to spinning modes. The operating conditions to evaluate this flame were first investigated by performing a FDF for different equivalence ratios to investigate the symmetry of the response. This section outlines the method of producing the FDFs shown in Article I. A thorough description of Flame Transfer/Describing Functions was outlined in Chapter 1. The flame describing function was defined by:

Figure 2.43: Image of CTC experimental setup outlining combustor and movable camera arm attached to setup. Note that the combustor shown has been modified from the one used in the CTC study.

$$\mathrm{FDF} = \frac{\langle|\hat{q}|\rangle/|\overline{q}|}{|\hat{u}|/U_b} \tag{2.30}$$

where the notation $\langle\cdot\rangle$ denotes the spatial average, $\hat{q}$ represents the Fourier amplitude of the HRR oscillations q'. $|\hat{u}|$ and U_b as defined before in § 2.2.3 represents the axial Fourier velocity amplitude and the bulk flow velocity, respectively. The axial velocity fluctuation was calculated from pressure measurements in the injector. The pressure and velocity oscillations are first calculated using the Multi-microphone method as outlined in § 2.2.3. The axial velocity fluctuations represented the value projected at the dump plane of the combustor and were varied by increasing the forcing amplitude. A wide range of amplitudes were investigated for both the ACW and CW spinning directions. The Heat Release Rate (HRR) measurements were determined from OH* chemiluminescence measurements and 10000 images were taken at each forcing level at an image rate of 10 kHz. The FDF was then calculated across the range of axial oscillations for both spinning directions across an equivalence ratio range of 0.8-1.1.

2.6.3 Camera Calibration

A camera calibration was required to convert image coordinates to real-world coordinates for each view. It was, therefore, essential to have the calibration plate placed in the exact location after the camera had been moved to locations shown in fig 2.41. A 3D printed calibration holder was manufactured to ensure the plate could be placed in the exact location after each run. The holder was designed to be push fitted into the three injectors securing the position of the plate. To assess the accuracy of the calibration plate placement, the plate and respective holder were placed into the combustor while images were taken after each placement. A measure known as the Structural Similarity Index (SSIM) quality indicator was used to assess any variability in the movement of the plate from the removal and replacement of the target into the combustor. The SSIM is defined by the product of luminance, contrast and structural terms Wang et al. (2004):

$$SSIM(x,y) = [l(x,y)^{\alpha}][c(x,y)^{\beta}][s(x,y)^{\gamma}] \tag{2.31}$$

$$l(x,y) = \frac{2\mu_x\mu_y + C_1}{\mu_x^2 + \mu_y^2 + C_1}, c(x,y) = \frac{2\sigma_x\sigma_y + C_2}{\sigma_x^2 + \sigma_y^2 + C_2}, s(x,y) = \frac{\sigma_{xy} + C_3}{\sigma_x\sigma_y + C_3} \tag{2.32}$$

where σ and μ represent the standard deviation and local mean, respectively. α, β, and γ are power exponents with a default value of 1, and C are constants included to avoid instability when the denominator is close to zero. A value close to unity (0.99) was achieved when placing the target into the combustor for all positions, ensuring that the target's position and the location of the calibration points remained repeatable in between each camera position. The calibration target used was a 2-level Lavision model 106-10 with a height and width of 160 mm, a level separation of 2 mm and dot spacing of 10 mm, which is shown with the 3D printed holder in fig 2.44. Before images are taken, a flood light is positioned 45° to the camera to maximise lighting on the plate which ensured that the dot detection was optimal.

The radial distortion due to the confinement was significant in this experimental setup. The curvature of the quartz outer wall produces unique reflections and radial distortion as the camera is rotated around the rig. During calibration, the effects of reflections by the quartz were first reduced by background subtraction of the calibration images. A light absorbing black target was placed at the position of the calibration target, and images

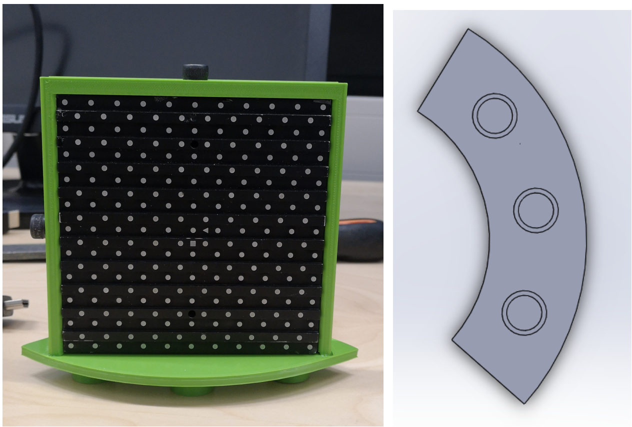

Figure 2.44: Calibration target and holder, (left) calibration plate secured into holder, (right) cad drawing outlining three holder caps used to fit into injectors.

were acquired. The images were then averaged and subtracted from the averaged calibration image. An example of the subtracted image is shown in fig 2.45(c). In the figure, it is clear that this image pre-processing step removes reflections from the quartz, and the calibration pixel error was reduced by 48 %. To further address the radial distortion effects of the quartz, the calibration model chosen was a modified pinhole model that accounts for curved enclosures (Liu et al. 2019, Paolillo and Astarita 2019). In addition, the model accounts for refractive changes in the quartz glass using Snell's law (Paolillo and Astarita 2019). The conventional pinhole camera model requires the fitting of extrinsic camera parameters such as translation and rotational matrices and camera intrinsic parameters such as focal length, skewness, lens distortion coefficients and principal point (Hartley and Zisserman 2004). These parameters are conventionally determined by imaging a target of known dimension, points of known location are extracted, and the relationship between image and world coordinates can be determined by fitting the mentioned intrinsic and extrinsic parameters:

$$\tilde{y} = \mathbf{GR}[I - x_c]\tilde{x} \tag{2.33}$$

where, $\mathbf{G}$, $\mathbf{R}$, I,are matrices representing intrinsic, extrinsic and an identity matrix, respectively. x_c represents the orientation in object space. An additional 8 parameters were used in this modified camera calibration model. The parameters included extrinsic parameters such as rotational and translational matrices with respect to the cylindrical quartz and intrinsic parameters that included the quartz thickness, refractive index, and internal

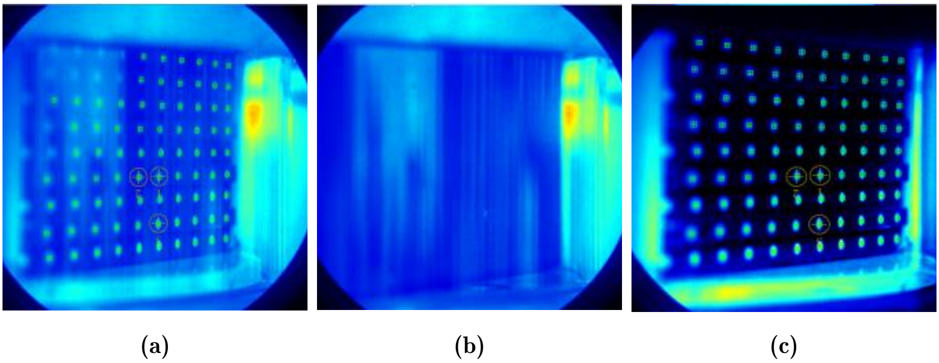
(a) (b) (c)

Figure 2.45: (a) Calibration image (b) image of light absorbing target (c) resulting background subtraction image.

radius at the point of incidence at the inner and outer quartz intersections. The additional parameters of the model were determined by imaging a calibration target with and without the quartz at each camera position. The mean calibration error obtained by this method was 0.16 mm.

Image Acquisition Procedure

The experimental acquisition procedure for the CTC method was as follows:

1. Calibration holder was securely placed into the rig, and 300 images are taken.

2. Calibration target was removed and replaced with light absorbing target, 300 images were taken of the target.

3. Combustor was ignited. After 10 seconds the speakers were turned on. The mode is monitored and if necessary fine tuning was applied. If major tuning was required, the rig is cooled down to 25 degrees, and further tuning was performed until the mode was at the correct amplitude. This often requires up to 4-5 iterations. The procedure of forcing has been outlined in §2.2.3.

4. After 20 seconds and while the temperature probe placed at $\Theta = 270^\circ$ is within a defined range, 10000 OH* chemiluminescence images are taken.

5. The rig is cooled down to room temperature and a post-calibration is taken, including imaging of black target for background subtraction.

6. The camera was moved to the next position, and the steps are repeated.

2.6.4 Reconstruction Algorithm

Each pixel in each image captured from 25 unique camera angles creates a set of finite projections of the flame object. Therefore, a reconstruction algorithm was required to match the projection data to best describe the flame object. To do this, a discretised approach was applied in which the solution of the projections takes the form of an algebraic series expansion. This method defines the problem as a set of basis functions forming a linear system to provide an approximation of the flame object (Herman 1980). The reconstruction problem was then defined as:

$$W f_{ob} = P_r \tag{2.34}$$

where P_r is the projection at each pixel from each OH* chemiluminescence image, f_{ob} represents the object matrix, and W represents a weighting matrix that relates the projection to every discretised point in the object volume. Equation 2.34 forms a set of linear equations. The complexity of solving such a system arises when considering the size of the system. Iterative methods are usually used to solve such systems due to their speed and ease of implementation (Natterer 1999). This study used a sequential scheme known as the Algebraic Reconstruction Technique (ART) (Gordon et al. 1970) to solve Eq. 2.34. As outlined by Floyd and Kempf (2011), the use of the ART algorithm provides the following advantages: (i) the algorithm is robust in dealing with noise, (ii) requires only a few views for reconstruction, especially for experimental setups with limited optical access, (iii) *a priori* information such as smoothness or boundedness can be incorporated in its implementation to improve the reconstruction, and (iv) the algorithm is not restricted by the geometry of projections or orientation. The reconstructed CTC volume consisted of 240 × 240 × 192 cubic voxels with a spatial resolution of 0.25 mm in height, width and length. The performance of the reconstruction accuracy was assessed by cross-correlation and the method is outlined in the next section.

A Measure of Reconstruction Accuracy

Accuracy was measured by omitting a view from the reconstruction. A slice from the reconstructed volume is then projected in the plane of the omitted view and compared. The difference between the images was quantified using a cross-correlation as follows Liu et al. (2019):

$$R_{corr}(C, D) = \frac{\sum_i [(C(i) - \langle C \rangle) \times (D(i) - \langle D \rangle)]}{\sqrt{\sum_i (C(i) - \langle C \rangle)^2} \times \sqrt{\sum_i (D(i) - \langle D \rangle)^2}} \qquad (2.35)$$

where R_{corr} represents the correlation coefficient between matrix C representing the independent image and matrix D representing the projected image from the 3D reconstruction. $\langle C \rangle$ and $\langle D \rangle$ represent the averaged value of each image and the index of each image, respectively.

Image convergence test

A convergence test was performed to determine the minimum number of images required from each viewing angle to produce a statistically convergent result. To this end, an FFT was performed on OH* chemiluminescence images taken in Article I across a variable range of images and the resulting Fourier amplitude was determined for each sample size. The amplitude of the resulting FFT is shown in Fig. 2.46. The amplitude determined after using 320 images starts to converge to a set value with minor deviations less than 1 %. It was therefore assumed that convergence is reached after 320 images. The number of images used for OH* chemiluminescence in the studies outlined used a minimum of 625 images in each phase bin which is large enough to reach statistical convergence by the definition presented here.

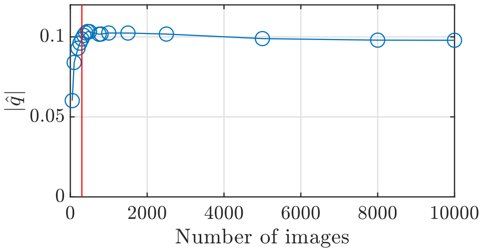

Figure 2.46: Image convergence test by estimating the FFT amplitude while varying the number of images used in the calculation. Red line represents point of convergence.

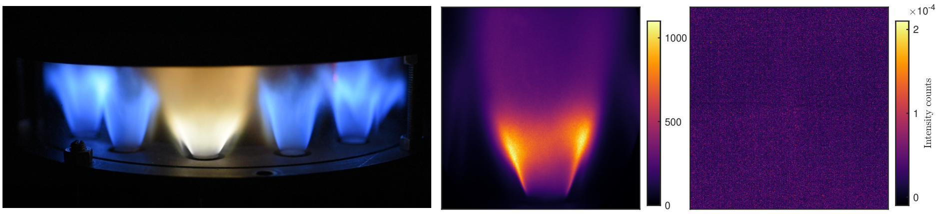

(a) (b)

Figure 2.47: (a) Image of multi-flame setup, (b) NH_2^* chemiluminescence image of (left) Ammonia/hydrogen flame and (right) Methane flame. Colorbars represent signal intensity counts

2.7 II. Tomographic reconstruction of 12 flame burner - A practical attempt, shortcomings and recommendations

It was shown that limitations in implementing the CTC technique (Article I) constrained investigations in the annular combustor to a single flame. This section will introduce a potential method to overcome this limitation. The CTC method relies on capturing chemiluminescence based on a specific wavelength. In this case, emissions of wavelengths blocked by the filter are cut out of the signal. Using this concept, a series of filters were tested on a combination of fuels. The aim was to identify a fuel blend that produced sufficient chemiluminescence for one bandwidth but not another. This would allow for reconstructing the HRR field of a single flame in the annular combustor while omitting light from neighbouring flames. Therefore filters that corresponded to species like NH radicals that do not form in high concentrations in hydrocarbon combustion but are formed in the combustion of ammonia were considered. Using a 623 nm (NH_2^* radical bandwidth) filter (Pugh et al. 2021), it was found that ammonia/hydrogen flames produced sufficient signal. However, methane flames did not produce any emission at this wavelength. Therefore, ammonia/hydrogen was introduced to a single injector in the annular rig. The remaining injectors were fed with methane/air. The multi-flame setup image is shown in Fig. 2.47(a). Introducing ammonia and hydrogen to the combustor required installing a secondary fuel/air delivery system to the annular rig, and sufficient flow conditioning was required to ensure a uniform flow. The equivalence ratio of the 60/40 molar % ammonia/hydrogen flame was chosen such that the laminar flame speed and adiabatic flame temperature were the same as those of the methane flames. The methane/air flames had an equivalence ratio of 0.8 and a bulk flow velocity of 18 m/s. An image showing the filtered ammonia/hydrogen flame and an image of the methane flames using the same filter is shown in fig. 2.47(b). Note how sufficient signal is observed in the ammonia/hydrogen flame, were as the filtered intensity produced by methane flames are effectively invisible. Using this multi-flame setup would introduce flame interaction and confinement effects that were omitted in Article I. The HRR response of this flame to azimuthal modes can then be investigated using the CTC method. In this thesis, OH* chemiluminescence and PLIF are extensively used to measure HRR. However, reports of the 632 nm filter as a marker for HRR are not well known. To test its applicability to measure HRR, both imaging of OH* and NH_2^* chemiluminescence of a forced ammonia/hydrogen flame and both signals were compared as shown in Fig. 2.48. It can be seen that both signals produce a similar trend, suggesting that the 632 nm filter can be used as a marker for HRR. Unfortunately, this study was not taken further due to time constraints during this thesis, and no reconstructions were performed to further this investigation. However, the presentation of this result here is a recommendation for future work as this result does hold some promise in evaluating multi-flame setups using CTC. This section provides some supporting discussion on the recommendation for CTC methods outlined in Chapter 5.

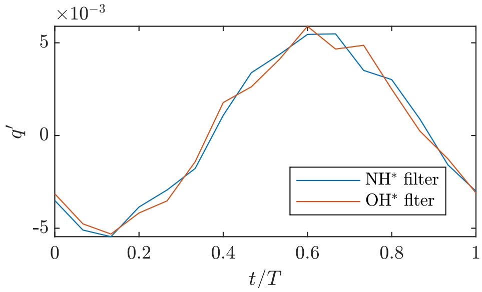

Figure 2.48: Comparison between OH* and NH_2^* chemiluminescence for a forced ammonia/hydrogen flame.

The description of the combustor and the details of the experimental implementation of the Scanning PLIF and CTC techniques to produce three dimensional volume outlining the HRR response of a flame in the annular combustor were outlined in this Chapter. The CTC method was used to produce the results in Article I and the Scanning PLIF technique was used for in the analysis in Article II and Article III. The Scanning PLIF technique was also used to investigate the HRR response of the flame at locations in a standing wave and the results will be presented in the next Chapter.

I love fools' experiments. I am always making them.
— Charles Darwin

3

Experimental results

In this Chapter, two additional studies will be briefly introduced. In depth analysis of this data was not completed due to time limitations, and therefore only brief highlights of these data sets are presented to illustrate their contents, and to describe some key features. The first study, presented in § 3.1, includes a three-dimensional phase-averaged analysis of the FSD of an unswirled flame in an annular combustor subjected to a standing mode. A few observations of the flame response at three locations in the standing wave will be briefly outlined here.

3.1 Three dimensional phase-averaged HRR analysis of flame response in a standing wave without swirl

Article II introduced the Scanning PLIF technique to reconstruct the three-dimensional Flame Surface Density based on two independent scan directions. This technique was applied to forced flames to investigate their phase-averaged response at three positions in a standing wave. The positions chosen for reconstruction were the pressure antinode (AN), node (N) and an intermediate position equidistant between the pressure node and antinode (IL). A brief description of the flame response will be outlined in this section.

3.1.1 Experimental setup

The annular combustor presented in Chapter 2 was used to obtain the data presented in this section. The experimental setup was identical to Article II, and a brief description of the setup and measurement procedure will be outlined here. The 12 injector configuration was used to investigate a single unswirled ethylene flame subjected to a standing wave in the NTNU annular combustor. This study omitted the swirler to investigate large-scale structures without additional complexity due to the locally rotating flow field and significant flame-flame interactions. Ethylene/air was introduced to the annular combustor at an equivalence ratio of $\phi = 0.7$ and a bulk flow velocity of U_b =17 m/s at the injector exit. Note that the equivalence ratio chosen here differed from Articles I and III and was chosen based on the study by Mazur et al. (2019), who showed that in this combustor configuration, this operating condition was not self-excited. The forcing procedure outlined in Chapter 2 was used to create a standing wave in the combustor at a forcing frequency of 1790 Hz which was chosen based on the resonance of the combustor. Changing the angular position of the forcing array allowed for repositioning the standing wave with respect to the flame of interest. The dual scan method outlined in § 2.3 of Chapter 2, in which scanning PLIF is performed for two orthogonal laser sheet orientations, was used to reconstruct the phase-averaged HRR response of the flame. OH PLIF imaging was performed using a v2012 camera with an imaging frequency of 10 kHz. A third-order polynomial camera model was used to transform pixel space to real-world coordinates with a maximum mean calibration error of 0.45 pixels (0.046 mm) for the three cases. Ten independent scans were performed for both the X-Z and Y-Z scan directions producing 700800 images in each direction. The coordinate system used in Fig. 2.10 was used in this analysis. Images were binned, using the forcing signal, into 16 phases. The laser sheet was positioned at 200 locations within the volume of interest, resulting in 220 images per a phase angle per laser sheet position. The reconstruction produced a 200 × 200 × 200 voxel volume representing a 40 mm × 40 mm × 40 mm volume. The FSD reconstruction method outlined in § 2.3.8 of Chapter 2 was used to reconstruct the HRR field for each phase angle. The resulting volumes, along with a planar cross-plane slice through the burner axis in the X-Z and Y-Z directions, will be presented in the following sections.

3.1.2 Modal characterisation

The quaternion formulation outlined in § 2.47 of Chapter 2 was used to characterise the standing mode inside the annular combustor. The velocity

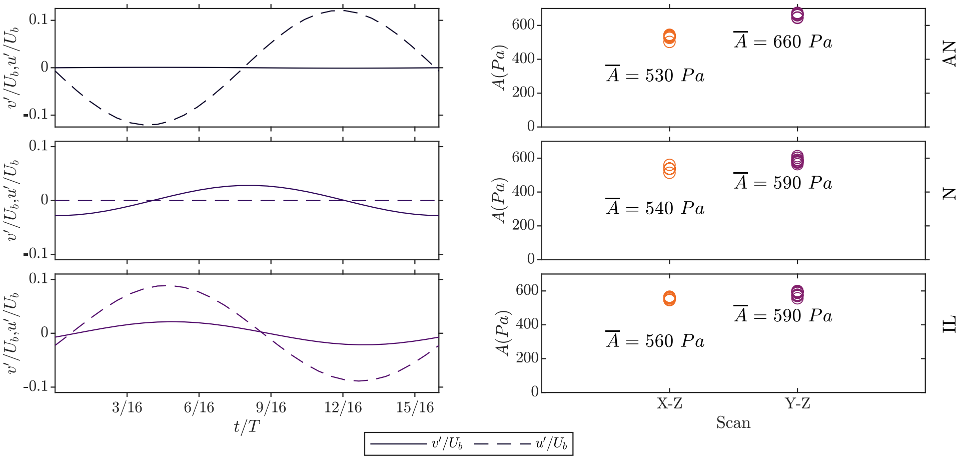

Figure 3.1: Azimuthal and axial velocity oscillations over a forcing cycle for the flame of interest (left column). Amplitude of the azimuthal pressure mode of each run taken during a dual scan, for AN, N and IL forcing cases (right column). Circular data points presented in the center columns plot refer to injector locations at which pressure was measured around the annular.

fluctuations and modal data for all three cases are presented in Fig. 3.1. When applying the dual scan method to forced flames, it is important that the flame modal response is identical for each scan direction and each run to ensure a consistent reconstruction. To assess the repeatability of the modal response, a plot of the azimuthal amplitude for each independent scan is shown in the third column of Figure 3.1. The azimuthal amplitude (A) was calculated using Eq. 2.47 of Chapter 2. For all three cases, the deviation between each run for each case is small, with a maximum standard deviation of 34 Pa. However, larger differences are present when comparing the amplitude between each scan direction for each case. The pressure AN, N, and IL cases produce a mean azimuthal amplitude difference of 130 Pa, 50 Pa, and 30 Pa between the scan directions, respectively. This large difference, especially in the case of the antinode, was due to the difficulty in controlling the forced modes. This difference in amplitude on the flame response is difficult to quantify or correct. Nonetheless, some observations on the flame response can be presented.

3.1.3 Flame response at the pressure antinode

The axial and azimuthal velocity oscillations, averaged all runs and scan directions, normalised by the bulk flow velocity of the antinode position are shown in Fig. 3.1. The flame at the antinode position experiences a max-

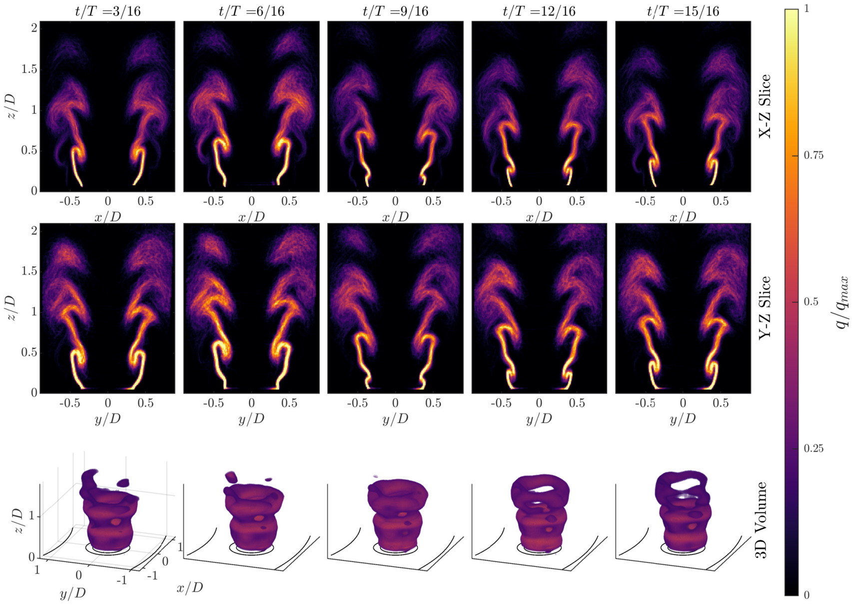

Figure 3.2: Cross plane slices of FSD of flame at antinode position. (top) X-Z Slice, (middle) Y-Z Slice and (bottom) 3D reconstruction. A threshold 15% of the maximum FSD value is applied to the 3D volumes to isolate regions of large magnitude.

imum axial velocity oscillations value of 0.11. In contrast, the azimuthal velocity oscillations are negligible. Figure 3.2 presents two cross-plane FSD slices and a three-dimensional FSD volume for five phase-averaged instances along a forcing cycle. In the X-Z FSD slices ($y/D = 0$), the inner shear layer is observed to roll up at the base of the flame, which can be seen through the large scale flame wrinkling. The flame surface curvature grows as the vortex is advected downstream. The roll-up of the flame surface is seen on both sides of the flame and is symmetric around the $x/D = 0$ axis. The stabilisation of the flame on the outer shear layer is not present at the dump plane. Eventually, the flame surface pinches off at the downstream location $z/D = 1.5$. A similar symmetric response is observed in the Y-Z FSD slice ($x/D = 0$). However, the flame response slightly differs at $y/D > 0.5$ close to the inner wall. Article II conjectured that the different conductivity and flow geometry between the inner and outer walls changed the flame shape. Similarly, the flame response close to the inner wall is more elongated than the flame response at the outer wall. The wall effects are minor when compared to the unforced flame in Article II. This is potentially due to the smaller flame height observed for forced flames. The three-dimensional FSD volumes are presented in the bottom row of Fig. 3.2. The three-dimensional HRR field shows an approximately an axisymmetric structure. A threshold of 15% of the maximum HRR value was applied to the reconstructions to remove small oscillations in HRR and non-physical flame elements. A three-dimensional representation of the pinch-off event produces a close to symmetric ring-like structure. The formation of this ring-like structure forms at the base due to axial velocity oscillations and grows in size, and eventually, the flame pinches off at $t/T = 12/16$. Small flame elements remain close to the inner wall after the pinch-off at $t/T = 3/16$. The three-dimensional structure of the flame at the antinode position produces a symmetric response with minor differences in the flame response between the cross planes. It is interesting to point out that the symmetry of the response shown at this position is similar to shown by Balachandran et al. (2005) as discussed in Chapter 1 for a forced single flame setup.

3.1.4 Flame response at pressure node

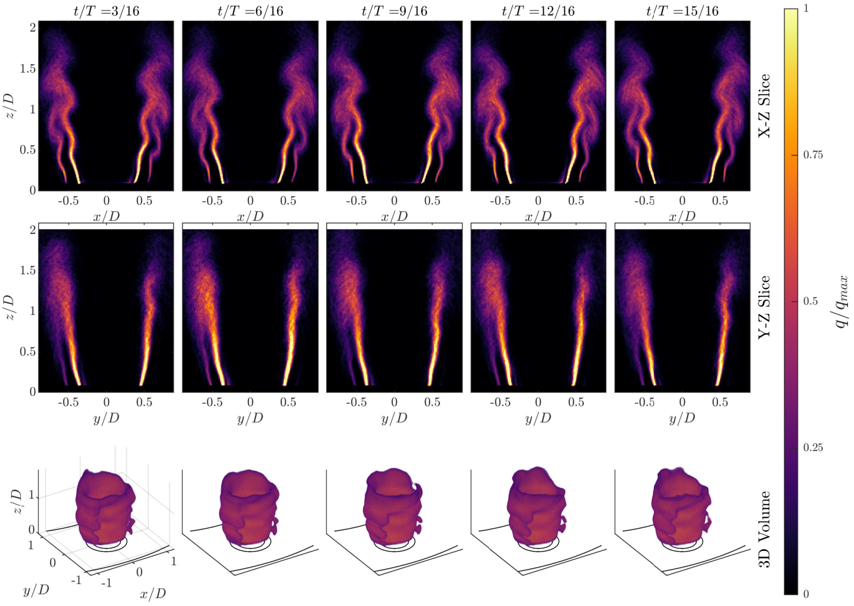

Figure 3.3: Cross plane slices of FSD of flame at Node position. (top) X-Z Slice, (middle) Y-Z Slice and (bottom) 3D reconstruction. A threshold 15% of the maximum FSD value is applied to the 3D volumes to isolate regions of large FSD.

The second position of interest in the standing wave is the nodal position.

At this position, as per Fig. 3.1, the azimuthal velocity oscillations are significant, with a maximum value of 0.03 when normalised by the bulk flow velocity, while the axial velocity oscillations are zero. A similar representation as that of Fig. 3.2 of the cross planes and three-dimensional HRR reconstruction is shown for the flame response at the nodal position in Fig. 3.3. From the X-Z planes, it can be seen that the flame response produces a non-symmetric response, and oscillations occur on either side of the flame in anti-phase producing a flapping motion. The outer shear layer also rolls up with a different timing than that of the inner shear layer. In contrast to the antinode, the presence of azimuthal velocity fluctuations results in stabilisation of the outer shear layers, and the modulations in the outer shear layer from azimuthal velocity fluctuations cause the flame to attach to the injector exit. This result was confirmed from OH^* chemiluminescence imaging and is not shown here for brevity.

However, the response drastically differs in the Y-Z FSD slices, and the flame response is minimal in this plane, with the flame looking similar to that of an unforced flame with slight modulations of the flame surface. It is also clear that the outer shear stabilisation is not present as in the X-Z plane. In Article II, it was seen that the outer shear layer of the unforced flame had a tendency to attach to regions closer to the combustor walls. Further asymmetry is observed in the Y-Z slices as the flame response is shorter at the inner combustor wall. The three-dimensional reconstruction shown in Fig. 3.3 shows a non-axis symmetric flame structure, with regions of the outer shear layers incident to the azimuthal mode attached to the injector exit forming an M-flame structure in these regions. Unlike the flame response at the antinode, the flame does not have a clear pinch-off event. The nodal position shows how the flame responds in a non-symmetric way to both the azimuthal velocity oscillation and confinement.

3.1.5 Flame response at location in between node and antinode (IL)

The cross-plane and reconstruction of FSD of the third position presented in the standing wave are at a location equidistant from both the antinode and node. At this position, the flame simultaneously experiences axial and azimuthal oscillations that are in phase with each other. The axial and azimuthal velocity oscillations reach a maximum velocity of 0.08 and 0.02 when normalised with the bulk flow velocity, respectively, as shown in Fig. 3.1. The flame surface rolls up at the base of the flame, which grows in size as it is advected downstream. In contrast to the antinode, the flame surface roll-up differs on both sides of the flame for both X-Z and Y-Z slices, as shown in Fig. 3.4. The timing of the azimuthal and axial velocity oscillations makes

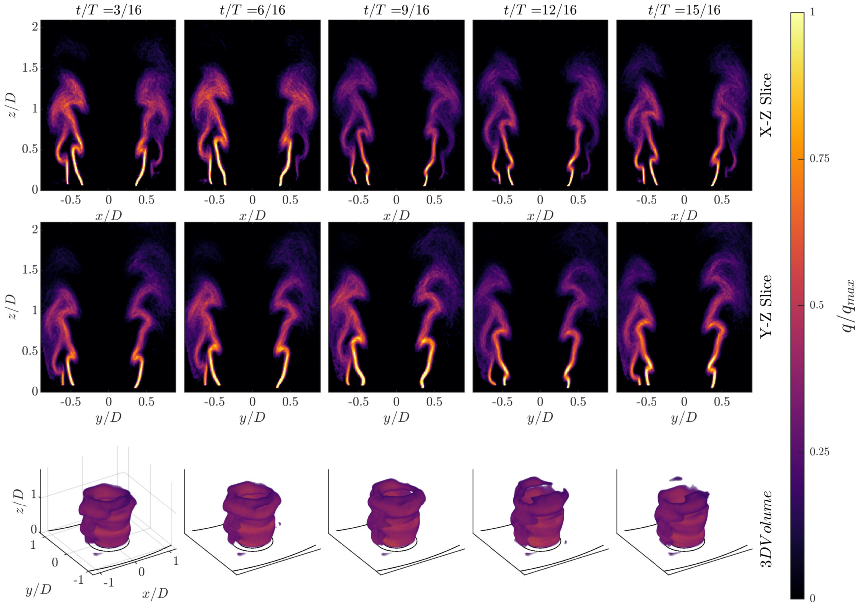

Figure 3.4: Cross plane slices of FSD of flame at IL position. (top) X-Z Slice, (middle) Y-Z Slice and (bottom) 3D reconstruction. A threshold 15% of the maximum FSD value is applied to the 3D volumes to isolate regions of large FSD.

the roll-up structures slightly asymmetric on either side. However, the roll-up of the flame surface in the X-Z slices are closely in phase with each other on both sides of the flame similar to that of the antinode suggesting that the response is dominated by axial velocity fluctuations. A similar response is also seen in the Y-Z FSD slices with a small phase difference between the flame structures at the inner and outer combustion walls. Unlike the antinode, the outer shear layers are stabilised for regions along the flame, except for the response at the inner combustion wall. After applying a threshold, it can be seen that the outer shear layer is more stabilised for locations $x/D < 0$ in the three-dimensional reconstruction in Fig. 3.4. A pinch-off is visible, however, these form asymmetric flame structures.

3.1.6 Local amplitude and phase of HRR oscillations

The flame response of the three positions in the standing wave will further be characterised using three-dimensional analysis of the HRR fluctuations amplitude and phase as outlined in §2.47 in Chapter 2. In Fig. 3.5, the amplitude of the HRR oscillations ($|\hat{q}|$) are represented as a single isosurface and the phase ($\angle\hat{q}$) is plotted on isosurfaces of a certain amplitude for

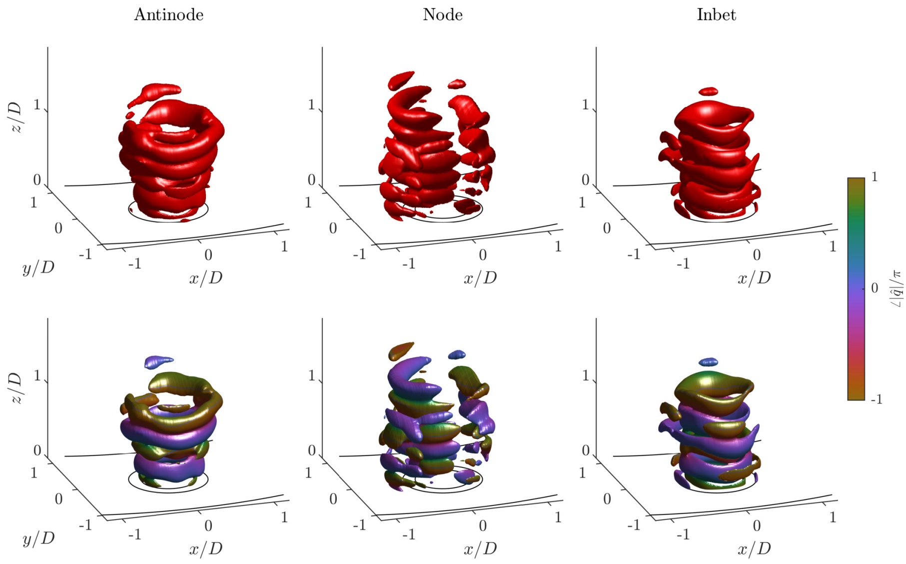

Figure 3.5: Iso-surface of FFT amplitude with iso value ($|\hat{q}|$) corresponding to 20% of the maximum FFT amplitude (Top row). Isosurfaces at value 20% of the maximum FFT amplitude colored with FFT phase, AN, N and IL cases (Bottom row).

the AN, N and IL cases. The iso-value used for the isosurface in Fig. 3.5 was chosen to highlight large amplitude oscillation structures in the flame, and the phase provides insight into the timing of these oscillations. Three distinct patterns are observed for each flame position. The flame response at the antinode is at a location that produces the largest HRR response in a standing wave (Mazur et al. 2019). At the antinode, large-scale structures take the form of concentric rings with a radius of $0.43D$ at the base of the flame and $0.55D$ close to pinch off further downstream. From the phase plots in the lower row of Fig. 3.5, the large ring-like structures are uniform in phase but are approximately π out of phase between each ring. However, the amplitude of the HRR oscillations at the node produces non-continuous crescent shaped structures on either side of the flame that is incident to the azimuthal mode. Large structures are also present on the outer shear layers, and no structures are observed along $x/D = 0$ axis for all downstream locations. Looking at the 3D phase of HRR oscillations at the nodal position shows that the timing of these structures is close to π out of phase on either side of the flame. The timing of these oscillations promotes cancelling of the global HRR at this location. In the IL case, the $|\hat{q}|$ isosurface produces ring-like structures that are distorted due to the combination of the transverse and axial velocity fluctuations resulting in an asymmetric and slanted oscillation structure. The structures are also smaller in radius and do not change in size with a downstream location like that of the antinode response.

This section presents some observations based on the reconstruction of the HRR field for a single flame at three locations along a standing wave. The response is different in each case, ranging from a symmetric response to a completely asymmetric one like that of the node. The flame response observation was possible by using the scanning PLIF technique discussed in this thesis, and although the discussion of these cases is mentioned briefly, it is worth noting that the three-dimensional analysis of an azimuthally forced flame in an annular combustor has not been produced in literature before.

And following our will and wind we may just go where no one's been. We'll ride the spiral to the end and may just go where no one's been

— *Tool*

4

Summary of research articles

This thesis contains three research articles and an additional Chapter outlining briefly results associated with a flame response in a standing wave in the annular combustor. The following Chapter summarises these studies.

4.1 Summary of papers

Article I

Tomographic reconstruction of an azimuthally forced flame in an annular chamber

Dirren Govender, Hecong Liu, Fan Peng, Weiwei Cai, Nicholas A. Worth (2022). *Proceedings of the Combustion Institute*, DOI: 10.1016/J.PROCI.2022.08.051

The aim of this study addresses research goal (i) in § 1.3 of Chapter 1. Computed Tomography of Chemiluminescence was used to reconstruct the three-dimensional HRR field of a single swirled flame in an annular combustor when forced by spinning ACW and CW azimuthal modes. The flame was first characterised by a Flame Describing Function. The equivalence ratio of the fuel was varied to change the flame shape and the interaction of the flame with the enclosure. It was found that richer flames interacted with the inner and outer walls, which also resulted in an FDF that differed between the ACW and CW modal responses. Two reconstructions were performed for a rich and lean fuel/air flame. The reconstruction error was quantified by performing a cross-correlation of an independent view. The richer case produced large errors in the reconstruction and was not used for detailed analysis. The lean case produced a high correlation value, and even though the FDF for this case was identical, the three-dimensional analysis of the HRR field highlighted key differences in the response between the ACW and CW modes. The analysis of the three-dimensional HRR oscillations volume showed that large HRR oscillations are present in regions facing the incoming pressure wave at the base of the flame. However, these regions of large HRR oscillations occur at different angular orientations downstream.

Article II

Large volume scanning laser induced fluorescence measurement of a bluff-body stabilised flame in an annular combustor
Dirren Govender. Samuel Wiseman, James R. Dawson, Nicholas A. Worth (2022). *Experiments in Fluids*, 63:62

This article addresses research goal (ii) in § 1.3 of Chapter 1. In this study, a Scanning PLIF method is introduced to resolve the three-dimensional HRR field of a flame in the annular combustor. The method was introduced to overcome CTC's limitations, allowing the flame response for the complete multi-flame setup to be captured. This study made use of synthetic PLIF images of a known object. Using this simulated study, experimental Scanning PLIF parameters were evaluated to ensure the parameters used in the experiment would produce high reconstruction accuracy. A key finding shown both with the synthetic images and the experiment itself was the bias in reconstructing the Flame Surface Density field as the laser sheet approached parallel alignment with the flame surface. The error was quantified using the synthetic data, and the error was experimentally overcome by introducing a second independent orthogonal scan direction. Two FSD volumes were reconstructed from these independent scans to produce a final volume where the biasing error was reduced. The final or combined volume helped identify asymmetries of an unforced flame in the annular combustor. Differences in the flame shape were seen at flame positions near the inner and outer annular combustor walls due the stabilising of the outer shear layer of the flame. This study highlighted the effects of the annular confinement on the flame shape and HRR spatial distribution inside the combustor.

Chapter 3

Three dimensional analysis of flame at three positions in standing wave in an annular combustor

This Chapter addresses research goal (iii) in § 1.3 of Chapter 1. The scanning PLIF technique introduced in Article II was used to reconstruct the HRR field for flames subjected to a forced standing mode in the NTNU annular combustor. Three positions were investigated, the pressure antinode, node and a position equidistant to the node and antinode. The analysis of the flame response was performed by evaluating FSD cross planes and three-dimensional FSD reconstructions. Additionally, the amplitude and phase of the HRR oscillations were investigated in three dimensions. Each position produced a unique flame response in the standing wave. The antinode produced symmetric ring-like HRR oscillation structures, with the node producing crescent shaped structures that were out of phase with each other, and the in-between cases produced a mixed response with ring like structures similar to the antinode, but some asymmetric elements.

Article III

Scanning PLIF measurement of azimuthally forced swirling flames in an annular combustor

Dirren Govender and Nicholas A. Worth (2022).

Under consideration for publication in Combustion and Flame.

This article meets aim (iv) in § 1.3 of Chapter 1, in which Scanning PLIF was used to reconstruct the three-dimensional FSD field of two interacting swirling flames in an 18 injector annular combustor subjected to ACW and CW spinning azimuthal forced modes. The aim of this article was to understand the difference between the magnitude of the response when forced in the ACW and CW directions. One of the key results was that the integrated HRR magnitude produced a larger response in the ACW direction confirming previous observations. The FSD volumes helped characterise the flame response and showed how flame structures form based on the annular confinement. The three-dimensional HRR fields revealed that the local response amplitude and phase differed in regions of the flame based on the mode direction. The flame response to ACW modes resulted in a phase difference of $\pi/2$ and an amplitude difference that was twice than the response in the CW case. This result highlights the role of the timing of the azimuthal velocity component on the HRR response which was more significant for the ACW case than the CW case. The 3D volumes were also used to calculate the convective velocity (which is based on or calculated from the convective wavelength) of high HRR oscillations in three dimensions. The analysis in this article showcases the benefits of having access to the 3D FSD providing a rich understanding of the timing of the response in the HRR oscillations for the different spinning directions.

It is not knowledge, but the act of learning, not possession but the act of getting there, which grants the greatest enjoyment'

— *Carl Friedrich Gauss*

5

Conclusions and Outlook

5.1 Concluding remarks

This thesis provides a better understanding of the flame dynamics in an annular combustor when subjected to azimuthal forced modes. This was accomplished by analysis of the HRR response to azimuthal modes based on two three-dimensional techniques. The first analysis involved implementing CTC to understand the response of a single flame in the annular combustor. The motivation behind studying a single flame in Article I is twofold: firstly, it removes the complexity of flame-flame interaction; and secondly, it allows for implementing the CTC method. Article I aimed to investigate the flame dynamics of a flame subjected to ACW and CW spinning modes. It was found by Nygård et al. (2019) that a higher HRR response is produced for the ACW compared to the CW case. However, the simplification of removing flame-flame interaction showed that the flame's response was identical irrespective of the direction of the spinning mode. This was shown by use of the Flame Describing Function. This analysis was extended to show that increasing the equivalence ratio introduces more interaction with the combustor, and rich air-fuel mixtures produce differences in the HRR response. Therefore, wall interaction is important for producing an asymmetric response. The analysis of the flame dynamics was based on CTC in three dimensions for an operating point that matched the conditions of

Nygård et al. (2019). The analysis of the HRR distribution of the unforced flame showed that the flame shape was asymmetric. The forced flames also produced an asymmetric flame shape due to the combination of azimuthal and axial velocity oscillations. The timing of these oscillations produced larger oscillations in HRR on one side of the flame that was incident to the pressure wave. This result was evident at the base of the flame and it was shown that the region of large HRR oscillations slowly rotates for downstream locations. Although the global flame response was the same for both forced cases, this article provided insight into the flame dynamics of these forced responses in three dimensions.

The findings of Article I provided insight into the results of Nygård et al. (2019). However, the lack of flame-flame interaction changes the stabilisation of the flame, and reduced wall interaction. The limitation of using the CTC technique to capture a single flame in the annular combustor motivated the development of an alternative three-dimensional technique. This formed the basis for Article II, in which a Scanning PLIF technique was developed. This article showed that a bias was produced in reconstructing the FSD volume from Scanning PLIF in a single scan. The FSD was underestimated at regions of flame where the laser sheet became close to parallel to the flame surface. A complementary synthetic experiment was presented to aid the development of the technique and the study also quantified the bias error for an ideal flame object. The synthetic experiment was also used to assess Scanning PLIF experimental parameters and the reconstruction method. It was shown that the parameters such as laser sheet thickness and spacing used in the experiment and the developed reconstruction method produced reasonable reconstruction accuracy. The bias in reconstructing the FSD volume was reduced by introducing a dual-scan technique that combined the FSD of two independent orthogonal scan directions. The Scanning PLIF technique was then applied to the 12 burner setup without any forcing. The three-dimensional analysis helped identify the asymmetry of the flame in response to the asymmetric confinement. The three-dimensional HRR distributions showed that the flame was more elongated at regions close to the annular walls in comparison to locations near its neighboring flames creating an asymmetric flame shape. Given that the technique was new, the results of Scanning PLIF were compared to OH* chemiluminescence imaging showing reasonable agreement.

The Scanning PLIF technique was then applied to the 12 burner combustor when subjected to a standing mode. The swirler was removed in this configuration to highlight large-scale structures in the response of the flame without the complexity due to locally rotating flow field and in the absence of flame-flame interactions. The positions investigated were the pressure antinode, node and an intermediate location between the node and antinode. A symmetric response was observed at the pressure antinode, where as the node produced an asymmetric response with oscillations that were out of phase on either side of the flame. This observation was evident along the flame surface that was incident to the pressure wave but minor oscillations were observed close to the annular combustor walls. The flame shape resembled that of the unforced flame in Article II at these locations. The flame response of an intermediate location between the antinode and node was also investigated. The HRR distribution showed that the flame response takes on slight asymmetric ring-like structures with the outer shear layer stabilising for regions of the flame that was not observed for the antinode.

To conclude this thesis, Scanning PLIF was applied to an 18-annular burner configuration and is presented in Article III. Additional burners were introduced to promote flame-flame interaction, and the response to both ACW and CW spinning modes was investigated through the three-dimensional reconstruction of the FSD distribution of two interacting swirled flames. FSD was used to describe the distribution of the HRR response. The flame response in both cases were asymmetric with regions of large HRR oscillations in the inner shear layers. It was shown that the global HRR response of the ACW forced flame was larger than the CW forced flame. The differences in the HRR oscillations between the ACW and CW cases were not clear from the FSD volumes. However, performing a Fourier analysis helped isolate the amplitude and phase of HRR oscillations for each case. Large amplitudes in the HRR response was observed at the base of the flame for both cases. However, spatially integrating thick slices of the amplitude volume showed that the base did not significantly contribute to the global response due to cancellation. In contrast, the flame tips produced a significant contribution to the global response, irrespective of the lower local amplitude in these regions. Tracking the phase of these slices showed that the ACW response phase lagged by $\sim -\pi/2$ for one half of the flame which coincided with the timing of the azimuthal and axial velocity fluctuations. The HRR oscillation amplitude was also greater for this half flame, outlining that the response is both influenced by timing and magnitude. Having access to the three-dimensional phase allowed for the estimation of the convective wavelength for each case. Using the convective wavelength, velocities of disturbances along the flame were calculated that highlighted asymmetries in the flame with large differences observed in the circumferential direction. The application of the three-dimensional measurement allowed for a better understanding in the different global responses when subjected to azimuthal modes.

5.2 Future outlook

This thesis aimed to understand the flame response to standing and spinning azimuthal modes in an annular combustor. The three-dimensional analysis of the HRR oscillation field helped to better understand the flame response. The techniques introduced here were developed to be implemented to the annular rig but can be applied to other applications. Difficulties and drawbacks were outlined in each of the studies. A few recommendations to improve these techniques will be outlined below:

- In the Scanning PLIF method, the reconstruction method relied on flame front tracking to calculate FSD. The FSD volumes were then used to identify how the flame responds to the velocity field. However, the underlying flow field can not be captured using PLIF. Therefore, a recommendation would be to study these flames with tools that can spatially resolve the velocity and vorticity flow field to provide more understanding of the flame dynamics. In the current work the link between vortical structures and flame sheet deformation is conjectured, but resolving the vorticity field would allow this to be linked more definitively.

- In the Scanning PLIF technique, many independent scans were used to reconstruct a single HRR volume. Therefore, it was crucial that each scan produced the same flame response. That is, the mirror positions, flame operating conditions, and, the mode in the combustor be constant. Unfortunately, the control of the mode, as outlined in Chapter 2, was not easily repeatable. This was often due to the temperature dependence on the forced modal state in the combustor. A potential recommendation for improving this aspect with be to introduce cooling water into the outer walls of the combustor to ensure more uniform temperatures during combustion. A consistent forced modal state would produce more repeatable reconstructions.

- In Article II, a biasing was found based on the orientation of the laser sheet and flame. This biasing was overcome by introducing a second scanning direction. However, a potential correction may exist that, if applied correctly, could account for the laser sheet orientation positional error. An alternate way to avoid this bias would be to scan the volume parallel to the flow (90 degrees from the setup in Article II). This idea was not tested. However, the synthetic experiment was used to show that this was the most optimal way to reconstruct the volume. Experimentally this would be challenging, as PLIF imaging would need to be performed from overhead. Chemiluminescence measurements were taken from overhead, as shown in Article II, by placing a mirror in the exhaust gas. However, the mirror would need to be repositioned to ensure sufficient spatial resolution but positioning the mirror closer to the combustor would require extensive cooling. The cooling of the mirror, at the combustion temperature of the conditions of this thesis, was not trivial, and the mirror used often broke. However, this would still be possible with a well-designed mirror cooling system.

- In Article I, the limitations of the CTC method were introduced. The method being a Line-of-Sight method, restricted the reconstruction to a single flame setup. In § 2.7 of Chapter 3, a potential solution is proposed to overcome this limitation. This involved using different fuel types and isolating a single flame in a multi-flame setup using chemiluminescence. The solution has promise however, a thorough investigation is required to produce a successful implementation.

Bibliography

X. Sun, X. Wang, Fundamentals of Aeroacoustics with Applications to Aeropropulsion Systems: Elsevier and Shanghai Jiao Tong University Press Aerospace Series, Elsevier, 2020.

H. S. Gopalakrishnan, A. Gruber, J. Moeck, Computation of Intrinsic Instability and Sound Generation From Autoignition Fronts, Journal of Engineering for Gas Turbines and Power (2022).

T. J. Poinsot, A. C. Trouve, D. P. Veynante, S. M. Candel, E. J. Esposito, Vortex-driven acoustically coupled combustion instabilities, Journal of Fluid Mechanics 177 (1987) 265–292.

T. Indlekofer, The dynamic nature of self-excited azimuthal modes in annular combustors, Doctoral theses, Norwegian University of Science and Technology, 2021.

P. Breeze, Advanced Gas Turbine Design, in: P. Breeze (Ed.), Gas-Turbine Power Generation, Academic Press, 2016, p. iv.

N. Noiray, D. Durox, T. Schuller, S. Candel, A unified framework for nonlinear combustion instability analysis based on the flame describing function, Journal of Fluid Mechanics 615 (2008) 139–167.

R. Balachandran, B. Ayoola, C. Kaminski, A. Dowling, E. Mastorakos, Experimental investigation of the nonlinear response of turbulent premixed flames to imposed inlet velocity oscillations, Combustion and Flame 143 (2005) 37–55.

L. Duffo, Impact of Turbulence and various thermo-acoustic phenomena[Unpublished doctoral dissertation], Ph.D. thesis, Norwegian Institute of Science and Technology, 2023.

H. T. Nygård, G. Ghirardo, N. A. Worth, Azimuthal flame response and symmetry breaking in a forced annular combustor, Combustion and Flame 233 (2021) 111565.

J. O'Connor, T. Lieuwen, Recirculation zone dynamics of a transversely excited swirl flow and flame, Physics of Fluids 24 (2012) 075107.

A. Saurabh, C. O. Paschereit, Combustion instability in a swirl flow combustor with transverse extensions, in: Proceedings of the ASME Turbo Expo, volume 1 B, American Society of Mechanical Engineers Digital Collection, 2013.

J. O'Connor, V. Acharya, T. Lieuwen, Transverse combustion instabilities: Acoustic, fluid mechanic, and flame processes, 2015.

A. Saurabh, C. O. Paschereit, Dynamics of premixed swirl flames under the influence of transverse acoustic fluctuations, Combustion and Flame 182 (2017) 298–312.

N. A. Worth, J. R. Dawson, Tomographic reconstruction of OH* chemiluminescence in two interacting turbulent flames, Measurement Science and Technology 24 (2013).

J.-F. Bourgouin, D. Durox, J. P. Moeck, T. Schuller, S. Candel, Self-Sustained Instabilities in an Annular Combustor Coupled by Azimuthal and Longitudinal Acoustic Modes, in: Volume 1B: Combustion, Fuels and Emissions, ASME, 2013, p. V01BT04A007.

N. A. Worth, J. R. Dawson, Modal dynamics of self-excited azimuthal instabilities in an annular combustion chamber, Combustion and Flame 160 (2013) 2476–2489.

M. Mazur, H. T. Nygård, J. R. Dawson, N. A. Worth, Characteristics of self-excited spinning azimuthal modes in an annular combustor with turbulent premixed bluff-body flames, Proceedings of the Combustion Institute 37 (2019) 5129–5136.

N. A. Worth, J. R. Dawson, Self-excited circumferential instabilities in a model annular gas turbine combustor: Global flame dynamics, Proceedings of the Combustion Institute 34 (2013) 3127–3134.

H. T. Nygård, Experimental Measurement of Flame Describing Functions in an Azimuthally Forced Annular Combustor, Doctoral thesis (phd), Norwegian University of Science and Technology, 2021.

M. I. Najafabadi, L. Egelmeers, B. Somers, N. Deen, B. Johansson, N. Dam, The influence of charge stratification on the spectral signature of partially premixed combustion in a light-duty optical engine, Applied Physics B: Lasers and Optics 123 (2017).

J. Floyd, A. M. Kempf, Computed Tomography of Chemiluminescence (CTC): High resolution and instantaneous 3-D measurements of a Matrix burner, Proceedings of the Combustion Institute 33 (2011) 751–758.

J. R. Dawson, N. A. Worth, Flame dynamics and unsteady heat release rate of self-excited azimuthal modes in an annular combustor, Combustion and Flame 161 (2014) 2565–2578.

A. G. Olabi, M. A. Abdelkareem, Renewable energy and climate change, Renewable and Sustainable Energy Reviews 158 (2022) 112111.

C. Xu, T. A. Kohler, T. M. Lenton, J. C. Svenning, M. Scheffer, Future of the human climate niche, Proceedings of the National Academy of Sciences of the United States of America 117 (2020).

United Nations Environment Programme, Emissions Gap Report 2020, United Nations, 2020 edition, 2021.

P. A. Owusu, S. Asumadu-Sarkodie, A review of renewable energy sources, sustainability issues and climate change mitigation, Cogent Engineering 3 (2016) 1167990.

E. Stefan, B. Talic, Y. Larring, A. Gruber, T. A. Peters, Materials challenges in hydrogen-fuelled gas turbines, International Materials Reviews 67 (2022) 461–486.

L. Han, S. Cai, M. Gao, J. Y. Hasegawa, P. Wang, J. Zhang, L. Shi, D. Zhang, Selective Catalytic Reduction of NOx with NH3 by Using Novel Catalysts: State of the Art and Future Prospects, 2019.

R. K. Srivastava, W. Neuffer, D. Grano, S. Khan, J. E. Staudt, W. Jozewicz, Controlling NO x emission from industrial sources, Environmental Progress 24 (2005) 181–197.

A. F. Sarofim, R. C. Flagan, NOx control for stationary combustion sources, Progress in Energy and Combustion Science 2 (1976) 1–25.

S. Candel, Combustion dynamics and control: Progress and challenges, Proceedings of the Combustion Institute 29 (2002) 1–28.

B. S. Brewster, S. M. Cannon, J. R. Farmer, F. Meng, Modeling of lean premixed combustion in stationary gas turbines, 1999.

N. Docquier, S. Candel, Combustion control and sensors: A review, 2002.

P. Chiesa, G. Lozza, L. Mazzocchi, Using hydrogen as gas turbine fuel, Journal of Engineering for Gas Turbines and Power 127 (2005) 73–80.

V. Lieuwen, Timothy C and Yang, Combustion instabilities in gas turbine engines: operational experience, fundamental mechanisms, and modeling, American Institute of Aeronautics and Astronautics Inc, AIAA, 2005.

T. Poinsot, Prediction and control of combustion instabilities in real engines, Proceedings of the Combustion Institute 36 (2017) 1–28.

Rayleigh, The explanation of certain acoustical phenomena, Nature 18 (1878) 319–321.

T. C. Lieuwen, V. Yang, Combustion Instabilities In Gas Turbine Engines, American Institute of Aeronautics and Astronautics, 2006.

J. C. Oefelein, Y. Vigor, Comprehensive review of liquid-propellant combustion instabilities in f-1 engines, Journal of Propulsion and Power 9 (1993) 657–677.

C. P. Mark, A. Selwyn, Design and analysis of annular combustion chamber of a low bypass turbofan engine in a jet trainer aircraft, Propulsion and Power Research 5 (2016) 97–107.

J. C. Oefelein, Y. Vigor, Comprehensive review of liquid-propellant combustion instabilities in f-1 engines, Journal of Propulsion and Power 9 (1993) 657–677.

Y. Huang, V. Yang, Dynamics and stability of lean-premixed swirl-stabilized combustion, 2009.

P. L. Rijke, LXXI. Notice of a new method of causing a vibration of the air contained in a tube open at both ends, The London, Edinburgh, and Dublin Philosophical Magazine and Journal of Science 17 (1859) 419–422.

R. L. Raun, M. W. Beckstead, J. C. Finlinson, K. P. Brooks, A review of Rijke tubes, Rijke burners and related devices, 1993.

H. J. Merk, Analysis of heat-driven oscillations of gas flows - I. General considerations, Applied Scientific Research, Section A 6 (1957) 317–336.

T. C. Lieuwen, Unsteady combustor physics, volume 9781107015, Cambridge University Press, 2009.

W. Polifke, Modeling and analysis of premixed flame dynamics by means of distributed time delays, 2020.

T. Schuller, T. Poinsot, S. Candel, Dynamics and control of premixed combustion systems based on flame transfer and describing functions, 2020.

L. Boyer, J. Quinard, On the dynamics of anchored flames, Combustion and Flame 82 (1990) 51–65.

B. H. Chao, C. K. Law, Asymptotic theory of flame extinction with surface radiation, Combustion and Flame 92 (1993) 1–24.

P. Clavin, J. Sun, Theory of Acoustic Instabilities of Planar Flames Propagating in Sprays or Particle-Laden Gases, Combustion Science and Technology 78 (1991) 265–288.

N. Darabiha, S. Candel, The influence of the temperature on extinction and ignition limits of strained hydroaen-air diffusion flames, Combustion Science and Technology 86 (1992) 67–85.

M. Fleifil, A. M. Annaswamy, Z. A. Ghoneim, A. F. Ghoniem, Response of a laminar premixed flame to flow oscillations: A kinematic model and thermoacoustic instability results, Combustion and Flame 106 (1996) 487–510.

C. K. Law, Dynamics of stretched flames, Symposium (International) on Combustion 22 (1989) 1381–1402.

K. C. Schadow, E. Gutmark, K. J. Wilson, Active Combustion Control in a Coaxial Dump Combustor, Combustion Science and Technology 81 (1992) 285–300.

P. Wolf, G. Staffelbach, L. Y. Gicquel, J. D. Müller, T. Poinsot, Acoustic and Large Eddy Simulation studies of azimuthal modes in annular combustion chambers, Combustion and Flame 159 (2012) 3398–3413.

I. Hernández, G. Staffelbach, T. Poinsot, J. C. Román Casado, J. B. Kok, LES and acoustic analysis of thermo-acoustic instabilities in a partially premixed model combustor, 2013.

Z. X. Chen, I. Langella, N. Swaminathan, M. Stöhr, W. Meier, H. Kolla, Large Eddy Simulation of a dual swirl gas turbine combustor: Flame/flow structures and stabilisation under thermoacoustically stable and unstable conditions, Combustion and Flame 203 (2019) 279–300.

E. Courtine, L. Selle, T. Poinsot, DNS of Intrinsic ThermoAcoustic modes in laminar premixed flames, Combustion and Flame 162 (2015) 4331–4341.

K. Kashinath, S. Hemchandra, M. P. Juniper, Nonlinear thermoacoustics of ducted premixed flames: The influence of perturbation convection speed, Combustion and Flame 160 (2013) 2856–2865.

S. Hemchandra, Premixed flame response to equivalence ratio fluctuations: Comparison between reduced order modeling and detailed computations, Combustion and Flame 159 (2012) 3530–3543.

S. Wiseman, M. Rieth, A. Gruber, J. R. Dawson, J. H. Chen, A comparison of the blow-out behavior of turbulent premixed ammonia/hydrogen/nitrogen-air and methane–air flames, Proceedings of the Combustion Institute 38 (2021) 2869–2876.

S. Ducruix, D. Durox, S. Candel, Theoretical and experimental determinations of the transfer function of a laminar premixed flame, Proceedings of the Combustion Institute 28 (2000) 765–773.

K. Kunze, C. Hirsch, T. Sattelmayer, Transfer function measurements on a swirl stabilized premix burner in an annular combustion chamber, in: Proceedings of the ASME Turbo Expo 2004, volume 1, American Society of Mechanical Engineers Digital Collection, 2004, pp. 21–30.

C. Külsheimer, H. Büchner, Combustion dynamics of turbulent swirling flames, Combustion and Flame 131 (2002) 70–84.

T. Schuller, D. Durox, S. Candel, Self-induced combustion oscillations of laminar premixed flames stabilized on annular burners, Combustion and Flame 135 (2003) 525–537.

B. Schuermans, V. Bellucci, C. O. Paschereit, Thermoacoustic modeling and control of multi burner combustion systems, in: American Society of Mechanical Engineers, International Gas Turbine Institute, Turbo Expo (Publication) IGTI, volume 2, pp. 509–519.

C. J. Lawn, R. W. Schefer, Scaling of premixed turbulent flames in the corrugated regime, Combustion and Flame 146 (2006) 180–199.

P. Palies, D. Durox, T. Schuller, S. Candel, The combined dynamics of swirler and turbulent premixed swirling flames, Combustion and Flame 157 (2010) 1698–1717.

C. J. Lawn, W. Polifke, A model for the thermoacoustic response of a premixed swirl burner, Part II: The flame response, Combustion Science and Technology 176 (2004) 1359–1390.

C. Hirsch, D. Fanaca, P. Reddy, W. Polifke, T. Sattelmayer, Influence of the swirler design on the flame transfer function of premixed flames, in: Proceedings of the ASME Turbo Expo, volume 2, American Society of Mechanical Engineers Digital Collection, 2005, pp. 151–160.

P. R. Alemela, D. Fanaca, C. Hirsch, T. Sattelmayer, B. Schuermans, Determination and Scaling of Thermo Acoustic Characteristics of Premixed Flames, International Journal of Spray and Combustion Dynamics 2 (2010) 169–198.

K. T. Kim, J. G. Lee, B. D. Quay, D. A. Santavicca, Spatially distributed flame transfer functions for predicting combustion dynamics in lean premixed gas turbine combustors, Combustion and Flame 157 (2010) 1718–1730.

A. Cuquel, D. Durox, T. Schuller, Scaling the flame transfer function of confined premixed conical flames, Proceedings of the Combustion Institute 34 (2013) 1007–1014.

E. Æsøy, J. G. Aguilar, S. Wiseman, M. R. Bothien, N. A. Worth, J. R. Dawson, Scaling and prediction of transfer functions in lean premixed H2/CH4-flames, Combustion and Flame 215 (2020) 269–282.

H. T. Nygård, N. A. Worth, Flame Transfer Functions and Dynamics of a Closely Confined Premixed Bluff Body Stabilized Flame With Swirl, Journal of Engineering for Gas Turbines and Power 143 (2021).

C. A. Armitage, R. Balachandran, E. Mastorakos, R. S. Cant, Investigation of the nonlinear response of turbulent premixed flames to imposed inlet velocity oscillations, Combustion and Flame 146 (2006) 419–436.

E. Æsøy, J. G. Aguilar, S. Wiseman, M. R. Bothien, N. A. Worth, J. R. Dawson, Scaling and prediction of transfer functions in lean premixed H2/CH4-flames, Combustion and Flame 215 (2020) 269–282.

S. R. Stow, A. P. Dowling, Low-order modelling of thermoacoustic limit cycles, in: Proceedings of the ASME Turbo Expo 2004, volume 1, American Society of Mechanical Engineers Digital Collection, 2004, pp. 775–786.

A. P. Dowling, Nonlinear self-excited oscillations of a ducted flame, Journal of Fluid Mechanics 346 (1997) 271–290.

V. K. Rani, S. L. Rani, Development of a comprehensive flame transfer function and its application to predict combustion instabilities in a dump combustor, Combustion Science and Technology 190 (2018) 1313–1353.

S. R. Stow, A. P. Dowling, Thermoacoustic oscillations in an annular combustor, in: Proceedings of the ASME Turbo Expo, volume 2, American Society of Mechanical Engineers Digital Collection, 2001.

W. Polifke, C. Lawn, On the low-frequency limit of flame transfer functions, Combustion and Flame 151 (2007) 437–451.

C. J. Lawn, W. Polifke, A model for the thermoacoustic response of a premixed swirl burner, Part II: The flame response, Combustion Science and Technology 176 (2004) 1359–1390.

P. H. Paul, H. N. Najm, Planar laser-induced fluorescence imaging of flame heat release rate, in: Symposium (International) on Combustion, volume 27, pp. 43–50.

S. Candel, D. Durox, T. Schuller, J. F. Bourgouin, J. P. Moeck, Dynamics of swirling flames, Annual Review of Fluid Mechanics 46 (2014) 147–173.

H. T. Nygård, M. Mazur, J. R. Dawson, N. A. Worth, Flame dynamics of azimuthal forced spinning and standing modes in an annular combustor, Proceedings of the Combustion Institute 37 (2019) 5113–5120.

W. Krebs, P. Flohr, B. Prade, S. Hoffmann, Thermoacoustic stability chart for high-intensity gas turbine combustion systems, Combustion Science and Technology 174 (2002) 99–128.

M. Wolf, B. Lüthi, M. Holzner, D. Krug, W. Kinzelbach, A. Tsinober, Investigations on the local entrainment velocity in a turbulent jet, Physics of Fluids 24 (2012).

G. Vignat, D. Durox, A. Renaud, S. Candel, High amplitude combustion instabilities in an annular combustor inducing pressure field deformation and flame blow off, Journal of Engineering for Gas Turbines and Power 142 (2020).

G. Ghirardo, M. R. Bothien, Quaternion structure of azimuthal instabilities, Physical Review Fluids 3 (2018) 113202.

J. O'Connor, N. A. Worth, J. R. Dawson, Flame and flow dynamics of a self-excited, standing wave circumferential instability in a model annular gas turbine combustor, in: Proceedings of the ASME Turbo Expo, volume 1 B.

F. Lespinasse, F. Baillot, T. Boushaki, Responses of V-flames placed in an HF transverse acoustic field from a velocity to pressure antinode, 2013.

M. Hauser, M. Lorenz, T. Sattelmayer, Influence of transversal acoustic excitation of the burner approach flow on the flame structure, in: Proceedings of the ASME Turbo Expo, volume 2, American Society of Mechanical Engineers Digital Collection, 2010, pp. 803–812.

J. O'Connor, V. Acharya, T. Lieuwen, Transverse combustion instabilities: Acoustic, fluid mechanic, and flame processes, 2015.

J. O'Connor, T. Lieuwen, Disturbance field characteristics of a transversely excited burner, Combustion Science and Technology 183 (2011) 427–443.

D. Davis, B. Chehroudi, The effects of pressure and acoustic field on a cryogenic coaxial jet, in: AIAA Paper, pp. 10741–10759.

M. Malanoski, M. Aguilar, D. H. Shin, T. Lieuwen, Flame leading edge and flow dynamics in a swirling, lifted flame, Combustion Science and Technology 186 (2014) 1816–1843.

J. O'Connor, T. Lieuwen, Further characterization of the disturbance field in a transversely excited swirl-stabilized flame, in: Proceedings of the ASME Turbo Expo, volume 2, American Society of Mechanical Engineers Digital Collection, 2011, pp. 215–226.

V. Acharya, Shreekrishna, D. H. Shin, T. Lieuwen, Swirl effects on harmonically excited, premixed flame kinematics, Combustion and Flame 159 (2012) 1139–1150.

T. Steinbacher, W. Polifke, Convective Velocity Perturbations and Excess Gain in Flame Response as a Result of Flame-Flow Feedback, Fluids 7 (2022) 61.

A. Saurabh, C. O. Paschereit, Premixed Flame Dynamics in Response to Two-Dimensional Acoustic Forcing, Combustion Science and Technology 191 (2019) 1184–1200.

V. S. Acharya, T. C. Lieuwen, Premixed flame response to high-frequency transverse acoustic modes: Mean flame asymmetry effects, in: AIAA Scitech 2019 Forum, American Institute of Aeronautics and Astronautics Inc, AIAA, 2019.

J. O'Connor, S. Natarajan, M. Malanoski, D. Noble, T. Lieuwen, Response of an annular burner nozzle to transverse acoustic excitation, in: 48th AIAA Aerospace Sciences Meeting Including the New Horizons Forum and Aerospace Exposition, American Institute of Aeronautics and Astronautics Inc., 2010, pp. 2010–1151.

A. Orthmann, C. C. Hantschk, P. Zangl, S. Gleis, D. Vortmeyer, Application of active combustion instability control to a heavy duty gas turbine, Journal of Engineering for Gas Turbines and Power 120 (1998) 721–726.

G. Vignat, D. Durox, T. Schuller, S. Candel, Combustion Dynamics of Annular Systems, Combustion Science and Technology 192 (2020) 1358–1388.

N. Noiray, B. Schuermans, On the dynamic nature of azimuthal thermoacoustic modes in annular gas turbine combustion chambers, Proceedings of the Royal Society A: Mathematical, Physical and Engineering Sciences 469 (2013).

G. Ghirardo, H. T. Nygård, A. Cuquel, N. A. Worth, Symmetry breaking modelling for azimuthal combustion dynamics, in: Proceedings of the Combustion Institute, volume 38, Elsevier Ltd, 2021, pp. 5953–5962.

M. R. Bothien, N. Noiray, B. Schuermans, Analysis of Azimuthal Thermoacoustic Modes in Annular Gas Turbine Combustion Chambers, Journal of Engineering for Gas Turbines and Power 137 (2015).

B. Schuermans, C. O. Paschereit, P. Monkewitz, Non-linear combustion instabilities in annular gas-turbine combustors, in: Collection of Technical Papers - 44th AIAA Aerospace Sciences Meeting, volume 9, pp. 6634–6645.

N. A. Worth, J. R. Dawson, Effect of equivalence ratio on the modal dynamics of azimuthal combustion instabilities, Proceedings of the Combustion Institute 36 (2017) 3743–3751.

K. Prieur, D. Durox, J. Beaunier, T. Schuller, S. Candel, Ignition dynamics in an annular combustor for liquid spray and premixed gaseous injection, Proceedings of the Combustion Institute 36 (2017) 3717–3724.

T. Indlekofer, B. Ahn, Y. H. Kwah, S. Wiseman, M. Mazur, J. R. Dawson, N. A. Worth, The effect of hydrogen addition on the amplitude and harmonic response of azimuthal instabilities in a pressurized annular combustor, Combustion and Flame 228 (2021) 375–387.

A. Faure-Beaulieu, T. Indlekofer, J. R. Dawson, N. Noiray, Experiments and low-order modelling of intermittent transitions between clockwise and anticlockwise spinning thermoacoustic modes in annular combustors, in: Proceedings of the Combustion Institute, volume 38, Elsevier, 2021, pp. 5943–5951.

J. F. Bourgouin, D. Durox, J. P. Moeck, T. Schuller, S. Candel, Characterization and modeling of a spinning thermoacoustic instability in an annular combustor equipped with multiple matrix injectors, Journal of Engineering for Gas Turbines and Power 137 (2015).

J. G. Aguilar, J. R. Dawson, T. Schuller, D. Durox, K. Prieur, S. Candel, Locking of azimuthal modes by breaking the symmetry in annular combustors, Combustion and Flame 234 (2021) 111639.

J. R. Dawson, N. A. Worth, The effect of baffles on self-excited azimuthal modes in an annular combustor, Proceedings of the Combustion Institute 35 (2015) 3283–3290.

M. Mazur, H. T. Nygård, J. Dawson, N. Worth, Experimental Study of Damper Position on Instabilities in an Annular Combustor, American Society of Mechanical Engineers Digital Collection, 2018.

J. P. Moeck, M. Paul, C. O. Paschereit, Thermoacoustic instabilities in an annular Rijke tube, in: Proceedings of the ASME Turbo Expo, volume 2, American Society of Mechanical Engineers Digital Collection, 2010, pp. 1219–1232.

S. C. Humbert, J. P. Moeck, A. Orchini, C. O. Paschereit, Effect of an azimuthal mean flow on the structure and stability of thermoacoustic modes in an annular combustor model with electroacoustic feedback, Journal of Engineering for Gas Turbines and Power 143 (2021).

Y. Fu, J. Cai, S. M. Jeng, H. Mongia, Confinement effects on the swirling flow of a counter-rotating swirl cup, in: Proceedings of the ASME Turbo Expo, volume 2, American Society of Mechanical Engineers Digital Collection, 2005, pp. 469–472.

J. Daou, M. Matalon, Influence of conductive heat-losses on the propagation of premixed flames in channels, Combustion and Flame 128 (2002) 321–339.

A. C. McIntosh, J. F. Clarke, Second Order Theory of Unsteady Burner-Anchored Flames with Arbitrary Lewis Number, Combustion Science and Technology 38 (1984) 161–196.

A. C. Mcintosh, Combustion-Acoustic Interaction of a Flat Flame Burner System Enclosed Within an Open Tube, Combustion Science and Technology 54 (1987) 217–236.

K. R. Schreel, R. Rook, L. P. De Goey, The acoustic response of burner-stabilized premixed flat flames, Proceedings of the Combustion Institute 29 (2002) 115–122.

K. S. Kedia, H. M. Altay, A. F. Ghoniem, Impact of flame-wall interaction on premixed flame dynamics and transfer function characteristics, Proceedings of the Combustion Institute 33 (2011) 1113–1120.

J. F. Driscoll, Turbulent premixed combustion: Flamelet structure and its effect on turbulent burning velocities, 2008.

A. Tyagi, I. Boxx, S. Peluso, J. O'connor, Statistics of local flame-flame interactions in flame interaction zones of two v-flames, in: AIAA Scitech 2019 Forum, American Institute of Aeronautics and Astronautics Inc, AIAA, 2019.

D. Fanaca, P. R. Alemela, F. Ettner, C. Hirsch, T. Sattelmayer, B. Schuermans, Determination and comparison of the dynamic characteristics of a perfectly premixed flame in both single and annular combustion chambers, in: Proceedings of the ASME Turbo Expo, volume 3, American Society of Mechanical Engineers Digital Collection, 2008, pp. 565–573.

D. Fanaca, P. R. Alemela, C. Hirsch, T. Sattelmayer, Comparison of the flow field of a swirl stabilized premixed burner in an annular and a single burner combustion chamber, Journal of Engineering for Gas Turbines and Power 132 (2010).

N. A. Worth, J. R. Dawson, Cinematographic OH-PLIF measurements of two interacting turbulent premixed flames with and without acoustic forcing, Combustion and Flame 159 (2012) 1109–1126.

J. Samarasinghe, S. Peluso, M. Szedlmayer, A. De Rosa, B. Quay, D. Santavicca, 3-D chemiluminescence imaging of unforced and forced swirl-stabilized flames in a lean premixed multi-nozzle can combustor, in: Proceedings of the ASME Turbo Expo, volume 1 B, American Society of Mechanical Engineers Digital Collection, 2013.

J. Samarasinghe, W. Culler, B. D. Quay, D. A. Santavicca, J. O'connor, The effect of fuel staging on the structure and instability characteristics of swirl-stabilized flames in a lean premixed multi-nozzle can combustor, in: Proceedings of the ASME Turbo Expo, volume 4A-2017, American Society of Mechanical Engineers (ASME), 2017.

R. Rajasegar, J. Choi, B. McGann, A. Oldani, T. Lee, S. D. Hammack, C. D. Carter, J. Yoo, Mesoscale burner array performance analysis, Combustion and Flame 199 (2019) 324–337.

F. Bloch, Über die Quantenmechanik der Elektronen in Kristallgittern, Zeitschrift für Physik 52 (1929) 555–600.

C. K. Law, Combustion physics, Cambridge University Press, Cambridge, 2006.

T. Lu, C. K. Law, Toward accommodating realistic fuel chemistry in large-scale computations, 2009.

H. N. Najm, P. H. Paul, C. J. Mueller, P. S. Wyckoff, On the Adequacy of Certain Experimental Observables as Measurements of Flame Burning Rate, Combustion and Flame 113 (1998) 312–332.

M. Ferrarotti, R. Amaduzzi, D. Bascherini, C. Galletti, A. Parente, Heat Release Rate Markers for the Adelaide Jet in Hot Coflow Flame, Frontiers in Mechanical Engineering 6 (2020) 5.

Z. M. Nikolaou, N. Swaminathan, Heat release rate markers for premixed combustion, Combustion and Flame 161 (2014) 3073–3084.

C. M. Vagelopoulos, J. H. Frank, An experimental and numerical study on the adequacy of CH as a flame marker in premixed methane flames, Proceedings of the Combustion Institute 30 (2005) 241–249.

I. A. Mulla, A. Dowlut, T. Hussain, Z. M. Nikolaou, S. R. Chakravarthy, N. Swaminathan, R. Balachandran, Heat release rate estimation in laminar premixed flames using laser-induced fluorescence of CH2O and H-atom, Combustion and Flame 165 (2016) 373–383.

Y. Minamoto, N. Swaminathan, Scalar gradient behaviour in MILD combustion, Combustion and Flame 161 (2014) 1063–1075.

S. Böckle, J. Kazenwadel, T. Kunzelmann, D. I. Shin, C. Schulz, J. Wolfrum, Simultaneous single-shot laser-based imaging of Formaldehyde, OH, and temperature in turbulent flames, Proceedings of the Combustion Institute 28 (2000) 279–286.

B. O. Ayoola, R. Balachandran, J. H. Frank, E. Mastorakos, C. F. Kaminski, Spatially resolved heat release rate measurements in turbulent premixed flames, Combustion and Flame 144 (2006) 1–16.

R. L. Gordon, A. R. Masri, E. Mastorakos, Heat release rate as represented by [OH] × [CH2O] and its role in autoignition, Combustion Theory and Modelling 13 (2009) 645–670.

S. B. Dworkin, A. M. Schaffen, B. C. Connelly, M. B. Long, M. D. Smooke, M. A. Puccio, B. McAndrew, J. H. Miller, Measurements and calculations of formaldehyde concentrations in a methane/N2/air, non-premixed flame: Implications for heat release rate, Proceedings of the Combustion Institute 32 I (2009) 1311–1318.

B. Ayoola, G. Hartung, C. A. Armitage, J. Hult, R. S. Cant, C. F. Kaminski, Temperature response of turbulent premixed flames to inlet velocity oscillations, Experiments in Fluids 46 (2009a) 27–41.

B. Ayoola, G. Hartung, C. A. Armitage, J. Hult, R. S. Cant, C. F. Kaminski, Temperature response of turbulent premixed flames to inlet velocity oscillations, Experiments in Fluids 46 (2009b) 27–41.

M. Röder, T. Dreier, C. Schulz, Simultaneous measurement of localized heat-release with OH/CH 2O-LIF imaging and spatially integrated OH-chemiluminescence in turbulent swirl flames, Proceedings of the Combustion Institute 34 (2013) 3549–3556.

K. N. Gabet, R. A. Patton, N. Jiang, W. R. Lempert, J. A. Sutton, High-speed CH 2O PLIF imaging in turbulent flames using a pulse-burst laser system, in: Applied Physics B: Lasers and Optics, volume 106, Springer, 2012, pp. 569–575.

N. A. Doan, N. Swaminathan, Analysis of Markers for Combustion Mode and Heat Release in MILD Combustion Using DNS Data, Combustion Science and Technology 191 (2019) 1059–1078.

A. G. Gaydon, The Spectroscopy of Flames, Springer Netherlands, Dordrecht, 1 edition, 1974.

C. Schulz, A. Dreizler, V. Ebert, J. Wolfrum, Combustion diagnostics, in: Springer Handbooks, Springer, 2007, pp. 1241–1315.

D. Alviso, M. Mendieta, J. Molina, J. C. Rolón, Flame imaging reconstruction method using high resolution spectral data of OH*, CH* and C2* radicals, International Journal of Thermal Sciences 121 (2017) 228–236.

L. C. Haber, U. Vandsburger, A global reaction model for OH* Chemiluminescence applied to a laminar flat-flame burner, Combustion Science and Technology 175 (2003) 1859–1891.

Y. Liu, J. Tan, M. Wan, L. Zhang, X. Yao, Quantitative Measurement of OH* and CH* Chemiluminescence in Jet Diffusion Flames, ACS Omega 5 (2020) 15922–15930.

J. Kojima, Y. Ikeda, T. Nakajima, Basic aspects of OH(A), CH(A), and C2(d) chemiluminescence in the reaction zone of laminar methane-air premixed flames, Combustion and Flame 140 (2005) 34–45.

M. Shim, K. Noh, W. Yoon, Flame structure of methane/oxygen shear coaxial jet with velocity ratio using high-speed imaging and OH* CH* chemiluminescence, Acta Astronautica 147 (2018) 127–132.

L. He, Q. Guo, Y. Gong, F. Wang, G. Yu, Investigation of OH* chemiluminescence and heat release in laminar methane–oxygen co-flow diffusion flames, Combustion and Flame 201 (2019) 12–22.

Y. Hardalupas, M. Orain, C. S. Panoutsos, A. M. Taylor, J. Olofsson, H. Seyfried, M. Richter, J. Hult, M. Aldén, F. Hermann, J. Klingmann, Chemiluminescence sensor for local equivalence ratio of reacting mixtures of fuel and air (FLAMESEEK), in: Applied Thermal Engineering, volume 24, Pergamon, 2004, pp. 1619–1632.

F. M. Quintino, T. P. Trindade, E. C. Fernandes, Biogas combustion: Chemiluminescence fingerprint, Fuel 231 (2018) 328–340.

Y. Hardalupas, M. Orain, Local measurements of the time-dependent heat release rate and equivalence ratio using chemiluminescent emission from a flame, Combustion and Flame 139 (2004) 188–207.

C. S. Panoutsos, Y. Hardalupas, A. M. Taylor, Numerical evaluation of equivalence ratio measurement using OH* and CH* chemiluminescence in premixed and non-premixed methane-air flames, Combustion and Flame 156 (2009) 273–291.

Y. Hardalupas, C. S. Panoutsos, A. M. Taylor, Spatial resolution of a chemiluminescence sensor for local heat-release rate and equivalence ratio measurements in a model gas turbine combustor, Experiments in Fluids 49 (2010) 883–909.

A. Hossain, Y. Nakamura, A numerical study on the ability to predict the heat release rate using CH* chemiluminescence in non-sooting counterflow diffusion flames, Combustion and Flame 161 (2014) 162–172.

L. Lv, J. Tan, J. Zhu, Visualization of the heat release zone of highly turbulent premixed jet flames, Acta Astronautica 139 (2017) 258–265.

H. Liu, B. Sun, W. Cai, kHz-rate volumetric flame imaging using a single camera, Optics Communications 437 (2019) 33–43.

Y. Hu, J. Tan, L. Lv, X. Li, Investigations on quantitative measurement of heat release rate using chemiluminescence in premixed methane-air flames, Acta Astronautica 164 (2019) 277–286.

M. Lauer, T. Sattelmayer, On the Adequacy of Chemiluminescence as a Measure for Heat Release in Turbulent Flames With Mixture Gradients, Journal of Engineering for Gas Turbines and Power 132 (2010).

M. M. Tripathi, S. R. Krishnan, K. K. Srinivasan, F. Y. Yueh, J. P. Singh, Chemiluminescence-based multivariate sensing of local equivalence ratios in premixed atmospheric methane-air flames, Fuel 93 (2012) 684–691.

V. N. Nori, J. M. Scitzman, CH* chemiluminescence modeling for combustion diagnostics, Proceedings of the Combustion Institute 32 I (2009) 895–903.

Y. Ikeda, J. Kojima, H. Hashimoto, Local chemiluminescence spectra measurements in a high-pressure laminar methane/air premixed flame, Proceedings of the Combustion Institute 29 (2002) 1495–1501.

J. G. Lee, D. A. Santavicca, Experimental Diagnostics for the Study of Combustion Instabilities in Lean Premixed Combustors, Journal of Propulsion and Power 19 (2003) 735–750.

J. Kojima, Y. Ikeda, T. Nakajima, Spatially resolved measurement of OH*, CH*, and C* chemiluminescence in the reaction zone of laminar methane/air premixed flames, Proceedings of the Combustion Institute 28 (2000) 1757–1764.

L. Ma, Y. Wu, W. Xu, S. D. Hammack, T. Lee, C. D. Carter, Comparison of 2D and 3D flame topography measured by planar laser-induced fluorescence and tomographic chemiluminescence, Applied Optics 55 (2016) 5310.

W. Xu, A. J. Wickersham, Y. Wu, F. He, L. Ma, 3D flame topography obtained by tomographic chemiluminescence with direct comparison to planar Mie scattering measurements, Applied Optics 54 (2015) 2174.

L. Ma, Q. Lei, J. Ikeda, W. Xu, Y. Wu, C. D. Carter, Single-shot 3D flame diagnostic based on volumetric laser induced fluorescence (VLIF), Proceedings of the Combustion Institute 36 (2017) 4575–4583.

T. D. Upton, D. D. Verhoeven, D. E. Hudgins, High-resolution computed tomography of a turbulent reacting flow, Experiments in Fluids 50 (2011) 125–134.

W. Cai, X. Li, F. Li, L. Ma, Numerical and experimental validation of a three-dimensional combustion diagnostic based on tomographic chemiluminescence, Optics Express 21 (2013) 7050.

A. Dreizler, A. Johchi, B. Böhm, J. Pareja, T. Li, A study of the spatial and temporal evolution of auto-ignition kernels using time-resolved tomographic OH-LIF, Proceedings of the Combustion Institute 37 (2018) 1321–1328.

Y. Ishino, N. Ohiwa, Three-dimensional computerized tomographic reconstruction of instantaneous distribution of chemiluminescence of a turbulent premixed flame, JSME International Journal, Series B: Fluids and Thermal Engineering 48 (2005) 34–40.

G. T. Herman, A. Lent, Iterative reconstruction algorithms, Computers in Biology and Medicine 6 (1976) 273–294.

W. R. Madych, Radon's inversion formulas, Transactions of the American Mathematical Society 356 (2004) 4475–4491.

C. L. Byrne, Accelerating the EMML algorithm and related iterative algorithms by rescaled block-iterative methods, IEEE Transactions on Image Processing 7 (1998) 100–109.

D. E. Goldberg, J. H. Holland, Genetic Algorithms and Machine Learning, 1988.

C. T. Foo, A. Unterberger, F. J. W. A. Martins, M. M. Prenting, C. Schulz, K. Mohri, Investigating spray flames for nanoparticle synthesis via tomographic imaging using multi-simultaneous measurements (TIMes) of emission, Optics Express 30 (2022) 15524.

A. Unterberger, K. Mohri, Evolutionary background-oriented schlieren tomography with self-adaptive parameter heuristics, Optics Express 30 (2022) 8592.

K. D. Kihm, D. P. Lyons, Optical tomography using a genetic algorithm, Optics Letters 21 (1996) 1327.

J. Wang, Y. Song, Z.-h. Li, A. Kempf, A.-z. He, Multi-directional 3D flame chemiluminescence tomography based on lens imaging, Optics Letters 40 (2015) 1231.

D. Verhoeven, Limited-data computed tomography algorithms for the physical sciences, Applied Optics 32 (1993) 3736.

S. M. Wiseman, M. J. Brear, R. L. Gordon, I. Marusic, Measurements from flame chemiluminescence tomography of forced laminar premixed propane flames, Combustion and Flame 183 (2017) 1–14.

A. Unterberger, M. Röder, A. Giese, A. Al-Halbouni, A. Kempf, K. Mohri, 3D instantaneous reconstruction of turbulent industrial flames using computed tomography of chemiluminescence (CTC), Journal of Combustion 2018 (2018).

T. R. Meyer, B. R. Halls, N. Jiang, M. N. Slipchenko, S. Roy, J. R. Gord, High-speed, three-dimensional tomographic laser-induced incandescence imaging of soot volume fraction in turbulent flames, Optics Express 24 (2016) 29547.

G. Gilabert, G. Lu, Y. Yan, Three-dimensional tomographic reconstruction of the luminosity distribution of a combustion flame, IEEE Transactions on Instrumentation and Measurement 56 (2007) 1300–1306.

Y. Ishino, K. Takeuchi, S. Shiga, N. Ohiwa, Non-scanning 3D-CT measurement with 40-lens tracking camera for turbulent propane/air rich-premixed flame, in: 6th International Energy Conversion Engineering Conference, IECEC, American Institute of Aeronautics and Astronautics Inc., 2008.

T. Yu, Q. Wang, C. Ruan, F. Chen, W. Cai, X. Lu, M. Klein, A quantitative evaluation method of 3D flame curvature from reconstructed flame structure, Experiments in Fluids 61 (2020) 61–66.

M. M. Moinul Hossain, G. Lu, Y. Yan, Optical fiber imaging based tomographic reconstruction of burner flames, in: IEEE Transactions on Instrumentation and Measurement, volume 61, pp. 1417–1425.

E. J. Mohamad, R. A. Rahim, S. Ibrahim, S. Sulaiman, M. S. Manaf, Flame imaging using laser-based transmission tomography, Sensors and Actuators, A: Physical 127 (2006) 332–339.

G. E. Elsinga, F. Scarano, B. Wieneke, B. W. van Oudheusden, Tomographic particle image velocimetry, Experiments in Fluids 41 (2006) 933–947.

B. Wieneke, S. Taylor, Fat-sheet PIV with computation of full 3D-strain tensor using tomographic reconstruction, 13Th International Symposium on Applications of Laser Techniques To Fluid Mechanics 13 (2006) 26–29.

S. J. Grauer, K. Mohri, T. Yu, H. Liu, W. Cai, Volumetric emission tomography for combustion processes, 2023.

J. W. Daily, Laser induced fluorescence spectroscopy in flames, Progress in Energy and Combustion Science 23 (1997) 133–199.

S. A. Filatyev, J. F. Driscoll, C. D. Carter, J. M. Donbar, Measured properties of turbulent premixed flames for model assessment, including burning velocities, stretch rates, and surface densities, Combustion and Flame 141 (2005) 1–21.

J. Hult, S. Gashi, N. Chakraborty, M. Klein, K. W. Jenkins, S. Cant, C. F. Kaminski, Measurement of flame surface density for turbulent premixed flames using PLIF and DNS, Proceedings of the Combustion Institute 31 I (2007) 1319–1326.

M. Ryan, M. Gruber, C. Carter, T. Mathur, Planar laser-induced fluorescence imaging of OH in a supersonic combustor fueled with ethylene and methane, Proceedings of the Combustion Institute 32 II (2009) 2429–2436.

M. Tanahashi, S. Murakami, G. M. Choi, Y. Fukuchi, T. Miyauchi, Simultaneous CH-OH PLIF and stereoscopic PIV measurements of turbulent premixed flames, Proceedings of the Combustion Institute 30 (2005) 1665–1672.

Y. Zhao, C. Tong, L. Ma, Kinetics of I2 and HI photodissociation with implications in flame diagnostics, Applied Physics B: Lasers and Optics 104 (2011) 689–698.

Z. Yan, T. Chenning, L. Ma, Demonstration of a new laser diagnostic based on photodissociation spectroscopy for imaging mixture fraction in a non-premixed jet flame, Applied Spectroscopy 64 (2010) 377–383.

M. M. Koochesfahani, P. E. Dimotakis, Laser-induced fluorescence measurements of mixed fluid concentration in a liquid plane shear layer, AIAA Journal 23 (1985) 1700–1707.

F. Q. Zhao, M. Taketomi, K. Nishida, H. Hiroyasu, PLIF measurements of the cyclic variation of mixture concentration in a SI engine, in: SAE Technical Papers, SAE International, 1994.

T. L. Medford, P. M. Danehy, S. B. Jones, B. F. Bathel, J. A. Inman, N. Jiang, M. Webster, W. Lempert, J. Miller, T. Meyer, Stereoscopic planar laser-induced fluorescence imaging at 500 kHz, in: 49th AIAA Aerospace Sciences Meeting Including the New Horizons Forum and Aerospace Exposition.

J. C. McDaniel, B. Hiller, R. K. Hanson, Simultaneous multiple-point velocity measurements using laser-induced iodine fluorescence, Optics Letters 8 (1983) 51.

J. M. Seitzman, G. Kychakoff, R. K. Hanson, Instantaneous temperature field measurements using planar laser-induced fluorescence, Optics Letters 10 (1985) 439.

A. C. Eckbreth, Laser Diagnostics for Temperature and Species in Unsteady Combustion, in: Unsteady Combustion, Springer, Dordrecht, 1996, pp. 393–410.

J. P. Crimaldi, Planar laser induced fluorescence in aqueous flows, Experiments in Fluids 44 (2008) 851–863.

R. Knikker, D. Veynante, C. Meneveau, A priori testing of a similarity model for large eddy simulations of turbulent premixed combustion, Proceedings of the Combustion Institute 29 (2002) 2105–2111.

F. Halter, C. Chauveau, I. Gökalp, D. Veynante, Analysis of flame surface density measurements in turbulent premixed combustion, Combustion and Flame 156 (2009) 657–664.

M. Zhang, J. Wang, W. Jin, Z. Huang, H. Kobayashi, L. Ma, Estimation of 3D flame surface density and global fuel consumption rate from 2D PLIF images of turbulent premixed flame, Combustion and Flame 162 (2015) 2087–2097.

S. M. Candel, T. J. Poinsot, Flame Stretch and the Balance Equation for the Flame Area, Combustion Science and Technology 70 (1990) 1–15.

K. N. C. Bray, Studies of the turbulent burning velocity, Proceedings of the Royal Society of London. Series A: Mathematical and Physical Sciences 431 (1990) 315–335.

M. Wirth, N. Peters, Turbulent premixed combustion: A flamelet formulation and spectral analysis in theory and IC-engine experiments, Symposium (International) on Combustion 24 (1992) 493–501.

F. C. Gouldin, K. N. Bray, J. Y. Chen, Chemical closure model for fractal flamelets, Combustion and Flame 77 (1989) 241–259.

S. B. Pope, The evolution of surfaces in turbulence, International Journal of Engineering Science 26 (1988) 445–469.

D. Veynante, J. M. Duclos, J. Piana, Experimental analysis of flamelet models for premixed turbulent combustion, Symposium (International) on Combustion 25 (1994) 1249–1256.

J. M. Donbar, J. F. Driscoll, C. D. Carter, Reaction zone structure in turbulent nonpremixed jet flames - From CH-OH PLIF images, Combustion and Flame 122 (2000) 1–19.

G. G. Lee, K. Y. Huh, H. Kobayashi, Measurement and analysis of flame surface density for turbulent premixed combustion on a nozzle-type burner, Combustion and Flame 122 (2000) 43–57.

B. M. Deschamps, G. J. Smallwood, J. Prieur, D. R. Snelling, Ö. L. Gülder, Surface density measurements of turbulent premixed flames in a spark-ignition engine and a bunsen-type burner using planar laser-induced fluorescence, Symposium (International) on Combustion 26 (1996) 427–435.

Y. C. Chen, R. W. Bilger, Experimental investigation of three-dimensional flame-front structure in premixed turbulent combustion - I: Hydrocarbon/air bunsen flames, Combustion and Flame 131 (2002) 400–435.

J. B. Bell, M. S. Day, J. F. Grcar, M. J. Lijewski, J. F. Driscoll, S. A. Filatyev, Numerical simulation of a laboratory-scale turbulent slot flame, Proceedings of the Combustion Institute 31 I (2007) 1299–1307.

D. Veynante, J. Piana, J. M. Duclos, C. Martel, Experimental analysis of flame surface density models for premixed turbulent combustion, Symposium (International) on Combustion 26 (1996) 413–420.

I. G. Shepherd, Flame surface density and burning rate in premixed turbulent flames, Symposium (International) on Combustion 26 (1996) 373–379.

I. G. Shepherd, R. K. Cheng, T. Plessing, C. Kortschik, N. Peters, Premixed flame front structure in intense turbulence, Proceedings of the Combustion Institute 29 (2002) 1833–1840.

I. G. Shepherd, R. K. Cheng, The burning rate of premixed flames in moderate and intense turbulence, Combustion and Flame 127 (2001) 2066–2075.

G. Kychakoff, P. H. Paul, I. Van Cruyningen, R. K. Hanson, Movies and 3-D images of flowfields using planar laser-induced fluorescence, Technical Report 13, 1987.

K. Y. Cho, A. Satija, T. L. Pourpoint, S. F. Son, R. P. Lucht, High-repetition-rate three-dimensional OH imaging using scanned planar laser-induced fluorescence system for multiphase combustion, Applied Optics 53 (2014) 316.

V. A. Miller, V. A. Troutman, R. K. Hanson, Near-kHz 3D tracer-based LIF imaging of a co-flow jet using toluene, Measurement Science and Technology 25 (2014).

R. Wellander, M. Richter, M. Aldén, Time-resolved (kHz) 3D imaging of OH PLIF in a flame, Experiments in Fluids 55 (2014).

B. Yip, D. C. Fourguette, M. B. Long, Three-dimensional gas concentration and gradient measurements in a photoacoustically perturbed jet, Applied Optics 25 (1986) 3919.

B. Yip, M. F. Miller, A. Lozano, R. K. Hanson, A combined OH/acetone planar laser-induced fluorescence imaging technique for visualizing combusting flows, Experiments in Fluids 17 (1994) 330–336.

T. Li, J. Pareja, L. Becker, W. Heddrich, A. Dreizler, B. Böhm, Quasi-4D laser diagnostics using an acousto-optic deflector scanning system, Applied Physics B: Lasers and Optics 123 (2017) 1–7.

J. Weinkauff, M. Greifenstein, A. Dreizler, B. Böhm, Time resolved three-dimensional flamebase imaging of a lifted jet flame by laser scanning, Measurement Science and Technology 26 (2015).

G. R. Römer, P. Bechtold, Electro-optic and acousto-optic laser beam scanners, Physics Procedia 56 (2014) 29–39.

W. Xu, C. D. Carter, S. Hammack, L. Ma, Analysis of 3D combustion measurements using CH-based tomographic VLIF (volumetric laser induced fluorescence), Combustion and Flame 182 (2017) 179–189.

N. Jiang, M. N. Slipchenko, N. Jiang, M. N. Slipchenko, S. Roy, T. R. Meyer, High-speed three-dimensional tomographic measurements for combustion systems, in: 32nd AIAA Aerodynamic Measurement Technology and Ground Testing Conference, American Institute of Aeronautics and Astronautics Inc, AIAA, 2016, pp. 1–6.

Y. Wu, W. Xu, Q. Lei, L. Ma, Single-shot volumetric laser induced fluorescence (VLIF) measurements in turbulent flows seeded with iodine, Optics Express 23 (2015) 33408.

B. R. Halls, D. J. Thul, D. Michaelis, S. Roy, T. R. Meyer, J. R. Gord, Single-shot, volumetrically illuminated, three-dimensional, tomographic laser-induced-fluorescence imaging in a gaseous free jet, Optics Express 24 (2016) 10040.

A. Ratner, W. Pun, S. Palm, F. E. C. Culick, Comparison of Chemiluminescence , OR PLIF , and NO PLIF for Determination of Flame Response to Acoustic Waves (2000) 1–8.

A. P. Dowling, S. R. Stow, Acoustic Analysis of Gas Turbine Combustors, Journal of Propulsion and Power 19 (2003) 751–764.

A. F. Seybert, D. F. Ross, Experimental determination of acoustic properties using a two-microphone random-excitation technique, Journal of the Acoustical Society of America 61 (1977) 1362–1370.

A. V. Oppenheim, R. W. Schafer, Discrete-Time Signal Processing, Prentice Hall Press, USA, 3rd edition, 2009.

M. Gharib, E. Rambod, K. Shariff, A universal time scale for vortex ring formation, Journal of Fluid Mechanics 360 (1998) 121–140.

S. B. Rojas Chavez, K. P. Chatelain, T. F. Guiberti, R. Mével, D. A. Lacoste, Effect of the excitation line on hydroxyl radical imaging by laser induced fluorescence in hydrogen detonations, Combustion and Flame 229 (2021) 111399.

R. Hartley, A. Zisserman, Multiple View Geometry in Computer Vision, Cambridge University Press, 2004.

T. Trindade, A. Ferreira, E. Fernandes, Characterization of Combustion Chemiluminescence: An Image Processing Approach, Procedia Technology 17 (2014) 194–201.

G. Paolillo, T. Astarita, On the PIV/PTV uncertainty related to calibration of camera systems with refractive surfaces, Measurement Science and Technology 32 (2021) 094006.

C. Willert, Stereoscopic digital particle image velocimetry for application in wind tunnel flows, Measurement Science and Technology 8 (1997) 1465–1479.

J. S. Lim, Two-dimensional signal and image processing, Englewood Cliffs, NJ, Prentice Hall 710 (1990) 1.

P. Perona, J. Malik, Scale-Space and Edge Detection Using Anisotropic Diffusion, IEEE Transactions on Pattern Analysis and Machine Intelligence 12 (1990) 629–639.

C. A. Palma, F. A. Cappabianco, J. S. Ide, P. A. Miranda, Anisotropic diffusion filtering operation and limitations - Magnetic resonance imaging evaluation, in: IFAC Proceedings Volumes (IFAC-PapersOnline), volume 19, Elsevier, 2014, pp. 3887–3892.

G. Gerig, O. Kbler, R. Kikinis, F. A. Jolesz, Nonlinear Anisotropic Filtering of MRI Data, IEEE Transactions on Medical Imaging 11 (1992) 221–232.

J. Canny, A Computational Approach to Edge Detection, IEEE Transactions on Pattern Analysis and Machine Intelligence PAMI-8 (1986) 679–698.

J. Immerkær, Fast noise variance estimation, Computer Vision and Image Understanding 64 (1996) 300–302.

I. Amidror, Scattered data interpolation methods for electronic imaging systems: a survey, Journal of Electronic Imaging 11 (2002) 157.

D. G. Lilley, Swirl Flows in Combustion: A Review, AIAA Journal 15 (1977) 1063–1078.

J. M. Lawson, J. R. Dawson, A scanning PIV method for fine-scale turbulence measurements, Experiments in Fluids 55 (2014).

Z. Wang, A. C. Bovik, H. R. Sheikh, E. P. Simoncelli, Image quality assessment: From error visibility to structural similarity, IEEE Transactions on Image Processing 13 (2004) 600–612.

H. Liu, G. Paolillo, T. Astarita, C. Shui, W. Cai, Computed tomography of chemiluminescence for the measurements of flames confined within a cylindrical glass, Optics Letters 44 (2019) 4793.

G. Paolillo, T. Astarita, A novel camera model for calibrating optical systems including cylindrical windows, in: AIAA Scitech 2019 Forum, American Institute of Aeronautics and Astronautics Inc, AIAA, 2019.

G. T. Herman, Image Reconstruction from Projections : The Fundamentals of Computerized Tomography, Academic Press, London, 1980.

F. Natterer, Numerical methods in tomography, Acta Numerica 8 (1999) 107–141.

R. Gordon, R. Bender, G. T. Herman, Algebraic Reconstruction Techniques (ART) for three-dimensional electron microscopy and X-ray photography, Journal of Theoretical Biology 29 (1970) 471–481.

D. Pugh, J. Runyon, P. Bowen, A. Giles, A. Valera-Medina, R. Marsh, B. Goktepe, S. Hewlett, An investigation of ammonia primary flame combustor concepts for emissions reduction with OH*, NH2* and NH* chemiluminescence at elevated conditions, in: Proceedings of the Combustion Institute, volume 38, Elsevier, 2021, pp. 6451–6459.

Article I

Tomographic reconstruction of an azimuthally forced flame in an annular chamber

Dirren Govender, Hecong Liu, Fan Peng, Weiwei Cai and Nicholas A. Worth

In: Proceedings of the Combustion Institute 000(2022)1-9

Available online at www.sciencedirect.com
ScienceDirect
Proceedings of the Combustion Institute 000 (2022) 1–9
Proceedings of the Combustion Institute
www.elsevier.com/locate/proci

Tomographic reconstruction of an azimuthally forced flame in an annular chamber

Dirren Govender [a,*], Hecong Liu [b], Fan Peng [b], Weiwei Cai [b], Nicholas A. Worth [a]

[a] Department of Energy and Process Engineering, Norwegian University of Science and Technology, Trondheim N-7491, Norway
[b] Key Lab of Education Ministry for Power Machinery and Engineering, School of Mechanical Engineering Shanghai Jiao Tong University, 800 Dongchuan Road, Shanghai, 200240, China

Received 5 January 2022; accepted 23 August 2022
Available online xxx

Abstract

Azimuthally forced spinning modes on a single ethylene-air swirl flame in an annular combustor were investigated using phase-averaged three-dimensional (3D) Computed Tomography of Chemiluminescence. Strongly spinning azimuthal modes in the clockwise (CW) and anticlockwise (ACW) directions were introduced by means of carefully controlled acoustic forcing. Tomographic reconstructions were calculated based on 25 independent views for an unforced, and CW and ACW forced cases. Using only a single flame in an annular enclosure resulted in a flame shape that differed from previous multi-flame investigations. The flame experiences significantly less flame-wall and no flame-flame interactions. Results at high and low equivalence ratio indicate that in the absence of significant enclosure effects, the global heat release rate (HRR) response is the same for both forcing directions. The 3D HRR oscillation distributions were investigated in detail, and the local flame response to modes with opposite spin direction was shown to feature 180° rotational symmetry. High magnitude HRR oscillations are formed close to the flame base, but due to the combined azimuthal and axial excitation the response on one side of the flame is significantly higher in magnitude, and concentrations of HRR oscillations are seen close to the inner or outer annular walls during CW or ACW excitation respectively. Swirl also causes these high magnitude structures to rotate slowly with downstream distance, although the spatial redistribution of HRR oscillations through this effect is subtle. This improves our physical understanding of previous observations of differing global flame responses to CW and ACW azimuthal excitation.

© 2022 The Author(s). Published by Elsevier Inc. on behalf of The Combustion Institute.
This is an open access article under the CC BY license (http://creativecommons.org/licenses/by/4.0/)

Keywords: Tomography of Chemiluminescence; Flame Dynamics; Combustion instabilities

---

[*] Corresponding author.
E-mail address: dirren.govender@ntnu.no (D. Govender).

https://doi.org/10.1016/j.proci.2022.08.051

1540-7489 © 2022 The Author(s). Published by Elsevier Inc. on behalf of The Combustion Institute. This is an open access article under the CC BY license (http://creativecommons.org/licenses/by/4.0/)

Please cite this article as: D. Govender, H. Liu, F. Peng et al., Tomographic reconstruction of an azimuthally forced flame in an annular chamber, Proceedings of the Combustion Institute, https://doi.org/10.1016/j.proci.2022.08.051

1. Introduction

The occurrence of self-excited thermoacoustic instabilities is a major development issue for future low emission gas turbine engines. Such instabilities arise due to the coupling between the unsteady heat release rate and pressure oscillations in the combustion chamber, and must be eliminated or reduced to acceptable levels during design; a task which is hampered by our incomplete understanding of these.

The current study focuses on azimuthal instabilities in annular combustion chambers. The flame response during azimuthal modes depends on the amplitude and frequency of the mode, but also on additional state characteristics such as the spin ratio and mode orientation [1,2]. A number of recent studies of self-excited azimuthal modes have observed a dependence of the mode state on a variety of parameters such as the operating conditions [3,4], chamber geometry [5] and the absence of bulk swirl in the annular chamber [6]. Understanding the selection and dynamics of azimuthal mode states continues to be a focus of research efforts.

Theoretical work has demonstrated that spinning wave solutions exist as stable periodic attractors, but the presence of noise which typically exists in turbulent flames can “drive” the response towards standing solutions [7,8]. Recent work has also linked mode orientation preferences to system asymmetries, and the preference for different spin directions on the symmetry breaking in the heat release rate response [9]. In other words, when a swirling flame confined within annular geometry is subject to oppositely signed spinning waves, the magnitude of the response depends on the spinning wave direction [10,11], which can lead to the preferential excitation of one spinning direction state [9]. While these studies have described heat release rate symmetry breaking in the global response, the use of integrated line of sight methods make the asymmetric and highly three-dimensional flame dynamics more difficult to understand.

To address this the current study employs Computed Tomography of Chemiluminescence (CTC), which is a fully three-dimensional measurement method [12–15]. The method uses multiple integrated line of sight measurements, taken from a range of viewing angles, to reconstruct the three-dimensional (3D) OH* distribution. While it is possible to use multiple cameras, or fibre optic cables to measure different views, the present study uses a single re-positioned camera to reconstruct phase average data from multiple views [13]. The use of a single camera is also advantageous due to the lack of space around the annular combustor making the use of multiple cameras difficult, especially for a large number of views. Recent advances in controlling the azimuthal mode state using acoustic forcing [10,11] are employed in order to make multiple repeat measurements of two distinct spinning modes of opposite sign. The combination of well controlled acoustic forcing and 3D measurement methods provides a number of new insights into the complex flame dynamics in this practically relevant system.

2. Experimental setup and methods

2.1. Annular combustor

A complete description of the annular combustor used in this study can be found in [10], but is recalled here in brief. The combustor features 12 equally spaced injectors of diameter $D_{inj} = 18.9$ mm and length $l_{inj} = 150$ mm, which are fed from a common plenum of diameter $D_p = 211$ mm. A mesh grid was placed at the plenum inlet and one at the plenum exit to ensure flow uniformity. In this study 11 out of 12 injectors were blocked at the plenum/injector interface to ensure only a single flame is present in the combustor. The use of only a single flame allows the line-of-sight based CTC method to be applied, which would be extremely challenging with all 12 flames present. The present setup is therefore similar to previous studies of transversely forced single flames [16,17], but with curved walls, which have been shown to break the response symmetry [11].

The unblocked injector tube was fitted with a 13 mm diameter bluff body that was flush mounted with the dump plane, creating a blockage ratio of 50%. The $D_r = 5$ mm bluff body mounting rod also supported a 6 vane anti-clockwise swirler (with exit blade angle, $\alpha = 60^\circ$). The swirler trailing edge is positioned 10 mm upstream of the dump plane. The annular chamber is formed by an inner wall of height $h_i = 294$ mm and diameter $D_i = 127$ mm, and an outer wall with a total height $h_o = 175$ mm and diameter $D_o = 212$ mm. The lowest section (up to a height of $z = 50$ mm) of the outer annular wall is quartz for optical access.

Ethylene-air mixtures with a range of equivalence ratios ($\phi = 0.8$ to 1.1) were tested at a constant bulk velocity $U_b = 18$ m/s at the dump plane. Figure 1 shows the flame structure at two operating conditions. The flame structure differs noticeably from previous studies with 12 flames [10,18]. The flow angle relative to the z-direction is reduced, resulting in narrower flames. The $\phi = 1.1$ case is slightly shorter and wider, and interacts with the confinement more. This is more obvious when viewing obliquely from $\theta = 235^\circ$ and 340°, where the flame asymmetry due to the confinement can be observed. The flame shape will be discussed in detail in §3.1.

2.2. Acoustic forcing

A forcing array [10] was installed on the outer annular wall, positioned 172 mm from the speaker

Please cite this article as: D. Govender, H. Liu, F. Peng et al., Tomographic reconstruction of an azimuthally forced flame in an annular chamber, Proceedings of the Combustion Institute, https://doi.org/10.1016/j.proci.2022.08.051

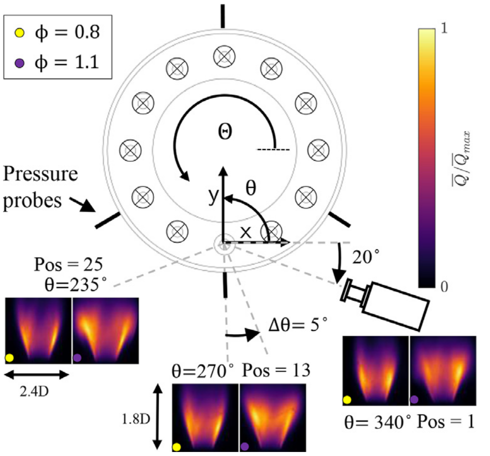

Fig. 1. Schematic of overhead view of experimental set up with OH* chemiluminescence images at positions $\Theta = 235°, 270°, 340°$, of flame for $\phi = 0.8$ and $\phi = 1.1$.

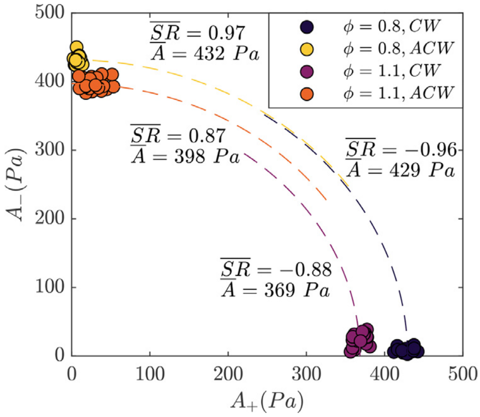

Fig. 2. Scatter plot of the mean amplitude of counter propagating acoustic waves in the annular chamber for the two forcing states. Each data point represents a single viewing angle from the tomographic experiment.

centerline to the the dump plane. The array consisted of four equally spaced Adastra HD60 horn drivers actuated by two QTX PRO 1000 amplifiers. To characterise the forced state three pairs of Kulite XCS-093-0.35D differential pressure transducers were installed in three injector tubes, at azimuthal locations $\Theta_k = 90°$, $210°$ and $330°$ as shown in Fig. 1. Note, that the annular and local injector coordinates are represented by Θ and θ respectively. The transducers were flush mounted with the injector walls 40 mm and 105 mm upstream of the dump plane. An additional pair of transducers was installed in the injector of interest to confirm velocity fluctuations at the injector exit. Pressure signals were amplified using a Fylde FE-579-TA bridge amplifier, and recorded using multiple NI-9234 24-bit DAQ modules at a sampling frequency of $f_s = 51.2\ kHz$.

Acoustic pressure in the injector is modelled as $\hat{p}_{inj}(z) = B_+e^{-ik_+z} + B_-e^{ik_-z}$, where the wavenumbers are calculated from the speed of sound, c, and the angular forcing frequency, ω_f, as $k_\pm = (\omega_f/c)/(1 \pm (U_b/c))$. Hat notation $(\hat{\cdot})$ denotes fluctuations in frequency space. The amplitude of the two axial counter propagating waves $B_\pm$ are calculated from measurements in each of the inlet ducts using the multi-microphone method [19]. Pressure oscillations are then propagated to the dump plane, taking account of both the swirler transfer matrix [4] and area change due to the bluff body. Axial velocity fluctuations at the dump plane are calculated as $\hat{u}(z) = (1/\rho c)[B_+e^{-ik_+z} - B_-e^{ik_-z}]$.

Next, following [10], the azimuthal pressure fluctuations in the annulus are modelled as the superposition of two azimuthal counter propagating waves, $\hat{p}(\Theta) = A_+e^{i(\Theta-\Theta_{nl})} + A_-e^{i(-\Theta+\Theta_{nl})}$, where $A_\pm$ are pressure wave amplitudes in the clockwise (CW) and anti-clockwise directions (ACW) respectively, and Θ_{nl} is the nodal line location. $A_\pm$ and Θ_{nl} are calculated from the propagated pressure at three azimuthal locations. The mode amplitude is then determined by $A = [A_+^2 + A_-^2]^{1/2}$, and the mode state through the spin ratio, $SR = (|A_+| - |A_-|)/(|A_+| + |A_-|)$.

Forcing frequencies, f_f, which produce the highest response were selected, with $f_f = 810\ Hz$ and $870\ Hz$ for $\phi = 0.8$ and 1.1 respectively. These frequencies are almost half of those previously reported by [10] when conventionally operating the combustor with 12 flames, due to the lower mean temperature of the annular chamber.

The phase and amplitude of each driver in the forcing array was controlled in order to generate spinning modes in both the CW and ACW directions, as described by [11]. The amplitude and spin ratio repeatability of the forcing state is shown in Fig. 2 for the two operating conditions. The scatter plot shows the mean amplitudes from each separate experimental run (which corresponds to a specific camera angle, as described in §2.3). The lower power $\phi = 0.8$ case resulted in less heating of the enclosure, and better mode control. However, both operating states are very repeatable, and highly spinning modes were generated in both cases. The forcing amplitudes for the $\phi = 0.8$ case correspond to $|\hat{u}|/U_b \approx 0.25$.

Due to the difference in flame shape and forcing frequency of this single flame configuration, the flame response will differ from [11], despite the similar operating condition. Flame Describing functions (FDF) were measured at several operating conditions to understand the response symmetry, as shown in Fig. 3. These show the variation of spatially integrated normalised heat release rate

Please cite this article as: D. Govender, H. Liu, F. Peng et al., Tomographic reconstruction of an azimuthally forced flame in an annular chamber, Proceedings of the Combustion Institute, https://doi.org/10.1016/j.proci.2022.08.051

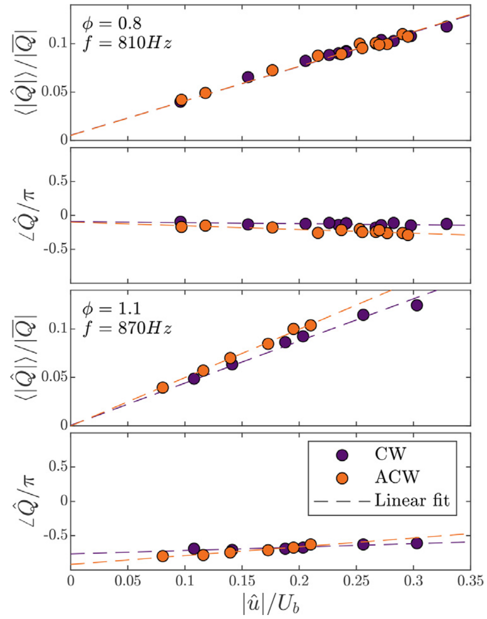

Fig. 3. Flame Describing Functions for two operating conditions in response to ACW ($SR > 0.89$) and CW ($SR < -0.85$) modes.

(HRR) oscillations, $\langle|\hat{Q}|\rangle/\langle\overline{Q}\rangle$, with normalised velocity fluctuations at the dump plane, $|\hat{u}|/U_b$, for both CW and ACW modes. In general the response of both ACW and CW forcing produces very similar linear HRR responses. Small differences in the FDF gains can be seen between the ACW and CW modes at $\phi = 1.1$. This asymmetry is similar to that in [11], with a larger response to ACW modes. These effects are not observed at $\phi = 0.8$ due to the lack of flame-wall interactions. However, even in the $\phi = 1.1$ case, the flame does not interact significantly with the walls, and the level of asymmetry is modest (gain difference $\sim 15\%$). Figure 3 also shows the phase of the FDFs for each equivalence ratio. The phase is similar for both ACW and CW modes and is also fairly constant across the range of $|\hat{u}|/U_b$ for both equivalence ratios. Therefore, while both cases are of interest, the present study will focus on the $\phi = 0.8$ case, due to the improved control of the mode available (as shown in Fig. 2), and difficulty reconstructing the $\phi = 1.1$ which is expected to result from the greater wall interactions.

2.3. Imaging and Tomographic reconstruction

The CTC reconstruction of OH* was performed by acquiring images from 25 independent views. These were acquired for an unforced case, and two different forced states. Each view was imaged using a single high speed Phantom v2012 camera with LaVision Intensified Relay Optics and a 100 mm focal length Cerco 2178 UV lens fitted with a 310 nm band bass filter. A camera aperture of f/8 ensured a sufficient depth of field. Images were acquired at a rate of $f_{cam} = 10$ kHz over a period of 1 second with a resolution of 1280 by 800 pixels at each position. Images were binned using the forcing signal and averaged into 16 phases over 810 cycles resulting in 625 images per phase.

The camera position was carefully controlled by a connecting arm to the burner support structure and each position was rotated $\Delta\theta \approx 5^\circ$ resulting in an included camera separation angle of 125°, as shown in Fig. 1. A two level square camera calibration target with a side length 106 mm and dot spacing of 10 mm was used for calibration. An alignment tool was manufactured allowing the calibration plate to be repeatably placed in the same physical position before each run. A Structural Similarity Index [20] value of 0.99 was calculated over 25 re-positioning tests demonstrating repeatability. A pinhole calibration model was applied with a refraction model [14] capable of characterising the curved quartz glass enclosure.

As the CTC reconstruction depends on multiple views it is important to maintain a similar flame structure and forcing state. A thermocouple was placed on the inner annular wall at $\Theta = 270^\circ$, ensuring the combustor was at constant temperature during each acquisition. The time taken from ignition to acquisition was also monitored and kept constant during each run. During this time the mode was carefully monitored and tuned when necessary to ensure that each run produced a similar response, as shown in Fig. 2.

The Tomographic reconstruction was processed using an in house code. Before reconstruction, background subtraction and thresholding were applied to reduce noise [21]. The volume of interest was discretized into a $240 \times 240 \times 192$ cubic voxel volume with a spatial resolution of 0.25 mm $\times$ 0.25 mm $\times$ 0.25 mm. Lines of sight from each view were modelled as a system of linear equations and solved using the Algebraic Reconstruction Technique (ART) [22]. The relaxation factor was set to 1 to maintain convergence and speed. Convergence was achieved with a maximum of 50 iterations and the reconstruction accuracy was measured by cross correlating the different views projected from the reconstructed flame with those taken during the experiment. A mean correlation value between all projected and imaged views of 0.99 and 0.93 were obtained for the $\phi = 0.8$ and the $\phi = 1.1$ respectively. In addition, the accuracy of the reconstruction was assessed by excluding a specific view from the reconstruction, and cross correlating the projection of the reconstructed volume with the independent view. A cross correlation value of 0.99 was achieved for the $\phi = 0.8$ case.

Please cite this article as: D. Govender, H. Liu, F. Peng et al., Tomographic reconstruction of an azimuthally forced flame in an annular chamber, Proceedings of the Combustion Institute, https://doi.org/10.1016/j.proci.2022.08.051

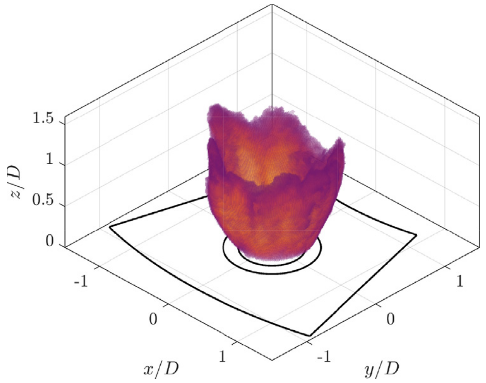

Fig. 4. Rendered 3D volume of the mean unforced HRR, $\phi = 0.8$. A schematic representation of the annular geometry is included to help orient the distribution.

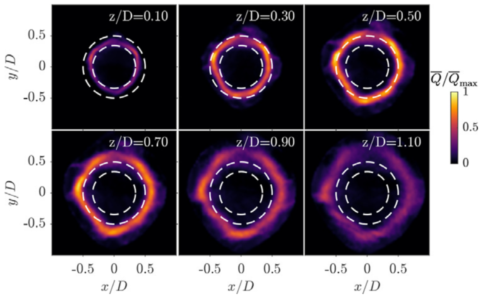

Fig. 5. Normalised HRR slices in the $x - y$ plane for the unforced flame, $\phi = 0.8$. White dashed lines represent the bluff body and inlet duct locations.

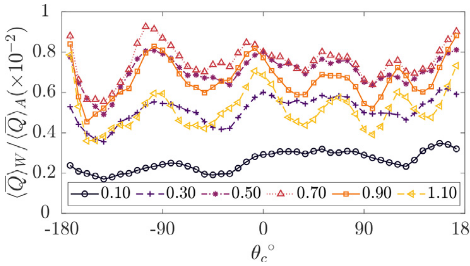

Fig. 6. Azimuthal variation of integrated HRR in wedge shaped regions, $\langle\overline{Q}\rangle_W$, normalised by the total integrated volume heat release rate, $\langle\overline{Q}\rangle_A$, $\phi = 0.8$. Legend describes the normalised downstream distances z_c/D of slices.

3. Results

3.1. Mean flame characterisation

In order to understand the asymmetry of the forced flame response, it is useful to first characterise the response of the flame without acoustic excitation.

A 3D rendering of the time-averaged HRR, $\overline{Q}$, for the unforced flame is presented in Fig. 4. For viewing clarity low intensity regions ($\overline{Q} < 0.25 \cdot \max(\overline{Q})$) were removed, in order to highlight the highest intensity structure. The flame shape resembles an inverted cone; a distribution commonly referred to as a V-flame. The flame is stabilised on the inner shear layer, which originates from the bluff body, and expands radially with downstream distance. Traces of six fold symmetry can be observed along angled ridges on the sides of the flame, and more clearly in height variations of the flame tip. This 6-fold symmetry, has been identified in a number of previous studies, and is a result of the swirler proximity to the dump plane [23]. Further to previous integrated line of sight approaches, additional asymmetry can be identified in the three-dimensional distribution, with more pronounced tip structures on one side of the flame (where $x/D \leq 0$).

Asymmetry can be more clearly observed in Fig. 5 which shows the HRR distribution in a number of downstream planes. Close to the burner exit ($z/D = 0.1$) an approximately circular distribution can be observed, with a slightly larger diameter than the bluff body. With increasing downstream distance the HRR distribution increases in diameter. The intensity increases and reaches a maximum at around $z/D = 0.5$. The HRR transitions from approximately circular close to the bluff body, to hexagonal with increasing downstream distance. Notably, the flame extends to a maximum diameter of approximately $1.2D$, which is significantly less than the annular wall spacing of $2.2D$. The flame shape in comparison with previous studies [11] is therefore significantly altered, due to the absence of neighbouring interacting flames. Therefore, in the absence of significant wall interactions the annular enclosure does not appear to strongly influence the flame symmetry, which is likely to affect the flame response. This is discussed later in §3.2.

The domain can be recast in cylindrical polar coordinates, and the asymmetry can be quantified by integrating the HRR distribution in wedge regions, according to eq. 1.

$$\langle\overline{Q}(\theta_c, z_c)\rangle_W = \sum_{r} \sum_{\theta=\theta_1}^{\theta_2} \sum_{z=z_1}^{z_2} \overline{Q}(r, \theta, z) \qquad (1)$$

Here, a centre wedge angle, θ_c, and angular wedge extent, $\theta_w = 15°$, are defined to produce the two angular limits, $\theta_{1,2} = \theta_c \mp \theta_w$. Similarly, the centre wedge height z_c and wedge height $z_w = 0.2D$ are used to fix the two limits $z_{1,2} = z_c \mp z_w$. Figure 6 shows the angular distribution of heat release rate at the same downstream distances examined in Fig. 5, normalised by the global HRR, $\langle\overline{Q}\rangle_A$. Close to the dump plane the heat release rate is relatively constant for all angles. However, with increasing downstream distance, small peaks are observed to

Please cite this article as: D. Govender, H. Liu, F. Peng et al., Tomographic reconstruction of an azimuthally forced flame in an annular chamber, Proceedings of the Combustion Institute, https://doi.org/10.1016/j.proci.2022.08.051

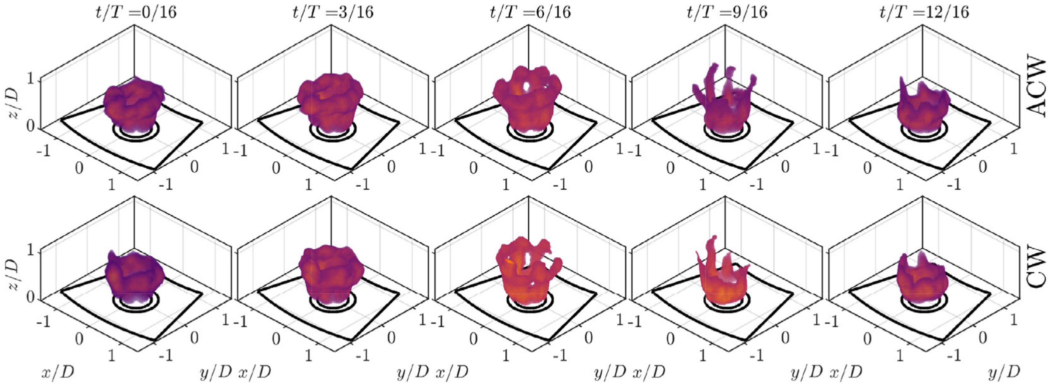

Fig. 7. Rendered 3D flame HRR for ACW and CW forcing at 5 phase angles ($\phi = 0.8$). A schematic representation of the annular geometry is included to help orient the distribution.

develop, which correspond to the most prominent flame structures asymmetries originating from the swirler. Quantified in this figure, these result in local fluctuations in the angular distribution of the heat release rate of up to approximately 30%.

3.2. ACW and CW forcing

Figure 7 shows the 3D distribution of HRR through a phase averaged cycle for both ACW and CW forced modes. A phase offset of $\pi/3$ was applied to the ACW case to exactly align the global HRR oscillations for the two cases, facilitating their comparison. The forcing results in a large ring-like HRR structure which is formed at $t/T = 0$, and is advected downstream. The flame elongates reaching a maximum length at $t/T = 9/16$ before pinch-off of the tip occurs, and the flame contracts. During pinch-off six elongated "fingers" can be identified due to the swirler imprint on the flow. While small differences can be observed between ACW and CW cases, these are examined in more detail through selected planes of interest.

Fig. 8 shows the reconstructed HRR distribution in the $x - z$ plane at $y = 0$ for both ACW and CW forcing. The previously observed ring-like structure can be observed to originate from wrinkles in the flame sheet, which start at the flame base and grow downstream. However, the flame structure on the left and right hand side ($x < 0$ and $x > 0$) are not symmetric. This asymmetry occurs due to the presence of both axial and azimuthal velocity oscillations, which depending on their phase can change the magnitude of vorticity oscillations on either side of the flame [24]. Comparing ACW and CW cases, similar structures occur at each phase angle, but with mirror symmetry about $x = 0$.

To characterise the asymmetry weighted phase plots of the HRR oscillations are calculated in $x - y$ planes at selected z/D locations, as shown in Fig. 9. The weighted phase calculation follows the approach of [25]. Briefly, the HRR Fourier amplitude, $|\hat{Q}|$, and phase, $\angle\hat{Q}$, are calculated at each voxel of interest. Weighted phase images are plotted at the forcing frequency by using colour to denote the phase angle of the oscillations, and brightness to denote amplitude. Zero padding ensured the frequency bin was located at an integer multiple of the forcing frequency, and Hann windowing reduced the dependence on the limited sample size.

Close to the flame base ($z/D = 0.27$) the high magnitude oscillations are confined to two concentric ring-like structures for both ACW and CW cases. While the oscillation amplitude (brightness) is close to uniform around the ring, the phase (colour) varies rapidly across across a line close to $x = 0$. This pattern is consistent with the presence of a transverse flapping motion due to the azimuthal velocity oscillations. Shear layer roll-up can be initiated by a flapping motion ([26]), or by axial pulsing ([27]). In this case despite the presence of both, the flapping introduced by the azimuthal velocity oscillations appear to control the shear layer roll-up timing.

The phase evolves with downstream distance, but more significantly the oscillation amplitude symmetry decreases. At $z/D = 0.4$ and $z/D = 0.6$ the outer of the two ring-like structures has a higher amplitude, and this is no longer uniform around the flame. For the ACW case, the highest intensity is towards the $x < 0$, $y < 0$ quadrant, and in the CW case it is instead towards the $x > 0, y > 0$ quadrant. The response magnitude is highest on the side of the flame facing the incoming pressure wave, consistent with previous studies [6]. However, the ability to study differing depth layers in this volumetric data show that while these structures appear to be formed at the flame base with mirror symmetry along $x = 0$, the regions of high HRR are rotated further downstream. The highest intensity fluctua-

Please cite this article as: D. Govender, H. Liu, F. Peng et al., Tomographic reconstruction of an azimuthally forced flame in an annular chamber, Proceedings of the Combustion Institute, https://doi.org/10.1016/j.proci.2022.08.051

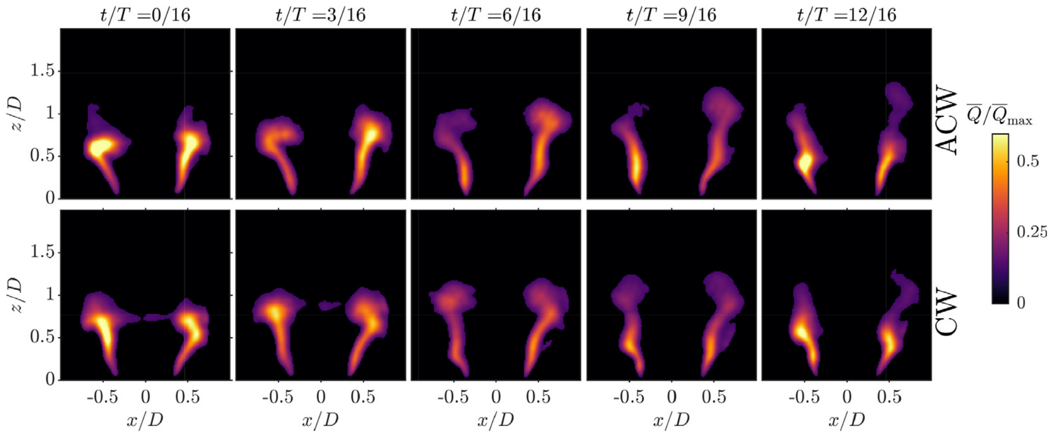

Fig. 8. Distribution of HRR in $x-z$ plane at $y=0$ for ACW and CW forcing at 5 phase angles ($\phi = 0.8$).

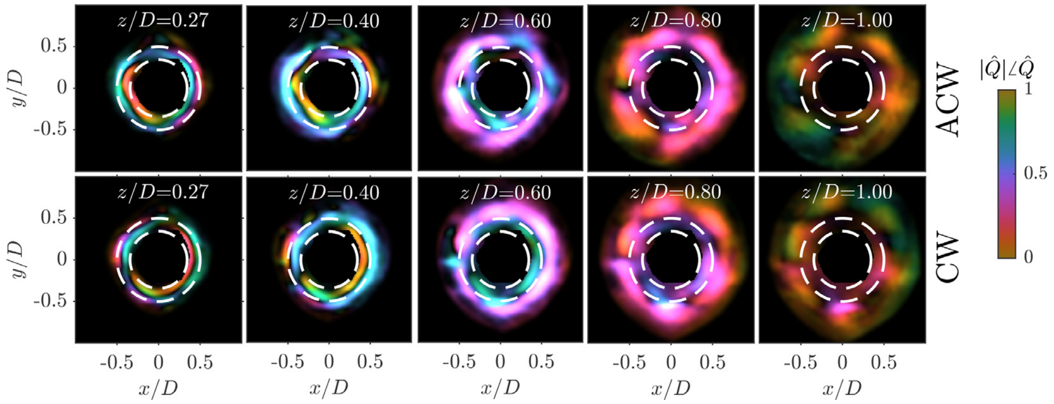

Fig. 9. Weighted phase plots of HRR oscillations in the $x-y$ plane, at different z/D locations for ACW and CW cases, $\phi = 0.8$.

tions occur towards the outer annular wall in the ACW case, and the inner annular wall in the CW case.

Towards the flame tip ($z/D > 0.8$) the phase around the flame becomes more uniform. This indicates that while the transverse oscillations play an important role at the flame base, controlling the roll-up timing and flame symmetry, far downstream large scale flame tip pinch-off occurs at one point in the cycle. Finally, at the flame tip ($z/D = 1$), six high intensity regions can be seen, which correspond to the swirler imprint on the flame.

The asymmetry of the HRR response to ACW and CW forcing is quantified in Fig. 10 for different downstream distances. As described previously, close to the flame base ($z/D \leq 0.27$) and at the flame tip ($z_c/D \geq 0.8$), the response is reasonably symmetric, although downstream 6 peaks associated with the swirler can be seen. However, at intermediate locations ($0.4 \leq z_c/D \leq 0.6$), where both the mean HRR and HRR oscillations are greatest, the response is clearly asymmetric. At $z_c/D = 0.4$ the ACW and CW distribution peaks at around $\theta_c = -180^\circ$ and $\theta_c = 20^\circ$ respectively, taking values which are double those at the troughs.

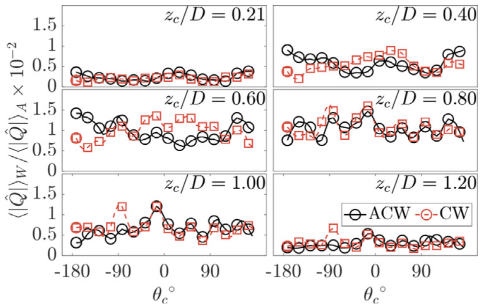

Fig. 10. Angular distribution of HRR oscillation magnitude around the flame, at various z_c/D for ACW and CW cases, $\phi = 0.8$..

Please cite this article as: D. Govender, H. Liu, F. Peng et al., Tomographic reconstruction of an azimuthally forced flame in an annular chamber, Proceedings of the Combustion Institute, https://doi.org/10.1016/j.proci.2022.08.051

To assess the role of swirl on the angular redistribution of HRR oscillations, the circumferential distribution of HRR oscillation magnitude peaks were tracked at different downstream locations (not shown here for brevity). The HRR oscillations rotate by approximately 0.2π radians per unit D downstream. This swirl induced rotation is insufficient to significantly redistribute the HRR oscillations from the sides of the flame to regions close to the inner and outer walls. Therefore, while swirl will contribute subtly to the distribution of fluctuations, it is likely that dynamically significant vortical structures are formed preferentially close to the inner and outer walls during CW and ACW forcing respectively, due to the combination of azimuthal and axial velocity fluctuations, and these then define the asymmetric distribution of HRR fluctuations.

4. Conclusion

Computed Tomography of Chemiluminescence has been used to capture the 3D phase averaged flame dynamics of a single flame with swirl in an annular enclosure subject to highly spinning ACW and CW modes. The shape of the unforced flame differs from the multi flame configuration, with no significant wall interactions. The response of the forced flame is asymmetric, due to the combination of axial and azimuthal velocity oscillations, resulting in greater heat release rate oscillations on one side of the flame. Additionally, the swirling flow results in a slow rotation of HRR oscillations with downstream distance, but the rotation rate is not sufficient to significantly reorient their angular distribution. However, due to the reduced wall interactions, the global response is the same for both forcing conditions. The current study therefore improves our understanding of the flame dynamics, and importantly demonstrates that the effective confinement of the flame is another important parameter in the symmetry of the HRR response.

Declaration of Competing Interest

The authors declare that they have no known competing financial interests or personal relationships that could have appeared to influence the work reported in this paper.

Acknowledgments

The authors gratefully acknowledge financial support from the European Research Council (ERC): Grant agreement 677931 TAIAC. We would also like to acknowledge Samuel Wiseman for continuous feedback and help with this research.

References

[1] W. Krebs, P. Flohr, B. Prade, S. Hoffmann, Thermoacoustic stability chart for high-intensity gas turbine combustion systems, Combust. Sci. Technol. 174 (7) (2002) 99–128.
[2] S. Evesque, W. Polifke, C. Pankiewitz, Spinning and azimuthally standing acoustic modes in annular combustors, in: 9th AIAA/CEAS Aeroacoustics Conference and Exhibit, 2003, p. 3182.
[3] K. Prieur, D. Durox, T. Schuller, S. Candel, A hysteresis phenomenon leading to spinning or standing azimuthal instabilities in an annular combustor, Combust. Flame 175 (2017) 283–291.
[4] T. Indlekofer, B. Ahn, Y.H. Kwah, S. Wiseman, M. Mazur, J.R. Dawson, N.A. Worth, The effect of hydrogen addition on the amplitude and harmonic response of azimuthal instabilities in a pressurized annular combustor, Combust. Flame 228 (2021) 375–387.
[5] N.A. Worth, J.R. Dawson, Modal dynamics of self--excited azimuthal instabilities in an annular combustion chamber, Combust. Flame 160 (11) (2013) 2476–2489.
[6] M. Mazur, H.T. Nygård, J.R. Dawson, N.A. Worth, Characteristics of self-excited spinning azimuthal modes in an annular combustor with turbulent premixed bluff-body flames, Proc. Combust. Inst. 37 (4) (2019) 5129–5136.
[7] G. Ghirardo, M. Juniper, J.P. Moeck, Weakly nonlinear analysis of thermoacoustic instabilities in annular combustors, J. Fluid Mech. 805 (2016) 52–87.
[8] G. Ghirardo, F. Gant, Averaging of thermoacoustic azimuthal instabilities, J. Sound Vib. 490 (2021) 115732.
[9] G. Ghirardo, H.T. Nygård, A. Cuquel, N.A. Worth, Symmetry breaking modelling for azimuthal combustion dynamics, Proc. Combust. Inst. 38 (4) (2021) 5953–5962.
[10] H.T. Nygård, M. Mazur, J.R. Dawson, N.A. Worth, Flame dynamics of azimuthal forced spinning and standing modes in an annular combustor, Proc. Combust. Inst. 37 (4) (2019) 5113–5120.
[11] H.T. Nygård, G. Ghirardo, N.A. Worth, Azimuthal flame response and symmetry breaking in a forced annular combustor, Combust. Flame 233 (2021) 111565.
[12] J. Floyd, P. Geipel, A. Kempf, Computed tomography of chemiluminescence (ctc): instantaneous 3d measurements and phantom studies of a turbulent opposed jet flame, Combust. Flame 158 (2) (2011) 376–391.
[13] S.M. Wiseman, M.J. Brear, R.L. Gordon, I. Marusic, Measurements from flame chemiluminescence tomography of forced laminar premixed propane flames, Combust. Flame 183 (2017) 1–14.
[14] H. Liu, G. Paolillo, T. Astarita, C. Shui, W. Cai, Computed tomography of chemiluminescence for the measurements of flames confined within a cylindrical glass, Opt. Lett. 44 (19) (2019) 4793–4796.
[15] H. Liu, Q. Wang, F. Peng, Z. Qin, W. Cai, Flame Emission Tomography Based on Finite Element Basis and Adjustable Mask, Opt. Exp. 29 (25) (2021) 40841–40853.

Please cite this article as: D. Govender, H. Liu, F. Peng et al., Tomographic reconstruction of an azimuthally forced flame in an annular chamber, Proceedings of the Combustion Institute, https://doi.org/10.1016/j.proci.2022.08.051

[16] A. Saurabh, R. Steinert, J.P. Moeck, C.O. Paschereit, Swirl flame response to traveling acoustic waves, Turbo Expo: Power for Land, Sea, and Air, volume 45691, American Society of Mechanical Engineers, 2014. p. V04BT04A043

[17] J. O'Connor, V. Acharya, T. Lieuwen, Transverse combustion instabilities: Acoustic, fluid mechanic, and flame processes, Progr. Energy Combust. Sci. 49 (2015) 1–39.

[18] J.R. Dawson, N.A. Worth, Flame dynamics and unsteady heat release rate of self-excited azimuthal modes in an annular combustor, Combust. Flame 161 (10) (2014) 2565–2578.

[19] A.F. Seybert, D.F. Ross, Experimental determination of acoustic properties using a two-microphone random-excitation technique, J. Acoust. Soc. AM. 61 (5) (1977) 1362–1370.

[20] Z. Wang, A.C. Bovik, H.R. Sheikh, E.P. Simoncelli, Image quality assessment: From error visibility to structural similarity, IEEE Trans. Image Process. 13 (4) (2004) 600–612.

[21] H. Liu, Z. Yang, W. Cai, Application of three-dimensional diagnostics on the direct-current electric–field assisted combustion, Aerospace Sci. Technol. 112 (2021).

[22] H. Liu, B. Sun, W. Cai, kHz-rate volumetric flame imaging using a single camera, Opt. Commun. 437 (2019) 33–43.

[23] H.T. Nygård, N.A. Worth, Flame transfer functions and dynamics of a closely confined premixed bluff body stabilized flame with swirl, J. Eng. Gas Turb. Power 143 (4) (2021) 041011.

[24] A. Saurabh, C.O. Paschereit, Dynamics of premixed swirl flames under the influence of transverse acoustic fluctuations, Combust. Flame 182 (2017) 298–312.

[25] M. Hauser, M. Lorenz, T. Sattelmayer, Influence of transversal acoustic excitation of the burner approach flow on the flame structure, J. Eng. Gas Turb. Power 133 (4) (2011).

[26] N.A. Worth, D. Mistry, T. Berk, J.R. Dawson, Vortex dynamics of a jet at the pressure node in a standing wave, J. Fluid Mech. 882 (2020).

[27] S.C. Crow, F. Champagne, Orderly structure in jet turbulence, J. Fluid Mech. 48 (3) (1971) 547–591.

Please cite this article as: D. Govender, H. Liu, F. Peng et al., Tomographic reconstruction of an azimuthally forced flame in an annular chamber, Proceedings of the Combustion Institute, https://doi.org/10.1016/j.proci.2022.08.051

Article II

Large volume scanning laser induced fluorescence measurement of a bluff-body stabilised flame in an annular combustor

Dirren Govender, Samuel Wiseman, James R. Dawson and Nicholas A. Worth

In: Experiments in Fluids (2022) 63:62

Experiments in Fluids (2022) 63:62
https://doi.org/10.1007/s00348-022-03406-9

RESEARCH ARTICLE

Large volume scanning laser induced fluorescence measurement of a bluff-body stabilised flame in an annular combustor

Dirren Govender[1] · **Samuel Wiseman**[1] · **James R. Dawson**[1] · **Nicholas A. Worth**[1]

Received: 15 October 2021 / Revised: 11 February 2022 / Accepted: 23 February 2022 / Published online: 23 March 2022
© The Author(s) 2022

Abstract

This study outlines a variant of three-dimensional OH planar laser-induced fluorescence and its application in characterising a single bluff body stabilised flame inside a 12 burner annular combustor. In this variant of the method a relatively large volume was scanned slowly in order to calculate the full three-dimensional Flame Surface Density (FSD) distribution. The method used a combination of two scanning directions to overcome bias errors associated with laser sheet positions close to the flame edges. The source of this bias error was confirmed numerically through a complimentary synthetic PLIF study, which was also used to refine the experimental setup. The bias error resulted in a reduction of FSD magnitude, although the method was still capable of capturing the flame structure. This was demonstrated by comparing the reconstructions from the two independent scan directions. Combining the data from both directions overcame the bias, and allowed flame asymmetry due to the confinement to be assessed. The FSD was used to determine the heat release rate of the flame with varying local azimuthal angle for different downstream regions. This highlighted the highly asymmetric structure, produced by the asymmetric confinement.

Graphical abstract

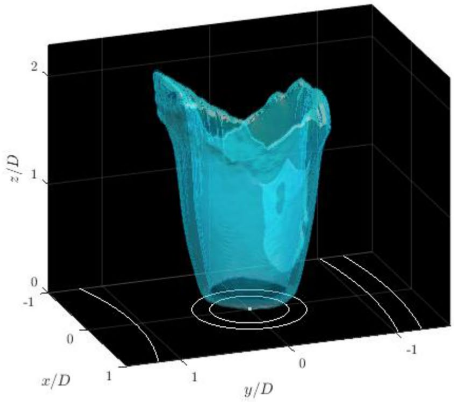

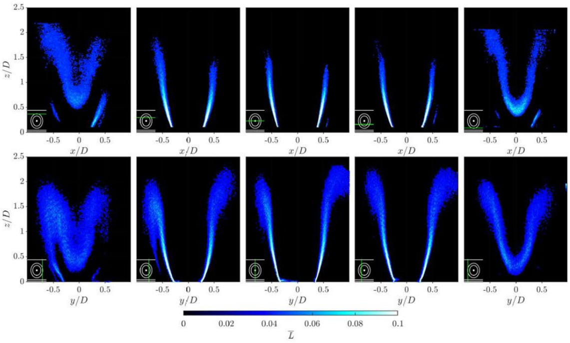

Keywords Flame surface density · Planar laser-induced fluorescence · Scanning · Flame structure

1 Introduction

The move to efficient low emission combustion systems requires a better understanding of the physics of reacting flows. In modern gas turbine engines, flames are often

---

✉ Dirren Govender
dirren.govender@ntnu.no

[1] Department of Energy and Process Engineering, Norwegian University of Science and Technology, Kolbjørn Hejes vei 2, Trondheim 7491, NO, Norway

confined within annular combustion chambers. However, a common simplification is to investigate the behaviour of single isolated flames in axisymmetric geometry. The characteristics of single flames have been extensively studied through the heat release rate distribution, which is often captured using two-dimensional (2D) planar or integrated line of sight techniques, such as for example OH planar laser-induced fluorescence (PLIF) (Hanson et al. 1990; Pun et al. 2003; Cho et al. 2013; Mulla et al. 2016), or OH chemiluminescence (OH*) (He et al. 2019; Sardeshmukh et al. 2017; Doan and Swaminathan 2019) imaging, respectively. Under an assumption of axisymmetry such methods are capable of describing the full three-dimensional (3D) distribution of the heat release rate, which is only strictly true in turbulent flames when describing the time-average or some phase-average distribution. However, such assumptions are no longer applicable even in a time average sense when the local flow symmetry of the flame is broken by the confinement; such as that which occurs in annular geometry (Fanaca et al. 2010; Worth and Dawson 2013b). Therefore, the current investigation focuses on a fully three-dimensional measurement technique, capable of characterising the asymmetric heat release rate structure of a flame confined in an annular combustion chamber.

The most widely used method of resolving the full 3D heat release rate field is Computed Tomography of Chemiluminescence (CTC) (Worth and Dawson 2013a; Cai et al. 2013; Dreizler et al. 2018; Ishino and Ohiwa 2005; Floyd and Kempf 2011). CTC uses the principles of tomography to reconstruct the 3D distribution of chemiluminescence based on multiple integrated line of sight measurements taken by multiple cameras at different viewing angles (Floyd and Kempf 2011). In these studies chemiluminescence from a limited spectral band is used as a proxy for the heat release rate. The approach requires optical access across a large range of viewing angles, and the reconstruction accuracy can be highly dependent on the number of views and angles used. Therefore, in order to obtain a sufficient number of views either a large number of cameras can be employed (Unterberger et al. 2018; Meyer et al. 2016; Gilabert et al. 2007; Ishino et al. 2008), views can be gathered by optic fibres and collected on a single camera (Liu et al. 2019; Yu et al. 2020; Moinul Hossain et al. 2012; Mohamad et al. 2006), or a single camera can be re-positioned to capture multiple views in order to capture the time average or phase average response (Floyd and Kempf 2011; Worth and Dawson 2012; Wiseman et al. 2017).

It is common to use a thin laser light sheet to perform PLIF measurements in order to capture the distribution of fluorescence intensity in a plane of interest (Wabel et al. 2018). However, a recent extension of this standard approach has been used to capture full 3D volumes, by using a thick laser light sheet to fluoresce a volume of interest in a method known as Volumetric LIF (VLIF) (Xu et al. 2017; Meyer et al. 2016; Jiang et al. 2016; Wu et al. 2015; Ma et al. 2017; Halls et al. 2016). In this method, fluorescence emissions are captured by multiple cameras with a range of viewing angles, and these views are used to tomographically reconstruct a three-dimensional distribution of the targeted species. A comprehensive study by Xu et al. (2017) outlines the fundamental capabilities and limitations of the VLIF technique, where the authors used a numerical study to show that the reconstruction of symmetric flames is possible with high accuracy. However the technique is constrained by laser power, resulting in relatively thin volumes of interest. Therefore, the technique is often used to highlight only small regions of interest. While such an approach would in principle be able to effectively highlight a single flame in an annular rig, capturing the entire three-dimensional structure of a flame may still be difficult since very high powered lasers and multiple cameras would be required.

An alternative method of capturing three-dimensional structures using LIF is realised by combining a PLIF setup with scanning optics (Kychakoff et al. 1987; Cho et al. 2014; Miller et al. 2014; Wellander et al. 2014; Yip et al. 1986, 1994; Li et al. 2017; Weinkauff et al. 2015). In Scanning-PLIF a three-dimensional flow can be resolved by rapidly scanning a laser sheet through a volume of interest, and reconstructing the three-dimensional distribution by combining data from planar slices. In this approach the technique is constrained by the scanning speed, which is required to be much faster than the flow speed, in order to effectively *freeze* the flow (Weinkauff et al. 2015). The moderate to high velocities present in turbulent reacting flows require very high-speed scanning optics, which operate at frequencies of order 0.1 to 3 MHz (Cho et al. 2014). Such scanning speeds are not possible with current scanning devices and a trade-off between scan depth and speed is often a limitation of such techniques (Römer and Bechtold 2014). Therefore, in comparison with mechanical scanning devices typically used in Scanning-PIV experiments for low speed flows (Lawson and Dawson 2014; Hori and Sakakibara 2004; Casey et al. 2013), high speed devices such as acousto-optic deflectors that can operate at a scanning rates of order 100 kHz have been used to scan reacting flows such as a lifted turbulent jet flame (Li et al. 2017), however the final scanning rate may also be limited by the laser or imaging systems. The scanning speed limitation again typically restricts such studies to reasonable small number of slices, and therefore to volumes of interest which are relatively thin.

In the current paper a new variant of the Scanning-PLIF approach is introduced, which aims to reconstruct the heat release rate (HRR) over a much larger volume of interest than previous approaches. This is achieved by focusing on characterising the time average structure of a reacting flow, meaning the restrictions on scanning speed can be relaxed.

This allows the use of a simple mechanical scanning mechanism to sweep a laser sheet across a large volume of interest in order to capture the asymmetric structure of a flame confined within an annular combustion chamber. The use of a LIF-based method allows a single flame in the annular rig to be highlighted and measured despite the presence of neighbouring flames; an undertaking that would be difficult using a CTC-based approach.

The remainder of the paper is organised as follows: Sect. 2 outlines the annular configuration and the details of the experimental technique. The technique is also evaluated in Sects. 3 and 4, using a numerical experiment that produces synthetic PLIF images of an idealised object, in order to estimate error associated with the experimental and reconstruction parameters. The experimental reconstruction of a flame in an annular rig is then presented Sect. 5.

2 Experimental methods

2.1 Annular combustor

The annular combustor which was reported previously by Mazur et al. (2019) features 12 equally spaced turbulent bluff body stabilised flames. The main features and dimensions will be recalled here briefly. An ethylene/air mixture was introduced through a cylindrical plenum chamber of diameter, $D_p = 212$ mm. Two mesh screens were located at the plenum inlet and outlet to improve flow uniformity. The flow is divided around a hemispherical body with a diameter of $D_h = 140$ mm, into 12 injection tubes of length $l_i = 150$ mm, each with a diameter $D = 18.9$ mm.

The injectors were equally spaced around a diameter of $D_{inj} = 169$ mm, and each was fitted with a $D_b = 13$ mm diameter bluff body flush mounted with the annular chamber at the location referred to as the dump plane. The bluff bodies are centrally mounted on a rod of diameter $D_r = 5$ mm, and have a half angle of 45° and a blockage ratio of approximately 50 %. Each bluff body is centered using three grub screws, which are located $L_g = 50$ mm upstream of the dump plane. The annular enclosure consisted of a stainless steel inner wall with a diameter of $D_i = 127$ mm and an outer cylindrical quartz wall to permit optical access with a diameter of $D_o = 212$ mm.

The reactant mixture was maintained at an equivalence ratio of $\phi = 0.7$ and a bulk velocity of $U_b = 17$ m/s at the dump plane. The equivalence ratio and flow velocity were chosen as these correspond to a thermoacoustically stable operating condition (Mazur et al. 2019). Dynamic pressure measurements were conducted using six pressure sensors at upstream locations inside three of the injector tubes, to confirm that the operating point remained thermoacoustically stable. The combustor was operated for approximately 20 seconds prior to data acquisition, in order to reach a quasi steady thermal state and maintain consistency between experiments.

2.2 Scanning OH-PLIF

OH radicals were excited using a Sirah Credo dye laser, pumped by a Nd:YAG Edgewave IS 400-2-L laser with a pulse energy of 10 mJ at 10 kHz. The laser wave length was regularly tuned to maximise the OH signal at approximately 283.54 nm with a dye laser power of ∼ 0.25 mJ per pulse. A series of optics were used to produce a laser sheet with a thickness with a mean value of $\delta \approx 0.4$ mm. The laser sheet thickness was measured using calibration images, as described in Sect. 2.3.

A Galvanometric scanning dynAXIS XS UV coated mirror is used to sweep the UV laser sheet across the flame, over a total depth of 40 mm. The position of the mirror was controlled using a voltage signal with a range of 0.5 V and precision of 4×10^{-5} V, which results in a sheet positional precision of 0.003 mm. A lens is not used to realign the sheet angle following the galvanometer, as the sheet is also passed through the curved surface of the outer quartz combustion chamber wall, resulting in an array of incidence angles due to refraction. Instead the location of each laser sheet is defined through calibration, as described later in Sect. 2.3. A total of 200 laser sheet positions were used, which based on the measured sheet thickness of $\delta \approx 0.4$ mm, results in a sheet overlap of 50%.

Two Phantom V2012 cameras equipped with Lavision Intensified Relay Optics and 100 mm focal length Cerco 2178 UV lenses were used to conduct the OH-PLIF measurements. The first camera equipped with a 310 nm UV filter (Full Width Half Maximum(FWHM) = 10 nm) imaged from the side and collected OH-PLIF measurements, while the second camera imaged from overhead, via an air cooled mirror, and was used to conduct the laser sheet calibration. Both cameras equipped with the 310 nm UV filters were additionally used to collect OH* chemiluminescence measurements of the flame. Side view OH* images were collected while all 12 flames were on using the camera arrangement shown in Fig. 1a in order to avoid capturing intensity from neighbouring flames. The side view resulted in a pixel resolution of 800 × 896 pixels, resulting in a spatial resolution of 10 pixels/mm for the PLIF measurements. The overhead camera used a resolution of 896 × 800 pixels to image an area of 40 mm × 40 mm, providing a resolution of 10 pixels/mm. Both PLIF and OH* measurements were conducted at an imaging frequency of 10 kHz. An aperture setting of f/8 was used for the PLIF measurements to ensure a sufficient depth of field. For the OH-PLIF measurements, at each sheet location a total of 354 images were acquired, resulting in a total of 70800 images for each scan. Four independent scans

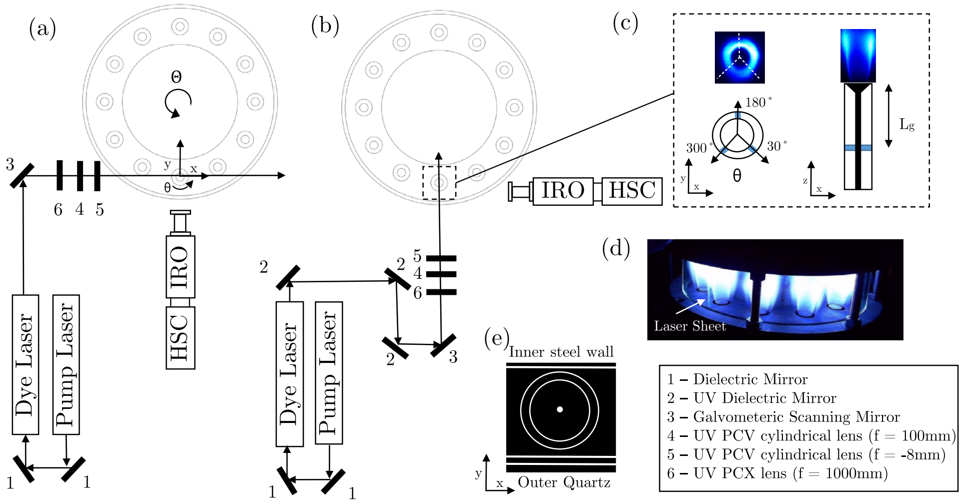

Fig. 1 Schematic of experimental setup viewed from above for **a** Scan XZ and **b** Scan YZ, **c** representation of injector from top and side views with positioning of grub screws in blue and images of OH chemiluminescence, **d** Image of annular rig during experiment **e** orientation of inner and outer annular walls

were performed to overcome the limitations of the camera's buffer size, resulting in a total of 283200 images.

A bias error was encountered when performing the Scanning-PLIF measurements (which is discussed in detail in Sect. 4), and therefore Scanning-PLIF measurements were made using two perpendicular scan directions, as shown in Fig. 1. These are labelled and referred to in the following as Scan XZ and Scan YZ, which correspond to the predominant orientations of the laser sheet and imaging planes. Care was also taken to ensure the laser sheet thickness and image spatial resolution were kept relatively constant for the two scan directions. Calibration is conducted to a common coordinate system, allowing the reconstructions to be combined, which is described in the next section.

2.3 Camera and laser sheet calibration

In order to reconstruct the 3D flame structure, two calibrations were employed: First a camera calibration model was used to define each pixel's line of sight through the volume, for both overhead and side views; and secondly a laser sheet calibration was used to define the spatial location and orientation of each each laser sheet in the scan. Calibrations of the two cameras and different scan directions were aligned with a single global coordinate system through the identification of a common reference point (center of the bluff bodies) and vector (orientation angle of the calibration plate).

The side camera calibration was performed by imaging a calibration target which was traversed in increments of 3 mm through a depth of 42 mm, resulting in 15 planes of calibration data. A third order polynomial model was used for the image to real space transformation, in order to account for refractive index effects of the curved quartz enclosure. The calibration of the side camera from both scan directions produced a mean error of 0.45 pixels (0.046 mm) with respect to all planes, and the overhead calibration produced a mean error of 0.08 pixels (0.008 mm). During the side camera calibration the plate was carefully aligned so that its face was perpendicular to the dump plane. Images of the calibration plate were taken using the overhead camera during the traverse. These images allow the plate position and therefore lines of sight from the side camera to be related to a global coordinate system in the frame of reference of the annular combustor.

In terms of the laser sheet calibration, different laser sheet locations were recorded by synchronising the camera signal and the signal sent to the scanner to move the laser sheets. First the vertical orientation of the laser sheets was assessed by positioning an angled calibration target in the volume, imaged from the side camera. Next, the orientation of the laser sheet on the dump plane was assessed. As the reflection of laser light from the dump plane of the annular combustor is weak, a reflective target was placed on the dump plane to ensure that the laser sheet was visible to the overhead camera. A total of 100 overhead images were averaged for each laser sheet position. The mean sheet location on the dump plane and the vertical orientation were calculated to subpixel accuracy from the two views, and a Gaussian distribution was fitted to characterise the beam width in terms of an intensity profile. The sheet coordinates were converted into real space through the overhead camera calibration.

The real space coordinates of all laser sheets were then fitted to a single laser sheet calibration model using a least squares approach. An equation of plane could then be defined for each laser sheet location from the calibration model.

The intersection of each pixel's line of sight from the side camera, as defined by the camera model, with the real space coordinates of the laser sheet plane can be used to project images into real space during the volume reconstruction. This process was done for both scanning directions and the definition of the global coordinate system allowed for alignment of the reconstruction from the two different scan directions.

2.4 Volumetric flame surface density

The PLIF images were used together with the laser and camera calibration models to calculate the 3D distribution of the Flame Surface Density (FSD). The FSD is defined as the flamelet surface area per unit volume under, averaged over time, the assumption of flamelet framework for premixed turbulent flames (Zhang et al. 2015). FSD will be used later in Sect. 5.4 to describe the flame structure and localised heat release rate.

FSD has been used previously in premixed flames as an indicator of heat release rate (Paul and Najm 1998; Knikker et al. 2002; Dawson and Worth 2014). A study by Balachandran et al. (2005) calculated the 2D Flame Surface Area (FSA), which represents the flame length per unit area, from a single measurement plane and inferred a 3D distribution of FSD by rotating this under the assumption of axisymmetry. The resulting integrated FSD was then related to integrated OH^* measurements of heat release rate fluctuations, showing good agreement. However, the authors highlight that FSD calculated in this manner neglects fine scale wrinkles typically present along the surface of turbulent flames. It also by construction neglects out-of-plane wrinkling, a detailed discussion of this limitation is included in Sect. 4.

In a similar manner, this study will relate the FSD determined from the reconstructed volumetric distribution of flame surface to the volumetric heat release rate, neglecting flame surface wrinkling beyond the measurement resolution, but preserving out-of-plane variations. While the 2D calculation of FSA uses edge locations binned into pixels, the 3D calculation of FSD relies on edge locations reprojected into a 3D volume, and binned into 3D voxels. This approach can be considered the 3D analog of 2D FSA calculations (Veynante et al. 1994; Zhang et al. 2014; Balachandran et al. 2005).

To determine instantaneous flame front locations PLIF images were first processed to correct for non-uniformities in the beam profile, and to accentuate the division between products and reactants. An intensity correction was applied to each image in both the horizontal and vertical directions which corrects for the Gaussian shape of the expanded laser sheet, and absorption as the beam passes through the combustor.

An edge preserving Gaussian filter and a nonlinear diffusion filter were then applied to the images to remove noise, before a Canny edge detection algorithm is applied to find the edge contours of the flame front separating burnt and unburnt gas. A gradient threshold was also applied during the edge detection procedure to remove any non-physical artefacts that were the result of intensity inhomogenity. An example of the raw PLIF image and the identified flame edges is shown in Fig. 2. Edge detection results in a sequence of instantaneous binary images, $L(i, j, n, t)$, in which the flame front location is defined by pixels with a value of 1, for each laser sheet location, n, in image space (i, j). A schematic example of this process is shown in Fig. 3a using three binary images representing flame edges at three instants in time.

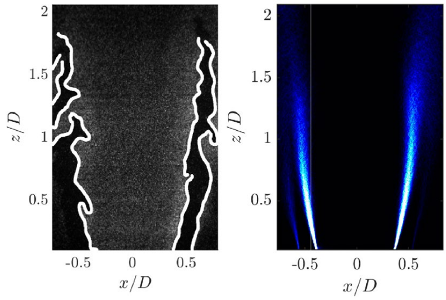

(a) Left: Raw PLIF image highlighting the location of detected edges, $L(x, y, z, n, t)$. Right: averaged occupancy rate from a single slice in real space, $\overline{L}(x, y, z, n)$.

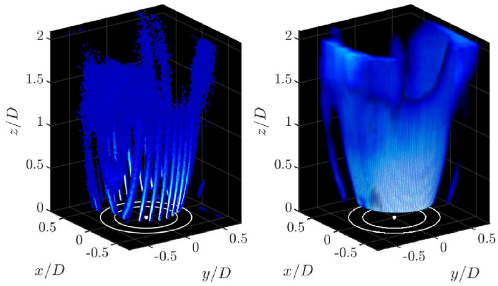

(b) Left: example showing 10 slices of projected edges in real space. Right: Remapped discretised volumetric distribution of FSD.

Fig. 2 Example calculation of volumetric Flame Surface Density

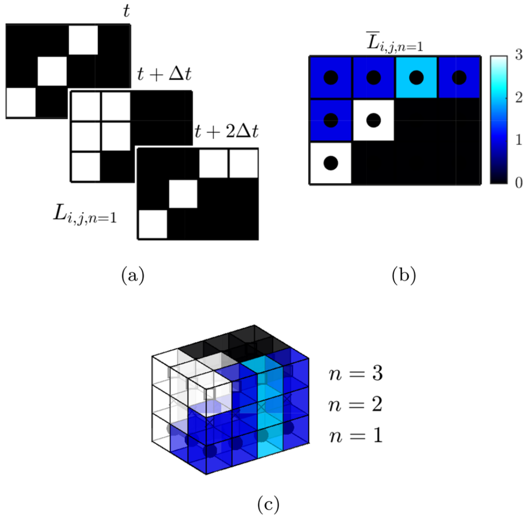

Fig. 3 Illustration of FSD calculation: **a** time averaging of flame edges, **b** time averaged flame edge for sheet number 1, dots represent center of pixel **c** Three-dimensional view of multiple sheets in real space prior to FSD calculation

It is important in the later reprojection step to ensure that the edge point count is not biased towards any of the three sampling directions (two in the imaging plane, and one in the laser sheet scanning direction). This is accomplished by binning the flame edge images such that the final image resolution matches the sheet spacing of 0.2 mm, preventing biasing of the FSD calculation in the laser scan direction. The laser sheet orientation is very close to orthogonal with the voxel layers in the discretised volume, meaning a correction is not required to account for the divergence of adjacent laser sheets in different parts of the volume.

The probability of flame front location or occupancy rate, $\overline{L}(i,j,n)$, is calculated by time-averaging all binary images from a single laser sheet location, n. Each pixel in $\overline{L}(i,j,n)$ was then projected onto the global coordinate system using the laser sheet and camera calibration models, to calculate the real space distribution of the time-averaged occupancy rate, $\overline{L}(x,y,z,n)$, for each laser sheet location, n. The result of the projection operation can be seen for a number of example planes from a single scan direction in Fig. 2. Again to illustrate the process schematically, an example of this calculation is shown in Fig. 3b, with the occupancy rate calculated from the three binary images in Fig. 3a.

To create a regular array of data, a volume was discretised at a resolution of 5 voxels/mm which was chosen to match the sheet displacement resolution in the scan direction, and the scattered data, $\overline{L}(x,y,z,n)$, was remapped onto this volume using a scattered linear interpolation scheme. This volumetric distribution of edge locations represents the time-averaged flame surface area, $\overline{A}_f(x,y,z)$. Again a visual representation of multiple sheets and respective voxels with $\overline{L}(x,y,z,n)$ are shown schematically in Fig. 3c as an example of this process. The FSD can then be calculated using Eq. 1 (Zhang et al. 2014),

$$\mathrm{FSD} = \lim_{\Delta x \to 0} \frac{\langle \overline{A}_f \rangle}{\Delta x^3} \tag{1}$$

where $\langle \overline{A}_f \rangle$ is the time-averaged surface area of flamelets, spatially integrated within a $5 \times 5 \times 5$ voxel cubic interrogation volume, Δx. The interrogation volume dimensions were chosen based on the findings of Donbar et al. (2000), and is smaller than the flame brush width. The FSD at each voxel location is therefore determined by the sum of $\overline{A}_f$ over the interrogation volume centred at that voxel, normalised by the interrogation volume. The volumetric FSD distribution of the experiment are shown in Fig. 2. The FSD is approximately proportional to the time-averaged distribution of the heat release rate, given that the heat release rate per flame surface area is relatively constant for fuel-air mixtures with unity Lewis number and are in the wrinkled flamelet regime, $Q(x,y,z) \approx \mathrm{FSD}(x,y,z)$.

It is useful to examine the local azimuthal variation of the heat release rate around the flame, and therefore the domain can be recast in cylindrical polar coordinates (as in Fig. 1c), and wedge shaped regions investigated. Each wedge, Q_θ, corresponds to the integrated FSD within a range of local azimuthal angles and downstream distances, as defined by Eq. 2.

$$Q_{\theta,z} = \sum_{r} \sum_{z=z_1}^{z_2} \sum_{\theta=\theta_1}^{\theta_2} \mathrm{FSD}(r,\theta,z) \tag{2}$$

Here, a centre wedge angle, θ_c, and angular wedge extent, θ_w, are defined to produce the two azimuthal limits, $\theta_{1,2} = \theta_c \mp \theta_w$, and z_1 and z_2 are the longitudinal limits. A wedge angle of $\theta_w = 10°$ is employed in the present study.

3 Synthetic experiment method

Despite previous implementations of Scanning LIF, the influence of experimental parameters have not been fully described. Therefore, in the current study, synthetic PLIF images were generated and processed in order to optimise the setup, and also to better understand any inherent weaknesses of the approach. The use of a synthetic experiment allows an ideal synthetic flame object of known geometry to be defined, enabling quantification of the errors associated with the reconstruction procedure, and the experimental parameters. Specifically, the synthetic experiment was used to understand the error associated with the laser sheet thickness, spacing, and orientation as well as image noise. Tests were also conducted to understand the ability of the method to resolve contorted flame fronts.

3.1 Synthetic PLIF image generation

Figure 4 shows a flow diagram of the synthetic experiment process, which will now be described. In order to generate synthetic PLIF images, an ideal flame surface object is first defined, which describes the exact location of a surface. For simplicity a conic section was used to define the surface position, as this is geometrically similar to a bluff body stabilised V-flame. The cone surface is defined by $r^2 = (5.7z + D_b/2)^2$ over a domain size of $40 \times 40 \times 40\ \mathrm{mm}^3$.

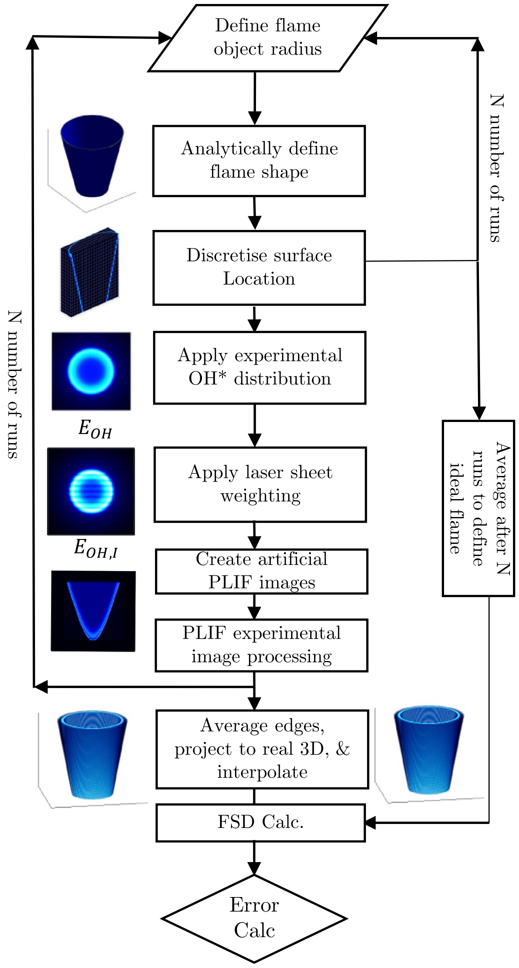

Fig. 4 Synthetic PLIF image generation and processing flow diagram

The present approach is aimed at reconstructing the time-averaged flame shape. Therefore, the radius of the ideal flame object was varied to replicate the unsteady flame motion. Flame objects were created with radii following a probability density function determined from the experimentally measured flame brush. In practice the variation of object radius is Gaussian in form with a standard deviation of 1.3 mm. A total of 160 instantaneous snapshots are used to simulate each time-averaged condition.

To replicate flame front curvature effects, sinusoidal variations of varying amplitude and frequency were added to the conic section surface. The amplitude and frequency were selected in order to replicate similar levels of curvature measured directly from the extracted flame edges. However, adding realistic levels of flame front curvature did not significantly affect the reconstructions, and therefore for brevity, these results are not reported herein.

Surface points on each flame object were first determined from the cone surface equation and then discretised onto a 3D array of voxels by using a scattered linear three-dimensional interpolation scheme. The volume was discretised at 5 voxels/mm which is consistent with the experiment. The average of all discretised flame objects is described as the ideal flame object surface, $\overline{A}_{f,ideal}$, and flame surface density FSD_{ideal}.

A representative experimental flame front intensity profile was determined directly from the detected flame front edges captured by the experimental measurements. This is described in detail in Appendix 1.

The distribution is applied normal to the flame surface location in order to produce a discretised ideal three-dimensional intensity distribution of OH. For convenience this operation is performed directly on the discretised flame object. The flame surface normal at each nonzero voxel in this discretised object is defined based on the equation of the cone, and intensity is distributed along this normal, scaled by the original voxel intensity, to produce a discretised flame object OH distribution, E_{OH}. The resulting intensity volume, E_{OH}, is then used to produce artificial PLIF images.

To replicate the fluorescence of OH, the laser illumination was modelled with a Gaussian intensity profile. An equation of plane was used to define the laser sheet location, and the illumination intensity in the volume was varied according to the normal distance from the plane, using Eq. (3) similar to that represented by (Lawson and Dawson 2014).

$$I(\mathbf{X}) = \exp(-8(d)^2/\delta^2) \tag{3}$$

Here $\mathbf{X}$, defines the coordinates of a plane, d represents the normal distance from the plane, and δ, represents the sheet thickness. In this synthetic study, the laser sheet normal is oriented in the y direction. The resulting distribution was used to calculate the illumination in each voxel of the discretised volume, E_{I}. The illumination volume was then used to scale the intensity in E_{OH} for each sheet location to produce $E_{\mathrm{OH,I}} = E_{\mathrm{OH}} \cdot E_{\mathrm{I}}$. For simplicity, laser sheet inhomogeneity and laser absorption across the field of view were neglected as these effects are removed somewhat through intensity correction when post processing PLIF images.

Synthetic PLIF images were generated by projecting each nonzero voxel of the volume, $E_{\mathrm{OH,I}}$, onto the image plane, using a simple pinhole camera model, with a similar spatial resolution as the experimental setup. The use of an ideal camera model eliminates potential error from camera calibration, although this can be taken into account through purposeful misalignment during parametric testing. It should be noted that while these synthetic images are not fully representative of the actual experimental images, they are sufficient for optimising the processing procedure, and provide insight into potential sources of error.

Synthetic images were produced for each laser sheet location, n, and were passed through the edge detection algorithm, to evaluate the simulation edge occupancy rate, $L_{sim}(i, j, n, N)$, in the image plane for each flame object snapshot, N. After each loop, the radius was updated and a new snapshot was processed. Averaging all snapshots allowed the average edge occupancy rate $\overline{L}_{sim}(i, j, n)$ to be calculated. The same process that was applied to the experimental results is then used to reconstruct the 3D discretised volumetric representation of the flame surface density, $\mathrm{FSD}_{sim}(x, y, z)$. This can then be compared to an ideal flame object flame surface density, FSD_{ideal}, as described in Sect. 3.2.

3.2 Error estimation

Defining the ideal flame surface with an exact expression allows for a direct assessment of reconstruction accuracy, which is quantified through the normalised correlation coefficient R in Eq. (5), and is similar to that defined by (Elsinga et al. 2006).

$$R = \frac{\sum_{x,y,z} \mathrm{FSD}_{\mathrm{ideal}}(x, y, z) \cdot \mathrm{FSD}_{\mathrm{sim}}(x, y, z)}{\sqrt{\sum_{x,y,z} (\mathrm{FSD}_{\mathrm{ideal}}(x, y, z))^2 \cdot \sum_{x,y,z} (\mathrm{FSD}_{\mathrm{sim}}(x, y, z))^2}} \tag{4}$$

The combination of a cylindrical flame object with a single scanning direction introduces asymmetry, and it is also of interest to consider the local reconstruction quality. The domain can be recast in cylindrical polar coordinates, and the reconstruction quality of wedge shaped regions can be investigated by applying Eq. 4. Again a wedge angle of $\theta_w = 10°$ is employed.

$$R_\theta = \frac{\sum_{r,z} \sum_{\theta=\theta_1}^{\theta_2} \mathrm{FSD}_{\mathrm{ideal}}(r, \theta, z) \cdot \mathrm{FSD}_{\mathrm{sim}}(r, \theta, z)}{\sqrt{\sum_{r,z} \sum_{\theta=\theta_1}^{\theta_2} \mathrm{FSD}_{\mathrm{ideal}}(r, \theta, z)^2 \cdot \sum_{r,z} \sum_{\theta=\theta_1}^{\theta_2} \mathrm{FSD}_{\mathrm{sim}}(r, \theta, z)^2}} \tag{5}$$

4 Synthetic experiment results

A series of parametric studies were conducted to help understand the accuracy of the method to changes in laser sheet thickness, sheet overlap, and image noise.

The sensitivity of reconstruction quality due to varying sheet thicknesses and noise are presented in Fig. 5a. A fixed sheet overlap of $\Delta\delta = 0\%$ is applied, and spatially white, non zero mean and random noise is added with levels ranging from $p = 0\%$ to 30%. The noise level is with respect to the maximum intensity of each image. For thin sheets the reconstruction accuracy is high, and as sheet thickness increases, the reconstruction accuracy decreases slowly. Thin sheets capture images with sharp OH gradients, improving the edge finding, and leading to higher reconstruction accuracy. In the experiment the laser sheet thickness is controlled by arrangement of the sheet optics, and cannot be arbitrarily thin. However, the thickness of $\delta = 0.4$ mm yields high correlation values, giving confidence that this is suitable. The addition of noise also reduces the reconstruction accuracy, which is expected since it decreases the precision of the edge finding algorithm. It should be noted that while noise levels up to $p = 30\%$ were tested, these may be considered extreme, and typically experimental noise is around $p \approx 10\%$. Even a modest addition of noise at this typical level results in a significant reduction in reconstruction correlation, which is discussed further below.

The sheet location is controlled in the experiment through the galvanometer mirror alignment, allowing an almost arbitrary choice of sheet overlap, $\Delta\delta$. Increasing the overlap increases the amount of data available, resulting in a potential improvement in resolution in the scan direction. However, when sheets overlap, the measurements are no longer necessarily independent. The reconstruction sensitivity to overlap was investigated based on a sheet width of $\delta = 0.4$ mm, with zero image noise. While the combination of overlap and sheet width define the number of sheets required to illuminate the domain, E_{OH}, for nonzero overlap values, a total of 100 sheets were used to illuminate the $\Delta\delta = 0$ case. Figure 5b shows that the reconstruction accuracy increases marginally with increasing overlap, reaching a maximum at $\Delta\delta \approx 50\%$. Therefore, while high overlap is desirable, the greater the overlap, the greater number of laser sheet locations will be required to illuminate a volume of interest, requiring a greater amount of data to be stored and processed. Based on these simulations an overlap of $\Delta\delta = 50\%$ was chosen in the current experiment.

The use of a rotationally symmetric flame object allows the local azimuthal reconstruction accuracy, R_θ, to be assessed in order to further demonstrate the location

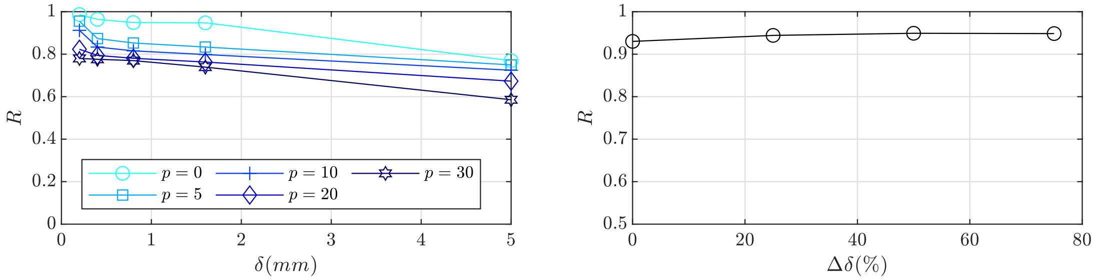

(a) Laser sheet thickness, δ

(b) Laser sheet overlap, $\varDelta\delta$

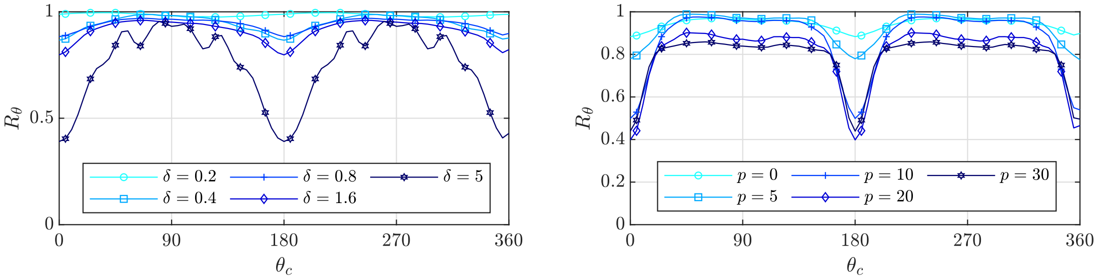

(c) Sheet thickness

(d) Image noise

Fig. 5 Global reconstruction quality as a function of laser sheet thickness and overlap **a** and **b**. Default values of $\delta = 0.4$ mm, $\varDelta\delta = 0\%$ (zero percent overlap represents sheets that are adjacent to each other), and zero image noise were used. Local reconstruction quality as a function of azimuthal location with respect to **c** sheet thickness with 50 percent overlap and **d** image noise with $\delta = 0.4$ mm and $\varDelta\delta = 50\%$

of the reconstruction error, as shown in Fig. 5c. A clear angular dependence on reconstruction accuracy can be observed. The highest correlation values are seen at angles of $\theta_c = 90°, 270°$, where the laser sheet is almost perpendicular to the flame surface. The reconstruction accuracy is shown to decrease with orientation angle, reaching a minimum for $\theta_c = 0°$ and $180°$, at which angles the laser sheet normal and flame surface normals are close to parallel. The local reconstruction accuracy also depends on the laser sheet width, with larger reductions in accuracy observed at $\theta_c \approx 0°$ for larger laser sheet widths in comparison with $\theta_c \approx 90°$.

This angular dependence of the reconstruction accuracy is an important source of bias error in the current method, which can be explained through the change in OH gradients on synthetic PLIF images. When laser sheets are orthogonal to the flame surface, the synthetic PLIF images have high OH gradients, which can be easily identified using the edge detection algorithm. However, when the laser sheet and flame surface alignment is closer to parallel, due to the finite laser sheet thickness, the OH gradient becomes much shallower. Shallower OH gradients result in larger uncertainty in the edge detection stage, resulting in lower reconstruction accuracies. Similarly, increasing the laser sheet thickness also reduces the magnitude of the OH gradient, resulting in reduced accuracy.

The local azimuthal reconstruction was also evaluated for simulations of different noise levels. A sheet thickness of $\delta = 0.4$ mm with an overlap of $\varDelta\delta = 50\%$ was used, and the noise sensitivity is presented in terms of the local reconstruction accuracy in Fig. 5d. The addition of noise reduces the reconstruction accuracy. However, the greatest decrease in accuracy occurs when the laser sheet and flame surface are close to parallel, $\theta_c \approx 0°$ and $180°$. The effect of noise compounds the shallow OH gradients resulting in large positional errors in the edge finding.

To better understand the decrease in accuracy observed, Fig. 6 shows a visual representation of a single slice of the FSD_{sim} volume in the $x - y$ plane for selected laser sheet thicknesses and noise levels. When the laser sheet is thin ($\delta = 0.2$ mm) and for zero image noise ($p = 0\%$) the reconstruction is symmetric and has uniform intensity. However, when the laser sheet thickness is increased the upper and lower edges of the reconstructed object lose intensity, and for large sheet thicknesses the circular shape becomes distorted. The detected edges show larger spatial deviations, and in some cases the edge detection fails completely and edges are not captured at all. This bias is further amplified

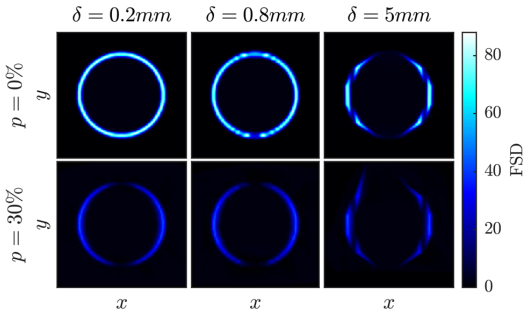

Fig. 6 Simulation result of $x - y$ slice at $z = 20$ mm, representing the reconstructed flame object, FSD_{sim} with varying sheet thickness, δ, and image noise, p

by the addition of noise which reduces the ability of the edge detection algorithm to find edges at the upper and lower parts of the object shown in Fig. 6. At these locations the laser sheet orientation is tangent to the flame surface. Therefore, while Fig 5c does not show any bias errors for very thin laser sheets ($\delta = 0.2$ mm), bias is always observed in the presence of noise.

The synthetic Scanning PLIF experiments demonstrate the reasonable accuracy that can be expected based on the obtainable experimental laser sheet thickness and an overlap of 50%, even for reasonably low signal to noise ratios. However, the numerical study also demonstrated a clear bias associated with the orientation of the laser sheet and flame surface. While high values of correlation coefficient are shown for thin sheets and low noise levels, positional biases in finding edges close to flame fronts may never be completely eliminated, which is discussed further in Appendix 2. It is worth highlighting that such a bias will not just affect the present measurements, but given the highly turbulent nature of many flows of interest, such errors may be present but not reported in a wide range of studies. To mitigate this bias error it was therefore decided to employ two almost perpendicular scan directions as described previously.

5 Experimental results

5.1 OH* chemiluminescence

Before presenting the OH PLIF results, it is useful to describe the flame using a conventional integrated line of sight method. OH* images were captured of the flame from the $x - z$ plane and overhead, and are shown in Fig. 7. The flame structure is similar to that observed previously (Mazur et al. 2019), with the flame stabilised primarily along the inner shear layer separating the annular jet and the recirculation zone above the bluff body. Some flame elements are also observed close to the flame tip along the outer shear layer. Despite the nominally axisymmetric inlet conditions, the flame shows significant asymmetry. This can be observed in the side view, with higher intensity observed on the right hand side of the flame. The overhead view also shows clear asymmetry between regions close to the inner and outer annulus.

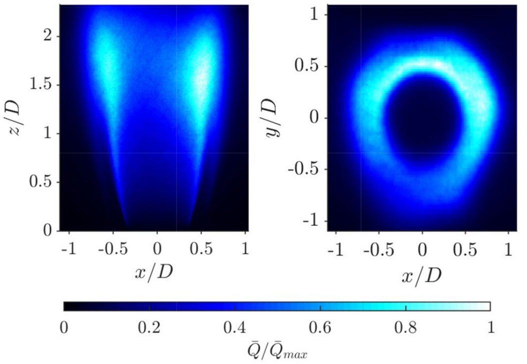

Fig. 7 Normalised averaged OH chemiluminescence of 10000 time resolved images from side view of Scan XZ (left) and top view (right). Colour bar represents the time-averaged mean intensity, $\bar{Q}$ normalised by its maximum, $\bar{Q}_{max}$

The asymmetry has a number of potential sources: First, the bluff body is centred with three grub screws which is known to introduce azimuthal asymmetry around the flame (Æsøy et al. 2020); second, the flame is confined in annular geometry, with a quartz outer annulus, a metal inner annulus, and neighbouring flames either side; third, the bluff body is expected to be imperfectly centered, and small manufacturing asymmetries may also be present; and forth, the flow from the cylindrical plenum upstream may not be perfectly uniform, due to the relatively short inlet tube length, l_i. From above, the OH* distribution has a slightly triangular shape, which is perhaps a result of the three grub screws. The region closest to inner wall has a higher intensity and appears wider in comparison with the region close to the outer wall, which is likely a result of the differing thermal conductivities associated with quartz and metal enclosure walls, and potentially the curvature of these. While it is difficult to fully describe the asymmetry based on integrated line of sight methods, this asymmetry will be described further through the volumetric PLIF measurements presented in the next section.

5.2 Instantaneous OH PLIF measurements

The time-dependent behaviour of the flame can be directly assessed using instantaneous snapshots obtained from the

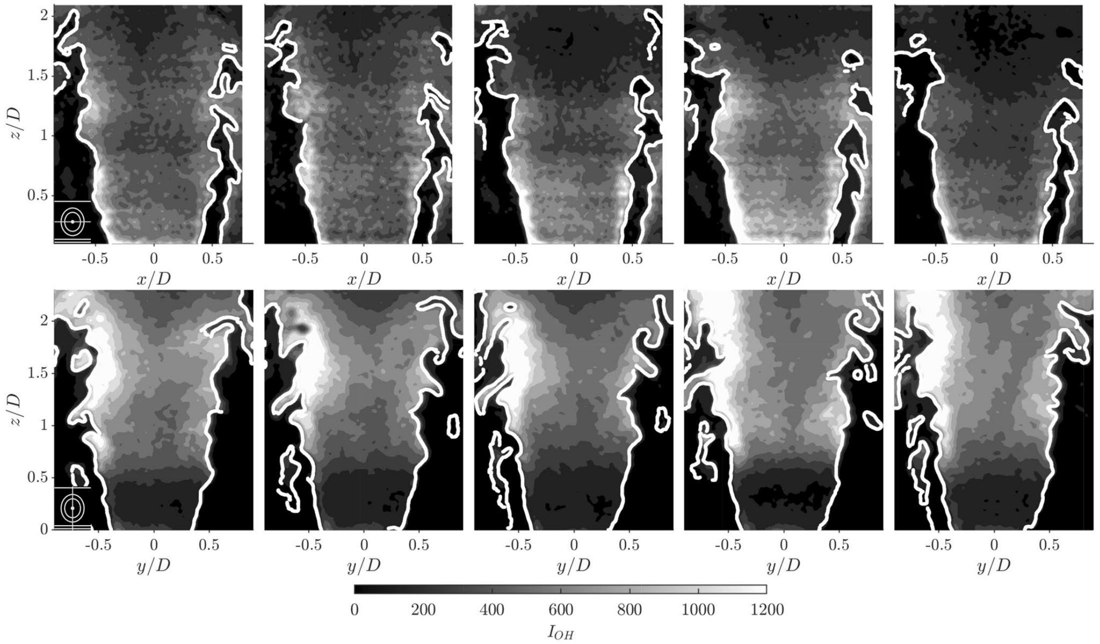

Fig. 8 Time Resolved OH PLIF images from two scan directions, along burner centre. Raw PLIF images were preprocessed using a Gaussian filter. Scan XZ (top row), Scan YZ (bottom). Δt of 0.2 ms between each image. Colour bar represents, I_{OH}, spatial distribution of OH fluorescence

high speed OH-PLIF measurements. Processed PLIF images are shown in both scan directions in Fig. 8, with the laser sheet in both instances passing through the bluff body centre. A small schematic representation of the burner showing the laser sheet orientation is included in the lower left corner of each time series. The PLIF images clearly show a cross section of the flame, cutting through the annular jet in two locations. However, it is interesting to compare these two cross plane slices.

The top row images were taken when the laser sheet was approximately aligned with the $x-z$ plane, and therefore this plane highlights the influence of flame-flame interactions between adjacent flames in the annulus. The $y-z$ images in Fig. 8 highlight the flame interaction with the annular walls. The flame fronts for both planes are highly contorted, due to the turbulent nature of the flow. Large scale flame wrinkles can be observed forming in the flame sheet as the flow moves downstream, resulting in flame sheet fragmentation in the upper part of the domain. In comparison with the bottom row, the flame slices in the top row exhibit a larger number of flame elements stabilised along the outer shear layer. The presence of a neighbouring flame is likely to increase the outer recirculation zone temperature, resulting in a higher probability of stabilising the flame on the outer shear layer. The presence of flame elements in the outer shear layer permits more flame channel closing events to occur, where flame fronts stabilised on inner and outer shear layers propagate into each other resulting in the formation of pockets of unburnt gas Worth and Dawson (2019). The events can be identified on the right hand side of flame in the top row, and unburnt gas pockets are observed to pinch-off and then be advected downstream.

5.3 Planar distributions of flame occupancy rate

Before considering the reconstructed volumetric distribution, it is useful to examine the mean projected occupancy rate, $\overline{L}$, as way to better understand the previously observed asymmetries. Figure 9 shows the distribution of $\overline{L}$ for both scan directions, at cross section locations through the flame. To help identify the laser sheet orientation, again a small schematic representation of the burner is included in the lower left corner of each sub figure.

Comparing first the $\overline{L}$ distributions when the laser sheet passes through the burner centre (middle column), the change in flame height can be clearly seen. In the $x-z$ plane in the upper row, the turbulent flame brush reaches a maximum height of $z/D \approx 1.5$, whereas in the $y-z$ plane it extends downstream much further to $z/D \approx 2.2$. Asymmetries are also observed between left and right hand sides

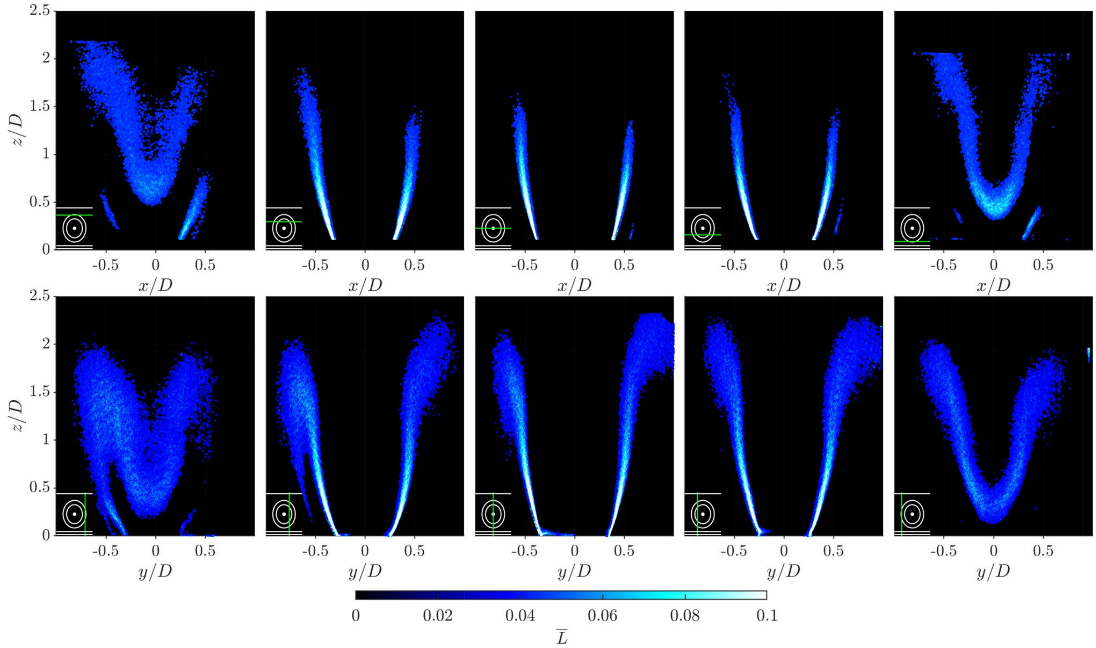

Fig. 9 Slices of projected averaged flame occupancy rate, $\overline{L}$, in Scan XZ (top row) and Scan YZ (bottom row). Slice position represented by green line relative to the bluff body from overhead view of the burner, laser positions are at -0.48D, -0.24D, 0D, 0.24D, 0.48D in the direction of each scan

of the flame in both scan directions. In the $x - z$ plane in the upper row, the slightly higher distribution on the left hand side is likely to result from imperfections in the bluff body alignment. However, a much larger asymmetry is observed in the $y - z$ plane in the bottom row, with a higher and wider flame brush that interacts with the inner annular wall on the right hand side, in comparison with the shorter more compact flame brush on the left hand side.

The source of this asymmetry may be due to either the effective confinement of the flame, or the material properties of the inner and outer walls. Due to the annular enclosure, the flow has a greater area to expand into towards the outer annular wall in comparison with the inner annular wall. This is likely to affect the strength of the recirculation zones, and the re-ignition of the flame along the outer shear layer. Furthermore, the thermal conductivity of the inner steel wall is approximately 10 times that of the outer quartz wall, potentially altering the recirculation zone temperature and re-ignition probability.

The synthetic experiment performed in Sect. 4 demonstrated that as the laser sheet and flame surface alignment becomes close to parallel, the accuracy of the method decreases. This can clearly be seen in the experimental results, when considering off-centre laser sheet locations, particularly those close to the flame edge. For example, in Fig. 9 the left and right hand side columns show slices through the flame close to the edge, and these show notably wider and more diffuse $\overline{L}$ distributions in comparison with the centre cross sections. The wider distributions are a result of the laser sheet and flame surface parallel alignment, which lowers the OH gradient magnitude, increasing the error associated with flame edge detection.

However, despite these wider distributions, the flame shape is still captured relatively accurately. To demonstrate this the full three-dimensional FSD was evaluated, using the procedure outlined in Sect. 2. The central cross plane slice locations can then be compared by superimposing the two independent measurements from the different scan directions. Selecting the centre cross plane sample for this comparison means that from one scan direction the laser sheet is approximately orthogonal to the flame surface, while from the other direction it is approximately parallel, allowing the worst case alignment to be evaluated. The comparison is presented in Fig. 10, which shows superimposed contours corresponding to a single plane of the 3D reconstructed FSD distribution from the two scan directions. Given the variation in FSD intensity, the contour levels do not match each other. However, the similar contour shape distributions

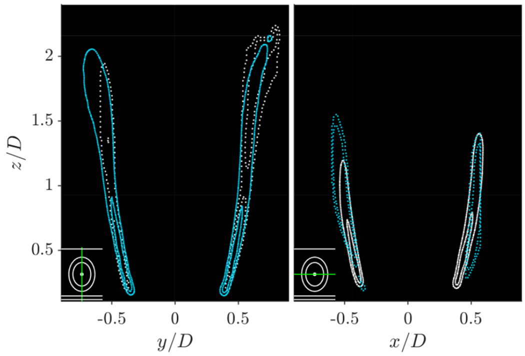

Fig. 10 Comparison of centre line slices of both scan directions outlined as a contour plot (iso-value= 0.6FSD$_{max}$) capturing the flame shape of the represented slice, blue represents Scan YZ and white represents Scan XZ. The solid and dotted line represents the orthogonal and parallel slice (laser sheet to flame edge orientation) of each scan direction, respectively. Subplot represents position of the slices relative to the annular combustor geometry

indicate that both scanning directions capture similar spatial distributions of FSD. The largest differences are observed in the $y-z$ plane, where the distribution close to the outer annular wall is notably wider when the reconstruction based on laser sheets aligned in the $x-z$ direction is considered. While not accounting entirely for this difference, the width of the distribution in the $x-z$ direction is affected by the size of the volume reconstructed, as data from laser sheet locations close to the flame edges had to be removed, due to the very low gradient values of the OH distribution, which prevented accurate flame edge detection. However, most of the differences are expected to arise from the differences in the OH gradients in the PLIF images from the two different scan directions, which the method has already been demonstrated to be sensitive towards. To further quantify this bias error, the entire FSD distribution in the measurement planes shown in Fig. 10 was integrated separately from the two separate scanning directions. This represents a worst case estimate of the bias error. It was found that the FSD in the $y-z$ and $x-z$ planes were under predicted by 68 and 51% by Scan XZ and Scan YZ, respectively. The larger FSD bias in the $y-z$ plane demonstrates that the underprediction is greater when the flame is close to the annular walls.

5.4 Three-dimensional flame surface density

Isosurfaces of the 3D FSD are shown in Fig. 11, based on both the two independent scan directions, and the combination of these. The combined volume is reconstructed by averaging both volumes in each scan direction as described in Sect. 2 into a single discretised domain, therefore representing the linear addition of the two independent scans.

The flame shape is observed to vary in height with local azimuthal location, θ, with the highest locations occurring close to the inner and outer annular walls. A similar flame shape can be observed in scans from both directions, albeit with portions of the flame surface poorly resolved in regions where the alignment of the laser sheet and flame surface were close to parallel. Therefore, a single scan is capable of broadly capturing the structure of the current flame, but care must be taken when interpreting the variation of FSD magnitude.

The independent measurements from the two scan directions raise the prospect of defining a correction factor to take account of the FSD magnitude change based on the laser sheet orientation. However, of the simple correction methods based on linear variation in the azimuthal polar or linear Cartesian directions, none were found that could adequately account for the observed intensity variations. However, by scanning from two separate directions, the weakness of the method to such bias error can be largely overcome, and the

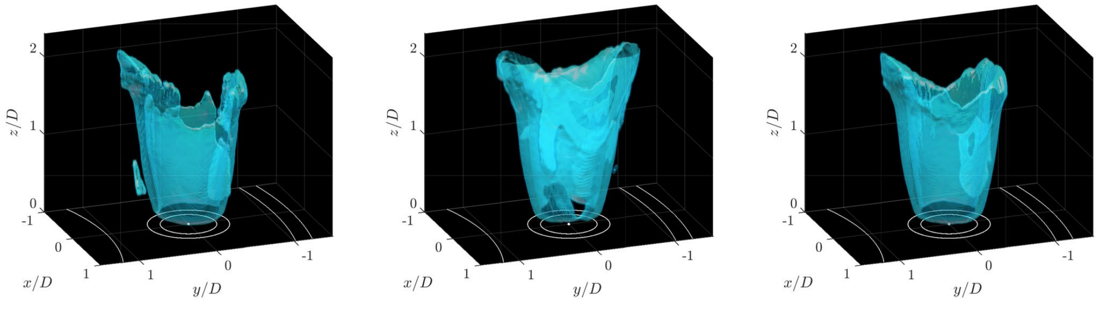

(a) (b) (c)

Fig. 11 Isosurfaces of 3D FSD. (a) Scan XZ, (b) Scan YZ, (c) Combined Scan YZ and XZ. White lines show schematic representation of annular chamber and burner inlet. Isosurface level is the spatial average of the FSD volumetric distribution in the combined reconstruction, shown on the right hand side of Fig. 11, produces a more uniform FSD distribution.

Flame asymmetry and orientation dependence of the reconstruction can be more accurately assessed by evaluating streamwise cross-sectional planes, as presented in Fig. 12. Three rows are presented, showing the two independent scan directions, and the combination of these. For each reconstructed volume $x - y$ plane slices are plotted for a range of downstream measurement locations, which is indicated in a small schematic in the lower left hand corner of each sub figure. Additionally, as a visual aid, the location of the circular bluff body and injection tube are show schematically, as solid white lines.

As described previously, the flame structure is described by all three rows. While the flame surface is poorly resolved in the top and middle row, when the laser sheets are almost parallel with the flame surface, the combination of these data sets reduces the underestimation of FSD significantly, and the flame structure is therefore best represented in the bottom row. Close to the dump plane, at $z/D = 0.5$, the flame structure is almost axisymmetric, with a diameter of approximately D. At increasing distance above the dump plane the flame expands radially, and the flame brush thickens. The distribution of FSD also becomes more asymmetric with increasing height, with lower FSD intensity where the flame is closest to the neighbouring flames ($|x/D| > 0.4$), as a result of the reduced flame length in these regions.

These cross plane slices clearly show the underestimation of the FSD due to the laser sheet alignment angle. In the upper row at $z/D = 0.5$ the left and right hand sides of the FSD distribution are around twice the intensity of the top and bottom edges. Similarly, in the middle row at $z/D = 0.5$ the top and bottom edges of the FSD distribution are much higher intensity than the left and right hand side.

It is also interesting to note that at the extremities of the flame ($|x/D| > 0.5, |y/D| > 0.5$) some flame elements are also captured in the outer shear layer. These flame elements appear only at the effective corners of the domain, and are likely a result of the complex recirculation zone pattern generated in the annular enclosure. This allows flame elements to be stabilised only at certain azimuthal locations, adding additional asymmetry to the flow. While asymmetry arising from the enclosure is clearly observed from the reconstructed FSD, asymmetry arising from other sources such as the grub screws, and flow conditioning from the plenum flow were not observed, meaning these are likely to play a more minor role in the symmetry of the mean flame structure.

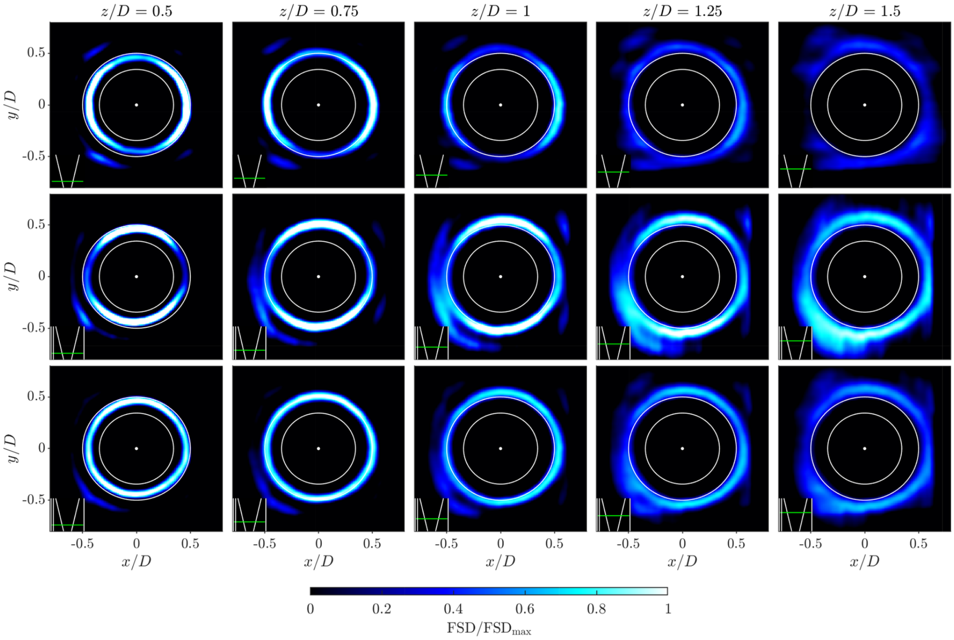

Fig. 12 Slices of FSD in the $x - y$ plane for Scan XZ (top row), Scan YZ (middle row), and combined Scan XZ and YZ (bottom row). Slice location represented by green line in bottom left corner schematic

5.5 Integrated local heat release rate

To provide a more quantitative assessment of the flame symmetry, the 3D heat release rate was integrated in wedge shaped regions (Eq. 2) over a range of downstream locations, and is presented in Fig. 13. The integrated regions were normalised by the maximum heat release rate of the wedges rotated around the entire flame, $Q_{\theta,max}$, to assess the local heat release rate contribution to the total heat release rate.

The fluctuation of the heat release rate and the loss of symmetry increases with downstream distance. In Fig. 13a, the HRR is represented for the base of the flame ($Z/D < 0.75$). When considering the individual scan directions a decrease in the HRR which represents the loss of axisymmetry is observed at locations orthogonal to the scan direction, that is $\theta_c \approx 0°$ and $\theta_c \approx 90°$ for Scan XZ and Scan YZ, respectively. However, the reconstruction of the flame based on both scan directions produces a fairly constant HRR, demonstrating the symmetry of the flame close to the exit of the injector. Similar symmetry features can be seen when integrating the flame over the middle region ($0.75 < Z/D < 1.5$), as shown in Fig. 13b, and again the combined case eliminates some of the asymmetric variations in intensity. Small peaks are also present for all reconstructions that highlight locations corresponding to flame elements stabilised in the outer shear layer. These can seen at locations $\theta_c \approx 45°, 130°, 220°$ and $320°$.

Larger departures from axisymmetry are visible in Fig. 13c, which shows the upper portion of the flame. The HRR decreases significantly at $\theta_c \approx 90°$ and $270°$ corresponding to significant variations in flame length due to the presence of walls or neighbouring flames. The combined case is dominated by data from scan direction YZ since the near walls regions, which contribute most in this part of flame, were not well resolved in Scan XZ. The large asymmetry in this upper region contributes significantly to the total integrated distribution shown in Fig. 13d. Although regions with a greater amount of flame elements stabilised in the outer shear layer can still be seen, these features are less prominent in the overall integrated FSD. A comparison of integrated FSD and overhead OH* chemiluminescence (calculated from the overhead image shown in Fig. 7) is also presented in Fig. 13d. There is reasonable agreement between integrated OH* and FSD measurements in some regions, with the former picking up many of the peaks and dips associated with the azimuthal variation of HRR around the flame. However, the OH* prediction of HRR is lower close to the outer wall ($\theta_c \approx 330°$), which may be caused by the differing role of heat losses or flame quenching in the two methods.

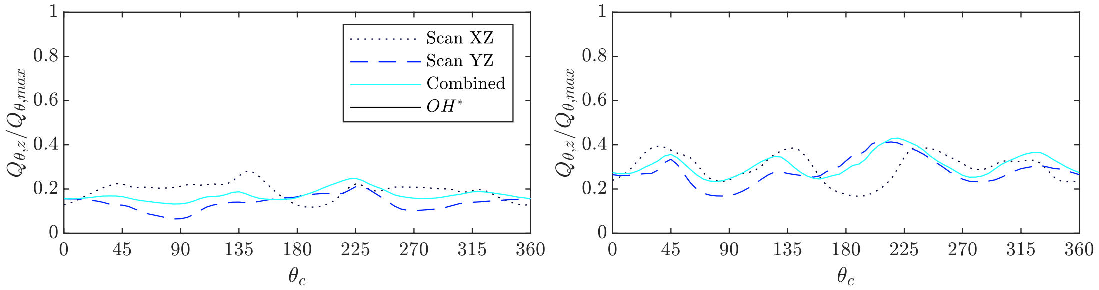

(a) $Z/D < 0.75$ (b) $0.75 < Z/D < 1.5$

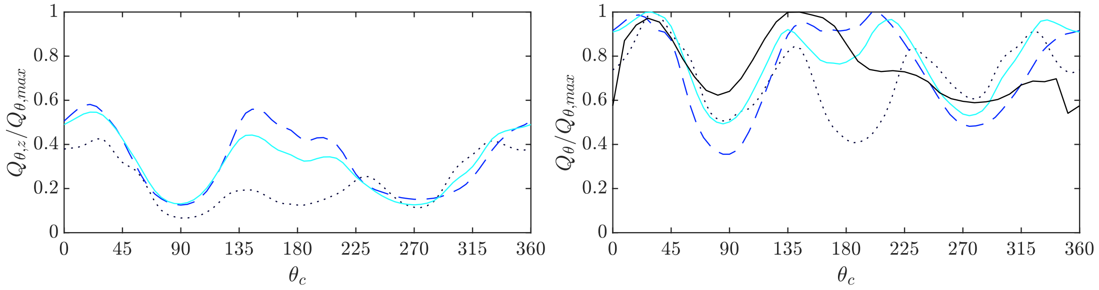

(c) $Z/D > 1.5$ (d) $Z/D > 0$

Fig. 13 Heat release rate of azimuthal wedges over the range of upstream positions of the flame normalized by maximum flame heat release rate of the entire flame for Scan XZ - dotted line, Scan YZ - dashed line, and the combination of both - solid line

6 Conclusions

In this study a three-dimensional reconstruction of a non-swirling bluff body stabilised flame inside an annular combustor is performed using a novel variant of Scanning PLIF. Having access to the three-dimensional heat release rate distribution provides insight into the flame structure and asymmetry in response to asymmetric confinement.

A synthetic PLIF study was first conducted in order to optimise the experimental setup, and also to investigate the source of bias error in the reconstructions. The numerical study demonstrated the reliability of the edge detection, and the reconstruction procedure, as well as justifying the choice of experimental laser sheet thickness and sheet overlap parameters. A significant source of bias error was identified, both in simulations and in the later experiments, which occurs when the flame front and laser sheet approach parallel alignment. A similar source of error may be present to some degree in all PLIF experiments, requiring the careful interpretation of results.

To address this issue, experimental measurements were conducted from two orthogonal scanning directions, with the results analysed both separately and through a combined FSD calculation. Reconstructions from the different scanning directions were showed to resolve similar flame shapes, but tangentially aligned regions produced a bias error when determining the magnitude of FSD. However, combining data from two orthogonal scans, largely resolved this bias, returning largely axisymmetric distributions of the heat release rate.

Having access to the full three-dimensional heat release rate permitted a detailed assessment of spatial distribution of this. In this manner the asymmetry of a nominally axisymmetric flame subject to asymmetric confinement was been described, providing insights into the flame structure. The reconstruction demonstrated that the bluff-body flames stabilised in annular chambers are significant affected by the asymmetric confinement. The flame was longer when it was close to the annular walls in comparison to when it was close to a neighbouring flame, resulting in significant asymmetry.

This study outlined the importance of the laser sheet to flame edge relative orientation. Two laser sheet orientations were tested in this work, but in future work it be may be advantageous to consider other orientations, which minimise instants of parallel alignment; for example orienting the laser sheet parallel with the dump plane. This was not considered in this study due to the significant technical challenge it presents. The possibility of implementing a correction factor to overcome the FSD underestimation when using a single scanning direction should also be the focus of future developments. While multiple attempts at finding a suitable correction were attempted in the present work, a suitable correction method was not identified. A correction factor may have implications for other studies in which FSD is calculated on multiple planes of interest.

Appendix 1: Experimental determination of OH distribution

The OH distribution captured through PLIF is a complex function of many parameters, such as fluorescence detector efficiency and gain, radical concentration, and excitation efficiency (Kohse-Höinghaus 1994; Hassel and Linow 2000). While DNS has been used previously to simulate the OH distribution (Atkinson et al. 2014), in the present study a simplified approach is used. The volumetric OH distribution is determined by combining the ideal surface location for each snapshot with the experimentally measured OH distribution through a flame front. In addition to its simplicity, the advantage of this approach is that the important flame front intensity distribution in the synthetic images closely resembles that of the experiment.

The measured intensity distribution normal to the flame front at a single pixel location along the flame front was extracted close to the flame base, where a clear gradient distribution was present. Similar distributions were extracted from a set of 10000 images. A single laser sheet location was used for this purpose, which was aligned with the centre of the bluff body, thereby cutting through the centre of the flame. The intensity profiles were then averaged, as shown in Fig. 14.

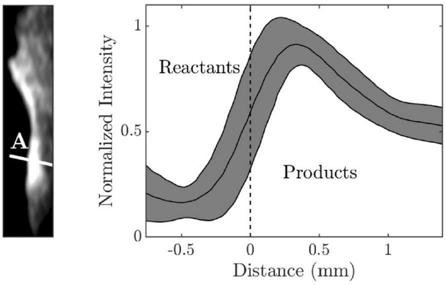

Fig. 14 Experimental determination of a mean OH intensity profile in terms of normal distance from the flame front. Left: enlarged raw PLIF image with line, A, representing normal to flame front from which intensity distribution was determined. Right: Black line represents mean OH profile, shaded region represents standard deviation of the extracted edge profiles. Dashed line indicates identified flame front location

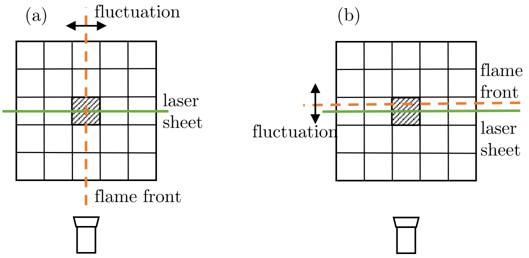

Fig. 15 Schematic of laser sheet position and flame sheet **a** perpendicular **b** parallel in orientation viewed from above with grid lines representing the voxels of the domain

Appendix B Positional bias in determining flame locations

This paper introduced the biases produced when finding edges of the flame and its respective sensitivity to laser sheet thickness and image noise. However, another form of bias exists simply based on the laser sheet position and the flame front orientation. To better demonstrate this effect consider Fig. 15a, which represents an overhead view of an experimental setup where the laser sheet and flame front are perpendicular to each other. For simplicity assume that the flame front only fluctuates perpendicular to the laser sheet. If the actual occupancy rate in a single voxel of interest (represented as the shaded voxel) is L_{act}, then the measured occupancy rate, $L_{measured}$, would be equal to the actual since the fluctuations in flame location will always be captured on the camera as it intersects with the laser sheet perpendicularly. In contrast consider the orientation where the laser sheet and the flame front are parallel as represented in Fig. 15b. This arrangement would result in $L_{measured} = 0$ since the flame front either does not intersect with the laser sheet, or is parallel to it when intersecting, making the gradient between products and reactants indistinguishable. This simple demonstration suggests that there is no ideal laser sheet that can completely resolve the flame when the mean flame shape produces fluctuations that are parallel to the laser sheet. It is worth highlighting that such a bias will not just affect the present measurements, but given the highly turbulent nature of many flows of interest, such errors may be present but not reported in a wide range of studies.

Acknowledgements The authors gratefully acknowledge financial support from the European Research Council (ERC): Grant agreement 677931 TAIAC.

Funding Open access funding provided by NTNU Norwegian University of Science and Technology (incl St. Olavs Hospital - Trondheim University Hospital).

Open Access This article is licensed under a Creative Commons Attribution 4.0 International License, which permits use, sharing, adaptation, distribution and reproduction in any medium or format, as long as you give appropriate credit to the original author(s) and the source, provide a link to the Creative Commons licence, and indicate if changes were made. The images or other third party material in this article are included in the article's Creative Commons licence, unless indicated otherwise in a credit line to the material. If material is not included in the article's Creative Commons licence and your intended use is not permitted by statutory regulation or exceeds the permitted use, you will need to obtain permission directly from the copyright holder. To view a copy of this licence, visit http://creativecommons.org/licenses/by/4.0/.

References

Æsøy E, Aguilar JG, Wiseman S, Bothien MR, Worth NA, Dawson JR (2020) Scaling and prediction of transfer functions in lean premixed H2/CH4-flames. Combust Flame 215:269–282

Atkinson C, Oberleithner K, Soria J (2014) PIV Illumination intensity: an unexpected source of error in particle displacement and calibration. In: 17th International symposium on applications of laser techniques to fluid mechanics, pp 7–10

Balachandran R, Ayoola B, Kaminski C, Dowling A, Mastorakos E (2005) Experimental investigation of the nonlinear response of turbulent premixed flames to imposed inlet velocity oscillations. Combust Flame 1430(1–2):37–55

Cai W, Li X, Li F, Ma L (2013) Numerical and experimental validation of a three-dimensional combustion diagnostic based on tomographic chemiluminescence. Opt Express 210(6):7050

Casey TA, Sakakibara J, Thoroddsen ST (2013) Scanning tomographic particle image velocimetry applied to a turbulent jet. Phys Fluids, 250(2)

Cho KY, Satija A, Pourpoint TL, Son SF, Lucht RP (2013) Time-Resolved 3D OH planar laser-induced fluorescence system for multiphase combustion. Technical report

Cho KY, Satija A, Pourpoint TL, Son SF, Lucht RP (2014) High-repetition-rate three-dimensional OH imaging using scanned planar laser-induced fluorescence system for multiphase combustion. Appl Opt 530(3):316

Dawson JR, Worth NA (2014) Flame dynamics and unsteady heat release rate of self-excited azimuthal modes in an annular combustor. Combust Flame 1610(10):2565–2578

Doan NA, Swaminathan N (2019) Analysis of markers for combustion mode and heat release in MILD combustion using DNS data. Combust Sci Technol 1910(5–6):1059–1078

Donbar JM, Driscoll JF, Carter CD (2000) Reaction zone structure in turbulent nonpremixed jet flames - From CH-OH PLIF images. Combust Flame 1220(1–2):1–19

Dreizler A, Johchi A, Böhm B, Pareja J, Li T (2018) A study of the spatial and temporal evolution of auto-ignition kernels using time-resolved tomographic OH-LIF. Proc Combust Inst 370(2):1321–1328

Elsinga GE, Scarano F, Wieneke B, van Oudheusden BW (2006) Tomographic particle image velocimetry. Exp Fluids 410(6):933–947

Fanaca D, Alemela PR, Hirsch C, Sattelmayer T (2010) Comparison of the flow field of a swirl stabilized premixed burner in an annular and a single burner combustion chamber. J Eng Gas Turbines Power, 1320(7)

Floyd J, Kempf AM (2011) Computed tomography of chemiluminescence (CTC): high resolution and instantaneous 3-D measurements of a matrix burner. Proc Combust Inst 330(1):751–758

Gilabert G, Lu G, Yan Y (2007) Three-dimensional tomographic reconstruction of the luminosity distribution of a combustion flame. IEEE Trans Instrum Meas 560(4):1300–1306

Halls BR, Thul DJ, Michaelis D, Roy S, Meyer TR, Gord JR (2016) Single-shot, volumetrically illuminated, three-dimensional, tomographic laser-induced-fluorescence imaging in a gaseous free jet. Opt Express 240(9):10040

Hanson RK, Seitzman JM, Paul PH (1990) Planar laser-fluorescence imaging of combustion gases. Appl Phys B Photophys Laser Chem 500(6):441–454

Hassel EP, Linow S (2000) Laser diagnostics for studies of turbulent combustion

He L, Guo Q, Gong Y, Wang F, Yu G (2019) Investigation of OH* chemiluminescence and heat release in laminar methane-oxygen co-flow diffusion flames. Combust Flame 201:12–22

Hori T, Sakakibara J (2004) High-speed scanning stereoscopic PIV for 3D vorticity measurement in liquids. Meas Sci Technol 150(6):1067–1078

Ishino Y, Ohiwa N (2005) Three-dimensional computerized tomographic reconstruction of instantaneous distribution of chemiluminescence of a turbulent premixed flame. JSME Int J Ser B Fluids Thermal Eng 480(1):34–40

Ishino Y, Takeuchi K, Shiga S, Ohiwa N (2008) Non-scanning 3D-CT measurement with 40-lens tracking camera for turbulent propane/air rich-premixed flame. In: 6th International energy conversion engineering conference, IECEC. American Institute of Aeronautics and Astronautics Inc

Jiang N, Slipchenko MN, Jiang N, Slipchenko MN, Roy S, Meyer TR (2016) High-speed three-dimensional tomographic measurements for combustion systems. In 32nd AIAA aerodynamic measurement technology and ground testing conference, pp 1–6. American Institute of Aeronautics and Astronautics Inc, AIAA

Knikker R, Veynante D, Meneveau C (2002) A priori testing of a similarity model for large eddy simulations of turbulent premixed combustion. Proc Combust Inst 290(2):2105–2111

Kohse-Höinghaus K (1994) Laser techniques for the quantitative detection of reactive intermediates in combustion systems

Kychakoff G, Paul PH, Van Cruyningen I, Hanson RK (1987) Movies and 3-D images of flowfields using planar laser-induced fluorescence. Technical Report 13

Lawson JM, Dawson JR (2014) A scanning PIV method for fine-scale turbulence measurements. Exp Fluids, 550(12)

Li T, Pareja J, Becker L, Heddrich W, Dreizler A, Böhm B (2017) Quasi-4D laser diagnostics using an acousto-optic deflector scanning system. Appl Phys B Lasers Opt 1230(3):1–7

Liu H, Sun B, Cai W (2019) kHz-rate volumetric flame imaging using a single camera. Opt Commun 437:33–43

Ma L, Lei Q, Ikeda J, Xu W, Wu Y, Carter CD (2017) Single-shot 3D flame diagnostic based on volumetric laser induced fluorescence (VLIF). Proc Combust Inst 360(3):4575–4583

Mazur M, Nygård HT, Dawson JR, Worth NA (2019) Characteristics of self-excited spinning azimuthal modes in an annular combustor with turbulent premixed bluff-body flames. Proc Combust Inst 370(4):5129–5136

Meyer TR, Halls BR, Jiang N, Slipchenko MN, Roy S, Gord JR (2016) High-speed, three-dimensional tomographic laser-induced incandescence imaging of soot volume fraction in turbulent flames. Opt Express 240(26):29547

Miller VA, Troutman VA, Hanson RK (2014) Near-kHz 3D tracer-based LIF imaging of a co-flow jet using toluene. Meas Sci Technol, 250(7)

Mohamad EJ, Rahim RA, Ibrahim S, Sulaiman S, Manaf MS (2006) Flame imaging using laser-based transmission tomography. Sens Actuators A Phys 1270(2):332–339

Moinul Hossain MM, Lu G, Yan Y (2012) Optical fiber imaging based tomographic reconstruction of burner flames. In: IEEE transactions on instrumentation and measurement, vol 61, pp 1417–1425

Mulla IA, Dowlut A, Hussain T, Nikolaou ZM, Chakravarthy SR, Swaminathan N, Balachandran R (2016) Heat release rate estimation in laminar premixed flames using laser-induced fluorescence of CH2O and H-atom. Combust Flame 165:373–383

Paul PH, Najm HN (1998) Planar laser-induced fluorescence imaging of flame heat release rate. In: Symposium (International) on Combustion, vol. 27, pp 43–50

Pun W, Palm SL, Culick FE (2003) Combustion dynamics of an acoustically forced flame. Combust Sci Technol 1750(3):499–521

Römer GR, Bechtold P (2014) Electro-optic and acousto-optic laser beam scanners. Phys Procedia 560(C):29–39

Sardeshmukh S, Bedard M, Anderson W (2017) The use of OH* and CH* as heat release markers in combustion dynamics. Int J Spray Combust Dyn 90(4):409–423

Unterberger A, Röder M, Giese A, Al-Halbouni A, Kempf A, Mohri K (2018) 3D instantaneous reconstruction of turbulent industrial flames using computed tomography of chemiluminescence (CTC). J Combust, (2018)

Veynante D, Duclos JM, Piana J (1994) Experimental analysis of flamelet models for premixed turbulent combustion. Symp Int Combust 250(1):1249–1256

Wabel TM, Zhang P, Zhao X, Wang H, Hawkes E, Steinberg AM (2018) Assessment of chemical scalars for heat release rate measurement in highly turbulent premixed combustion including experimental factors. Combust Flame 194:485–506

Weinkauff J, Greifenstein M, Dreizler A, Böhm B (2015) Time resolved three-dimensional flamebase imaging of a lifted jet flame by laser scanning. Meas Sci Technol, 260(10)

Wellander R, Richter M, Aldén M (2014) Time-resolved (kHz) 3D imaging of OH PLIF in a flame. Exp Fluids, 550(6)

Wiseman SM, Brear MJ, Gordon RL, Marusic I (2017) Measurements from flame chemiluminescence tomography of forced laminar premixed propane flames. Combust Flame 183:1–14

Worth NA, Dawson JR (2012) Cinematographic OH-PLIF measurements of two interacting turbulent premixed flames with and without acoustic forcing. Combust Flame 1590(3):1109–1126

Worth NA, Dawson JR (2013a) Tomographic reconstruction of OH* chemiluminescence in two interacting turbulent flames. Meas Sci Technol, 240(2)

Worth NA, Dawson JR (2013) Modal dynamics of self-excited azimuthal instabilities in an annular combustion chamber. Combust Flame 1600(11):2476–2489

Worth NA, Dawson JR (2019) Characterisation of flame surface annihilation events in self excited interacting flames. Combust Flame 199:338–351

Wu Y, Xu W, Lei Q, Ma L (2015) Single-shot volumetric laser induced fluorescence (VLIF) measurements in turbulent flows seeded with iodine. Opt Express 230(26):33408

Xu W, Carter CD, Hammack S, Ma L (2017) Analysis of 3D combustion measurements using CH-based tomographic VLIF (volumetric laser induced fluorescence). Combust Flame 182:179–189

Yip B, Fourguette DC, Long MB (1986) Three-dimensional gas concentration and gradient measurements in a photoacoustically perturbed jet. Appl Opt 250(21):3919

Yip B, Miller MF, Lozano A, Hanson RK (1994) A combined OH/acetone planar laser-induced fluorescence imaging technique for visualizing combusting flows. Exp Fluids 170(5):330–336

Yu T, Wang Q, Ruan C, Chen F, Cai W, Lu X, Klein M (2020) A quantitative evaluation method of 3D flame curvature from reconstructed flame structure. Exp Fluids 610(2):61–66

Zhang M, Wang J, Xie Y, Wei Z, Jin W, Huang Z, Kobayashi H (2014) Measurement on instantaneous flame front structure of turbulent premixed CH4/H2/air flames. Exp Thermal Fluid Sci 52:288–296

Zhang M, Wang J, Jin W, Huang Z, Kobayashi H, Ma L (2015) Estimation of 3D flame surface density and global fuel consumption rate from 2D PLIF images of turbulent premixed flame. Combust Flame 1620(5):2087–2097

Publisher's Note Springer Nature remains neutral with regard to jurisdictional claims in published maps and institutional affiliations.

Article III

Scanning PLIF measurement of azimuthally forced swirling flames in an annular combustor

Dirren Govender, and Nicholas A. Worth

Under review for Combustion and Flame

This paper is not yet published and is therefore not included.